p-ISSN 1811-1165
e-ISSN 2413-2179
VOLUME 18, No. 2(36), 2021

EURASIAN PHYSICAL TECHNICAL JOURNAL

E.A. BUKETOV KARAGANDA UNIVERSITY

KARAGANDA, THE REPUBLIC OF KAZAKHSTAN

EURASIAN PHYSICAL TECHNICAL JOURNAL

p - ISSN 1811-1165
e - ISSN 2413-2179

Volume 18, No. 2(36), 2021

1st issue – March, 2004

Journal Founder:

E.A. BUKETOV KARAGANDA UNIVERSITY

Е.А.БӨКЕТОВ АТЫНДАҒЫ ҚАРАҒАНДЫ УНИВЕРСИТЕТІ

КАРАГАНДИНСКИЙ УНИВЕРСИТЕТ ИМ. Е.А. БУКЕТОВА

Contact information:

Editorial board of EPhTJ (Build. 2, room 216)
E.A. Buketov Karaganda University
Universitetskaya Str.28, Karaganda,
Kazakhstan, 100028
Subscription index: 75240

Tel: +7(7212)77-04-03
Fax: +7(7212)77-03-84
E-mail: ephtj@mail.ru

Signed to print on 11.06.2021.
Format 60x84 1/8. Offset paper.
Volume 14,37 p.sh. Circulation 300 copies.
Agreed price. Order No. 63.

Басуға 11.06.2021 ж. қол қойылды.
Пішімі 60×84 1/8. Офсеттік қағазы.
Көлемі14,37 ес.-б.т. Таралымы 300 дана.
Бағасы келісім бойынша. Тапсырыс № 63.

Подписано к печати 11.06.2021.
Формат 60 × 84 1/8. Офсетная бумага.
Объем 14,37 печ.л. Тираж 300 экз.
Цена договорная. Заказ № 63.

Printed in the Publishing House
of the E.A.Buketov KarU

Е.А. Бөкетов атындағы ҚарУ баспасының
баспаханасында басылып шықты

Отпечатано в Издательстве
КарУ имени Е.А.Букетова

Registration Certificate No.4382-Zh, November 7, 2003.
Re-registration Certificate No.KZ50VPY00027647, October 6, 2020 issued by Information Committee of the Ministry of Information and Public Development of the Republic of Kazakhstan

Eurasian Physical Technical Journal, 2021, Vol. 18, No. 2(36)

CONTENTS

Dear authors and readers!
Dear Colleagues!

The formation of the "Eurasian Physical Technical Journal" as an international scientific publication with a non-zero impact factor, indexed in the Scopus database, continues to strengthen. Due to data as of June 4, 2021 the Cite Score 2020 index “Eurasian phys. tech. j." equal to 0.5 with a maximum percentile of 23% in Energy; SJR 2020 = 0.194; SNIP 2020 = 0.182 () (in 2019 the Cite Score was 0.2). At the moment, the Cite Score of 2021 is 0.6.

This confirmation of international recognition was achieved thanks to the “Eurasian phys. tech. j." authors who submitted for publication the results of scientific research on the most pressing problems of modern physics and technology, the high-quality work of the members of the editorial board and reviewers and the financial support of our university.

At the same time, due to the pandemic, 2020 brought a lot of changes in almost all areas of human activity: educational institutions and research centers switched to distance form, some production facilities were forced to suspend their work. There were many losses among colleagues, friends and relatives.

In 2020 professor Daribekov S.D. and his wife died. They made a great contribution to the methodology of teaching physics of our faculty. In May, Academician KM Aryngazin, the first dean of the Faculty of Physics and Technology, would have turned 85 years old, who has trained more than one generation of physicists, teachers, engineers and scientists.

Recently, we received information about the death of Doctor of Physical and Mathematical Sciences, Professor S.E. Kumekov, who worked at the Kazakh National Technical University named after K. Satpayev (Almaty). Full member of the Academy of Sciences of the Higher School and the Academy of Natural Sciences of the Republic of Kazakhstan, professor S.E. Kumekov successfully combined scientific and pedagogical work with organizational work. Almost from the very foundation of “Eurasian phys. tech. j. " was a member of the editorial board, colleagues remember his valuable advice and recommendations aimed at improving the quality of articles.

More than a year in quarantine conditions led us to a reassessment of everything around. There are an understanding of the value of each day of life and communication with loved ones and colleagues even remotely, the need to talk about warm relationships and wishes for good health and well-being. By tradition, we congratulate the birthday - editors and experts.

We congratulate the doctor of physical and mathematical sciences, professor of the Kazakh National University named after Al-Farabi named after al-Farabi Turmukhambetov Akylbek Zhursunovich on the 75th anniversary passed at February 2021! Professor A.Zh. Turmukhambetov is known as a representative of the Kazakh scientific school of thermal physics. He worked at the our Faculty of the E.A. Buketov Karaganda University for more than 30 years, having gone through the path of education from a teacher, associate professor, head of the department and dean. Author of over 200 publications, including monographs, textbooks and articles in prestigious publications. Hi is well known as an erudite professional, an experienced teacher and a principled leader who has brought up more than one generation of teachers, engineering and scientific personnel. Akylbek Zhursunovich has been an expert in the editorial board of “Eurasian phys. tech. j.”, works in joint scientific projects.

On May 4, 2021 member of the editorial board of “Eurasian phys. tech. j.”, professor Alexander Alekseevich Potapov celebrated his 70th birthday. Professor A.A. Potapov is a Chief Researcher at the Institute of Radio Engineering and Electronics named after V.A. Kotelnikov RAS, Moscow, Academician of the Russian Academy of Natural Sciences since 2007, Academician of the A. Prokhorov Academy of Engineering Sciences since 2008, President of the Chinese-Russian Laboratory of Information Technologies and Fractal Signal Processing, Guangzhou, China since 2011. A.A. Potapov was awarded 18 medals for outstanding achievements in the field of engineering sciences in the creation of fundamentally new fractal information technologies, awarded the title of Honorary Radio Operator of the Russian Federation (2006). He is author of fundamental research in the field of fractal and textural approaches to the problems of radio physics, radio engineering, radar and a wide range of related scientific and technological areas.

Professor A.A. Potapov is an initiator of pioneering research and development in the field of application of the theory of fractals in radiophysics, large-scale effects and fractal operators in radio systems in Russia. Currently, under the leadership of Potapov A.A. a unique scientific school of fractal methods was created, where he and his students formed a new fundamental direction "Fractal radiophysics and fractal radio electronics: construction of fractal radio systems". He published in over 1150 scientific papers, including over 45 monographs, 2 patents and 9 textbooks, according to the results of scientific works on fractal and texture processing of information in the presence of intense noise, on fractal radio systems and fractal radioelements, etc.

We sincerely wish our anniversaries good health, prosperity, great creative successes and achievements. We hope that in the future your work as a member of the editorial board will contribute to strengthening international cooperation and improving the quality of “Eurasian phys. tech. j."

This issue presents original scientific articles devoted to solving urgent problems of modern technical physics. The use of modern research methods allows authors to find new properties. For example, the possibility of obtaining macroscopic mesoporous structures with noticeably reduced values of the Curie temperature has been established. The description of the pore morphology was carried out using the methods of fractal geometry. In another work, modeling on the basis of a nonlinear fractal model of the relationship between the distance to the observed galaxy and its coordinate made it possible to determine the value of the global Hubble parameter from astrophysical observations without using the ΛCDM model.

Researchers at the Institute of Molecular Nanophotonics have succeeded in obtaining carbon quantum dots using the method of microwave synthesis using modern instrumental equipment. Another study showed that the addition of silver nanoparticles to porous alumina films leads to an increase in the absorption cross section and an increase in the quantum yield of dye fluorescence in porous alumina films. The results of a nanoscale study of the kinetics of radiation damage to heat-conducting, insulating and mechanical properties in polycrystalline ceramics based on aluminum nitride under irradiation with helium and hydrogen ions have interesting application in future.

The results of studying the electrical transfer in ceramic samples of Li – Ti ferrites sintered under radiation-thermal conditions; the influence of preliminary annealing of films of zinc acetate solution on the morphology, structure, optical properties of the formed ZnO films and also on the photovoltaic properties of polymer solar cells, etc. have an important practical application. The developed thermoacoustic converter of heat into mechanical vibrations, which are then converted into electric current, is very interesting from a practical point of view. The proposed methods of reducing the flammability of polymers by adding a matrix of special substances with the properties of blocking the combustion process are important for practice.

Our authors used modern instrumental and industrial equipment in their studies, for example, processing on an industrial pulsed accelerator in air, scanning electron microscopy, X-ray phase analysis and differential scanning calorimetry, etc. Modeling of macro and micro phenomena was carried out using modern numerical methods, and the use of computer analysis made it possible to create an effective energy analyzer of charged particle beams based on multipole electrode systems and to develop an algorithm for processing satellite data.

We hope that the proposed scientific works will interest our readers, as well as the materials of the next issues.

Respectfully,
Chief Editor, Saule E. Sakipova
Kazakhstan, June, 2021

DOI 10.31489/2021No2/6-11

UDC 537.622.3, 537.622.4, 539.611, 544.011, 544.226

ON THE TRANSITION BETWEEN FERROMAGNETIC AND PARAMAGNETIC STATES IN MESOPOROUS MATERIALS WITH FRACTAL MORPHOLOGY

Shishulin A.V.[1,*], Potapov A.A.[2,3], Shishulina A.V.[4,5]

[1]G.A. Razuvaev institute of organometallic chemistry, Russian Academy of sciences, Nizhny Novgorod, Russia, chichouline_alex@live.ru

[2]V.A. Kotel'nikov institute of radio engineering and electronics, Russian Academy of sciences, Moscow, Russia

[3]JNU-IREE RAS Joint Laboratory of Information Technology and Fractal Processing of Signals, Jinan University, Guangzhou, China

[4]R.E. Alekseev Nizhny Novgorod State technical University, Nizhny Novgorod, Russia

[5]N.I. Lobachevsky Nizhny Novgorod State University, Nizhny Novgorod, Russia

In this paper, we have shown how the presence of pores and pore morphology influence on magnetic phase transition temperatures in mesoporous ferromagnetic materials. Model calculations have demonstrated the possibility to obtain macroscopic mesoporous samples with notably reduced Curie temperatures which is also further depressed in the case the pore morphology is more complicated. The results have been obtained on the basis of the experimentally verified correlation between the Curie temperature and cohesive energy of the material and illustrated using the examples of pure mesoporous iron, nickel and cobalt while pore morphology has been determined by the methods of fractal geometry. Several practical applications of mesoporous materials with tuned values of the Curie temperature have also been discussed in the final section.

Keywords: mesoporous materials, second-order phase transition, ferromagnetism, Curie temperature, cohesive energy.

Introduction

Nanostructured ferromagnetic materials are objects of a considerable interest among researchers [1]. Tremendous attention is being attracted to such materials in recent years due to a wide range of their technological applications including high-density information storage devices [2], magneto-optical sensors [3], spintronics devices [4], biomedical technologies [5] etc, as well as a set of phenomena of fundamental interest such as superparamagnetism [6], giant magnetoresistance [7, 8], complicated dynamics of magnetic skyrmions [9] or magnetic catalysis [10]. One of the main and vital parameters which determine the behavior of ferromagnetic materials is the Curie temperature (temperature of a second-order phase transition when magnetic ordering disappears and ferromagnetic materials become paramagnetic). It is well-known that nanoscale particles or grains of a ferromagnetic material exhibit a lower Curie temperature [11-20] which is (as well as some other parameters, e.g. the saturation magnetization [16], characteristics of hysteresis loops [20] or magnetic anisotropy constants [21]) size- [11-20] and shape-dependent [14,15,20]. Such size- and shape effects in nanoparticles are commonly related to an increase in the surface-to-volume ratio with decreasing the size of a nanoparticle and "complicating" its shape which causes an increase in the fraction of lower coordinated atoms near the surface edge with magnetic characteristics (e.g. magnetic moments, exchange integrals etc. [19]) different from the bulk ones. Such regularities could be described using various approaches including models based on the spin-spin correlation length mechanism [11], on the bond order-length-strength correlation combined with the Ising preposition [12],on Monte-Carlo [19,20] and molecular-statics simulations on the Ising model [20] or on the size- and shape-dependent cohesive energy of nanostructures [14-16].

Note that high surface-to-volume ratios and fractions of surface atoms could be obtained not only in nanopowders or in nanocomposites containing nanoparticles distributed in a matrix, but also in microporous and mesoporous materials, while porous samples of such materials can be macroscopic-sized [22-24]. Formation of such structures is possible, for example, during the early stages of spark plasma sintering [25],

laser sintering [26] of nanopowders (a review of synthesis methods of nanosized powders has been presented by M.K. Berner *et al* [27]) as well as using a variety of other techniques, e.g. [28].

1. A cohesive energy-based model for magnetic phase transitions in mesoporous media.

The object of simulation is a mesoporous material with the given volume fraction of pores, α. In order to take into account possible irregular and complicated pore shapes [28], let us introduce two parameters for their description. The first one is the effective diameter of the pore, d_{eff}, which is equal to the diameter of a spherical pore of the same volume, and the second one could be, for example, the pore shape coefficient, k. The shape coefficient is the ratio between the surface area of the pore under consideration, A, and the surface area of the sphere of the same volume, A_0: $k = A/A_0$ (in details, such approach and its variants have been described in [29-32], being applied to porous structures. In [33], some other geometry considerations could be found). The number of pores in 1 g of a material, N_{por}, could be calculated as $N_{por} = 6\alpha \cdot 1\,\mathrm{g} \big/ \left(\pi\rho d_{eff}^3\right)$ where ρ is the material density. Factor 1 g has been introduced to match the units. The specific surface area, A_{sp}, could be expressed as $A_{sp} = N_{por} \cdot \pi k d_{eff}^2 = 6\alpha k \cdot 1\,\mathrm{g} \big/ \left(\rho d_{eff}\right)$. To estimate the influence of the pore morphology on the Curie temperature of a mesoporous material, let us use a simple expression describing the relation between the Curie temperature of a material and its cohesive energy:

$$\frac{T_c^{por}}{T_c^{bulk}} = \frac{E_{coh}^{por}}{E_{coh}^{bulk}}. \tag{1}$$

Here, E_{coh}^{por} and E_{coh}^{bulk} are the cohesive energies of porous and continuous materials, respectively; T_c^{por} and T_c^{bulk} are the Curie temperatures of a porous material and a material in the absence of pores, respectively.

This expression has been retrieved in Refs. [13-16] and experimentally justified by the authors of [16]. This expression is similar to the one used by G. Guisbiers, *et al* to describe different size-and shape-dependent material properties [34-36] and also found to be in a good agreement with experimental data. 1g of a porous material contains N atoms, where $N = 6\omega \cdot 1\,\mathrm{g} \big/ \left(\pi d_{at}^3 \cdot \rho\right)$. Here, d_{at} is the atomic diameter and ω is the lattice packing parameter in the crystal structure. N_s atoms are located on the pore walls: $N_s = \eta A_{sp} \big/ \pi d_{at}^2 = 6\alpha\eta k \cdot 1\,\mathrm{g} \big/ \left(\pi\rho d_{at}^2 d_{eff}\right)$ where η is the surface packing parameter. So, the number of atoms at the surface is given by

$$N_s = \left(\frac{6 \cdot 1\,\mathrm{g}}{\pi\rho}\right)^{1/3} \cdot \frac{\alpha\eta k}{\omega^{2/3} d_{eff}} N^{2/3}. \tag{2}$$

The estimates for the cohesive energy of a porous material could be obtained using the relations suggested by F. Aqra and A. Ayyad [37]:

$$\begin{aligned} E_{coh}^{bulk} &= \frac{1}{2}\beta N \varepsilon_b, \\ E_{coh}^{por} &= \frac{1}{2}\beta\varepsilon_b \left(\frac{1}{4}N_s + \left(N - N_s\right)\right), \end{aligned} \tag{3}$$

where β is the number of bonds per one atom in the structure and ε_b is the bond energy.

Therefore, from Eqs. (1-3) we have

$$E_{coh}^{por} = \frac{1}{2}\beta\varepsilon_b N \left(1 - \frac{3}{4}\left(\frac{6 \cdot 1\,\mathrm{g}}{\pi\rho}\right)^{1/3} \frac{\alpha\eta k}{\omega^{2/3} d_{eff}} N^{-1/3}\right), \tag{4}$$

$$T_c^{por} = T_c^{bulk} \left(1 - \frac{3}{4}\left(\frac{6 \cdot 1\,\mathrm{g}}{\pi\rho}\right)^{1/3} \frac{\alpha\eta k}{\omega^{2/3} d_{eff}} N^{-1/3}\right). \tag{5}$$

.

Below, the Curie temperatures of mesoporous materials have been estimated by using Eq. 5. High values of shape coefficient k could be obtained, for example, in the case of porous materials where the pores have the shapes similar to simple non-spherical geometric structures (for example, k=1.49 for a tetrahedron, k=1.52 for a cone, k=3.20 for a star icosahedron (an icosahedron with a tetrahedron at each face)) or structures extended in one direction (for example, values k>2.00 correspond to oblate spheroids with aspect ratio a/b>5 or to prolate spheroids with a/b>3). Moreover, high surface-to-volume ratios are also characteristic for pores of complicated and irregular shapes, in order to take into account their morphology, the notion of fractal geometry is often used [29,30,38-42]. According to the approach suggested by us in [30, 40-42], the shape of a pore can be characterized by its fractal dimension D which correlates its volume V and surface area A: $A = CV^{2/D}$, where C is a numerical coefficient.

Without any losses of generality, coefficient C, which also matches dimensions, is accepted below to be 4π for the sake of convenience. For real irregular morphologies of materials structure elements, D<3 and is typically non-integer. The most classic examples of fractal structures are *worm-like*, *amoeba-like,* and *porcupine-like* ones [30, 40-43].

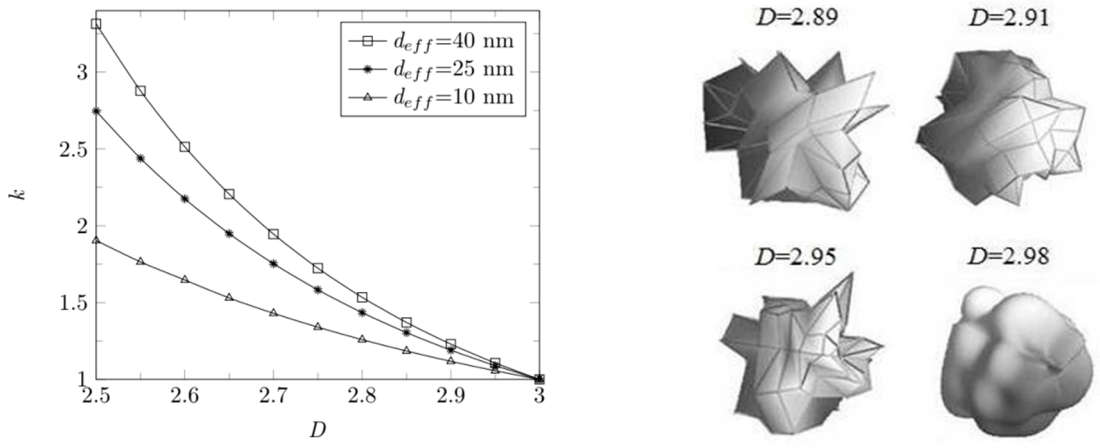

a *b*

Fig. 1. a) shape coefficient k of a pore versus its effective diameter d_{eff} and fractal dimension D; b) examples of "amoeba-like" and "porcupine-like" fractal structures with various D.

The correlation between shape coefficient k (the ratio between the surface areas of the pore under consideration and the spherical pore of the same volume), pore volume $V = \pi d_{eff}^3/6$ and its fractal dimension D is determined as follows: $k(V,D) = V^{2/D}/(3V/4\pi)^{2/3}$ (see Fig. 1a). Several examples of *amoeba-like* and *porcupine-like* structures with various fractal dimensions are presented in Fig. 2b.

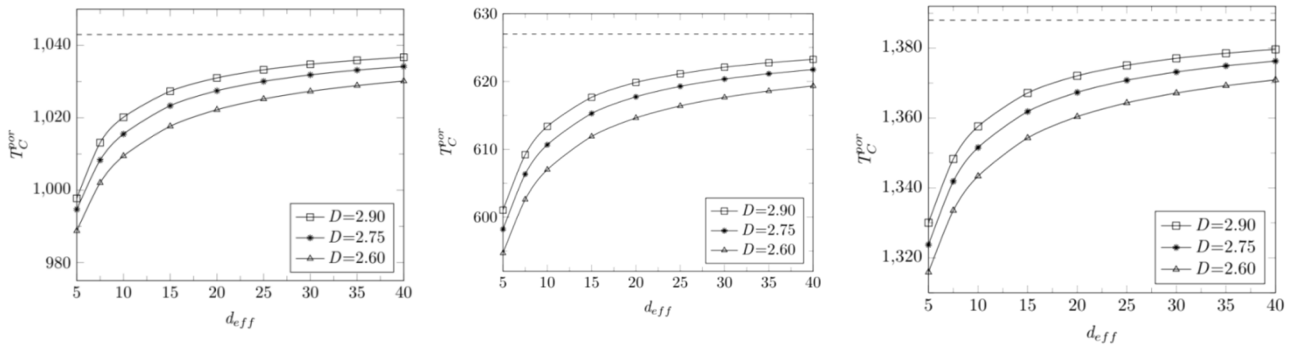

a *b* *c*

Fig. 2. The dependences of the Curie temperatures for mesoporous Fe (a), Ni (b), Co (c) on pore geometric characteristics (fractal dimensions D and effective diameters d_{eff} of pores). The Curie temperatures for continuous macroscopic samples are 1043 for Fe, 627 K for Ni,1388 K for Co.

It is necessary to note that such parameters as shape coefficients or fractal dimensions generalize different but equivalent variants of materials morphology: the structures which differ in their geometric outlook but share the same values of k or D (see Fig. 1b in [41], for example) have the same fraction of surface atoms and demonstrate the same behavior in the case considered in the present paper.

Specific surface areas in micro- and mesoporous materials can reach extremely high values (from 500m^3/g [22] to 1000 m^3/g [23] or even several thousands of m^3/g [24]). In the present paper, however, we limit ourselves to considering materials with not very high specific surface areas (in comparison with the values obtained in [22-24]), mostly below 200-300 m^3/g (α=0.85). The dependences of the Curie temperature on pore size and shape for mesoporous iron (*a*), nickel (*b*) and cobalt (*c*) are plotted in Fig. 2. For these metals, material densities and atomic diameters are accepted in our estimates to be 7.874 g/cm^3 and 252 pm, respectively, for Fe; 8.902 g/cm^3 and 248 pm, respectively, for Ni; 8.900 g/cm^3 and 250 pm, respectively, for Co. The structure of nickel is *fcc* within the entire temperature range up to the melting point. At the same time, cobalt has two stable polymorphic modifications: β-Co with a *fcc* crystal lattice which is equilibrium in the considered temperature range and low-temperature hexagonal α-Co (the temperature of the α↔β polymorph transition is about 700 K). At the temperatures under consideration, the structure of Fe is *bcc* (α-Fe), iron exhibits the α↔γ polymorph transition between *bcc* and *fcc* modifications at about 1190 K. Packing parameters are ω=0.74, η = 0.91 for *fcc* structures [37,44] and ω=0.68, η = 0.83 for *bcc* ones [44].

Fig. 2 shows that reducing the effective pore diameter, d_{eff}, and increase the shape coefficient, k, (an increase in the specific surface area of a material) are accompanied with a decrease in the Curie temperature. Note that in the case of pores filled with a substance, such estimates are to be corrected, for example, by modifying the approach suggested by C. Ling-fei *et al*. [14] for embedded nanoparticles. Increasing the specific surface area of porous materials up to the values obtained experimentally by the authors of [22-24] allows expecting much more significant shifts of the magnetic transition temperatures similar to the ones obtained in [19] for free-standing nanoparticles.

Conclusion

It is also worth noting that micro- and mesoporous materials (with functionalized pore walls [45], maybe) have a wide range of technological applications e.g. nanoreactor matrices [46]. For multiple applications, a great interest is attracted by magnetocaloric effects in ferromagnetic nanostructures, for example, heating ferromagnetic nanoparticles - invasive agents in alternating magnetic fields (magnetic hyperthermia treatment for cancer) due to hysteresis losses, losses for re-orientation of the magnetization vector etc. and maintaining their temperature near the Curie point [5, 47]. In the case considered in this paper, the possibility to tune the Curie temperature of materials by preparing the samples with different pore morphologies and specific surface areas shows possibilities to obtain mesoporous materials/nanoreactors with self-imposed limits of raising the temperature in alternating magnetic fields and the possibility of autonomous temperature control. The considered ferromagnetic materials have also high catalytic activity in a variety of commonly used chemical reactions [36]; meanwhile, materials with a higher specific surface area of pores (up to the ones from [24]) allow expecting a more significant decrease in the Curie temperatures down to the values demonstrated in [19].

Acknowledgments

The research has been performed in the framework of the state task for IOMC RAS.

REFERENCES

1 Binns C. (ed.) *Nanomagnetism: fundamentals and applications*. Newnes, Front. nanosc. 2014, 328 p.

2 Tannous C., Comstock R.L. *Magnetic information-storage materials.* In: Springer handbook of electronic and photonic materials. Cham, Springer. 2017, pp. 1185 – 1220. https://doi.org/10.1134/S1063776117010046.

3 Wang S.X., Li G.. Advances in giant magnetoresistance biosensors with magnetic nanoparticle tags: review and outlook. *IEEE trans. magn.* 2008, Vol. 44, pp. 1687 – 1702. https://doi.org/10.1109/TMAG.2008.920962.

4 Lashkarev G.V., Radchenko M.V., Bugaiova M.E., et.al. Ferromagnetic nanocomposites as spintronic materials with controlled magnetic structure. *Low temp. phys.* 2013, Vol. 39, No. 1, pp. 66–75. https://doi.org/10.1063/1.4776232.

5 Spirou S.V., Basini M., Lascialfari A., et al. Magnetic hyperthermia and radiationtherapy: radiobiological principles and current practice. *Nanomaterials.* 2018, Vol. 8, No. 401. https://doi.org/10.3390/nano8060401.

.

6 Mihaela O. Study about the possibility to control the superparamagnetism-superferromagnetism transition in magnetic nanoparticle systems. *J. magn. magn. mater.* 2013, Vol. 343, pp. 189 – 193. https://doi.org/10.1016/j.jmmm.2013.05.011.

7 Marrows C.H., Perez M., Hickey B.J. Finite size scaling effects in giant magnetoresistance multilayers. *J. phys.: condens. matter.* 2006, Vol. 18, No. 243. https://doi.org/10.1088/0953-8984/18/1/017.

8 Lobov I.D., Kirillova M.M., Romashev L.N., et al. Magnetorefractive effect and giant magnetoresistance in Fe(t_x)/Cr superlattices. *Phys. solid state*. 2009, Vol. 51, No. 12, pp. 2337 – 2341. https://doi.org/10.1134/S1063783409120099.

9 Temiryazev A.G., Temiryazeva M.P., Zdoroveyshchev A.V., et al. Formation of a domain structure in multilayer CoPt films by magnetic probe of an atomic force microscope. *Phys. solid state*. 2018, Vol. 60, No. 11, pp. 2200 – 2206. https://doi.org/10.1134/S1063783418110318.

10 Filev V.G., Raskov R.C. Magnetic catalysis of chiral symmetry breaking: a holographic perspective. *Adv. high energy phys*. 2010, No. 473206. https://doi.org/10.1155/2010/473206.

11 Fisher M.E, Barber M.N. Scaling theory for finite-size effects in the critical region. *Phys. rev. lett.* 1972, Vol. 28, pp. 1516 – 1519. https://doi.org/10.1103/PhysRevLett.28.1516.

12 Sun C.Q., Zhong W.H., Li S., et al. Coordination imperfection suppressed phase stability of ferromagnetic, ferroelectric, and superconductive nanosolids. *J. phys.chem. B.* 2004, Vol. 108, pp. 1080 – 1084. https://doi.org/10.1021/jp0372946.

13 Yang C.C., Jiang Q. Size and interface effects on critical temperatures of ferromagnetic, ferroelectric and superconductive nanocrystals. *Acta mater.* 2005, Vol. 53, pp. 3305 – 3311. https://doi.org/10.1016/j.actamat.2005.03.039.

14 Ling-fei C., Dan X., Ming-xing G., et al. Size and shape effects on Curie temperature of ferromagnetic nanoparticles. *Trans. nonferrous met. soc. China.* 2007. Vol. 17, pp. 1451 – 1455. https://doi.org/10.1016/S1003-6326(07)60293-3.

15 Delavari H., Hosseini H.M., Simchi A. A simple model for the size- and shape-dependent Curie temperature of freestanding Ni and Fe nanoparticles based on the average coordination number and atomic cohesive energy. *J. chem. phys.* 2011, Vol. 383, pp. 1 – 5. https://doi.org/10.1016/j.chemphys.2011.03.010.

16 He X., Zhong W., Au C.-T., et al. Size dependence of the magnetic properties of Ni nanoparticles prepared by thermal decomposition method. *Nanoscale res. lett.* 2013, Vol. 8, No. 446. https://doi.org/10.1186/1556-276X-8-446.

17 Nikiforov V.N., Koksharov Yu.A., Polyakov S.N., et al. Magnetism and Verwey transition in magnetite nanoparticles in thin polymer film. *J. alloys compd*. 2013, Vol. 569, pp. 58 – 61. https://doi.org/10.1016/j.jallcom.2013.02.059.

18 Shuai Z., Li H. Size-dependent piezoelectric coefficient and Curie temperature of nanoparticles. *Nanomaterials and energy*. 2017, Vol. 6, No. 2, pp. 53 – 58. https://doi.org/10.1680/jnaen.16.00014.

19 Nikiforov V.N., Ignatenko A.N., Irkhin V.Yu. Size and surface effects on the magnetism of magnetite and maghemite nanoparticles. *J. exp. theor. phys.* 2017, Vol. 124, No. 2, pp. 304 – 310. https://doi.org/10.1134/S1063776117010046.

20 Essajai R., Benhouria Y., Rachadi A., et al. Shape-dependent structural and magnetic properties of Fe nanoparticles studied through simulation methods. *RSC adv*. 2019, Vol. 9, pp. 22057 – 22063. https://doi.org/10.1039/C9RA03047F.

21 Stolyar S.V., Komogortsev S.V., Chekanova L.A., et al. Magnetite nanocrystals with a high magnetic anisotropy constant due to the particle shape. *Tech. phys. lett.* 2019, Vol. 45, No. 9, pp. 878 – 881. https://doi.org/10.1134/S1063785019090116.

22 Gaev D.S., Rekhviashvili S.Sh. Kinetics of crack formation in porous silicon. *Semiconductors*. 2012, Vol. 46, No. 2, pp. 137 – 140. https://doi.org/10.1134/S1063782612020108.

23 Błaszczyński T., Ślosarczyk A., Morawski M. Synthesis of silica aerogel by supercritical drying method. Procedia eng. 2013, Vol. 57, pp. 200 – 206. https://doi.org/10.1016/j.proeng.2013.04.028.

24 Chae H.K., Siberio-Pérez D.Y., Kim J., et al. A route to high surface area,porosity and incusion of large molecules in crystals. *Nature*. 2004, Vol. 427, pp. 523 – 527. https://doi.org/10.1038/nature02311.

25 Chuvil'deev V.N., Nokhrin A.V., Kopylov V.I., et al. Spark plasma sintering for high-speed diffusion bonding of the ultrafine-grained near-α Ti–5Al–2V alloy with high strength and corrosion resistance for nuclear engineering. *J. mater. sci*. 2019, Vol. 54, pp. 14926 – 14949. https://doi.org/10.1007/s10853-019-03926-6.

26 Ganeriwala R., Zohdi T.I. Multiphysics modeling and simulation of selective laser sintering manufacturing processes. *Procedia CIRP*. 2014, Vol. 14, pp. 299 – 304. https://doi.org/10.1016/j.procir.2014.03.015.

27 Berner M.K., Zarko V.E., Talawar M.B. Nanoparticles of energetic materials: synthesis and properties (review). *Combust., explos., shock waves*. 2013, Vol. 49, pp. 625 – 647. https://doi.org/10.1134/S0010508213060014.

28 Hakamada M., Mabuchi M. Nanoporous Ni fabricated by dealloying of rolled Ni-Mn sheet. *Procedia eng*. 2014, Vol. 81, pp. 2159 – 2164. https://doi.org/10.1016/j.proeng.2014.10.302.

29 Zhanabaev Z.Zh., Ibraimov M.K., Sagidolda E. Electrical properties of fractal nanofilms of porous silicon. *Eurasian phys. tech. j.* 2013, Vol. 10, No.1, pp. 3 – 6.

30 Shishulin A.V., Fedoseev V.B. On some peculiarities of stratification of liquid solutions within pores of fractal shape. *J. mol. liq*. 2019, Vol. 278, pp. 363 – 367. https://doi.org/10.1016/j.molliq.2019.01.050.

31 Shishulin A.V., Fedoseev V.B. Peculiarities of phase transformations of polymer solutions in deformable porous matrices. *Tech. phys. lett*. 2019, Vol. 45, No. 7, pp. 697 – 699. https://doi.org/10.1134/S1063785019070289.

32 Shishulin A.V., Fedoseev V.B. Stratifying polymer solutions in microsized pores: phase transitions induced by deformation of a porous material. *Tech. phys*. 2020, Vol. 65, No. 3, pp. 340 – 346. https://doi.org/10.1134/S1063784220030238.

33 Magomedov M.N. Size dependence of the shape of a silicon crystal during melting. *Tech. phys. lett*. 2016, Vol. 42, No. 7, pp. 761 – 764. https://doi.org/10.1134/S1063785016070245.

34 Guisbiers G., Buchaillot L. Universal size/shape-dependent law for characteristic temperatures. *Phys. lett. A*. 2009, Vol. 374, pp. 305 – 308. https://doi.org/10.1016/j.physleta.2009.10.054.

35 Guisbiers G. Size-dependent materials properties toward a universal equation. *Nanoscale res. lett.* 2010, Vol. 5, No. 1132. https://doi.org/10.1007/s11671-010-9614-1.

36 Guisbiers G., Abudukelimu G. Influence of nanomorphology of the melting and catalytic properties of convex polyhedral nanoparticles. *J. nanopart. res*. 2013, Vol. 15, No. 1431. https://doi.org/10.1007/s11051-013-1431-x.

37 Aqra F., Ayyad A. Surface free energy of alkali and transition metal nanoparticles. *Appl. surf. sci*. 2014, Vol. 324, pp. 308 – 313. https://doi.org/10.1016/j.apsusc.2014.07.004.

38 Potapov A.A. On the issues of fractal radio electronics: Processing of multidimensional signals, radiolocation, nanotechnology, radio engineering elements and sensors. *Eurasian phys. tech. j.* 2018, Vol. 15, No. 2, pp. 5 – 15.

39 Fedoseev V.B., Potapov A.A., Shishulin A.V., Fedoseeva E.N. Size and shape effect on the phase transitions in a small system with fractal interphase boundaries. *Eurasian phys. tech. j.* 2017, Vol. 14, No.1, pp. 18 – 24.

40 Shishulin A.V., Fedoseev V.B., Shishulina A.V. Melting behavior of fractal-shaped nanoparticles (the example of Si-Ge system). *Tech. phys.* 2019, Vol. 64, No. 9, pp. 1343 – 1349. https://doi.org/10.1134/S1063784219090172.

41 Shishulin A.V., Fedoseev V.B. On mutual solubility in submicron-sized particles of the Pt-Au catalytic system. *Kinet. catal*. 2019, Vol. 60, No. 3, pp. 315-319. https://doi.org/10.1134/S0023158419030121.

42 Shishulin A.V., Potapov A.A., Fedoseev V.B. *Phase equilibria in fractal core-shell nanoparticles of* $Pb_5(VO_4)_3Cl$ – $Pb_5(PO_4)_3Cl$ *system: the influence of size and shape*. In: Z. Hu, S. Petoukhov, M. He (eds.). Advances in artificial systems for medicine and education II. Cham., Springer. 2020, pp. 405 – 413. https://doi.org/10.1007/978-3-030-12082-5_37.

43 Fedoseev V.B., Shishulin A.V. On the size distribution of dispersed fractal particles. *Tech. phys*. 2021, Vol. 66, No. 1, pp. 34 – 40. https://doi.org/10.1134/S1063784221010072.

44 Attarian Shandiz M. Effective coordination number model for the size dependency of physical properties of nanocrystals. *J. phys.: condens. matter*. 2008, Vol. 20, No. 325237. https://doi.org/10.1088/0953-8984/20/32/325237.

45 Len'shina N.A., Arsenyev M.V., Shurygina M.P., et al. Photoreduction of o-benzoquinone moiety in mono- and poly(quinone methacrylate) and on the surface of polymer matrix pores. *High energy chem*. 2017, Vol. 51, pp. 209 – 214. https://doi.org/10.1134/S0018143917030080.

46 Bronstein L.M., Sidorov S.N., Valetskii P.M. Nanostructured polymeric systems as nanoreactors for nanoparticle formation. *Russ. chem. rev.* 2004, Vol. 73, No. 5, pp. 501 – 515. https://doi.org/10.1070/RC2004v073n05ABEH000782.

47 Villanueva A., De la Presa P., Alonso J.M., et al. Hyperthermia *hela cell* treatment with silica-coated manganese oxide nanoparticles. *J. phys. chem. C*. 2010, Vol. 114, pp. 1976–1981. https://doi.org/10.1021/jp907046f.

Article accepted for publication 23.04.2021

.

DOI 10.31489/2021No2/12-17

UDC 535.34, 535.372, 54.05

SPECTRAL AND LUMINESCENT PROPERTIES OF CARBON QUANTUM DOTS FUNCTIONALIZED WITH N- AND S-CONTAINING GROUPS

Ibrayev N.Kh., Dzhanabekova R.Kh., Amanzholova G.S.

Institute of molecular nanophotonics, E.A Buketov Karaganda University, Karaganda, Kazakhstan, rumiya_j@mail.ru

In the presented work, carbon quantum dots were obtained by microwave synthesis based on citric acid and L-cysteine. The resulting particles were characterized by electron and probe microscopy, dynamic light scattering and Fourier transform infrared spectroscopy. The spectral and luminescent properties were investigated for the initial solution of carbon quantum dots, as well as solutions obtained as a result of dialysis of the synthesized product. It is shown that all samples exhibit the same optical properties. At the same time, the measurement of quantum yields showed that carbon dots that have passed through the dialysis membrane have the best fluorescent ability.

Keywords: carbon quantum dots, microwave synthesis, fluorescence, electron microscopy, atomic force microscopy, fluorescence quantum yield.

Introduction

Carbon quantum dots (CQDs) are nanoparticles less than 10 nm in size with a carbon structure [1, 2]. This new member of the family of carbon nanomaterials is attracting more and more attention due to its promising properties, such as fluorescent radiation, chemical inertness, resistance to photobleaching, high water solubility, low toxicity, biocompatibility, and relatively simple and cheap synthesis methods. All these properties make carbon dots a promising material in such areas as photocatalysis, sensing, bioimaging, solar energy conversion, and the creation of light-emitting diodes [1-4]. There are two main approaches to obtaining CQDs: “top-down” and “bottom-up”. The first group includes mechanical grinding, laser ablation, chemical oxidation, electrochemical oxidation. Methods such as microwave synthesis, hydrothermal synthesis, and pyrolysis belong to the second approach to CQDs production. A variety of hydrocarbons, including vegetable and food ones, can be used as raw materials [2, 3].

Despite the fact that there are quite a few synthesis methods and applications for CQDs, the question of the source of fluorescence is still unclear. It is believed that the fluorescence of carbon quantum dots is determined by their size and the presence of functional groups [5-7], at the same time, some studies have revealed the contribution of molecular fluorophores to the fluorescence of carbon dots] [8-10]. For example, Essner's group showed that fluorescent impurities are formed as by-products of the synthesis of carbon dots, and CQDs must be sufficiently purified to obtain reliable results [10]. The aim of work is to study the spectral and luminescent properties of carbon dots functionalized with N- and S-containing groups. To study the effect of the carbon dots size on their optical properties, the synthesized product was purified by dialysis. Comparative studies of the initial solution (without dialysis), the dialysate obtained on the first day, and the solution remaining in the dialysis bag (retentate) were carried out.

1. Experimental part

Carbon quantum dots were obtained by microwave synthesis from citric acid (Sigma Aldrich) and L-cysteine (Sigma Aldrich). An equimolar aqueous solution of the starting materials (5 ml) in a borosilicate glass tube was placed in a Monowave 200 microwave reactor (Anton Paar) and heated at 200 °C for an hour with vigorous stirring. Then the solution was cooled to 70 °C in a microwave reactor, and then to room temperature in vivo. As a result of the synthesis, a dark brown solution was obtained, which, according to the literature data [3, 5, 7], indicates the formation of carbon quantum dots. To remove large particles, the resulting solution was centrifuged at 10,000 rpm for 30 minutes. The decantate for further purification was dialyzed using a dialysis bag (MWCO 3.5 kDa) for 48 hours with periodic replacement of the dialysate with pure water. The structure and sizes of carbon dots were studied using a scanning electron microscope MIRA

3 (TESCAN) using a transmitted electron detector (STEM), an atomic force microscope JSPM-5400 (JEOL), and dynamic light scattering on a submicron particle size analyzer Zetasiser Nano ZS (Malvern).

FTIR spectra were obtained on an FSM 1201 FT-IR spectrometer (Infraspec). Absorption spectra were measured on a Carry 300 spectrophotometer (Agilent). Luminescence spectra and luminescence excitation spectra were measured on an Eclips spectrofluorimeter (Agilent). The kinetics of fast fluorescence of CQDs solutions was measured on a pulsed spectrofluorometer with picosecond resolution and recording in the time-correlated photon counting mode (Becker & Hickl). The fluorescence of the samples was excited using a pulsed semiconductor laser with a generation wavelength λ_{gen} = 375 nm. The kinetic curves were analyzed using the SPCM-Image software (Becker & Hickl). The fluorescence quantum yield was measured by the absolute method using an AvaSphere 30-REFL integrating sphere and an AvaSpec-ULS2048 spectrometer (Avantes) [11, 12].

2. Results and discussion

Fig. 1 and Fig. 2 show STEM and AFM images of carbon dots from the initial solution and retentate. In the initial solution particles with sizes from 10 nm to 400 nm are observed, the average size is 50 nm ± 10 nm. Large particles are irregular, small and medium particles are rounded. The AFM image shows that the maximum particle height is no more than 1.57 nm. STEM images of CQDs that have not passed through the dialysis membrane show large rounded particles ranging in size from several tens of nanometers to several micrometers and irregularly shaped particles from 10 to 70 nm, from which larger particles are possibly formed. From the images obtained, it can be assumed that small particles are "flakes" resembling graphene structures that can aggregate to form "disk-shaped" particles.

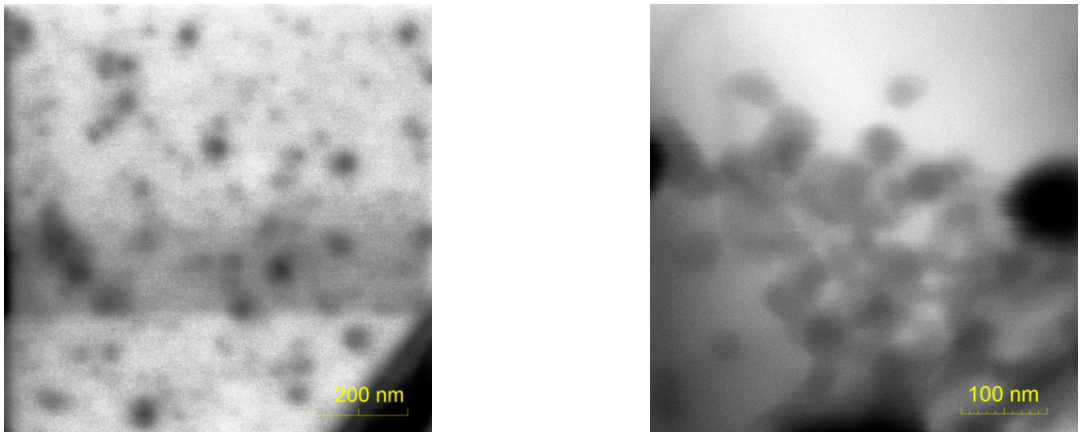

a b

Fig.1. STEM images of CQDs from initial solution (a) and retentate (b)

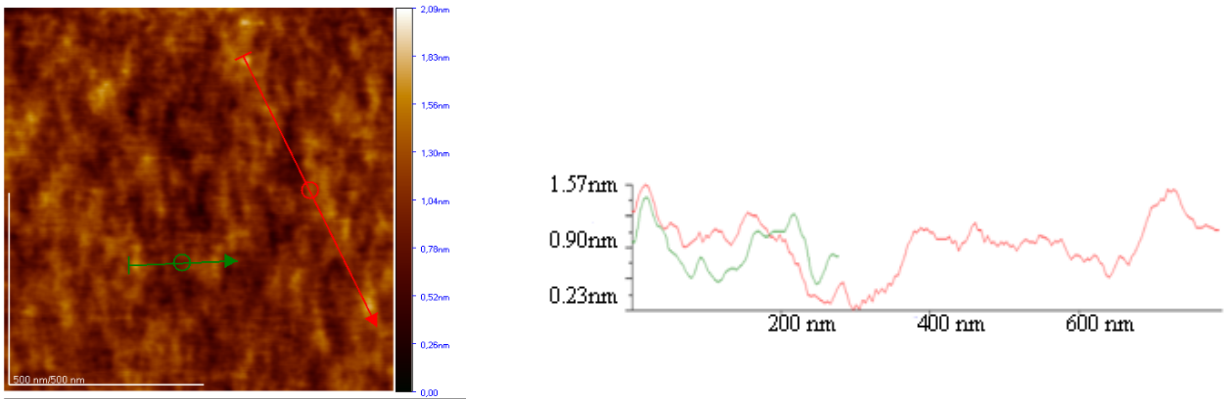

a) b)

Fig.2. AFM image (a) and surface profile (b) of CQDs from the initial solution

The average size of carbon dots passing through the dialysis membrane was obtained by dynamic light scattering and has a value of ~ 3.5 nm (Fig.3). It was not possible to obtain images of particles from the dialysate on an SEM using a detector of transmitted electrons due to the insufficient resolution of the microscope.

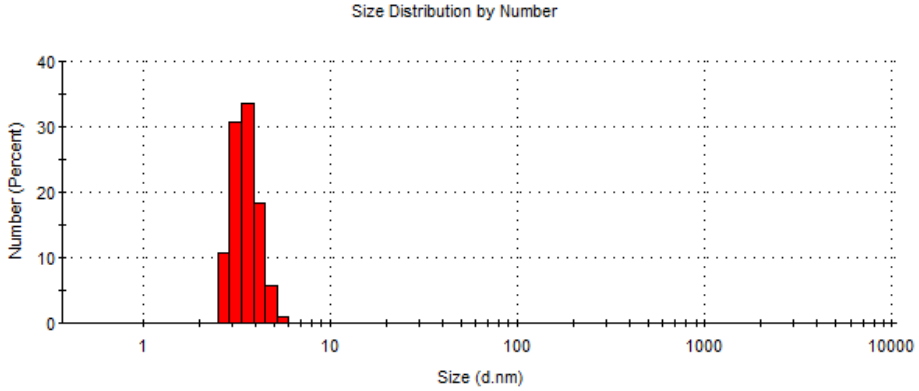

Fig.3. Particle size distribution in dialysate.

Fig. 4 shows the FTIR spectrum of the initial product. The FTIR spectra of the synthesized CQDs agree with the FTIR spectra obtained for the CQDs in [7, 13, 14]. The spectra show peaks at 3431 and 3179 cm^{-1}, which refer to the absorption peaks of stretching vibrations of O-H and NH groups, a weak band at 2928 cm^{-1} can be caused by stretching vibrations of the C-H bond, the band at 1580 cm^{-1} is connected with vibrations of the carbon skeleton of the aromatic ring, weak characteristic peaks in the region of 2500-2600 cm^{-1} correspond to the peaks of stretching vibrations of the SH group, the band at 1705 cm^{-1} is caused by stretching vibrations of the C = O bond, the peak at 1400 cm^{-1} is associated with stretching vibrations of bonds CN, NH and –COO [7, 13, 14].

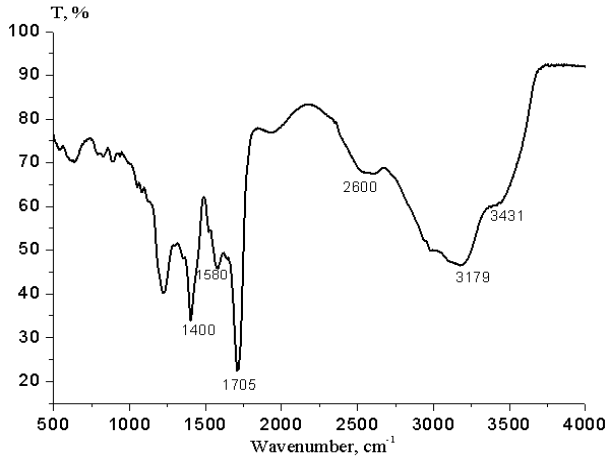

Fig.4. FTIR spectrum of synthesized CQDs

Fig.5. shows the absorption, luminescence, and excitation spectra of the solutions under study. The absorption spectra of all solutions have a band with a maximum at 340-348 nm and a shoulder at 230-240 nm and are similar to the absorption spectra of the CQDs obtained in [5, 7]. The shoulder at 230 nm is attributed to the π-π* transition [5, 15], the absorption band at 340-350 nm is attributed to the n-π* transition caused by carboxyl, amino and other groups [5, 7, 15].

It should be noted that the long-wavelength wing of the absorption spectra of the initial solution and retentate extends to the near-IR region of the spectrum. This is especially noticeable for the retentate spectrum. The fluorescence spectra obtained upon excitation at the wavelength of the absorption maximum (λ=350 nm) are located in the wavelength range of 350–650 nm with a maximum at λ=430 nm. Fluorescence excitation spectra for all solutions correlate with absorption spectra. Table 1 shows the main characteristics of the spectra, from which it follows that the centers of absorption and luminescence in solutions have the same nature.

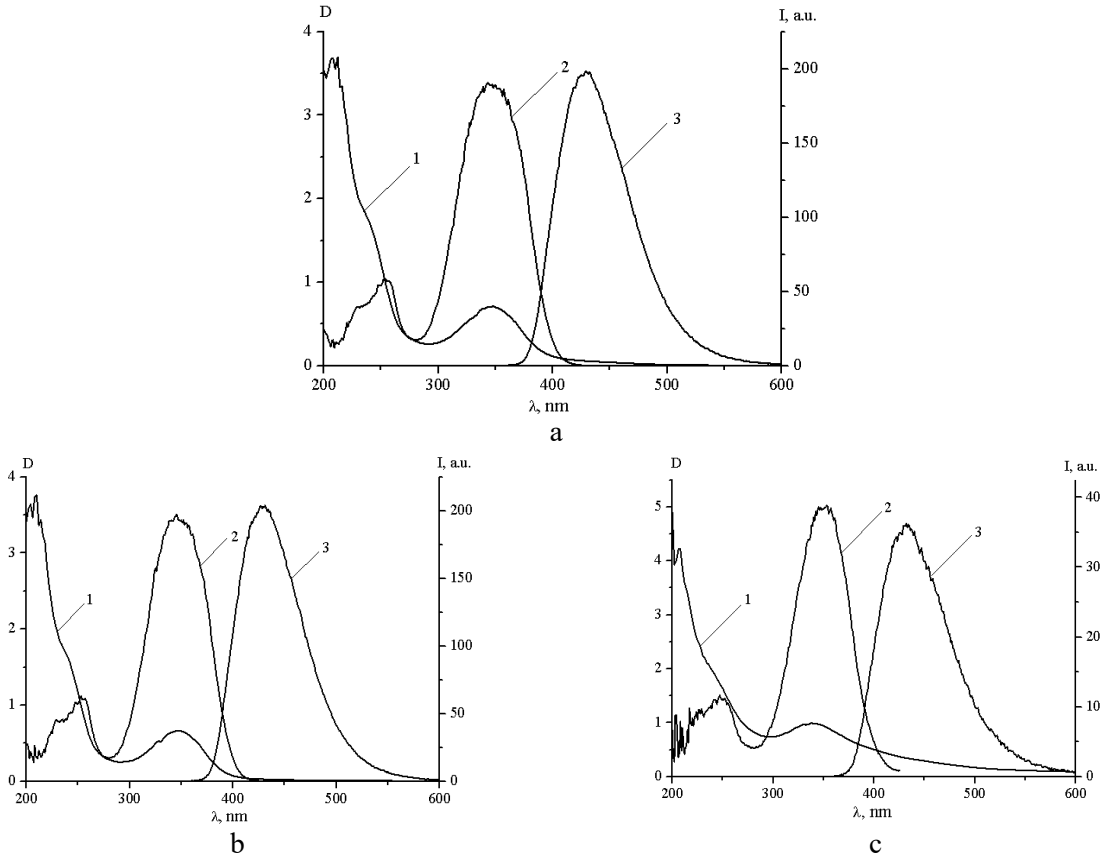

Fig.5. Spectra of absorption (1), excitation of fluorescence (2) and fluorescence (3) of the initial solution (a), dialysate (b) and retentate (c).

Table 1. Characteristics of absorption, fluorescence and excitation spectra of aqueous solutions of CQDs

Sample	λ_{max}^{abs}, nm	FWHM (abs), nm	λ_{max}^{fl}, nm	FWHM (fl), nm	λ_{max}^{ex}, nm	FWHM (ex), nm
Initial solution	348	64	430	74	348	69
Dialysate	348	64	429	74	348	66
Retentate	340	-	432	79	350	63

The quantum yields obtained by the absolute method are 0.47, 0.68, and 0.03 for the initial solution, dialysate and retentate, respectively. The fluorescence lifetimes measured by the time-correlated photon counting method are 7.8 ns for the initial solution, 7.3 ns for dialysate, and 5.9 ns for retentate. A characteristic feature of the CQDs is the dependence of the luminescence spectra on the excitation wavelength. We measured the fluorescence spectra of the studied solutions under excitation in the range from 350 to 550 nm (Fig. 6).

The maximum luminescence intensity is observed upon excitation at a wavelength of 350 nm. With increasing excitation wavelength, the fluorescence band shifts to longer wavelengths. In this case, along with a decrease in the luminescence intensity, broadening of the spectra is observed. The shift of the luminescence spectra indicates different luminescence centers, as indicated in [16, 17]. Luminescence spectra with maxima around 430-450 nm are the result of deactivation of electronic excitation inside the carbon core of quantum dots and electron-hole recombination. Whereas the red-shifted spectra appear as a result of the capture of electronic excitation by surface traps of different energies or functional groups. This is clearly seen in the absorption and excitation spectra. As can be seen from Fig. 5, it is the carbon core that most intensively absorbs the incident light in the UV region, the band at about 350 nm is less manifested. In the fluorescence excitation spectrum, on the contrary, the band responsible for functional groups is more manifested. Thus, in synthesized CQDs, it is the surface groups that make the greatest contribution to the total luminescence.

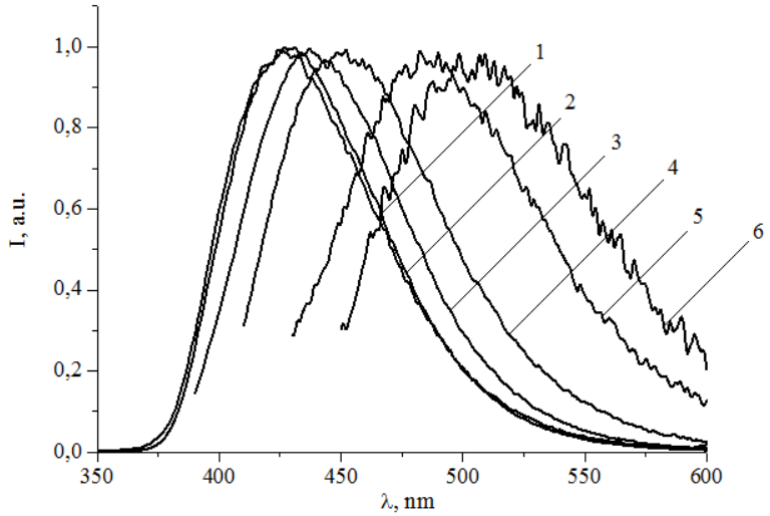

Fig. 6. Normalized CQD fluorescence spectra at different excitation wavelengths:
1 – 300 nm; 2 –350 nm; 3 –380 nm; 4 –400 nm; 5 – 420 nm; 6 – 440 nm

Their composition, as can be seen from the FTIR spectrum, is very diverse, which is responsible for the shift and different intensities of the red-shifted fluorescence of the carbon dots under study.

Conclusion

Investigations of the structural and spectroscopic properties of carbon quantum dots synthesized by the microwave method have been carried out. It was found by microscopic methods and dynamic light scattering that the resulting particles have the shape of disks, the size of which varies from 3.5 to 400 nm.

FTIR spectra contain characteristic peaks confirming the presence of O, N and S-containing functional groups. The positions of the electronic absorption and fluorescence bands are practically the same for the initial solution, dialysate, and retentate. The best luminescent ability with a fluorescence quantum yield of 0.68 is possessed by dialysate carbon dots with a size of ~ 3.5 nm. With an increase in the excitation wavelength, a long-wavelength shift of the fluorescence spectra occurs, accompanied by a broadening of the spectra. The data obtained can be used in optical nanotechnology to create light-emitting systems based on carbon materials.

The novelty and fundamental difference of the obtained data from similar works is the use of microwave synthesis in the preparation of CQDs from the above-mentioned components. The resulting carbon structures have a rather high quantum yield. This will allow them to be used in various applications, such as laser technology, optoelectronic devices, organic and nanocomposite LEDs and photodetectors, organic photovoltaics. It is also possible to use them as biomarkers and sensors in bioimaging and biophysics.

Acknowledgments

The authors are grateful to Professor S.E. Kumekov for a fruitful discussion of the results obtained.
This research is funded by the Science Committee of the Ministry of Education and Science of the Republic of Kazakhstan (Grant No. AP09259913).

REFERENCES

1 Molaei M.J. The optical properties and solar energy conversion applications of carbon quantum dots: A review. *Solar Energy,* 2020, Vol.196, pp. 549–566.

2 Wang Y., Hu A. Carbon quantum dots: synthesis, properties and applications. *J. Mater. Chem. C*, 2014, Vol.2, pp. 6921–6939.

3 Jhonsi M.A. Carbon Quantum Dots for Bioimaging. Available at: www.intechopen.com/books/state-of-the-art-in-nano-bioimaging/carbon-quantum-dots-for-bioimaging (June 20, 2018)

4 Yuan T., Yuan F., Li X., et al. Fluorescence–phosphorescence dual emissive carbon nitride quantum dots show 25% white emission efficiency enabling single-component WLEDs. *Chem. Sci.*, 2019, Vol.10, pp. 9801–9806.

5 Dong Y., Pang H., Yang H.B., et al. Carbon-Based Dots Co-doped with Nitrogen and Sulfur for High Quantum Yield and Excitation-Independent Emission. *Angew. Chem. Int. Ed*., 2013, Vol.52, pp. 7800–7804.

6 Qu S., Liu X., Guo X., et al. Amplified Spontaneous Green Emission and Lasing Emission From Carbon Nanoparticles. *Adv. Funct. Mater.,* 2014, Vol.24, pp. 2689–2695.

7 Lin H., Huang J., Ding L. Preparation of carbon dots with high-fluorescence quantum yield and their application in dopamine fluorescence probe and cellular imaging. *Journal of Nanomaterials*. 2019, Article ID 5037243, pp. 1 – 9. Available at: https://doi.org/10.1155/2019/5037243 (Oct 17, 2019)

8 Song Y., Zhu Sh., Zhang Sh. et al Investigation from chemical structure to photoluminescence mechanism: a type of carbon dots from the pyrolysis of citric acid and an amine. *J. Mater. Chem. C,* 2015, Vol. 3, pp. 5976–5984.

9 Wang T., Wang A., Wang R., et al Carbon dots with molecular fluorescence and their aplication as a “turn-of” fuorescent probe for ferricyanide detection. *Scientific Reports,* 2019, Vol.9. Available at: www.nature.com/articles /s41598-019-47168-7 (July 24, 2019)

10 Essner J.B., Kist J.A., Polo-Parada L., et al Artifacts and Errors Associated with the Ubiquitous Presence of Fluorescent Impurities in Carbon Nanodots. *Chem. Mater.* 2018, Vol.30, pp. 1878−1887.

11 Ibrayev N.Kh., Ishchenko A.A., Afanasyev D.A., et al Active laser medium for near-infrared spectral range based on electron-unsymmetrical polymethine dye and silver nanoparticles. *Appl. Phys. B.* 2019, Vol.125, pp. 1–7.

12 Seliverstova E., Ibrayev N., Omarova G., et al Competitive influence of the plasmon effect and energy transfer between chromophores and Ag nanoparticles on the fluorescent properties of indopolycarbocyanine dyes. *Journal of Luminescence,* 2021, Vol. 235, p.118000. DOI:10.1016/j.jlumin.2021.118000

13 Wanga W., Zeng Zh., Zeng G., et al. Sulfur doped carbon quantum dots loaded hollow tubular g-C3N4as novel photocatalyst for destruction of Escherichia coliand tetracycline degradation under visible light. *Chemical Engineering Journal,* 2019, Vol. 378, p.122132. DOI:10.1016/j.cej.2019.122132

14 Xia Ch., Hai X., Chen X.W., et al. Simultaneously fabrication of free and solidified N, S-doped graphene quantum dots via a facile solvent-free synthesis route forfluorescent detection. *Talanta,* 2017, Vol.168, pp. 269–278.

15 Wang Y., Kalytchuk S., Zhang Y., et al. Thickness-Dependent Full-Color Emission Tunability in a Flexible Carbon Dot Ionogel. *Phys. Chem. Lett*., 2014, Vol.5, pp. 1412−1420.

16 Roy P., Po-Cheng Chen P., Periasamy A.P., et al. Photoluminescent carbon nanodots: synthesis, physic-chemical properties and analytical applications. *Materials Today*, 2015, Vol. 18, No 8, pp. 447-458. DOI:10.1016/j.mattod.2015.04.005

17 Park M., Kim H.S., Yoon H., et al. Controllable Singlet–Triplet Energy Splitting of Graphene Quantum Dots through Oxidation: From Phosphorescence to TADF. *Advanced materials*, 2020, Vol. 32, No. 31, pp. 2000936 (1-10). DOI: 10.1002/adma.202000936.

Article accepted for publication 23.04.2021

.

DOI 10.31489/2021No2/18-22

UDC 616.874

ELECTROMIGRATION IN LITHIUM-TITANIUM FERRITE CERAMICS SINTERED IN RADIATION-THERMAL MODE

Surzhikov A.P.[1], Malyshev A.V.[1*], Lysenko E.N.[1], Sheveleva E.A.[1], Stary O.[2], Ghyngazov A.S.[3]

[1] Tomsk Polytechnic University, Tomsk, Russia, malyshev@tpu.ru
[2]Ceské vysokéucenítechnické v Prague, Prague, Czech Republic
[3]NIKI Joint Stock Company, Tomsk, Russia

The study investigates electro-migration in Li–Ti ferrite ceramic samples sintered in radiation-thermal mode. To reveal radiation effects, similar measurements are performed for samples sintered in thermal mode. The effect of the state of grain boundaries and the presence of a low-melting additive on electrical properties of sintered ferrites is studied. It is found that structural rearrangement during radiation-thermal sintering occurs in early sintering stages, including the heating period. Study demonstrates that such behavior associated with radiation-induced intensification of the liquid phase spreading over the array of powder grains. In addition, it was shown that structural transformation may be caused by stimulation of intergranular slippage.

Keywords: electrical resistance, ferrites, sintering, electron beams, grain boundaries, low-melting additive.

Introduction

In terms of ceramic technology, the quality of sintering depends not only on the degree of sample compaction, but also on microstructure parameters, grain boundaries being most critical. Therefore, it is essential to determine the quality of grain boundaries formed in radiation-thermal (RT) sintering mode.In addition, it is supposed that the characteristics of radiation-induced intensification of compaction in the presence of a low-melting additive in early sintering stages (including the non-isothermal stage) differ from those observed in later stages. It can be assumed that these differences may be due to the effect of radiation on liquid-phase processes. To elaborate these ideas, the electrical transfer in Li–Ti ceramic ferrite samples sintered in RT mode was investigated. Similar measurements were performed for samples sintered in thermal (T) mode to reveal the radiation effects.

A universal requirement for the microstructure of ferrites is the maximum material density and equigranularity of its structure [1, 2]. To meet this requirement within economically reasonable annealing times, a number of methods have been developed to stimulate sintering processes: two-stage introduction of components, additional ferrite burdening by the ferrite powder of the same composition, liquid phase, accelerated sintering, the use of ultrasound [1, 3, 4–12].In recent years, the effect of ionizing radiation fluxes has been employed in the production and modification of materials. A fundamental phenomenon of multiple acceleration in the synthesis of multicomponent powder materials [13, 14] and sintering [15–19] in RT mode was discovered. Sintering processes of lithium-titanium ferrites have been most well studied under specific combined action of high temperatures and intense electron fluxes [20, 21]. The patterns of compaction of ferrite compacts were revealed and a multiple increase in the compaction rate of lithium-titanium ferrite samples under RT sintering in RT mode was shown [22, 23].Almost all the studies investigated structural, phase and mechanical properties of the materials produced in this mode, i.e. touched upon such branches of science as physics of sintering and powder metallurgy. The ultimate goal of any ferrite production technology is to achieve a desired level of performance properties. In this case, the main functional characteristics of ferrimagnets are electromagnetic properties. Therefore, controlled formation of the main electromagnetic properties can enhance the development of new technological processes. On the other hand, magnetic reversal processes and electromigration in ferrites relate to their microstructural features.

Therefore, the patterns of changes in electromagnetic properties can be used as a source of information on the nature of the processes occurring in sintering to provide an in-depth interpretation of the RT sintering mechanisms. In [24], the patterns of the formation of magnetic properties (parameters of the hysteresis loop) for ferrites sintered in thermal (T) and radiation-thermal (RT) modes are considered. However, the question

about the electrical properties of ferrites sintered in T and PT modes remains open. Methods of studying the electrical conductivity are widely used to investigate the properties of oxide systems, including ferrites [25]. Similar to magnetic properties, electrical conductivity is a structure-sensitive parameter. However, in contrast to magnetic properties, the conductivity (resistance) is more sensitive to point defects and the type of the mixed-valence ion. No doubt, experimental data on electrical conductivity are also of applied interest since conductivity determines the level of eddy-current losses in microwave ferrites.

2. Experimental part

2.1 Materials

The study used powders of lithium-titanium ferrite synthesized from the mechanical mixture of oxides and carbonates containing (wt%): Li_2CO_3 – 11.2; TiO_2 – 18.65; ZnO – 7.6; $MnCO_3$ – 2.74; the rest was Fe_2O_3. Part of the sample was produced with the addition of 10% polyvinyl alcohol solution in the amount of 12 wt. % of the synthesized mixture. All samples were prepared by cold single-action compaction. The compacts were 13 mm in diameter and 2 mm thick.

2.2 Characterization techniques

The compaction mode used in the study was as follows: P = 130 MPa, 1 min holding time of the material under pressure; two sintering modes: RT and T. For RT sintering, the samples were exposed to a pulsed electron beam with energy of (1.5–2.0) MeV using an ILU-6 accelerator. The beam current in the pulse was (0.5–0.9) A, the irradiation pulse duration was 500 μs, the pulse repetition rate was (5–50) Hz, and the heating rate of the samples was 1000 °C/min. The samples were irradiated in a lightweight chamotte box with a wall bottom thickness of 15 mm. On the exposed side, the box was covered with a radiation-transparent protector with a mass thickness of 0.1 $g \cdot cm^{-1}$. The temperature was measured using a control sample placed in close proximity to the sintered samples.

T sintering was carried out in a preheated electric chamber furnace to provide the heating rate comparable to the radiation heating rate. The cell design and temperature control technique were similar to those used for RT sintering. Sintering in both modes was performed in the air. The electrical resistivity of ferrites was measured at a constant current based on a two-electrode scheme using pellet-shaped samples with a deposited near-electrode layer of soft graphite. The measurement temperature changed in the interval from (290–1300) K. The air pressure in the measuring cell did not exceed 19 Pa, and the heating rate was 10 degrees per minute. The electric field applied to the sample attained 10 V/cm.

3. Results and discussion

Figure 1 shows temperature dependences of the electrical resistivity (ρ_v) on the reciprocal temperature of ferrite samples after 30 min sintering at 1273 K (curves *1–3*). Curve *4* describes the resistance of the samples measured during their cooling in the measuring cell and during repeated measurements of ρ_v. Thus, curve *4* shows the resistance of vacuum heat treated samples ($\tau \geq 5$ min) at 1273 K. The curve is plotted based on the results obtained in measuring ρ_v for all samples, including those unsintered but vacuum heat treated. Vacuum heat treated samples restore their initial resistance after short-term (~5 min) annealing in air at 1273 K. The exception is unsintered samples, which show resistance after heating in air comparable to that of heat sintered samples, that is, the temperature dependence corresponds to curve *2* in Fig. 1.The analysis of ρ_v temperature dependences shows that the resistance of ferrite samples in the low-temperature region (up to 650 K) decreases in the following order: sample sintered in heating mode → sintered in RT mode → heated in vacuum up to 1273 K. In the high-temperature region of (~700 K), the ρ_v approach significantly.

The monotonically decreasing dependencies indicate a complex spectrum of activation energy for charge carriers. In an explicit form, this spectrum can be obtained by differentiating the curves, Fig. 1:

$$E = k \frac{d\left(\lg \rho_V\right)}{d\left(1/T\right)} \tag{1}$$

The results of differentiation are shown in Fig.2. Fig.1 and Fig.2 show the sintering technique in the presence of a low-melting additive affects the specific electrical resistance, but the activation energy spectrum remains unchanged. In case no additive is used, ρ_v similar to the activation energy spectrum does not depend on the sintering technique.

.

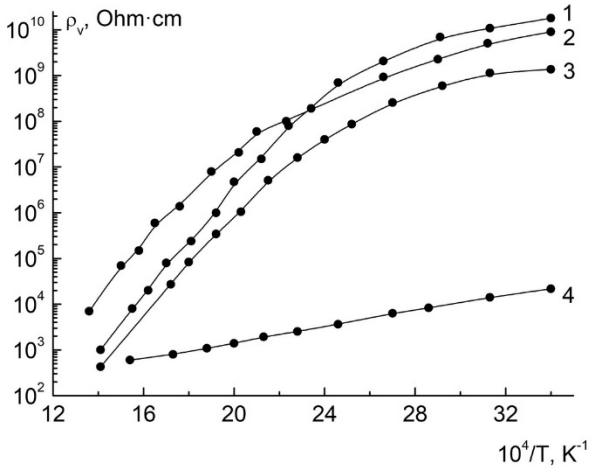

Fig.1. Temperature dependences ρ_v of Li–Ti ferrites. Solid-phase (*1*) and liquid-phase (*2, 3*) in T (*1, 2*) and RT (*3, 4*) sintering at 1237 K for 30 min and after vacuum heating at 1237 K for 10 min (*4*).

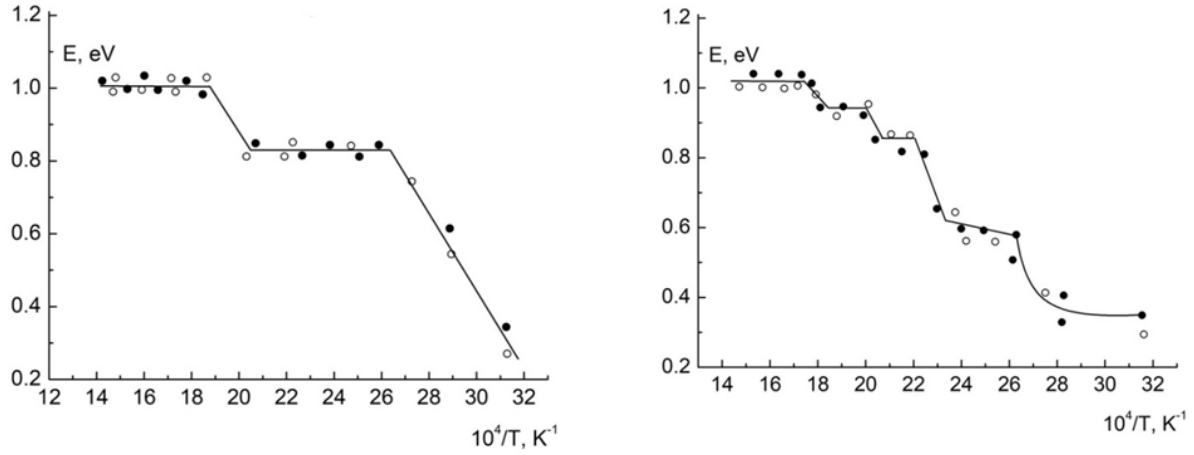

a) b)

Fig.2. Activation energy spectra for electromigration in Li–Ti ferrites. Solid-phase (*a*) and liquid-phase (*b*) in T (•) and RT (o) sintering modes.

After vacuum heating, ρ_v and electromigration activation energy exhibit the lowest values, irrespective of the sintering technique (Fig.1, curve 4).A short heat treatment time sufficient for changes observed in $\rho_v$indicates that the structural rearrangement of the compacted sample significant for ferrite electrical properties occurs in early stages of sintering, including the heating period. This is confirmed by the volumetric shrinkage dependences of samples presented in Fig. 3.

Fig. 3 clearly shows that the samples are compacted by the start of isothermal sintering, and the degree of compaction in RT sintering mode is higher. A short heating period required for gas exchange with the atmosphere indicates redox reactions occurring in the surface layers of the sample structural elements. To interpret the results obtained, we consider the model of grains and inter layers and the hopping mechanism of electromigration with the participation of Fe^{2+} ions used for polycrystalline ferrites. In this model, the compacted sample is considered as a set of low-resistance ferrite particles separated by high-resistance interlayers. In the initial state, the compacted sample exhibits an undeveloped network of contacts and contains insignificant amount of Bi_2O_3 particles. The surfaces of powder ferrite grains are oxidized, therefore they show high resistance due to the minimum content of Fe^{2+} ions. Electromigration occurs through a hopping mechanism with the participation of mixed-valence ions (Fe^{2+}, Mn^{2+}, etc.).

Thus, the activation energy spectrum for electromigration is generated by barriers of intercrystalline interlayers formed during interparticle slippage at the initial stage of powder particle sintering. The number and cross-section of intergranular contacts (shunting effect) significantly affect ρ_v. Interparticle contacts are formed mainly when non-conductive oxidized surfaces of powder grains come into contact. Some of the boundaries become more conductive due to sintering. The conductivity of boundaries determines the sample

resistance after sintering. Heating of the sample corresponds to reduction annealing in vacuum (due to oxygen volatility). Effective removal of oxygen from the developed network of oxidized grain boundaries leads to Fe^{2+} ion enrichment and sharply decreased resistance.

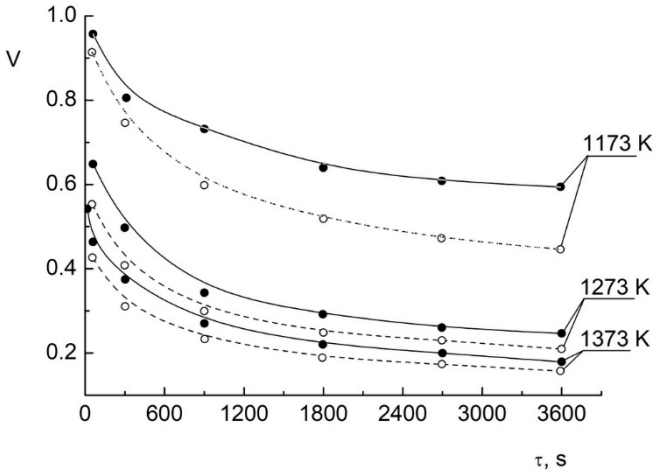

Fig.3. Dependences of the sample compaction on sintering time at different temperatures:
(•) T sintering; (○) RT sintering.

Curve *4* describes the conductivity of the sample in this state (Fig. 1). Shunting of the 'eutectic' boundaries of higher resistance makes the contribution of the latter to electromigration insignificant at this stage. However, additional annealing in air oxidizes looser 'non-eutectic' boundaries, and the sample resistance returns to its original values.

A decrease in the ρ_v of the samples sintered in RT mode in the presence of a low-melting additive shows a larger number of relatively low-resistance intergranular interlayers and indicates radiation-induced interparticle slippage. This effect can be observed only in the presence of a low-melting additive; therefore, the process can be identified with the radiation-induced intensification of liquid-phase processes, including liquid phase spreading over the array of powder grains.

The low-temperature (up to 373 K) region in $\rho_v = f(T)$ dependences mostly satisfies the above conditions. In this temperature range, the number and perfection of boundaries that limit electromigration increase during RT sintering mode in the presence of a fusible additive (Fig. 1). The absence of high-energy barriers in the activation energy spectrum indicates the highest perfection of the boundaries (Fig. 2). A decrease in the ρ_v indicates an increased effective area of the boundaries. In case of poor spreading of the liquid phase over the surface of powder particles, excessively thick films of this phase may form in some of its areas. In these conditions, the film impedes sintering of powder particles due to the repulsion effect [26]. It is probably due to this reason that the resistance of the compacted sample in the high-temperature region (T> 580 K) obtained in T sintering mode with the addition of Bi_2O_3 is higher compared to ρ_v of the sample obtained by solid-phase sintering.

Conclusion

In a comparative study, the influence of radiation-thermal sintering on the ferrite ceramic electromigration was determined. It was first shown that the structural rearrangement during radiation-thermal sintering occurs during early stages of sintering. Herewith the scientific significance of the results is determined by data on the reduction of electrical resistivity of samples obtained by radiation-thermalsintering compared to thermal sintering. This effect is caused by the formation of a large number of low-resistance intercrystalline layers, intensification of the liquid phase spreading process over the array of powder grainsand also by the radiation-induced stimulation of the intergranular slippage process.

Acknowledgments

The research is funded by the Ministry of Education and Science of the Russian Federation as part of the "Science" Program (project No. FSWW-2020-0014).

.

REFERENCES

1 Letyuk L.M., Nifontov V.A., Babich E.A., Gorelik S.S. Effect of low-melting additives on the formation of the microstructure and the properties of ferrites with a rectangular hysteresis loop. *Izv. Akad. NaukNeorg. Mater*. 1976, Vol. 12, pp. 2023 – 2026.[in Russian]

2 Zhuravlev G.I., Golubkov L.A., Strakhova T.A. Basic types of microstructure of ferrites and means of obtaining them. *Soviet Powder Metallurgy and Metal Ceramics*. 1990, Vol. 29, pp. 478 – 480.[in Russian]

3 Dmitriev M.V., Letyuk L.M., Shipko M.N. Study of oxygen diffusion in the surface layers of Mn-Zn ferrites. *Technical physics*. 1982, Vol. 27, pp. 338 – 339.

4 Letyuk L.M. Recrystallization of ferrites and its effect on the processes of microstructure formation in ferrospinels. *Soviet Powder Metallurgy and Metal Ceramics*. 1980, Vol.19, No. 5, pp. 359 – 364.

5 Zinovik M.A., Zinovik E.V. Ferrites with rectangular and square hysteresis loops. Powder Metallurgy and Metal Ceramics. 2005, Vol. 44, p. 66 – 74.

6 Letyuk L.M., et al. Special features of the formation of the microstructure of ferrites sintered in the presence of a liquid phase. *Izv.VysshikhUchebnykhZavedenij. ChernayaMetallurgiya*. 1979, Vol. 11, pp. 124 – 127. [in Russian]

7 Micheli A.L. Preparation of lithium ferrites by coprecipitation.*IEEE Transactions on Magnetics*. 1970, Vol.6, pp. 606 – 608.

8 Bronshteyn I.M., Dyubua B.Ch., Karasik B.S., Khinich I.I. Secondary electron emission of a platinum-barium alloy made by evaporation. *Radio Eng. Electron Phys*. 1974, Vol. 19, pp. 108 – 111.

9 Minin V.M. Effect of sintering conditions on the microstructure and electromagnetic properties of Li-Mg-Mn ferrite memory elements. *Soviet Powder Metallurgy and Metal Ceramics*. 1982, Vol. 21, pp. 698 – 701.

10 Zahir R., Chowdhury F.-U.-Z., Uddin M.M., et al. Structural, magnetic and electrical characterization of Cd substituted Mg ferrites synthesized by double sintering technique. *J. Magn. Magn. Mater*. 2016, Vol. 410, pp. 55 – 62.

11 ManjuraHoque S., Abdul Hakim M., Mamun Al, et al. Study of the bulk magnetic and electrical properties of $MgFe_2O_4$ synthesized by chemical method. *Materials Sciences and Applications*. 2011, Vol.2, pp. 1564 – 1569.

12 Hu J., Yan M., Luo W., Wu J.M. Effects of microstructure on the temperature dependence of relative initial permeability of NiCuZn ferrites. *Physica B*. 2007, Vol. 400, pp. 119 – 123.

13 Surzhikov A.P., Pritulov A.M., Lysenko E.N., et al. Calorimetric investigation of radiation-thermal synthesized lithium pentaferrite. *Journal of Thermal Analysis and Calorimetry*. 2010, Vol. 101, No. 1, pp. 11 – 13.

14 Yurov V.M., Baltabekov A.S., Laurinas V.C., Guchenko S.A. Dimensional effects and surface energy of ferroelectric crystals. *Eurasian phys. tech. j.* 2019, Vol.16, No.1, pp. 18 – 23.

15 El-Shobaky G.A., Ibrahim A.A. Solid-solid interactions between ferric oxide and lithium carbonate and the thermal stability of the lithium ferrites produced. *Thermochim. Acta*. 1987, Vol.118, pp. 151 – 158.

16 Salimov R.A., Cherepkov V.G., Golubenko J.I., et al. D.C. high power electron accelerators of ELV-series: status, development, applications. *J. Radiation Phys. Chem*. 2000, Vol.57, pp. 661 – 665.

17 Cleland M.R., Parks L.A. Medium and high-energy electron beam radiation processing equipment for commercial applications. *Nucl. Instr. Meth. B.* 2003, Vol.208, pp. 74 – 89.

18 Mehnert R. Review of industrial applications of electron accelerators. *Nucl. Instr. Meth.B.* 1996, Vol.113, pp.81 – 87.

19 Neronov V.A., Voronin A.P., Tatarintseva M.I., Melekhova T.E., Auslender V.L. Sintering under a high-power electron beam. *J. Less-Common Metals*. 1986, Vol.117, pp. 391 – 394.

20 .Surzhikov A.P., Lysenko E.N., Malyshev A.V., Pritulov, A.M. Kazakovskaya, O.G. Influence of mechanical activation of initial reagents on synthesis of lithium ferrite. *Russian Physics Journal*, 2012, Vol. 55, No. 6, pp. 672-677.

21 Boldyrev V.V., Voronin A.P., Gribkov O.S., Tkachenko E.V., Karagedov G.R., Yakobson B.I., Auslender V.L. Radiation-thermal synthesis. Current achievement and outlook. *J. Solid State Ion*. 1989, Vol.36, pp. 1 – 6.

22 Surzhikov A.P., Frangulyan T.S., Ghyngazov S.A., Koval N.N. Structural-phase transformations in near-surface layers of alumina-zirconium ceramics induced by low-energy high-current electron beams.*Nucl. Instr. Meth. B.* 2009, Vol. 267, No. 7, pp. 1072 – 1076.

23 Surzhikov A.P., Peshev V.V., Pritulov A.M., Gyngazov,S.A. Grain-boundary diffusion of oxygen in polycrystalline ferrites. *Russian Physics Journal*. 1999, Vol. 42, No. 5, pp. 490-495.

24 Stary O., Malyshev A.V., Lysenko E.N., Petrova A. Formation of magnetic properties of ferrites during radiation-thermal sintering. . *Eurasian phys. tech. j.* 2020, Vol.17, No.2, pp. 6 – 10.

25 Nikolaev E.V., Astafyev A.L., Nikolaeva S.A., Lysenko E.N., ZeinidenovA.K. Investigation of electrical properties homogeneity of Li-Ti-Zn ferrite ceramics. . *Eurasian phys. tech. j.*2020, Vol.17, No.1, pp. 5 – 12.

26 Geguzin J.E. *Physics of Sintering*. 1984, Moscow, Nauka, 360p.

Article accepted for publication 24.04.2021

DOI 10.31489/2021No2/23-28

UDC 538.971

DETERMINATION OF CRITICAL DOSES OF RADIATION DAMAGE TO ALN CERAMIC UNDER IRRADIATION OF HELIUM AND HYDROGEN IONS

Kozlovskiy A.L.[1,2*]

[1] Institute of Nuclear Physics of the Republic of Kazakhstan, Almaty, Kazakhstan
[2] Kh. Dosmukhamedov Atyray University, Atyrau, Kazakhstan, kozlovskiy.a@inp.kz

The work is devoted to the study of the radiation damage kinetics to heat-conducting, insulating and mechanical properties in polycrystalline ceramics based on aluminum nitride under irradiation of helium and hydrogen ions, as well as the determination of critical doses that cause maximum irreversible consequences. The choice of ions for irradiation is due to the ability to simulate the radiation damage processes during the accumulation of helium and hydrogen ions in the structure of the near-surface layer with the subsequent formation of gas-filled bubbles. During the studies carried out, it was found that at doses of irradiation with helium ions above $1x10^{17}$ ion/cm^2, there is a sharp deterioration in thermal conductivity and a decrease in ceramic resistance, which is associated with the onset of the formation of helium bubbles and partial embrittlement of the near-surface layer. However, an increase in the radiation dose above $5x10^{17}$ ion/cm^2 does not lead to significant changes in thermal conductivity and insulation characteristics, which indicates the effect of radiation damage accumulation and a decrease in the ceramic degradation rate. In contrast to irradiation with helium ions, irradiation with hydrogen ions to doses higher than 1-$3x10^{17}$ ion/cm^2 does not lead to significant changes in the thermal insulation characteristics, which indicates the ceramic resistance to hydrogen absorption processes.

Keywords: aluminum nitride, ceramics, structural materials, radiation damage, helium swelling, embrittlement.

Introduction

One of the promising materials for nuclear power, in the case of creating high-temperature nuclear reactors, are nitride ceramics such as Si_3N_4, AlN, TiN, BN et.al. [1-5]. As is known, nitride ceramics have a number of unique properties such as high thermal conductivity, radiation and corrosion resistance, chemical inertia, high melting point (more than 1800-2300°C), good insulating properties [6,7]. Among all nitride ceramics, it is worth noting separately polycrystalline aluminum nitride, which, unlike silicon nitride, has high binding energy values, which leads to the absence of extended radiation damage along the trajectory of ions in the material, called latent tracks [8-10]. As is known, the formation of latent tracks in a ceramics material or dielectrics is associated with local changes in the electron density and its redistribution in the structure. At the same time, unlike metals, in which electrons torn from their places during radiation damage can return to their positions, for dielectrics such a return is very difficult [11-13].

The key factor determining the use and service life of ceramics as structural materials is radiation damage resistance, as well as the preservation of insulating and mechanical characteristics under prolonged radiation exposure [14-18]. At the same time, unlike irradiation with heavy ions and radiation damage caused by them in the form of local areas with changed electron density, as well as deformation of the crystal lattice, the most unstable are damage caused by irradiation of ceramics with helium or hydrogen ions [19-25]. In this case, not only the formation of local heterogeneities and distortions of the structure is observed, but also due to the weak solubility and high mobility of helium and hydrogen in the structure, the formation of gas-filled inclusions is possible, leading to swelling and embrittlement of ceramics. However, the exact data of critical radiation doses causing irreversible, catastrophic damage to the crystal structure and properties of ceramics has not been established for aluminum nitride to date, which is the main motivation for such studies [26-30].

Based on the foregoing, the purpose of this work is to conduct research to determine the critical radiation doses at which the maximum effect of swelling and degradation of the near-surface layer of ceramics based on aluminum nitride is observed. Determination of the radiation damage kinetics, as well as the subsequent evolution of gas-filled inclusions in the case of irradiation with helium and hydrogen ions, was carried out by irradiating ceramic with helium and hydrogen ions in a wide dose range from 10^{15} ion/cm^2

.

to $1x10^{18}$ ion/cm^2. The choice of the upper threshold of irradiation is due to the literature data, according to which the most pronounced swelling processes for carbide and nitride ceramics are observed at doses above 10^{17} ion/cm^2.

1. Experimental part

Polycrystalline ceramic of aluminum nitride (AlN) with a hexagonal type of crystal lattice and a density of 3.26 g/cm^3 were selected as objects of study. This type of ceramic is a commercial material used as a base for insulating substrates, as well as a base for structural materials.

Radiation damage was simulated by two types of ions, helium and hydrogen (protons). Irradiation with helium ions (He^{2+}) was carried out on a DC-60 heavy ion accelerator (Nur-Sultan, Kazakhstan), the ion energy was 40 keV, the irradiation dose was 10^{15} – 10^{18} ion/cm^2. Irradiation with 1.5 MeV hydrogen ions (protons) was carried out at the UKP-2 accelerator (Almaty, Kazakhstan), the irradiation doses were 10^{15} – $5x10^{17}$ ion/cm^2. To avoid overheating of samples during irradiation and to initiate thermal annealing of defects as a result of accumulated heat, the samples were placed on water-cooling targets during irradiation, which allow the temperature of the samples to be maintained near room temperature.

Investigation of mechanical properties of ceramics before and after irradiation was carried out by determination of value of crack resistance, bending strength and impact toughness. The study of heat-conducting properties was carried out using a stationary method for measuring the absolute longitudinal heat flux, followed by determining the value of the thermal conductivity coefficient using formula (1):

$$\lambda = \frac{q\delta}{t_{c1} - t_{c2}} \tag{1}$$

where q is the heat flux density, W/m^2; t_{c1} and t_{c2} are the temperature constants on the hot and cold sides of the wall, K; δ is the wall thickness, m; λ is the coefficient of thermal conductivity of the wall material, W/(m·K).

2. Results and discussion

Figure 1 shows the results of changing the value of the thermal conductivity coefficient depending on the type of ions and the radiation dose. The value of thermal conductivity characterizes the properties of materials to give off and conduct heat, which for structural materials is one of the important operating parameters that contribute to the stable removal of heat from the reactor zone. Moreover, in the event of a drop in this value, a decrease in thermal conductivity can lead to irreversible consequences, accompanied by overheating of the core. The change in the value of thermal conductivity under the action of irradiation is primarily associated with radiation damage caused by irradiation, which leads to the creation of additional defects, as well as regions of disorder, which leads to partial amorphization of the structure.

As a rule, the critical value of the decrease in thermal conductivity is a decrease by more than 20 % from the nominal value, which characterizes a large degradation of the material. In this case, in contrast to mechanical damage, the change in thermal conductivity can be more pronounced, which indicates changes at the crystalline level, as well as the formation of a large number of amorphous inclusions. As can be seen from the data presented, in the case of irradiation with hydrogen ions, even at maximum irradiation doses, the decrease in thermal conductivity coefficient does not exceed 10 %, which is within the permissible limits, and indicates the resistance of ceramic to irradiation by protons.

Another variation in the thermal conductivity is observed for samples irradiated with He^{2+} ions. The general nature of the changes can be divided into three characteristic regions, which will be hereinafter referred to as the I – irradiation dose region 10^{15} – 10^{17} ion/cm^2, the II – irradiation dose region 10^{17} – $5x10^{17}$ ion/cm^2, and the III – irradiation dose region $5x10^{17}$ – 10^{18} ion/cm^2. Region I is characterized by an insignificant decrease in thermal conductivity, comparable to the changes under irradiation with protons. Region II is characterized by a sharp decrease in thermal conductivity from 91 % to 74 % of the initial value, which indicates a sharp change in the structural properties of the irradiated ceramic. Region III is characterized by a decrease in thermal conductivity coefficient by 3-5 % in comparison with the changes characteristic of region II. Such a change for region III indicates the effect of the radiation damage accumulation and a decrease in the material degradation rate. In fact, according to previous studies, it has been established that the mechanism of helium swelling at doses above $3x10^{17}$ ion/cm^2 slows down, since the radiation damage accumulation obeys an exponential law, and at high radiation doses it reaches the so-called

saturation plateau of radiation defects [31, 32]. In turn, a sharp drop in thermal conductivity at radiation doses of 10^{17} – 5x10^{17} ions/cm^2 indicates the formation of a cumulative effect of radiation-induced defects in the structure of the near-surface layer, as well as the formation of helium inclusions and bubbles that can cause partial amorphization of the near-surface layer, which leads to a decrease in heat removal and deterioration of the insulation properties of ceramic. The obtained thermal conductivity variation dependences indicate that this type of polycrystalline ceramic has rather high indicators of irradiation resistance with both proton and helium beams up to doses of 3-5x10^{17} ion/cm^2.

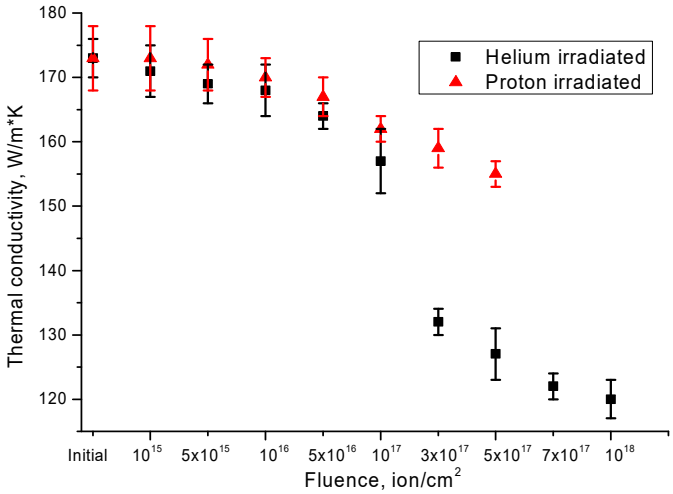

Fig.1. Graph of thermal conductivity coefficient change depending on type of ions and irradiation dose.

Important characteristics of the use of ceramics as structural materials are their mechanical and strength properties, the change in which under the influence of radiation can affect the operational characteristics, as well as the service life of these materials. One of these quantities characterizing the change in the materials strength is the crack resistance of the materials, which characterizes the pressure required to create a microcrack in the near-surface layer. Figure 2 shows a graph of the change in the crack resistance depending on the irradiation dose, which reflects the dynamics of crack resistance of ceramic as a result of the change in the concentration of defects formed by the irradiation. As can be seen, the change in crack resistance in the case of proton irradiation is two-step in nature, which is characterized by small changes at irradiation doses up to 10^{17} ion/cm^2 and a drop in crack resistance by 7-11 % for irradiation doses 3x10^{17} and 5x10^{17} ion/cm^2, respectively. In the case of irradiation with He^{2+} ions, the main changes occur at doses above 3x10^{17} ions/cm^2, and are characterized by a decrease in crack resistance by 20-30 % of the initial value. This behavior of crack resistance changes indicates a deterioration in the strength of the ceramic and a decrease in their cracking resistance as a result of external influences.

Deterioration of crack resistance of ceramic at high radiation doses is related to processes of accumulation of implanted helium, which, as shown earlier in works [33-35], due to its mobility, is able to form helium bubbles, the dimensions of which vary from 50 nm to several microns depending on the radiation dose. According to the general theory of the helium bubbles formation [35], the mobility of helium leads to the filling of voids formed as a result of deformation and crystal structure distortion as a result of radiation damage, as well as the subsequent evolution of point defects in the structure of the damaged layer. The filling of such voids with helium leads to the formation of additional stresses in the crystal lattice, which are capable of exerting pressure on the structure, thereby squeezing the deformed volume onto the surface, forming hillocks or gas-filled bubbles. A further increase in the concentration of implanted helium leads to an increase in the volume of the bubbles, and, consequently, to an increase in the stress in them, which ultimately leads to their rupture with the formation of craters or microcracks. This behavior is well described in [33–35], where the authors studied various mechanisms of the formation of gas-filled bubbles and blisters upon irradiation with helium ions, and their further evolution, leading to degradation of the near-surface layer. The destruction of the near-surface layer at irradiation doses above 3x10^{17} ions/cm^2 leads to a sharp decrease in the ceramic strength, as well as an increase in the likelihood of cracking as a result of external influences.

.

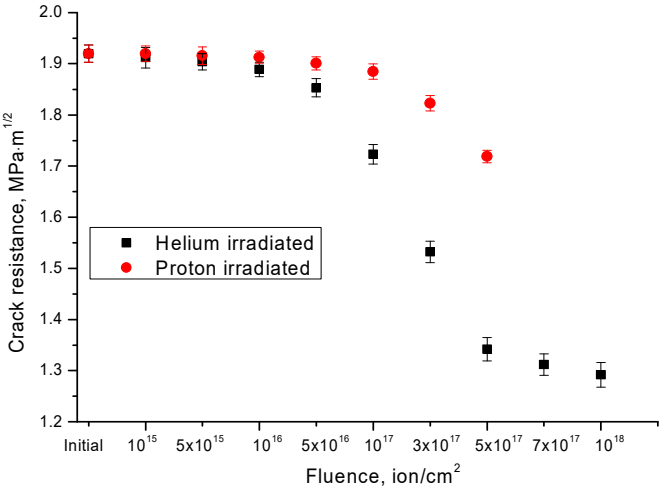

Fig.2. Graph of the change in crack resistance depending on the radiation dose

Figure 3 shows the results of changes in bending strength and impact strength of ceramic exposed to hydrogen and helium ions.

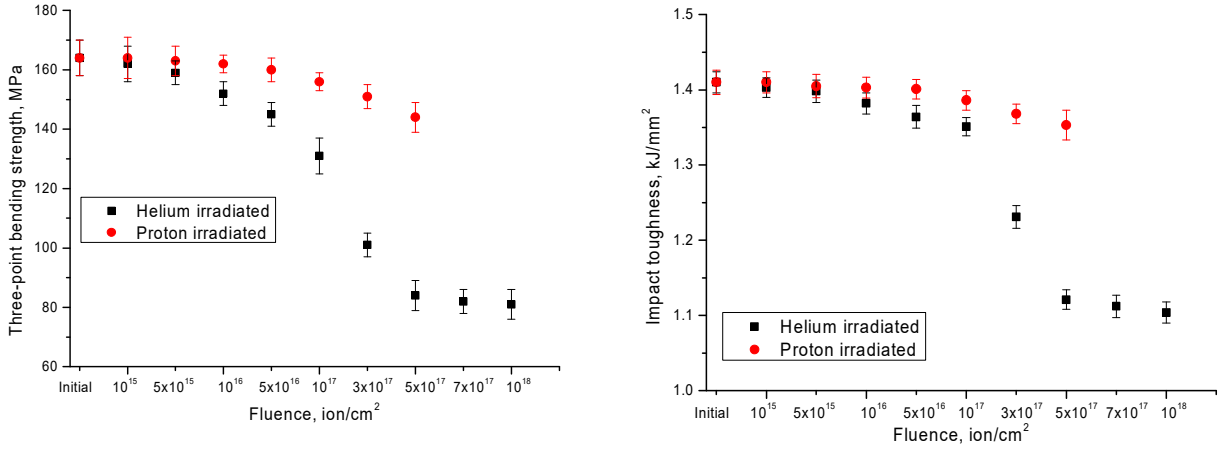

a) b)

Fig.3. a) Graph of bending strength change depending on irradiation dose and type of ions; b) Graph of impact strength change depending on irradiation dose

The general appearance of the change in these values is characteristic of such changes in the crack resistance of ceramic and indicates that, as in the case of crack resistance, irradiation with protons does not lead to a significant decrease in strength characteristics, while irradiation with He^{2+} ions at doses higher than $3x10^{17}$ ions/cm^2 leads to a sharp deterioration in strength characteristics.

Conclusion

In conclusion, we can summarize the results of the experimental work, which are as follows. First, the AlN polycrystalline ceramic under study showed good stability in maintaining mechanical and heat-conducting properties in the dose range of 10^{15}-10^{17} ion/cm^2 for both types of selected ions. This behavior indicates that this type of ceramic has a high degree of resistance to radiation damage arising from the interaction of ions and the subsequent formation of gas-filled inclusions. Secondly, in the case of irradiation with protons, the studied ceramic in the entire dose range showed a decrease in heat-conducting and strength characteristics within 5-10 %, which is good indicators of radiation resistance. At the same time, for samples irradiated with He^{2+} ions, the critical values of doses at which there is a decrease in heat-conducting and strength properties by more than 25-30% are doses of 3-5x10^{17} ions/cm^2, however, a further increase in irradiation doses does not lead to significant changes in the properties of ceramic, which indicates the radiation damage cumulative effect and a decrease in the material degradation rate.

The results obtained can later be used to expand the theory of radiation damage to nitride ceramic, as well as to predict and design high-temperature reactors of a new generation, based on which it is planned to use a new class of structural materials based on ceramics.

Acknowledgments

This research was funded by the Science Committee of the Ministry of Education and Science of the Republic of Kazakhstan (No. AP08051975).

REFERENCES

1 Aitkaliyeva A., et al. Irradiation effects in Generation IV nuclear reactor materials. *Structural Materials for Generation IV Nuclear Reactors*. Woodhead Publishing, 2017, pp. 253 – 283.

2 Milosavljević M., et al. A comparison of Ar ion implantation and swift heavy Xe ion irradiation effects on immiscible AlN/TiN multilayered nanostructures. *Materials Chemistry and Physics*. 2012, Vol.133, pp. 884 -892.

3 Zinkle S.J., et al. Microstructure of Swift Heavy Ion Irradiated SiC, Si 3 N 4 and AIN. *MRS Online Proceedings Library*. 2000, 650.1, pp. 3191 – 3196.

4 Crespillo M.L., Agulló-López F., and Zucchiatti A. Cumulative approaches to track formation under swift heavy ion (SHI) irradiation: Phenomenological correlation with formation energies of Frenkel pairs. *Nuclear Instruments and Methods in Physics Research section B: Beam Interactions with Materials and Atoms*. 2017, Vol. 394, pp. 20 – 27.

5 Al-Douri Y. Structural phase transition of boron nitride compound. *Solid state communications*. 2004, Vol.132.7, pp. 465 – 470.

6 Lushchik A., et al. Distinctive features of diffusion-controlled radiation defect recombination in stoichiometric magnesium aluminate spinel single crystals and transparent polycrystalline ceramics. *Scientific reports*. 2020, pp.1 – 9.

7 Yang Wei, et al. Preparation and performance of alumina ceramic coating doped with aluminum nitride by micro arc oxidation. *Ceramics International*. 2020, Vol. 46.10, pp. 17112 – 17116.

8 Tuleushev A.Z., et al. Ion charge influence on the molecular structure of polyethylene terephthalate films after irradiation with swift heavy ions. *Crystals*. 2020, Vol.10.6, pp. 479.

9 Li Shuyao, et al. Manipulating the triboelectric surface charge density of polymers by low-energy helium ion irradiation/implantation. *Energy & Environmental Science*. 2020, Vol.13.3, pp. 896-907.

10 Harris J.H. Sintered aluminum nitride ceramics for high-power electronic applications. *JOM*. 1998, Vol. 50.6, pp. 56-60.

11 Popov A.I., Balanzat E.F centre production in CsI and CsI–Tl crystals under Kr ion irradiation at 15 K. *Nuclear Instruments and Methods in Physics Research Section B: Beam Interactions with Materials and Atoms*. 2000, Vol. 166, pp. 545-549.

12 Xiao Xiazi, and Long Yu. Nano-indentation of ion-irradiated nuclear structural materials: A review. *Nuclear Materials and Energy.* 2019, pp. 100721-100730.

13 Murty K.L., Charit I. Structural materials for Gen-IV nuclear reactors: Challenges and opportunities. *Journal of Nuclear Materials.* 2008, Vol. 383, pp. 189-195.

14 Lushchik A., et al. Influence of complex impurity centres on radiation damage in wide-gap metal oxides. *Nuclear Instruments and Methods in Physics Research Section B: Beam Interactions with Materials and Atoms*. 2016, Vol. 374, pp. 90-96.

15 Singh Fouran, et al. Micro-Raman investigations on zirconium oxide film during swift heavy ion irradiation to study crystalline-to-crystalline phase transformation kinetics by cascade overlap model. *Journal of Applied Physics*. 2019, Vol. 126.2, pp. 025901-025910.

16 Kozlovskiy A.L., et al. Radiation resistance of thin TiN films as a result of irradiation with low-energy Kr14+ ions. *Ceramics International*. 2020, Vol. 46.6, pp. 7970-7976.

17 Gladkikh T., et al. Changes in optical and structural properties of AlN after irradiation with C2+ ions of 40 keV. *Vacuum.* 2019, Vol. 161, pp.103-110.

18 Kimura Kazuie, Sumit Sharma, and Anatoli Popov. Fast electron–hole plasma luminescence from track-cores in heavy-ion irradiated wide-band-gap crystals. *Nuclear Instruments and Methods in Physics Research Section B: Beam Interactions with Materials and Atoms*. 2002, Vol. 191, pp. 48-53.

19 Averback R.S., et al. Defects in ion implanted and electron irradiated MgO and Al2O3. *Radiation effects and defects in solids*. 1995. Vol. 136.1-4, pp. 169-173.

20 Kotomin E.A., Kuzovkov V.N., and Popov A.I. The kinetics of defect aggregation and metal colloid formation in ionic solids under irradiation. *Radiation effects and defects in solids*. 2001. Vol. 155.1-4, pp. 113-125.

21 Tang Jinjin, et al. Effect of proton irradiation on the mobility of two-dimensional electron in AlGaN/AlN/GaN high electron mobility transistors at low temperature. *Journal of Vacuum Science & Technology B,*

.

Nanotechnology and Microelectronics: Materials, Processing, Measurement, and Phenomena. 2020, Vol. 38.2, pp. 023202-023210.

22 Qarra H.H., et al. Heavy ion irradiation damage in Zr2AlC MAX phase. *Journal of Nuclear Materials*. 2019, Vol.523, pp. 1-9.

23 Yano T., et al. Neutron irradiation effects on isotope tailored aluminum nitride ceramics by a fast reactor up to 2× l026 n/m2. *Journal of Nuclear Materials*. 2004, Vol. 329, pp. 1471-1475.

24 Bakan Emine, et al. High-temperature materials for power generation in gas turbines. *Advanced Ceramics for Energy Conversion and Storage*. 2020. Vol. 3, pp. 62-70.

25 Kozlovskiy A.L., et al. The influence of the energy of incident protons on the defect formation and radiation resistance of AlN ceramics. *Solid State Sciences*. 2020. Vol. 107, pp. 106367-106380.

26 Kozlovskiy A., et al. Dynamics of changes in structural properties of AlN ceramics after Xe+ 22 ion irradiation. *Vacuum*. 2018, Vol. 155, pp. 412-422.

27 Patino M.I., Doerner R.P., and Tynan G.R. Exposure of AlN and Al2O3 to low energy D and He plasmas. *Nuclear Materials and Energy*. 2020, pp. 100753-100760.

28 Werdecker Waltraud, and Fritz Aldinger. Aluminum nitride-an alternative ceramic substrate for high power applications in microcircuits. *IEEE transactions on components, hybrids, and manufacturing technology*. 1984, Vol. 7.4, pp. 399-404.

29 Bocanegra-Bernal M.H., and Matovic B. Mechanical properties of silicon nitride-based ceramics and its use in structural applications at high temperatures. *Materials Science and Engineering: A*. 2010, Vol.527.6, pp. 1314-1338.

30 Kozlovskiy A., et al. Optical and structural properties of AlN ceramics irradiated with heavy ions. *Optical Materials*. 2019, Vol. 91, pp. 130-137.

31 Kozlovskiy A., et al. Influence of He-ion irradiation of ceramic AlN. *Vacuum*. 2019. Vol. 163. pp. 45-51.

32 Zdorovets M., et al. Study of helium swelling in nitride ceramics at different irradiation temperatures. *Materials*. 2019, Vol. 12.15, pp. 2415-2430.

33 Uglov V.V., et al. Surface blistering in ZrSiN nanocomposite films irradiated with He ions. *Surface and Coatings Technology*. 2020, pp. 125654-125660.

34 Uglov V.V., et al. Blistering in Helium-Ion-Irradiated Zirconium, Aluminum, and Chromium Nitride Films. *Journal of Surface Investigation: X-ray, Synchrotron and Neutron Techniques.* 2020, Vol.14, pp. 359-365.

35 Evans J.H. An interbubble fracture mechanism of blister formation on helium-irradiated metals. *Journal of Nuclear Materials.* 1977. Vol. 68.2, pp. 129-140.

Article accepted for publication 21.05.2021

DOI 10.31489/2021No2/29-34

UDC 535.3; 535.374; 621.373.826

FEATURES OF STIMULATED EMISSION OF A MEROCYANINE DYE IN THE PORES OF ANODIZED ALUMINUM

Ibrayev N.Kh.[1], Afanasyev D.A.[1,2], Omarova G.S.[1]

[1]Institute of Molecular Nanophotonics, E.A. Buketov Karaganda University, Karaganda, Kazakhstan, guldenserikovna@mail.ru
[2]Institute of Applied Mathematics, Karaganda, Kazakhstan

The results of the study of the spectral-luminescent properties and the generation of stimulated emission of merocyanine dye molecules in a porous aluminum oxide films are presented. The addition of silver nanoparticles to the porous aluminum oxide films leads to an increase in the absorption cross section and an increase in the quantum yield of dye fluorescence in the alumina films. However, in the alumina films with silver nanoparticles, the generation of stimulated emission of dye molecules was not detected. We also studied the effect of polymethyl methacrylate polymer deposited on the surface of the alumina films with a dye on the spectral-luminescent properties and generation of stimulated emission of this dye. An increase in the optical density in the absorption band of the dye and an increase in the fluorescence intensity in samples with a deposited polymethyl methacrylate film are observed. The generation threshold of polymethine dye is reduced by a factor of 40 in the porous aluminum oxide sample with polymethyl methacrylate.

Keywords: porous aluminum oxide, electrochemical anodizing, merocyanine dye, stimulated emission, polymethyl methacrylate.

Introduction

Recently, the creation of active media based on nanostructured solid-state matrices doped with dye molecules has been a great attention. In this aspect, porous aluminum oxide (PAO) is one of the promising materials on the basis of which laser active media can be created. The films of PAO have a high specific surface area and thermal conductivity, and they are also optically transparent materials. The structure of the films is a system of tightly packed ordered pores. The pores are located perpendicular to the film surface. Diameter and distance between pores can be varied by changing the anodizing conditions [1]. If the cavities of cylindrical resonators are filled with organic dye molecules with a high fluorescence quantum yield, then such a system can be used as an active medium for a tunable laser. Stimulated emission has been obtained in porous aluminum oxide films for a number of dyes. It is shown that the use of metal nanoparticles (NPs) leads to a decrease in the generation threshold and an increase in the intensity of stimulated emission [2-4].

The aim of this work was to obtain metal-enhanced generation of a meracyanine dye in porous alumina films. For this, the PAO films were doped with silver and gold nanoparticles. However, the addition of silver and gold NPs didn't lead to the generation of stimulated emission of the samples. We studied the effect of a polymer film of polymethyl methacryolate (PMMA) applied to the surface of PAO with dye molecules. This promoted an increase in the stimulated emission intensity and a decrease in the generation threshold for dye molecules in PAO films with supported PMMA as compared to PAO without PMMA.

1. Experimental part

For the preparation of porous aluminum oxide, polished aluminum plates with a degree of purity (99.99%), deionized water (purified using an AquaMax water purification system), ethanol (anhydrous) were used. The H_2SO_4 electrolyte was used for anodizing. All reagents were analytically pure and were used without further purification. The method of preparing aluminum plates and the anodizing process are detailed in the work [5].

Films of porous alumina were synthesized under conditions including two stages of anodization at a voltage of U=40 V. The synthesis of PAO films was carried out in accordance with the procedure given in the works [3, 6]. Merocyanine dye **1** was used for the investigated (Fig.1).

.

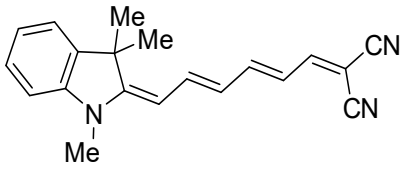

Fig.1. Merocyanine dye **1**

The method for preparation and purification of the dye **1** is described in the work [7]. The choice of this dye is due a high photochemical stability, soluble in the solvents used in the work. Dye 1 also has stimulated emission in solutions. The surface morphology of the obtained PAO films was investigated on a Tescan Mira-3 (Tescan) scanning electron microscope (SEM). The absorption spectra of the solutions and films under study were measured on a Cary-300 spectrophotometer (Agilent). Fluorescence spectra were measured on a Cary Eclipse spectrofluorometer (Agilent). The lifetimes of the excited state of the dye molecules were measured using a time-correlated photon counting pulsed spectrofluorimeter (Becker & Hikl, Germany). The fluorescence quantum yield (φ_f) of the dye was measured by the absolute method using an integrating sphere (Avantes).

2. Discussion of results

Optical properties of PAO films doped with silver NPs and molecules of the dye **1** were studied. The properties of stimulated emission of meracyanine **1** in PAO and the effect of silver NPs on this properties are studied. The concentration of Ag nanoparticles in PAO films was varied concentration of the precursor of silver NPs (silver nitrate). Precursor concentrations of 0.002 M and 0.02 M were used. The corresponding films were designated conventionally I and II. The pore diameter is on average 15-20 nm (Fig. 2, a).

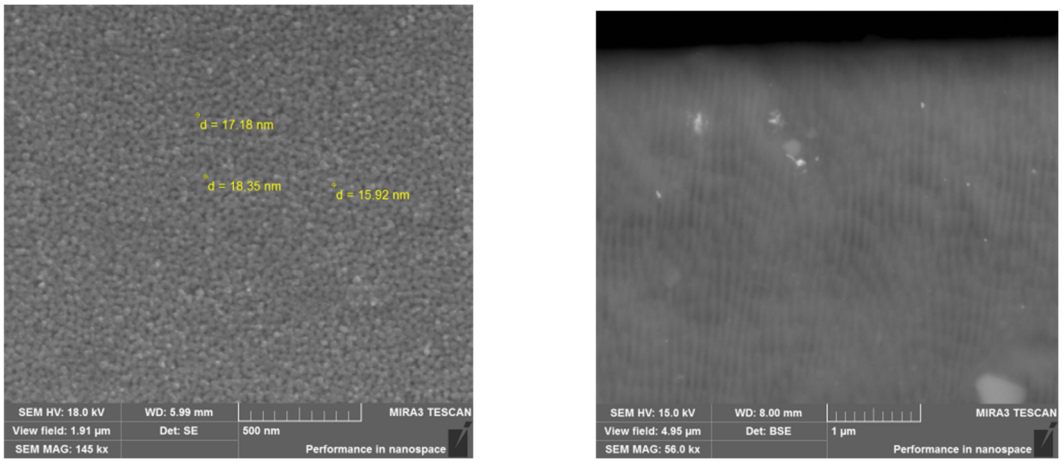

a b

Fig.2. SEM images of the surface of the PAO film (a) and a transverse chipping (b) of the sample obtained by anodizing in sulfuric acid at 15 V.

Images of PAO films doped with silver NPs are shown in Fig. 2. Light particles on the surface and in pores are silver NPs, which is confirmed by the results of X-ray spectral microanalysis (Fig. 3, c). The absorption spectra of the dye in the PAO films are shown in Fig. 4. The maximum fluorescence of the dye is at 652 nm. The fluorescence intensity depends on the concentration of NPs in the pores. The maximum luminescence intensity is observed in films I (Fig. 4). For dye **1** in solution and in films, the fluorescence quantum yield (φ_f) was determined. In ethanol solution, the quantum yield of the dye was φ_f=0.05 at $C_{cr}=10^{-6}$ mol/L and φ_f=0.01 at $C_{cr}=10^{-4}$ mol/L. These values of the quantum yield are close to the values obtained in the work [8]. The fluorescence quantum yield of the dye in PAO films has similar values. For example, in PAO films without silver NPs φ_f=0.003. In the presence of silver NPs, the luminescence quantum yield increases to φ_f=0.015 for the films I and φ_f= 0.004 for the films II. The decay of the luminescence of the dye in the solution occurs exponentially with τ_f=0.4 ns (Fig. 5, a).

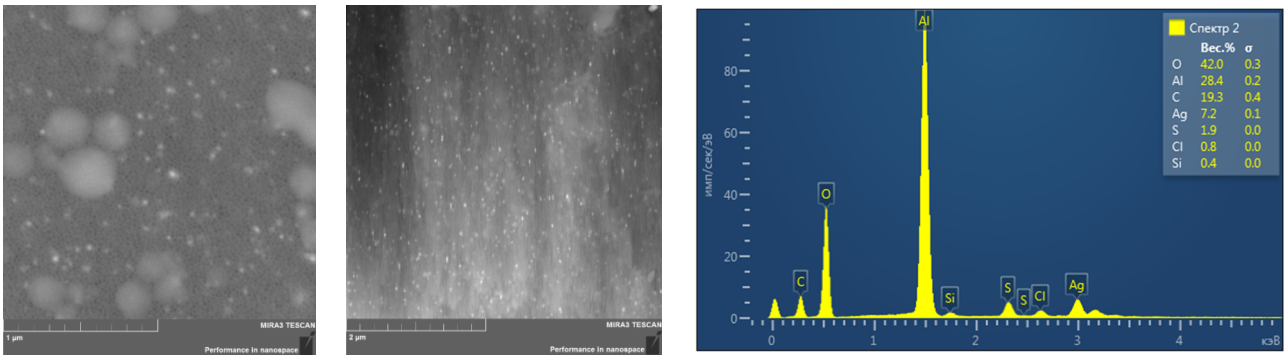

a b c

Fig.3. SEM images of the surface (a), chipping (b), and X-ray spectrum (c) of the PAO film doped with silver NPs.

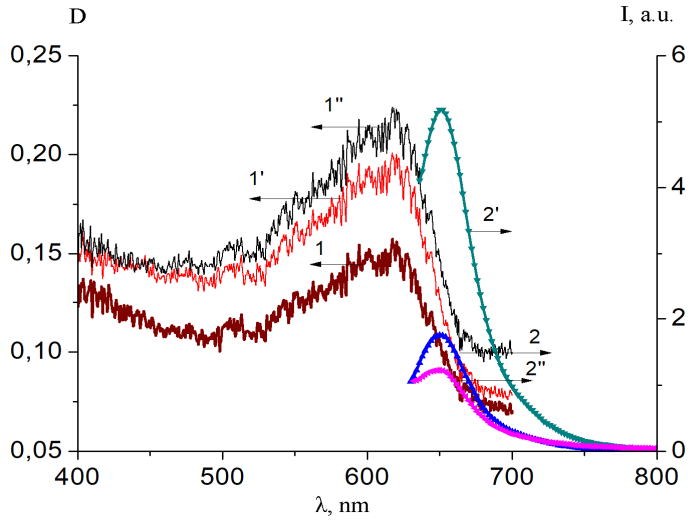

Fig.4. Absorption spectrum (1, 1 ', 1' ') and fluorescence (2, 2', 2 '') of the dye in POA films:
1, 2 - spectra of the dye in PAO without silver NPs; 1', 2' - sample I; 1", 2 " - sample II

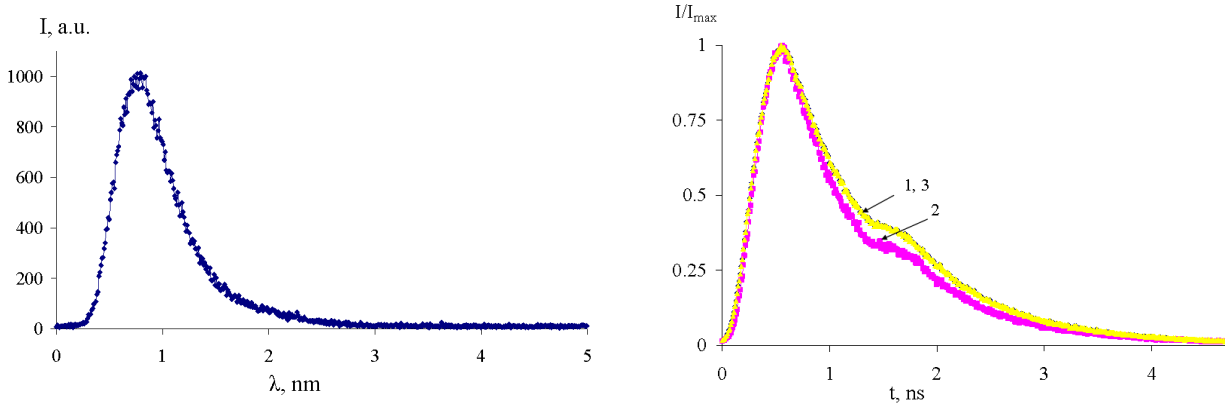

a b

Fig.5. Kinetics of fluorescence decay of dye **1** in solution (a) and in porous films of POA (b):
1 - samples without silver NPs; 2 - sample I; 3 - sample II.

For PAO films with a dye, the kinetic fluorescence curves have a certain inflection, which is observed at the decay of the luminescence intensity. The fluorescence lifetime of the dye in the films is 0.98 ns, 0.95 ns, and 1.06 ns in the series of samples – without silver NPs, with NPs sample I and with NPs sample II, respectively (Fig. 5, b). In this case, for film II, an insignificant increase in the fluorescence lifetime is observed. An increase in the luminescence lifetime in the presence of silver NPs was also observed for an

.

ethanol solution of merocyanine dye **1** and can be associated with the reverse energy transfer from NPs to the dye molecules [9]. The spectrum of stimulated emission of the dye in ethanol with C_{cr} = 2.5×10^{-4} mol is shown in Fig. 6, curve 1. The length of the active medium in the quartz cell was 1 cm. At a pump source power density (P) below 4 MW/cm^2, only spontaneous fluorescence of the dye with a half-width of the band $\Delta\lambda_{1/2}$=30 nm is observed. At P=5.2 MW/cm^2, a narrow lasing band with $\Delta\lambda_{1/2}$=3 nm appears against the background of the fluorescence spectrum.

The lasing spectrum has three maxima at wavelengths of 677 nm, 679.5 and 682 nm. The observed maxima in the lasing spectrum are modes of laser radiation, since they are equidistant from each other [10]. The emission spectrum of the dye in PAO is shown in Fig. 6, curve 2. The stimulated emission spectrum has one maximum at 667 nm. Dye radiation is generated at high values of the pump power density (~ 100 MW/cm^2). The reasons for such an ineffective dye generation may be cis-trans photoisomerization of merocyanine dye molecules [11], as well as the interaction of dye molecules with molecular oxygen [12].

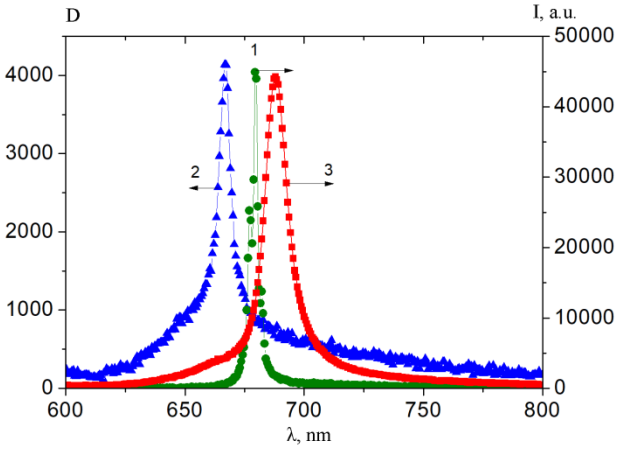

Fig.6. Spectra of stimulated emission of the dye in different media:
1 - in ethanol C=2.5·10^{-4} mol, P=5.2 MW/cm^2; 2 - in PAO matrix before surface modification,
P = 160 MW/cm^2; 3 - in PAO matrix with a PMMA film applied to the PAO surface, P=40 MW/cm^2

Dependences of the FWHM (full width at half maximum) and the intensity of stimulated emission in the PAO on the value of P were plotted from the measured emission spectra (Fig.7). The values of generation threshold for the samples were determined. The lasing threshold was 103 MW/cm^2 for PAO film with dye **1** without NPs (Fig. 7).

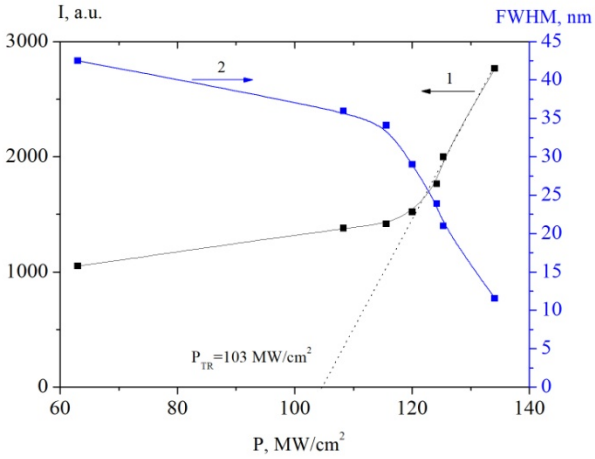

Fig.7. Dependence on the pump power density of the luminescence intensity (1) and the half-width of the emission band (2) of the dye in PAO (λ_{gen}=532 nm).

The emission spectra of PAO films doped with dye **1** and Ag NPs were measured. The measurement results show the absence of stimulated emission in PAO films doped with Ag NPs. The generation of stimulated emission from the dye in PAO films doped with Au NPs was also not detected. PAO films and the technique of doping of films with gold NPs are described in the work [13]. It was proposed to deposit a

polymer film of polymethyl methacrylate (PMMC) on the surface of the PAO for reducing number of dye molecules nonradiatively transforming into S_0 upon laser photoexcitation. It is the main polymer used for the manufacture of active laser media with dye molecules [14]. This was the reason for the choice the PMMC. The spectrum of stimulated emission in the modified film is shown in Fig.6, curve 3.

The addition of polymer leads to an increase in the stimulated emission intensity, a decrease in the lasing threshold to 3 MW/cm2, and a shift of the lasing maximum to longer wavelengths to 687 nm. In this case, the value of Q-factor has similar values for films before the application of the polymer film and after its application (Q≈57). Measurements of the absorption, fluorescence, and fluorescence excitation spectra of the PAO films with dye **1** before and after the application of the PMMA polymer were taken. Fig. 8, a shows that the absorption band of the dye in the PAO matrix has a maximum at a wavelength of λ=610 nm.

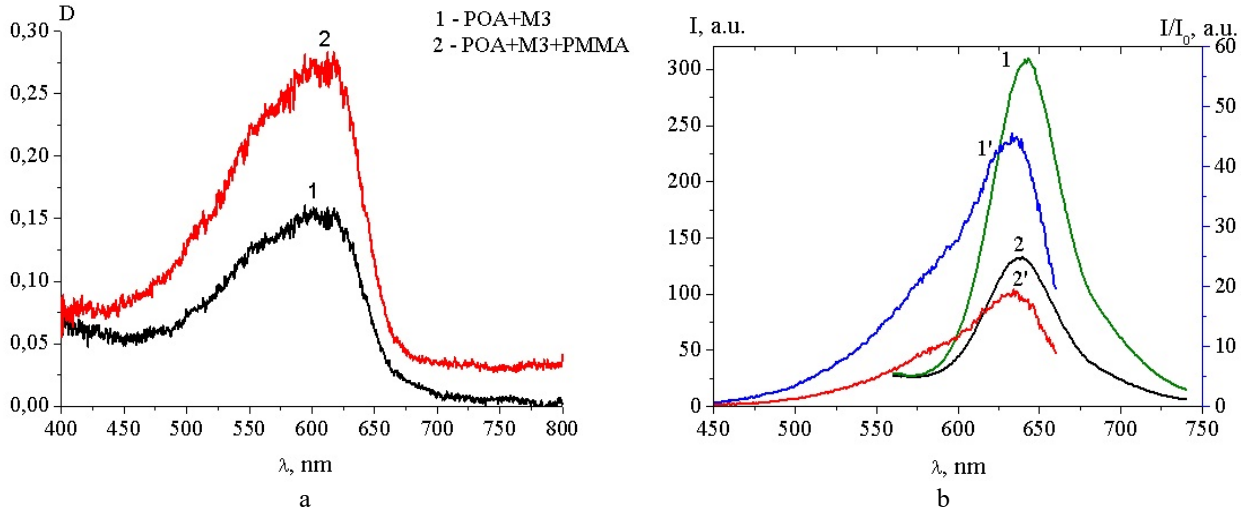

Fig.8. Absorption spectra (1, 2) (a), fluorescence (1, 2) and fluorescence excitation spectra (1', 2') (b) of PAO films: 1, 1'– POA+dye **1**+PMMC Fl; 2, 2'– POA+ dye **1**.

The deposition of the polymer on the surface of the PAO film does not change the shape of the absorption spectrum of the dye, but leads to a twofold increase in the optical density D. Since the concentration of dye molecules in the POA doesn't change. The increase in the value of D of the dye molecules can be associated with an increase in the extinction coefficient of the dye **1** when the PMMA polymer is applied to the surface of the POA. Photoexcitation of the fluorescence of the dye in the samples was carried out in the absorption band of the dye at a wavelength equal to λ=640 nm. The fluorescence spectrum and fluorescence excitation spectra show no changes in the shape of the spectra when the PMMC polymer is applied to the surface of the PAO. The intensity of the fluorescence spectra of the dye in the POA+PMMC films increases by a factor of 2.4 in comparison with the sample without PMMC. Thus, measurements of the absorption and fluorescence spectra of the dye in the PAO films showed an increase in the optical density in the absorption band of the dye and an additional increase in the fluorescence intensity of the dye in the PAO films with the polymer PMMC deposited on their surface.

Conclusions

The photonics of the merocyanine dye **1** in POA films was investigated. Low-Q stimulated emission of the dye is observed in the samples. The addition of silver nanoparticles to POA films leads to an increase in the absorption cross-section and an increase in the quantum yield of dye fluorescence in POA films. In the presence of silver and gold NPS in the pores of aluminum oxide, stimulated dye radiation wasn't observed. It is proposed to apply a PMMC polymer film to the surface of the POA for the reducing the influence of the external environment on the properties of the stimulated radiation of the dye in the POA films. There is a 2-fold increase in the optical density in the dye absorption band and a slight increase in the fluorescence intensity in samples with a PMMC film. The generation threshold of the merocyanine dye **1** is reduced by a factor of 40 in a POA sample with PMMC. But the Q-factor of the resonator doesnt change (Q≈57).

.

Acknowledgements

This research is funded by the Science Committee of the Ministry of Education and Science of the Republic of Kazakhstan (Grant No. AP08856161).

REFERENCES

1 Diggle J.W., Downie T.C., Coulding C. W. Printing on Anodized Aluminium Surface. *Chemical Reviews.* 1969, Vol. 69, pp. 365 – 405.

2 Shelkovnikov V.V., et al. Lasing of a solid-state active element based on anodized aluminum oxide film doped with rhodamine 6G. *Russian Physics Journal.* 2017, Vol. 59, No. 12, pp. 1989 – 1995.

3 Ibrayev N.Kh., Aimukhanov A.K. Influence of plasmon resonance in silver nanoparticles on the properties of stimulated emission of 1, 3, 5, 7, 8 - pentamethyl - 2,6-diethylpyrromethene difluoroborate molecules in film of porous aluminum oxide. *Optics and Laser Technology.* 2019, Vol. 115, pp. 246 – 250.

4 Afanasyev D.A., Ibrayev N.Kh., Omarova G.S., et al. Spectral-Luminescence and Lasing Properties of Merocyanine Dye Solutions in the Presence of Silver Nanoparticles. *Optics and Spectroscopy*. 2020, Vol. 128, No.1, pp.61 – 65.

5 Napolskii K.S., Barczuk P.J., Vassiliev S.Yu., et al. Templating of electrodeposited platinum group metals as a tool to control catalytic activity. *Electrochimica Acta.* 2007, Vol. 52, No. 28, pp. 7910 – 7919.

6 Aimukhanov A.K., Ibrayev N. Kh. Influence of gold nanoparticles on the properties of stimulated emission of 6-amino-1h-phenalen-1-one in the pores of anodized aluminum oxide. *Journal of Luminescence.* 2018, Vol. 204, pp.216 – 220.

7 Kulinich A.V., Derevyanko N.A., Ishchenko A.A., et al. Synthesis and spectral properties of malononitrile-based merocyanine dyes. *Russian Chemical Bulletin.* 2019, Vol. 54, No. 12, pp. 2820 – 2830

8 Bondarev S.L., et al. Fluorescence and solvatochromism of a merocyanine dye with a high quadratic polarizability in solutions and polymer films. *Journal of Luminescence*. 2007, Vol. 124, No. 1, pp.178 – 186.

9 Yang M., Moroz P., Jin Z., et al. Delayed photoluminescence in metal-conjugated fluorophores. *JACS.* 2019, Vol. 141, No. 28, pp.11286 – 11297.

10 Ibrayev N.Kh., Ishchenko A.A., Afanasyev D.A., Zhumabay N.D. Active laser medium for near-infrared spectral range based on electron-unsymmetrical polymethine dye and silver nanoparticles. *Applied Physics B: Lasers and Optics.* 2019, Vol. 125, pp. 1 – 7.

11 Chibisov A.K., Zakharova G.V., Gorner H., et al. Photorelaxation Processes in Covalently Linked Indocarbocyanine and Thiacarbocyanine Dyes. *Journal of Chemical Physics.* 1995, Vol. 99, pp. 886 – 893.

12 Butrimovich O.V., Voropay E.S., Ksenofontova N.M. *Study of the photostability of active media based on polymethine dyes*. All-Union Meeting: Inverse Population and Lasing on Transitions in Atoms and Molecules, 1986, 52 p. [in Russian].

13 Omarova G.S., Afanasyev D.A., Ibrayev N. Kh. Generation of stimulated emission of electron-unsymmetrical polymethine dye in films of porous aluminum oxide doped with gold nanoparticles. *Theoretical and Applied Science.* 2019, Vol. 78, No. 10, pp. 351 – 358.

14 Peterson O.G., Snavely B.B. Stimulated emission from flashlamp-exsited organic dyes in polymethyl methacrylate. *Applied Physics Letters*. 1968, Vol. 12, pp. 238 – 240.

Article accepted for publication 21.05.2021

DOI 10.31489/2021No2/35-39

UDC 691.175.5.8

STUDY ON THE INFLUENCE OF ELECTRON BEAM ON THE PHYSICOCHEMICAL PROPERTIES OF POLYAMIDE 6

Rakhadilov B.K.[1,2], Akatan K.[1], Maulet M.[1], Kabdrakhmanova S.K.[1], Magazov N.M.[1*]

[1] S.Amanzholov East Kazakhstan University, Ust-Kamenogorsk, Kazakhstan, magazovn@mail.ru

[2] Plasma Science LLP, Ust-Kamenogorsk, Kazakhstan

In this research work has been studied the effect of electron irradiation on the properties and structure of PA6 polyamide. The treatment was carried out with an industrial pulse accelerator in air with an irradiation dose in the range of 100-400 kGy. The processed polymer was also studied by Fourier-transform infrared spectroscopy, scanning electron microscopy, X-ray phase analysis and differential scanning calorimetry. According to the results of the study was known that electron beam treatment affects the crystal structure of polyamide-PA6, reducing its size. Also, it was found that the radiation dose of 200 kGy is optimal for preserving the crystal structure in comparison with 100, 300 and 400 kGy.

Keywords: polyamide, electron beam, crystal structure, polymer, surface treatment.

Introduction

As a result of the development of science and technology, polymer materials have become increasingly important not only as electrical isolation in electrical installations but also as substitutes for traditional metal parts. This allows obtaining modified polymers that are economically effective and have the necessary physical and mechanical properties [1]. The method of processing polymer materials with an electron beam (EB) has been used for the last 50 years in production [2]. EB treatment has several advantages compared to the chemical modification method. In particular, the product does not contain any catalyst residues and by-products the process is repeated and simple, the exact amount of energy and temperature affected can be controlled [2-6].

Polyamide is one of the most widely used polymers in manufacturing due to its high strength, resistance to corrosion and aggressive environment and self-lubricating properties [7, 8]. But in the process of using as a movable particle under heavy loads at low temperatures, the friction coefficient of polyamide is large, a high degree of wear and under the influence of polar functional groups and hydrogen bonds in the molecule, absorbing a large amount of moisture mechanically changes to a more soft and plastic. This negatively affects the quality of the material and reduces the practical application [9-13]. At 22 kGy using red phosphorus with a mass fraction of 12.5% as a binding agent was found the fire resistance of PA6-polyamide increases [14]. It is investigated that by processing polyamide-PA6 EB obtained without a binding agent, and it is possible to increase the thermal properties and reduce the water-absorbing properties [15]. Making the necessary changes in the properties of polymers due processing with high-energy electrons increases their practical significance. This proposed that studying polymer modification using EB and its changes leading to the polymer properties is relevant today.

It was found that the mechanism of processing the EB polymer is complex, and the possibilities of random processes are huge [16].In this study was studied the effect of electron beam treatment at various doses on the microstructure and morphology of the surface and the thermal properties of polyamide-PA6.

1. Research materials and methods

The study was used the disc-shaped sample TECAMID-6 (polyamide-6, Russia) (PA6) with a thickness of 0.1 cm, diameter 2.5 cm, carried out processing of industrial pulse accelerator (IL-10, Russia) in the air with an energy of 1.3 MeV, a current of 12mA, conveyor speed 3.5 m/min, the dose of 100, 200, 300, 400kGy. The chemical structure of the treated PA6 with EB was studied on a Fourier-IR spectrometer (Simex FTIR-801, Russia), the surface morphology on a scanning electron microscope (SEM) (JSM-

.

6390LV), the thermal characteristic on a differential scanning calorimeter (Labsys Evo Setaram, France) in the temperature range of 20-300C0, the heating rate in the nitrogen atmosphere +10 C0/min.

2. Results and discussion

Figure 1 is shown the IR spectrum of PA6 untreated samples and treated samples under EB with irradiation doses of 100, 200, 300, and 400 kGy. Comparing the spectra, we see that all the absorption peaks of the PA6 samples treated by EB are similar to untreated PA6 sample's absorption peaks and do not have a new signal.The study was determined in the PA6 molecule at the peak of 976 cm-1 of the CO-NH group gave a β-crystal structure, 1118 cm-1 C-C, 1168 cm-1 III-amide and the CO-NH group giving α-crystal structure absorption values 928 cm-1-1260 cm-1.These values similar to previous studies [10, 16].

The symmetric and asymmetric motion of the 1640 cm-1-1530 cm-1 N–H group and 2860 cm-1-3080 cm-1 CH2 absorption peaks are seen. And at a wavelength of 3300 cm-1, there is a signal of a very weak variable hydrogen bond between N-H and C=O [17].The change in the absorption intensity of the critical peaks that provide information from changes in the chemical structure of PA6 after EB treatment is presented in Table 1.

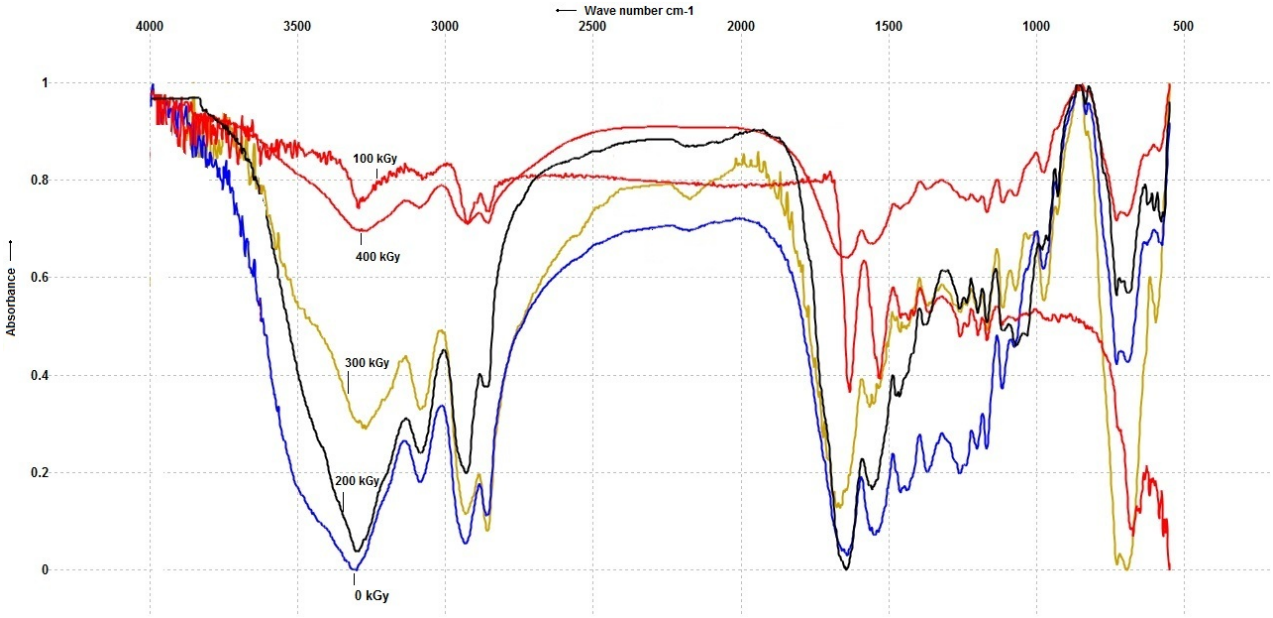

Fig.1. Comparative IR spectra of PA6 not treated with EB and treated at different EB doses.

Table 1. The relative intensity of PA6 in different IR absorption regions, varying within the radiation dose range from 0 to 400 kGy

Electron beam dose, kGy	absorption intensity change, %		
	3300 cm-1	1200 cm-1	976 cm-1
0	0.997	0.752	0.548
100	0.259	0.525	0.208
200	0.944	0.505	0.565
300	0.971	0.489	0.614
400	0.303	0.265	0.277

Based on the results in Table 1, we see that when the radiation dose was increased from 0 kGy to 100 kGy, the absorption intensity of 3300 cm-1 immediately decreased from 0.997% to 0.259%. This indicates the break of the weak hydrogen bond between N-H and C=O after the EB irradiation [18]. We see that between 976 cm-1 and 1200 cm-1 the intensity of crystal building signals decreases from 0.548% to 0.277% and from 0.752% to 0.265%, respectively, with an increase in the radiation dose. In the process of electron absorption, the polymer chain disintegrates, which is explained by the appearance of changes in the crystal lattice [19]. This phenomenon is clearly seen in Figure 3 as a result of the X-ray phase analysis.

Figure 2 shows a micrograph obtained from an electron scanning microscope (ESM) of changes in the polyamide surface morphology before treatment with PA6 EB and after treatment with different doses. The surface of the untreated PA6 sample with EB has a uniform spherulitic structure with minor scratches (Fig. 2a). With an increase in the EB dose from 0 kGy to 400 kGy, a change in the surface topography of the sample and a violation of the spherulitic structure (2b-2e). This phenomenon is explained by the fact that under the action of the electron flow, the surface volume of polyamide increases, and the crystal properties decrease [19].

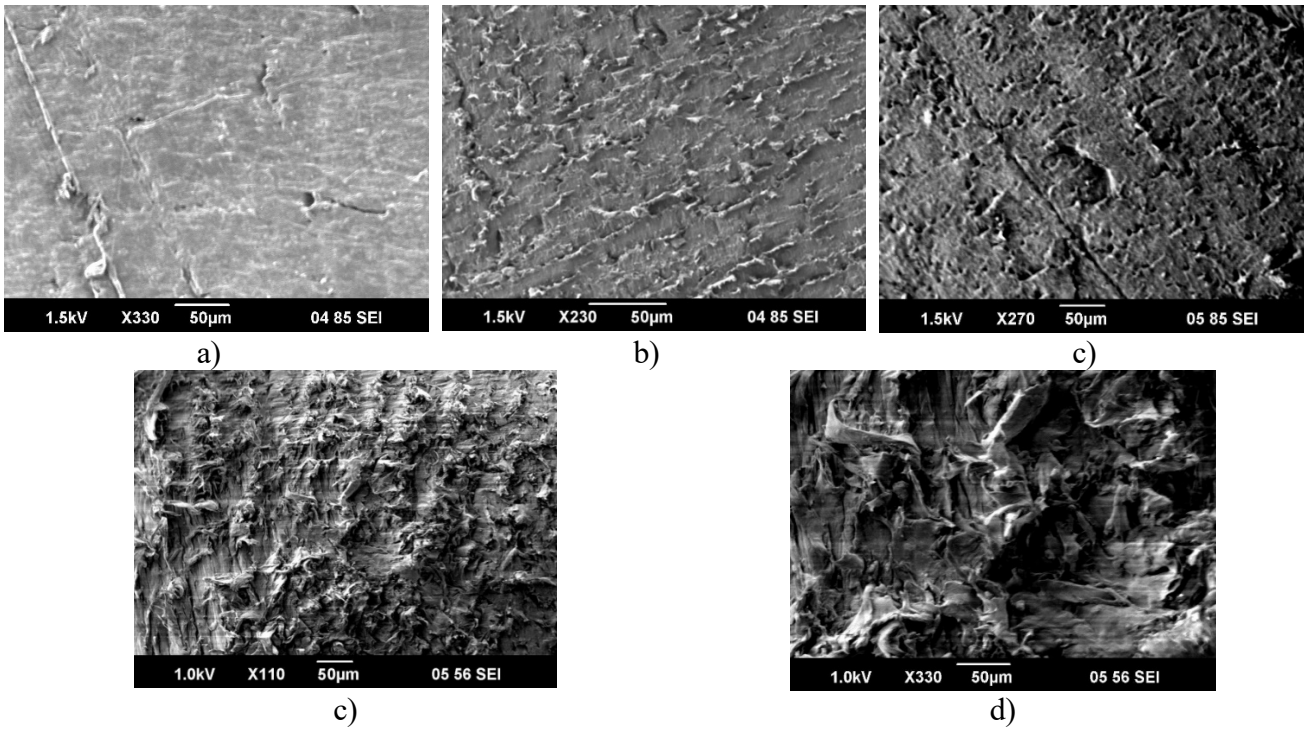

Fig. 2. SEM micrograph of untreated with EB and treated with EB samples PA6 in different doses: a)-0 kGy; b)-100 kGy; c)-200 kGy; d)-300 kGy; e)-400 kGy

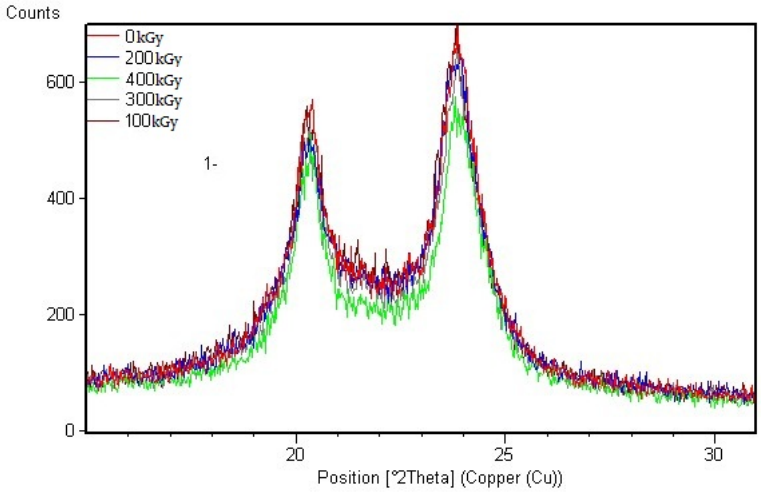

Fig.3. X-ray diffractogram PA6, not treated with EB and treated with EB in different doses

The X-ray phase analysis of PA6 sample not treated with EB and treated at different doses are shown in Figure 3.On the diffractogram 2θ 200 and 240 from all the samples, we observe two intense peaks. This is the α-crystalline phase of polyamide-PA6 [19]. The α-crystal phase is visible at these angles is said in these studies [20, 21]. It can be seen that as the radiation dose increases from 0 kGy to 400 kGy, the intensity of the peaks decreases compared to 0 kGy. This phenomenon is clearly seen in the thermal result of the DSC in Figure 4 and

.

Table 2.At 0 kGy, the melting point is 220^{0}C, the melting enthalpy is 57.33 J ·g^{-1}, and with an increase in the radiation dose to 400 kGy, the melting temperature and enthalpy respectively decreased to 215^{0}C, 27.52 J·g^{-1}.

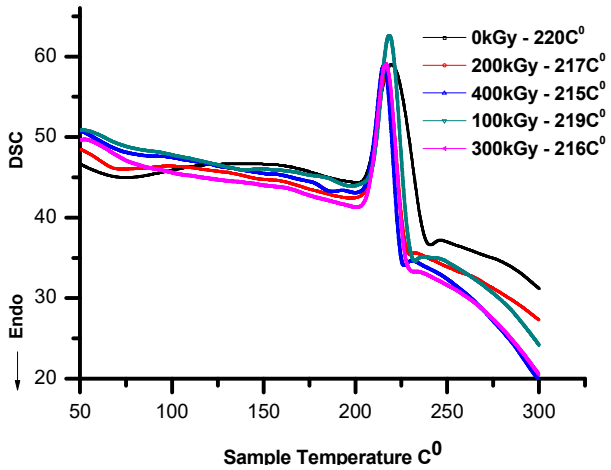

Fig.4. DSC thermogram samples -PA6, not treated with EB and treated with EB in different doses.

Table 2. DSC values of polyamide-PA6 untreated and treated with EB

Radiationdose, kGy	Meltingpoint, C^0	Meltingenthalpy, J·g^{-1}
0	220	57.33
100	219	57.07
200	217	56.55
300	216	27.65
400	215	27.52

During the process, the crystallinity decreases due to the inhibition of recombination and pyrolysis, the sewing of free radicals under the action of external electrons [22].

Conclusion

Based on the results of IR, SEM X-ray diffractometer and DSC was known that during the processing of EB, the variable hydrogen bond in the polyamide-PA6 molecule disappears, crystallization decreases, but free radicals between the monomers bind under the action of an external electron flow. It was found that at a radiation dose of 200 kGy, the crystal structure is preserved in comparison with 100, 300 and 400 kGy. It was revealed that the melting point of the PA6 polymer decreases from 220°C to 215°C after EB. It was found that after EB there is a change in the topography of the sample surface and a violation of the spherulite structure. This phenomenon is explained by the fact that, under the action of an electron beam, the volume of the polyamide surface increases, and the properties of the crystal deteriorate.

Acknowledgments

The work was carried out within the framework of grant funding for scientific research on 2021 year by the Science Committee of the Ministry of Education and Science of the Republic of Kazakhstan (AP08957765).

REFERENCES

1 Raghu S., Archana K., Sharanappa C., et al. Electron beam and gamma ray irradiated polymer electrolyte films: Dielectric properties. *Journal of Radiation Research and Applied Sciences*, 2016, Vol. 9, pp. 117-124.

2 Leisen C., DrummerD. Infrared welding of cross-linkable polyamide 66. *eXPRESS Polymer Letters*,2016, Vol.10, No.10, pp. 849 – 859.

3 Mondal M., Gohs U., Wagenknecht U., Heinrich G. Additive free thermoplastic vulcanizates based on natural rubber. *Macromol. Chem. Phys.*2013, Vol.143, pp. 360-366.

4 Boldt R., Gohs U., Wagenknecht U., Stamm M. Effect of electron-induced reactive processing on morphology and structural properties of high-density polyethylene. *Polymer 95,* 2016, Vol.95, pp. 1-8.

5 Rakhadilov B.K., Sagdoldina Z.B., Ocheredko I.A., et al. Impact research of electron beam processing on the structure and properties of PA6 polyamide. *Eurasian Physical Technical Journal.* 2019, Vol.16, No.2, pp. 43-47.

6 Pramanik N.K., Haldar R.S., Bhardwaj Y.K. Radiation processing of Nylon 6 by e-beam for improved properties and performance. *Radiat. Phys. Chem.*, 2009, Vol.78, pp.199-205.

7 Duxin Li, Ying Xie, Wen Juan Li, Yi Lan You, Xin Deng. Tribological and Mechanical Behaviors of Polyamide 6/Glass Fiber Composite Filled with Various Solid Lubricants. *The Scientific World Journal*, 2013, Vol.2013, pp. 1-9. doi: 10.1155/2013/320837.

8 Ovsik M., Stanek M., Senkerik V. Influence of electron beam irradiated on the surface properties of polyamide measured by micro-indentation test. *MATEC Web of Conferences 125*, 2017, Vol.125, pp. 1 – 4.

9 Meng H., Sui G. X., Xie G. Y., Yang R. Friction and wear behavior of carbon nanotubes reinforced polyamide 6 composites under dry sliding and water lubricated condition. *Composites Science and Technology*, 2009, Vol. 69, No.5, pp. 606-611.

10 Zhao R. G., Luo W. B., Xiao H. M., Wu G. Z. Water absorptivity and mechanical behaviors of PTFE/PA6 and PTFE/PA66 blends. *Transactions of Nonferrous Metals Society of China*, 2006, Vol. 16, Suppl. s2, pp. 498-503.

11 Chen Z., Li T., Yang Y., Liu X., Lv R. Mechanical and tribological properties of PA/PPS blends. *Wear*, 2004, Vol. 257, No. 7-8, pp. 696-707.

12 Burillo G., Adem E., Muñoz E., Vásquez M. Electron beam irradiated polyamide-6 at different temperatures. *Radiat. Phys. Chem.,* 2013, Vol.84, pp.140-144.

13 Timus D.M., Cincu C., Bradley D.A., Craciun G., Mateescu E. Modification of some properties of polyamide-6 by electron beam induced grafting. *Appl. Radiat. Isot.*, 2000, Vol.53, pp.937-944.

14 Pramanik N.K., Haldar R.S., Bhardwaj Y.K. Radiation processing of Nylon 6 by e-beam for improved properties and performance. *Radiat. Phys. Chem.*, 2009, Vol.78, pp.199-205.

15 Dasgupta S., Hammond W.B., Goddard III W.A. Crystal structures and properties of nylon polymers from theory. *Journal of American Chemical Society*, 1996, Vol.118, No. 49, pp. 12291-12301.

16 Kim J.Y., Kim O.S., Kim S.H., Jeon H.Y. Effects of electron beam irradiation on poly(ethylene 2,6-naphthalate)/poly(ethylene terephthalate) blends. *Polym.Eng.Sci.*2004, Vol.44, pp. 395-405.

17 Pramanik N.K., Sarwar Alam M., Khanda R.K. Electron Beam Irradiation of Nylon 66: Characterization by IR Spectroscopy and Viscosity Studies. *International Journal of Innovative Research in Science.* 2015, Vol. 4, Issue 1, pp. 18547-18555. doi: 10.15680/IJIRSET.2015.0401019.

18 Makuuchi K., Cheng S. *Radiation Processing of Polymer Materials and Its Industrial Applications.* New Jersey, 2012, 444 p.

19 Shifeng Zhu, Meiwu Shi, Meifang Zhu. Effects of Electron-Beam Irradiation Crosslinking on PA6 Fibers. *Fibers and Polymers,* 2013, Vol.14, No.4, pp. 525-529.

20 Sibilia J.P. A *Guide to Material Characterization and Chemical Analysis*. New York, 1996, 318 p.

21 Shailesh M.K., Kumar A. Radiation-induced grafting of vinylbenzyl trimethyl ammonium chloride onto nylon-6 fabric. *Radiat. Phys. Chem.*, 2007, Vol.76, pp. 901 – 906.

22 Nalwa H.S. *Ferroelectric Polymers*, New York, 1995, 895p.

Article accepted for publication 21.05.2021

.

DOI 10.31489/2021No2/40-46
UDC 535.215; 539.23; 535.3; 538.9

INFLUENCE OF STRUCTURAL FEATURES OF ZNO FILMS ON OPTICAL AND PHOTOELECTRIC CHARACTERISTICS OF INVERTED POLYMER SOLAR ELEMENTS

Zeinidenov A.K.[1], Abisheva A.K.[1*], Ilyassov B.R.[1,2], Aimukhanov A.K.[1], Abilmazhinov S.E.[2]

[1] E.A Buketov Karaganda University, Research center of Nanotechnology and Functional Nanomaterials, Karaganda, Kazakhstan
[2]Sh.Ualikhanov Kokshetau University, Kokshetau, Kazakhstan, a7jan@mail.ru

In this work we investigated the effect of preliminary annealing of zinc acetate solution films on the morphology, structure, optical properties of the formed ZnO films and also on the photovoltaic properties of polymer solar cells based on the obtained ZnO films. It was found that the pre-annealing temperature significantly affects the morphology and structure of the obtained ZnO films. At pre-annealing temperatures below 200 °C the films have a strongly relief morphology (wrinkled morphology), while at pre-annealing temperatures above 200°C the surface morphology of the films is smooth. The relief of ZnO films affects the photocurrent density of solar cells. Cells based on ZnO films with wrinkled morphology showed a higher photocurrent compared to smooth morphology, which is due to strong light scattering and, as a result, the optical path of light in the photoactive layer is increased due to multiple reflection of light in the wrinkled structure of ZnO. In addition, with increasing pre-annealing temperature, the photovoltage of solar cells and the rate of recombination of charge carriers increases, but the diffusion coefficient of charge carriers decreases, which indicates an increase in the density of defects in the crystal lattice of ZnO. Thus, it has been shown that smooth or highly relief thin ZnO films with controlled properties can be obtained from a zinc acetate solution.

Keywords: zinc oxide, thin films, annealing, surface morphology, absorption spectra, inverted polymer solar cells.

Introduction

In recent years, much attention has been paid to the development of organic solar cells (OSC) due to their rapid increase in energy conversion efficiency, economy, ease of processing and flexibility. Research has experienced a renaissance with the introduction of high-performance, low-bandgap polymer donors and non-fullerene acceptors. Today, the energy conversion efficiency of polymer solar cells reaches 17-18% [1, 2]. In addition to innovations in the molecular aspects of OSC, it has also been found that processing methods and buffer layers also play a key role in obtaining better performance parameters. Various oxides of n-type metals with a wide band gap, such as TiO_2, ZnO, Cs_2CO_3 and some polyelectrolytes with a large dipole moment, have been successfully used as interfacial electron transport layers in inverted devices [3]. In addition, various forms of film nanostructuring, surface treatment, and processing aids have been studied to improve the efficiency of charge collection, transport, and selectivity [4].Therefore, the current research is focused on the study of the electron transport layer, in our case, zinc oxide (ZnO), in inverted polymer solar cells (IPSC).

Zinc oxide is one of the most promising materials for electron transfer in IPSC due to its good environmental resistance, high transparency in the visible and near infrared regions, and high electron mobility. ZnO films are obtained by various methods, including the sol-gel method. The sol-gel method is a technologically simple process that allows you to obtain better quality coatings. It should be noted that the important crystal properties of thin ZnO films strongly depend on the growth conditions, the growth technique, and the substrate [5]. ZnO-based materials can be used in various optoelectronic devices, sensors, transistors, and solar cells [6]. Also, good operational stability of IPSC with ZnO was noted, due to the fact that ZnO blocks ultraviolet light, which leads to negligible photodegradation of organic materials [7]. Previous studies have presented similar effective structures of zinc oxide for IPSC. Various names have been given to these structures, such as nano-comb, ripple, wavy or wrinkled structure. For example, in article [4], nano-combs were obtained, formed by a simple process of linear annealing. In work [8], the influence of the flat and nano-ribbed morphology and thickness of the ZnO layer on the parameters of the device was studied, thereby emphasizing the sensitivity of these devices to the active film thickness. At the same time, it was

mentioned that there was no significant difference in performance between the structures. In a study [9], the wrinkled structure of the surface was optimized by adding ZnO nanoparticles to a zinc acetate solution. As a result, it was found that the productivity of a device based on wrinkled ZnO with nanoparticles was two times higher than that of smooth thin films. Kim and others [10] found that the properties of wrinkled structures can be tuned by changing the concentration of zinc in the precursor solution. In addition to the uniformity and ordering of wrinkles and cavities in such surface structures, defects on them also play an important role in the operation of the device. Therefore, there is a need for a detailed study of the properties of thin ZnO films with a wrinkled structure.

In this regard, this work presents a method for obtaining thin ZnO films with different morphologies and investigates the effect of preliminary annealing on their morphological, optical, and electrophysical properties. For a complete description of morphology in detail various statistical parameters are calculated based on the AFM images. The measurement results allow to define features of the surface topography of ZnO films by pre-annealing.

1. Methods and materials

To carry out photoelectric measurements, OSCs were prepared, shown in figure 1a. The energy diagram of the functional layers of a solar cell is shown in figure 1b. The device was fabricated on pre-cleaned ITO coated glass substrates. The substrates were sonicated for 15 minutes each in acetone, deionized water, and ethanol. After ultrasonic cleaning, the substrates were dried with a stream of nitrogen (N_2) and then subjected to ultraviolet (UV) treatment for 30 minutes.

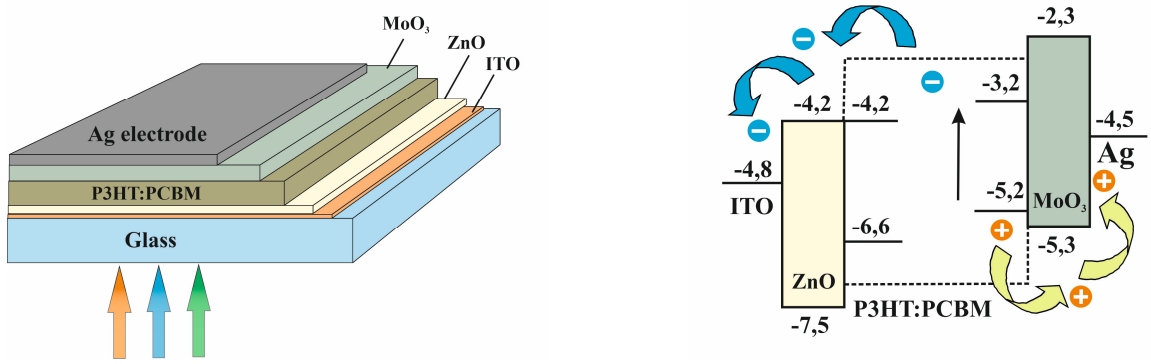

a) b)

Fig.1. Structure of the organic solar cell (a) and the energy diagram of the cells (b).

A solution of ZnO was obtained by a sol-gel method in an aqueous solution using zinc acetate dihydrate [Zn $(CH_3COO)_2$* $2H_2O$], isopropyl alcohol (C_3H_8O), and monoethanolamine (C_2H_7NO) (MEA) [11]. The concentration of zinc acetate and monoethanolamine in the solution was 0.5 M. The resulting colloidal solution was stirred for 1 hour on a magnetic stirrer at a temperature of 60 ° C until a homogeneous and transparent solution appeared. The film-forming ZnO solution was kept for 24 hours with constant stirring, after which the solution was filtered through a filter with a porosity of 0.45 μm. The resulting colloidal solution was applied onto pre-cleaned glass substrates by spin-coating. The ZnO films were applied at a centrifuge speed of 3000 rpm, and the centrifuge rotation time was 90 seconds. The obtained ZnO films were preliminarily annealed at t = 100-300°C for 20 minutes. Then, to obtain a polycrystalline ZnO film, the final annealing was carried out at t = 450°C for 30 minutes.

To obtain organic solar cells, a photoactive P3HT: PCBM layer (Sigma Aldrich,> 99.9%) at a concentration of 1:0.8 was applied to the surface of the electron transport ZnO layer by spin-coating. After that, the samples were annealed in air at a temperature of 140 ° C for 10 min, then then sprayed onto the surface of p-type layer MoO_3, then the silver electrode (Figure 2). The surface topography of the samples was studied using a JSPM-5400 high-resolution atomic force microscope (AFM) (JEOL, Japan). A special modular program for analyzing scanning probe microscopy data (Win SPMII Data-Processing Software) was used to process the images obtained with AFM. Surface morphology, roughness, grain size of thin ZnO films were analyzed from AFM images. The images of the ZnO films surface were obtained in the semicontact scanning mode.

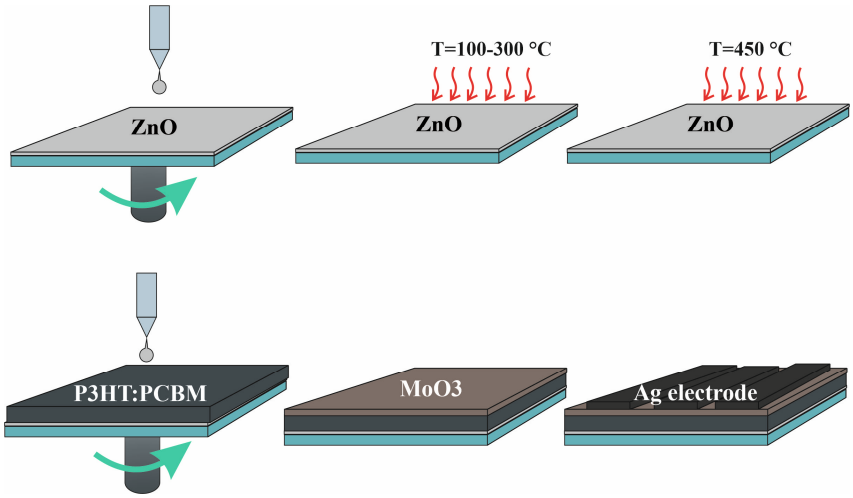

Fig.2. Scheme of obtaining organic solar cells.

The registration of the absorption spectra of the samples under study was carried out on an AvaSpec-ULS2048CL-EVO spectrometer manufactured by Avantes, which records absorption spectra in the range of 200-1100 nm and has an optical resolution of 0.4 nm. The current-voltage characteristics (CVC) of the organic photosensitive element were measured using a P20X potentiostat-galvanostat in a linear sweep mode at an illumination intensity of 100 mW/cm^2. The values of the open circuit voltage Uoc, short circuit current Isc, and fill factor FF were determined by the method [12]. The impedance spectra were measured using a P45X potentiostat-galvanostat in the impedance mode using the setup described in detail in [13].

2. Results and discussion

Pictures of the surface morphology of ZnO films at a scale of 20x20 μm are shown in Figure 3. As can be seen from the AFM images, the temperature of preliminary annealing affects the surface morphology.

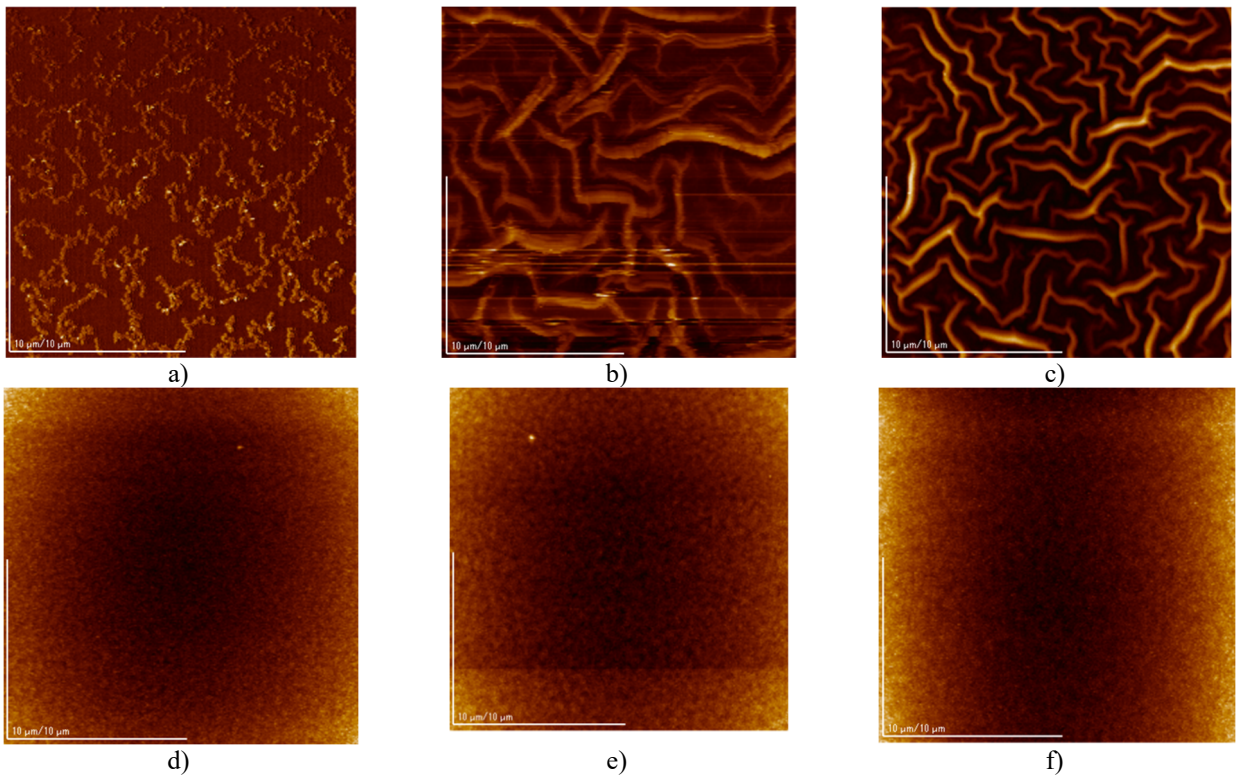

Fig.3. Images of the ZnO films surface depending on preliminary annealing at different temperatures: a - 20°C, b - 100 °C, c - 150°C, d - 200°C, e – 300 °C, f - 450 °C

The morphology of the ZnO film with preliminary annealing at a temperature of 100°C (fig. 3b) and 150°C (fig. 3c) has branched protrusions (wrinkles). The average distance between the protrusions during annealing at 100°C was 1213 nm, at 150°C 995 nm, the average height of the protrusions was 287 nm and 124 nm, respectively. A further increase in the preliminary annealing temperature of 200-450°C (fig. 3 d-f) leads to a smoothing of the surface ZnO films. An analysis of the surface roughness was carried out at a scale of 20 μm*20 μm and the grain size of ZnO on an enlarged scale (1 μm*1 μm). The calculated average grain diameter showed that a change in the pre-annealing temperature affects the grain size, that is, when the film surface is smoothed, the grain diameter decreases from 9.3 nm to 0.8 nm. There is also a decrease in the surface roughness of the ZnO films with increasing temperature (Table 1).

Table 1. Roughness of the film surface and the particle diameter of ZnO grains depending on the temperature of preliminary annealing.

Parameters	Pre-annealing temperature				
	100^0C	150^0C	200^0C	300^0C	450^0C
Roughness, R_a	78 nm	47 nm	7 nm	7 nm	3.5 nm
Grain diameter	9.3 nm	6.6 nm	1.3 nm	1.2 nm	0.8 nm

The absorption (a) and transmission (b) spectra of ZnO layers deposited at different annealing temperatures on glass substrates are shown in figure 4. It can be seen from the figure that the morphology and surface roughness also influenced the optical properties of the ZnO layer, such as light transmission and absorption, which are the key factors in the use of the material in the manufacture of solar cells. ZnO layers at a pre-annealing temperature of 200-450^{0}C showed insignificant absorption and light transmission efficiency of about 90% (fig. 4a, 4b).

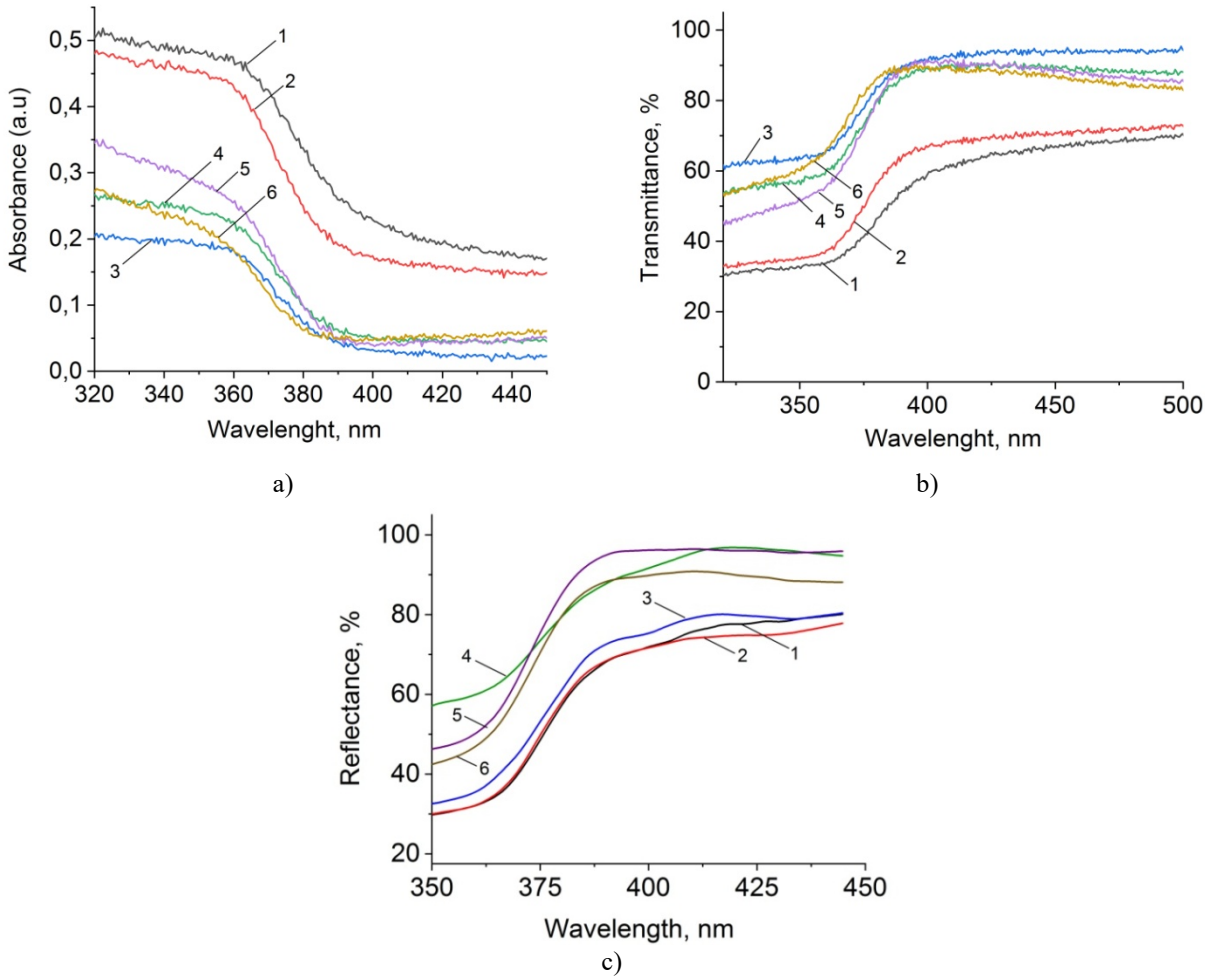

Fig.4. Absorption (a), transmission (b) and reflection (c) spectra of ZnO films:
1 - 100°C, 2 - 150 °C, 3 - 175°C, 4 - 200°C, 5 – 300 °C, 6 - 450 °C

However, at low pre-annealing temperatures (100°C-150°C), the light transmission of the ZnO layer decreased (correspondingly, the optical density increased) due to the formation of wrinkled structures, which leads to strong diffuse scattering. The reflectance spectra are shown in Fig.4c.

The influence of ZnO layers with different surface morphology on the electrophysical properties of solar cells is shown in figure 5. The main characteristics are shown in table 2. As can be seen from the CVC in figure 5 and the data in the table, the dynamics of an increase in the photovoltage and the dynamics of a decrease in the photocurrent with an increase in the pre-annealing temperature are observed. The decrease in the photocurrent is due to a change in the relief of the film. Films with a wrinkled structure, due to strong scattering, increase the optical path of light in the photoactive layer and thereby increase the probability of absorption, which leads to an increase in the photocurrent.

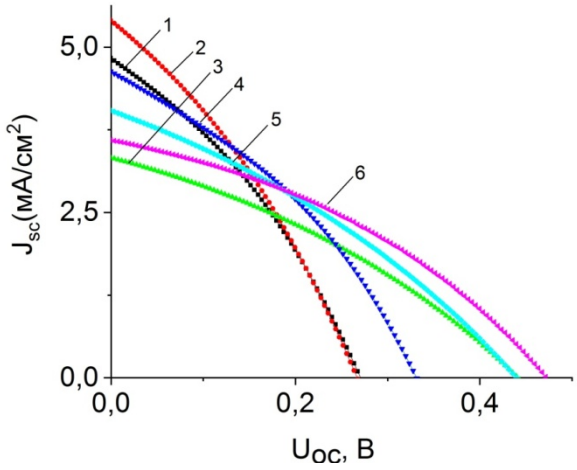

Fig.5. Current-voltage characteristics of inverted polymer solar cells:
1 - 100°C, 2 - 150 °C, 3 - 175°C, 4 - 200°C, 5 – 300 °C, 6 - 450 °C

Table 2. Electrophysical properties of films obtained at different annealing temperatures

Sample (^{0}C)	U oc, (mV)	Jsc, (mA/cm^2)	FF, (%)	PCE, %
100	260	4.76	30	0.442
150	270	5.45	30	0.456
175	450	3.35	33	0.496
200	330	4.64	35	0.541
300	440	4.08	32	0.577
450	480	3.59	37	0.638

The photovoltage of inverted polymer solar cells is due to the energetics of the photoactive layer and selective electrodes. In our cells, these are molybdenum oxide and zinc oxide. However, molybdenum oxide and the photoactive layer were deposited under the same conditions, and the observed changes in the photovoltage of the cells are due to the influence of the structure of zinc oxide. The position of the quasi-Fermi level of electrons in ZnO determines the cell photovoltage and depends on the density and types of lattice defects. The higher the position of the quasi-Fermi level of electrons to the bottom of the conduction band, the higher the generated photovoltage. It is known that defects forming shallow donor levels shift the Fermi level of electrons to the bottom of the conduction band. Thus, the observed increase in the photovoltage of the cells with an increase in the pre-annealing temperature can be associated with an increase in the density of defects in the ZnO crystal lattice.

For a detailed understanding of the influence of the electron transport layer of ZnO on the mechanisms of charge carrier transport, we measured the impedance spectra of polymer solar cells. To interpret the impedance spectra, a standard equivalent electrical circuit was used, where R_{rec} is the low-frequency resistance, CPE is the capacitance, and R_{ext} is the high-frequency resistance (figure 6 a).

The spectra were simulated using the EIS-analyzer software package and the main electrical transport properties of the films were calculated (table 3), where: D_{eff} is the effective diffusion coefficient of electrons,

k_{eff} is the effective rate of electron recombination, τ_{eff} is the effective lifetime of an electron. Resistance to electron transport in the zinc oxide film R_{ext}, charge transfer resistance R_{rec} associated with electron recombination were calculated from the central arc of the impedance spectra. The charge transfer mechanism and the transport of electrons in the IPSC are shown in figure 6b. The analysis of the impedance measurement results was carried out according to the diffusion – recombination model. Figure 6c shows the impedance spectra of the films under study. It can be seen from the figure that the hodograph diameter of a film with a smooth surface is smaller than that of a wrinkled film. This means that the sample annealed at 450^{0}C has a lower value of the charge transfer resistance. Table 3 shows the values of the electrophysical parameters of the films.

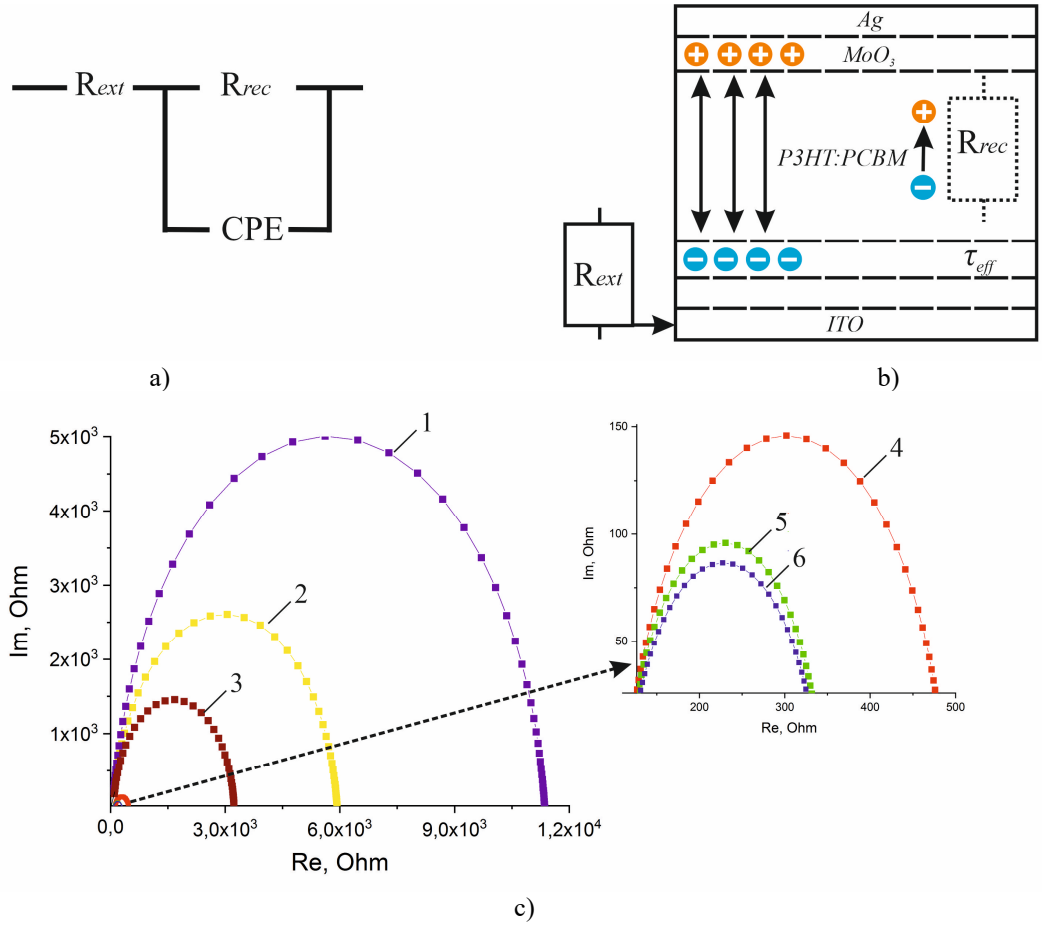

Fig.6. Equivalent electrical circuit (a), charge transfer mechanism (b) and impedance hodographs (c) of inverted polymer solar cells: 1 - 100ºC, 2 - 150 ºC, 3 - 175ºC, 4 - 200ºC, 5 – 300 ºC, 6 - 450 ºC

Table 3. The value of the electrophysical parameters of the ZnO film.

t, ^{0}C	D_{eff}, (cm^2s^{-1})	k_{eff}, (s^{-1})	τ_{eff}, (ms)	R_{rec}, (Ohm)	R_{ext}, (Ohm)	Con,(Ohm*cm*s^{-1})	L, (nm)
100^{0}C	4.67*10^{-6}	0.4	678	11304	57	66.6	40
150^{0}C	5.17*10^{-6}	0.87	318	5873	57	73.8	40
175^{0}C	2.92*10^{-6}	1.21	230	3156	75	54.8	40
200^{0}C	2.1*10^{-7}	1.17	236	366	118	6.19	40
300^{0}C	5.21*10^{-7}	2.28	122	242	61	7.95	40
450^{0}C	3.47*10^{-7}	1.74	159	238	69	5.99	40

Using the EIS-analyzer software package, R_{rec} and R_{ext} are calculated, and k_{eff} is determined from the maximum of the hodograph arc by the formula $\omega_{max} = k_{eff}$. The thickness of the films was determined using a scanning probe microscope. It can be seen from table 3 that with an increase in the pre-annealing temperature, the effective diffusion coefficient D_{eff} decreases, as does the resistance $R_{rec.}$, which characterizes the recombination channels. This dynamic is due to an increase in the density of crystal lattice

defects with an increase in the pre-annealing temperature. The lower the temperature, the slower the crystallization process occurs and a less defective structure is formed, and at higher temperatures the crystallization process is accelerated, which leads to an increase in the density of defects. The defects of the crystal lattice serve as traps of charge carriers and centers of recombination, and with an increase in their density, D_{eff} and R_{rec}, the recombination of charge carriers is enhanced.

Conclusion

Thus, the characteristics of inverted organic solar cells based on ZnO have been investigated at different temperatures of preliminary annealing from 150°C to 450°C. As a result of studies, it was found that preliminary annealing leads to a change in the morphology, optical properties, and structural features of ZnO films. The temperature of preliminary annealing of the zinc acetate solution film controls the rate of formation of the ZnO film and also affects the relief of the film surface. With an increase in temperature, a decrease in the surface relief and an increase in the density of ZnO lattice defects are observed. Thus, preliminary annealing of films of zinc acetate solution at temperatures below 200°C followed by annealing at 450°C leads to the formation of a highly relief (wrinkled) morphology with a lower density of ZnO lattice defects. Whereas the films obtained at a pre-annealing temperature above 200ºC have a smooth surface, but with a high density of defects.

Solar cells based on ZnO films with a wrinkled morphology generally have a greater value of the photocurrent density due to the effect of light scattering, while cells with a smooth morphology have a large photovoltage value, which is caused by a high density of defects that raise the position of the quasi-Fermi level of electrons. Thus, this study has shown the possibility of optimizing the photovoltaic parameters of solar cells by varying the pre-annealing temperature of ZnO films.

Acknowledgments

This research is funded by the Science Committee of the Ministry of Education and Science of the Republic of Kazakhstan (Grant No. AP09561879).

REFERENCES

1 Lin Y., Adilbekova B., Firdaus Y., et al. 17% Efficient Organic Solar Cells Based on Liquid Exfoliated WS2 as a Replacement for PEDOT:PSS. *Adv. Mater*. 2019, Vol.31, No. 46, pp. 1902965 - 1902965

2 Liu Q., Jiang Y., Jin K., Qin J., Xu J., Li W., Xiong J., Liu J., Xiao Z., Sun K., Yang S., Zhang X., and Ding L. 18% Efficiency organic solar cells. *Sci. Bull.* 2020, Vol.65, No 4, pp.272 -275.

3 Sun Y., Seo J. H., Takacs C. J., Seifter J., et al. Inverted Polymer Solar Cells Integrated with a Low-Temperature-Annealed Sol-Gel Derived ZnO Film as an Electron Transport Layer. *Adv. Mater.* 2011, Vol.23, pp.1679–1683.

4 Sekine N., Chou C.-H., Kwan W.L., Yang Y. ZnO Nano-Ridge Structure and Its Application in Inverted Polymer Solar Cell. *Org. Electron*. 2009, Vol.10, pp. 1473 – 1477.

5 Srinivasan G., Gopalakrishnan N., Yu Y. S., Kesavamoorthy R. and Kumar J. Influence of post-deposition annealing on the structural and optical properties of ZnO thin films prepared by sol-gel and spin-coating method. *Superlattices and Microstructures.* 2008, Vol.43, No. 2, pp. 112–119.

6 Aimukhanov A.K., Zeinidenov A.K., Zavgorodniy A.V., Ilyassov B.R., Pazyl B.M. The research of photo-electrophysical properties of cobalt phthalocyanine film. *Eurasian phys. tech. j.* 2019, Vol. 16, pp. 16 – 20.

7 Yang T.B., Cai W.Z., Qin D.H., et al. Y. Solution-processed zinc oxide thin film as a buffer layer for polymer solar cells with an inverted device structure. *Journal of Physical Chemistry C*. 2010, Vol.114, pp. 6849-6853.

8 Richardson B. J., Wang X., Almutairi A., et al. High Efficiency PTB7-Based Inverted Organic Photovoltaics on Nano-Ridged and Planar Zinc Oxide Electron Transport Layers. *J. Mater. Chem. A*. 2015, Vol.3, pp. 5563–5571.

9 Lim D. C., et al. Spontaneous Formation of Nanoripples on the Surface of ZnO Thin Films as Hole-Blocking Layer of Inverted Organic Solar Cells. *Sol. Energy Mater. Sol. Cell*. 2011, Vol.95, pp. 3036–30409.

10 Kim M.S., Yim K.G., Lee D., et al. Effect of cooling rate and post heat treatment on properties of ZnO thin films deposited by sol–gel method. *Appl. Surf. Sci.* 2011, Vol.257, pp 9019–9023.

11 Ilyassov B. R., Ibraev N. Kh., Abzhanova D. B. Effect of morphology of ZnO nanowire arrays on photovoltaic and electron transport properties of DSSC. *Proceeding of the IOP Conf. Series: Materials Science and Engineering*. 2015, Vol. 81, pp. 012046 – 012046.

12 Khanam Jobeda J., Foo Simon Y. Modeling of High-Efficiency Multi-Junction Polymer and Hybrid Solar Cells to Absorb Infrared Light. *Polymers.* 2019, Vol.11, No. 2, pp. 2323-2325.

13 Bisquert J., Mora-Sero I., Fabregat-Santiago F. Diffusion–Recombination Impedance Model for Solar Cells with Disorder and Nonlinear Recombination. *ChemElectroChem.* 2014, Vol.1, No. 1, pp. 289-296.

Article accepted for publication 21.05.2021

DOI 10.31489/2021No2/47-55

UDC 536.46+536.24

COMBUSTION OF ALUMINUM POWDER-AIR SUSPENSION IN A SWIRL FLOW

Moiseeva K.M.[1*], Krainov A.Yu.[1], Krainov D.A.[2]

[1] National Research Tomsk University, Tomsk, Russia, Moiseeva_KM@t-sk.ru

[2] National Research Tomsk Polytechnic University, Tomsk, Russia

The article is devoted to the numerical solution of the problem of the combustion of powder metal fuel in a combustion chamber with swirling flow. A physico-mathematical model of the flow of an air suspension of aluminum powder in a swirling flow in a cylindrical combustion chamber with a sudden expansion is presented. The physical and mathematical formulation of the problem is based on the approaches of the mechanics of two-phase reacting media. The solution was carried out using the arbitrary discontinuity decay method. The results of a numerical parametric study of the features of the combustion of an air suspension of aluminum powder depending on its composition, the axial flow rate of the mixture at the entrance to the combustion chamber, and the value of the swirl speed are shown.

Keywords: powder metal fuel, flow swirling, mechanics of two-phase reacting media, aluminum combustion.

Introduction

Aluminum is one of the most popular metals currently used in powdered metallic fuels. The studies [1 - 6] propose using aluminum powder as an independent energy carrier in ramjet rocket engines. The studies provide the results of the experimental and numerical investigation on the influence of the mixture parameters and characteristics of the combustion chamber on the combustion of the aluminum powder-air suspension (ALAS) in the airflow. The research [1] is devoted to the ignition, combustion and flame stabilization processes of the aluminum-air mixture in a high-speed airflow. The study summarizes the controlling methods of the highly dispersed aluminum combustion in the direct-flow combustion chamber. The paper [2] presents the physical-mathematical model and the results of the numerical modelling of the aerodynamics and combustion of the aluminum-air mixture in a swirling flow inside an axisymmetric channel with a sudden expansion. The probability of the reverse flow formation in the chamber is shown. The studies [3, 4] investigates the critical conditions for the ignition of an ALAS and the effect of the turbulence on the formation of the ignition sites. The manuscript [5] provides the experimental data on the effect of swirl flow on the length of the reverse flow zone, temperature and length of the flame. The region of the aluminum powder stable combustion in a high-speed airflow is determined in [6]. The authors of the study have obtained the dependence of the flame blow off velocity in the aluminum-air mixture flow on the value of the excess air ratio.

Swirling combustion is currently one of the most important engineering problems for the combustion physics. There is a hypothesis about an increase in the combustion efficiency of reacting gas mixtures in combustion chambers with swirling flow [7], as well as an increase in the efficiency of the fuel combustion devices due to swirling [8 - 11]. It is believed that swirling leads to the intensification of the heat and mass transfer and, accordingly, to an increase in the efficiency of the gas-dispersed fuel combustion. Usually to simulate the swirling flows, the Reynolds equations [9] or the Navier-Stokes equations [7] are used.

Our previous studies [12, 13] are dedicated to the combustion problems of the mixed solid fuels under a change in pressure [12] and under the high-speed blowing [13]. The present study is devoted to the combustion problem of the high-energy materials in the high-speed swirl flows. The interest of such problem is associated with the development of new methods to improve the efficiency of the power-producing units. In this paper we have investigated the features of the ALAS flow and its combustion in a cylindrical channel with a sudden expansion and under the swirling conditions at the channel inlet. This problem is of practical importance, since, depending on the parameters of the suspension and swirl flow, stagnant zones can form in the cylindrical channel during the combustion (zones of particle accumulation or particle-free zones). In case

.

of power-producing units, the irregularity of the particle distribution along the flow can significantly affect the speed of flame propagation through the channel.

A sudden expansion of the cylindrical channel can lead to a change in the characteristics of the air suspension flow. Gas swirling at the inlet of the channel also significantly changes the nature of the air suspension flow. In contrast to the study [3], the formulation of the problem in the present paper is based on the approaches of the mechanics of the two-phase reaction media [14].

1. Physics and mathematics model and solution method

The problem of the aluminum particles-air suspension flow and its combustion in a cylindrical channel with a sudden expansion is solved. The problem formulation is based on the approaches of the mechanics of the two-phase reaction media [14]. The initial gas tangential velocity is set to take into account the swirl of the flow. It is assumed that the aluminum-air suspension with the given mass fraction of the aluminum particles, particle radius r_p, velocity along the axial direction u_{xb}, zero velocity along the radial direction and velocity u_ϕ along the tangential direction is supplied from the inlet on the left side of the channel. The schematic diagram of the cylindrical channel is shown in Figure 1 (the notations are: R is the radius of the channel at the outlet, r is the radius of the channel at the inlet, l is the length of the narrow section of the channel, L is the total length of the cylindrical channel). The arrows show the direction of the suspension feeding into the channel.

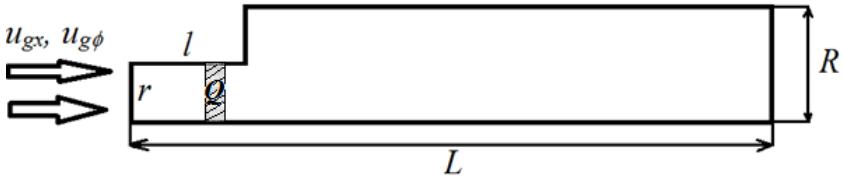

Fig.1. Scheme of the cylindrical channel with a sudden expansion/

Since the convective heat and mass transfer is much greater than the one by thermal conductivity and diffusion, the diffusion and heat conduction processes in gas phase are neglected. There is an ignition source with constant heat release inside the channel in the narrow section of the channel, schematically indicated by a shaded area (Figure 1). The rate of the heat release inside the chamber is equal to Q. The suspension flows through the chamber, heats up, and the heated aluminum particles start to ignite. The combustion mechanism of the aluminum particles is described in detail in [15 - 17]. The aluminum particles are supposed to ignite when they reach the ignition temperature T_{pz}. The rate of the heterogeneous chemical reaction on particle surface is defined taking into account the mass transfer. It is assumed that during the combustion of an aluminum particle, the radius of the melted aluminum in the particle r_{Al} decreases, while as the radius of the whole particle r_p grows due to the forming oxide layer. The thermal and dynamic interactions between aluminum particles and gas phase are taken into account under the assumption of the model. The developed mathematical model under the made assumption has the following form:

gas mass-conservation equation:

$$\frac{\partial r\rho_g}{\partial t}+\frac{\partial r\rho_g u_g}{\partial x}+\frac{\partial r\rho_g v_g}{\partial r}=-rG\,, \tag{1}$$

gas impulse-conservation equation:

$$\frac{\partial r\rho_g u_g}{\partial t}+\frac{\partial r\left(p_g+\rho_g u_g^2\right)}{\partial x}+\frac{\partial r\rho_g u_g v_g}{\partial r}=-r\tau_x-rGu_g\,, \tag{2}$$

$$\frac{\partial r\rho_g v_g}{\partial t}+\frac{\partial r\rho_g u_g v_g}{\partial x}+\frac{\partial r\left(p_g+\rho_g v_g^2\right)}{\partial r}=-r\tau_r-rGv_g+p_g+\rho w_g^2, \tag{3}$$

$$\frac{\partial r\rho_g w_g}{\partial t}+\frac{\partial r\rho_g w_g u_g}{\partial x}+\frac{\partial r\rho_g w_g v_g}{\partial r}=-r\tau_\phi-rGw_g-\rho_g w_g v_g\,, \tag{4}$$

oxygen mass-conservation equation:

$$\frac{\partial r\rho_{O2}}{\partial t}+\frac{\partial r\rho_{O2}u_g}{\partial x}+\frac{\partial r\rho_{O2}v_g}{\partial r}=-rG \tag{5}$$

gas energy-conservation equation:

$$\frac{\partial r\varepsilon_g}{\partial t}+\frac{\partial ru_g\left(\varepsilon_g+p_g\right)}{\partial x}+\frac{\partial rv_g\left(\varepsilon_g+p_g\right)}{\partial r}=-rGc_{gp}T_g+$$
$$r\left[u_p\tau_x+v_p\tau_r+w_p\tau_\phi+n_p\alpha_pS_p\left(T_g-T_k\right)-0.5G\left(u_g^2+v_g^2+w_g^2\right)\right], \tag{6}$$

..

particle mass-conservation equation:

$$\frac{\partial r\rho_p}{\partial t}+\frac{\partial r\rho_pu_p}{\partial x}+\frac{\partial r\rho_pv_p}{\partial r}=rG \tag{7}$$

particle impulse-conservation equation:

$$\frac{\partial r\rho_pu_p}{\partial t}+\frac{\partial r\rho_pu_p^2}{\partial x}+\frac{\partial r\rho_pu_pv_p}{\partial r}=r\tau_x+rGu_g, \tag{8}$$

$$\frac{\partial r\rho_pv_p}{\partial t}+\frac{\partial r\rho_pu_pv_p}{\partial x}+\frac{\partial r\rho_pv_p^2}{\partial r}=r\tau_r+rGv_g+\rho w_p^2, \tag{9}$$

$$\frac{\partial r\rho_pw_p}{\partial t}+\frac{\partial r\rho_pw_pu_p}{\partial x}+\frac{\partial r\rho_pw_pv_p}{\partial r}=r\tau_\phi+rGw_g-\rho_pw_pv_p, \tag{10}$$

particle energy-conservation equation:

$$\frac{\partial r\varepsilon_p}{\partial t}+\frac{\partial ru_p\varepsilon_p}{\partial x}+\frac{\partial rv_p\varepsilon_p}{\partial r}=rQ_{ch}G-rn_p\alpha_pS_p\left(T_g-T_p\right)-$$
$$-r\left[u_p\tau_x+v_p\tau_r+w_p\tau_\phi+Gc_{gp}T_g+0.5G\left(u_p^2+v_p^2+w_p^2\right)\right], \tag{11}$$

particles number equation:

$$\frac{\partial rn_p}{\partial t}+\frac{\partial rn_pu_p}{\partial x}+\frac{\partial rn_pv_p}{\partial r}=0 \tag{12}$$

the gas equation:

$$p_g=\rho_gT_gR_g, \tag{13}$$

initial conditions:

$$u_g\left(x,r,0\right)=v_g\left(x,r,0\right)=w_g\left(x,r,0\right)=u_p\left(x,r,0\right)=v_p\left(x,r,0\right)=w_p\left(x,r,0\right)=0,$$
$$n_p\left(x,r,0\right)=\rho_p\left(x,r,0\right)=0,T_p\left(x,r,0\right)=T_g\left(x,r,0\right)=T_b, \tag{14}$$
$$\rho_g\left(x,r,0\right)=\rho_{gb},\ \rho_{O2}\left(x,r,0\right)=a_{O2b}\rho_{gb},$$

Boundary conditions on the symmetry axis, r = 0: (15)

.

$$\frac{\partial u_g(x,0,t)}{\partial r}=\frac{\partial u_p(x,0,t)}{\partial r}=\frac{\partial v_g(x,0,t)}{\partial r}=\frac{\partial v_p(x,0,t)}{\partial r}=0,$$
$$\frac{\partial w_g(x,0,t)}{\partial r}=\frac{\partial w_p(x,0,t)}{\partial r}=0,\ \frac{\partial n_p(x,0,t)}{\partial r}=\frac{\partial \rho_p(x,0,t)}{\partial r}=0,$$
$$\frac{\partial T_p(x,0,t)}{\partial r}=\frac{\partial T_g(x,0,t)}{\partial r}=\frac{\partial \rho_g(x,0,t)}{\partial r}=\frac{\partial \rho_{O2}(x,0,t)}{\partial r}=0.$$

The following initial conditions (16) are set at the inlet of the channel ($x = 0$): the enthalpy, the gas and particle flow rate, the axial, radial and tangential velocity of the gas and particles, the mass concentration of the oxidizer in the gas and the number of particles.

$$\begin{gathered}T_p(0,r,t)=T_g(0,r,t)=T_{st},\ \rho_g(0,r,t)=\rho_{gb},\ \rho_p(0,r,t)=\Delta_p\rho_{gb},\\ a_{O2}(0,r,t)=a_{O2b},u_g(0,r,t)=u_p(0,r,t)=u_{xb},\ v_g(0,r,t)=v_p(0,r,t)=0,\\ w_g(0,r,t)=w_p(0,r,t)=u_\phi=A_z(r/R)u_{xb},\ n_p=\Delta_p\rho_{gb}/\left(V_p\rho_p^0\right).\end{gathered}\tag{16}$$

Atmospheric pressure is assumed at the outlet of the channel ($x = L$).

The notations in Eqs. (1) – (16): $\varepsilon_g=p_g/(\gamma-1)+0.5\rho_g\left(u_g^2+v_g^2+w_g^2\right)$ is the gas total energy, $\varepsilon_p=c_pT_p\rho_p+0.5\rho_p\left(u_p^2+v_p^2+w_p^2\right)$ is the particle total energy, $\alpha_p=Nu_p\lambda_g/(2r_p)$ – is the gas-particle heat exchange coefficient, $\gamma=c_{pg}/c_{vg}$ is the adiabatic exponent, τ_x,τ_r,τ_ϕ are the friction force along axial, radial and tangential direction, respectively, ρ is the density, *u, v, w* – are the velocity components along axial, radial and tangential direction, respectively, *t* is the time, *x*, *r* are the coordinates, *p* is the pressure, *T* is the temperature, $A_z$is the constant of the swirling law, Δ_p is the particle mass fraction in the mixture, $Q_{ch}$is the reaction heat effect; a_{O2} – oxidizer mass fraction in the gas phase. Indexes: *b* is for the initial conditions of the parameters; *p* is for the particle parameters, *g* – gas parameters, O_2 – oxygen,*st* – parameters at the inlet.

The current values of the aluminum radius in the particle r_{Al} and the whole particle radius r_p are determined as in the studies [16, 17] and are defined from the expressions:

$$r_{Al}=\sqrt[3]{\left(\frac{\mu_{Al}+3/2\,\mu_O}{\mu_{Al}}r_{pb}^3-\frac{\rho_p}{(4/3)\pi n_p\rho_p^0}\right)\frac{2\mu_{Al}}{3\mu_O}},\tag{17}$$

$$r_p=\sqrt[3]{\frac{3\rho_p}{4\pi\rho_p^0 n_p}},\tag{18}$$

where μ_O, μ_{Al} are the molar masses of oxygen and aluminum, respectively, ρ_p^0 is the density of aluminum, r_{pb} is the initial radius of the aluminum particle. Deriving the Eg. (17), we have assumed that the alumina (Al_2O_3) remaining on the particle surface as a spherical layer. This assumption is introduced to determine the current value of the aluminum mass in a particle during its combustion. The aluminum particle burning rate is defined from the experimental data [15]. Taking into account the diffusional resistance of the reaction, the mass change rate of aluminum in the particle is written as:

$$G=\alpha_1 n_p\rho_p^0 S_{Al}\frac{k\left(a_{O2,}r_{Al}\right)\beta_m}{\left(k\left(a_{O2,}r_{Al}\right)+\beta_m\right)}\tag{19}$$

where $k\left(a_{O2,}r_{Al}\right)=k_0a_{O2}^{0.9}/\sqrt{r_{Al}}$ is the combustion law of a single aluminum particle under the excess of the oxidizer, $S_{Al}=4\pi r_{Al}^2$ is the area of the unreacted aluminum surface, k_0 is the reaction rate constant, $\beta_m=\lambda_g(T)Nu_D/\left(c_g\rho_g r_p\right)$ is the particle mass-transfer coefficient.

The friction force along the axial direction is determined from the expression $\tau_x = n_p F_x$ [14, 15], where $F_x = C_x S_m \rho_g \left(u_g - u_p\right)\left|u_g - u_p\right|/2$ is the interaction force of a single particle with gas along the axial direction, $C_x = 24\left(1 + 0.15\,\mathrm{Re}_x^{0.682}\right)/\mathrm{Re}_x$ is the friction coefficient, $\mathrm{Re}_x = 2\rho_g r_p \left|u_g - u_p\right|/\eta$ is the Reynolds number, S_m is the midsection area, η is the dynamic viscosity of the gas. The components of the friction force along the radial and tangential directions are determined in a similar way.

The developed mathematical model has been solved numerically using the S.K. Godunov's scheme and is based on algorithms [18, 19]. The size of the computational grid cells along the axial and radial directions is equal to $10^{-3} m$. The time step is determined from the Courant stability criteria [19]

$$\frac{1}{\Delta t} < \frac{1}{\Delta t_x} + \frac{1}{\Delta t_r},$$

where $\Delta t_x = \dfrac{h_x}{\max\left[\left|u_g\right| + c_g\right]}$, $\Delta t_x = \dfrac{h_r}{\max\left[\left|v_g\right| + c_g\right]}$, c_g is the sound velocity in gas.

The verification of the numerical solution for the equations system (1) - (16) and the developed computer program for the reliability has been carried out by calculating the adiabatic combustion temperature and controlling for the conservation laws of the mass and total energy of the gas. According to the verification, the calculation error is about 0.03%.

2. Results and discussion

We have carried out the parametric investigation on the effect of the swirling on the establishment of the ALAS combustion front in the channel and on the completeness of the particle combustion. The variable parameters in the calculations are the size and mass concentration of the particles, the value of the axial and angular velocities of the aluminum-air suspension supplied to the channel. All the calculations have been conducted under the following thermophysical and kinetic parameters borrowed from [17]: $Q = 36.6\ MJ/kg, k_0 = 1.11 \cdot 10^{-6}\ m^{1.5}/s$, $\alpha_1 = 0.889$, $\lambda_{st} = 0.025\ W/(m \cdot K)$, $T_b = 300\ K$, $\mu_{Al} = 27 \cdot 10^{-3}\ kg/mol$, $\mu_O = 16 \cdot 10^{-3}\ kg/mol$, $c_{pg} = 1065\ J/(kg \cdot K)$, $c_{vg} = 768.2\ J/(kg \cdot K)$, $c_p = 904\ J/(kg \cdot K)$, $\rho_p^0 = 2380\ kg/m^3$, $\eta = 2 \cdot 10^{-5}\ Pa \cdot s$, $\rho_{O2,b} = 0.264\ kg/m^3$, $p_b = 0.1\ MPa$, $\rho_b = p_b / R_g T_b$, $T_{pz} = 1400\ K$, $r = 0.02\ m$, $R = 0.1\ m$, $L = 0.3\ m$, $l = 0.03\ m$.

The results of some calculations are presented in Figures 2-9. Figures 2 - 9 are plotted for the steady-state regimes of the ALAS flow and its combustion. Figure 2 shows the stationary combustion regime for the ALAS in the case when the swirling is implemented according to the law $w_g(0,r,t) = A_z(r/R)u_{xb}$, where R is the radius of the cylindrical channel, A_z is the coefficient in the swirling law, u_{xb} is the axial feed velocity. The calculation has been performed for the suspension with the axial feed velocity $u_{xb} = 1\ m/s$, under the coefficient of the angular component of the flow velocity, $A_z = 75$, under the mass concentration of the particles - $\rho_{pb} = 0.1\ kg/m^3$, and with particle radius $r_{pb} = 5 \cdot 10^{-6} m$. Figure 2a shows the gas temperature in the channel, Figure 2b shows the mass concentration of the suspension. Under the selected swirl coefficient, the maximum angular velocity of the air suspension is $u_{\varphi,\max} = 1.5\,m/s$.

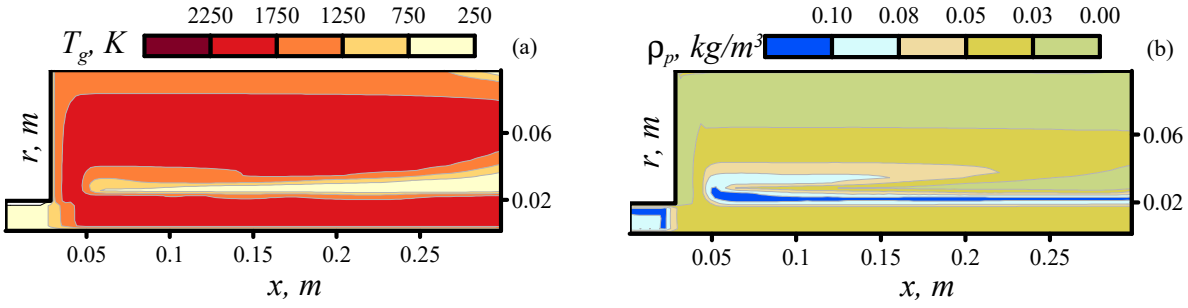

Fig.2. Gas temperature (a), mass concentration of the suspension (b), $\rho_{pb} = 0.1\ kg/m^3$, $r_p = 5 \cdot 10^{-6}\ m$, $u_b = 1\ m/s$, $A_z = 75$.

In this case, the maximum concentration of the particles is observed at close range from the inlet of the channel at the height corresponding to the width of the inlet. The region of the maximum gas temperature is straight after the channel expand at x = 0.04 m. With an increase in the particle mass concentration of the supplied mixture (Figure 3), the maximum temperature reached in the channel rises. The shape of the flame front remains practically unchanged. From a comparison of Figures 2a and 3a, it can be seen that the heated gas zone stretches along the channel radius and slightly curves. Under the selected ratios of the axial and angular components of the mixture feed velocity at the inlet, the particles enter the combustion zone, ignite immediately at the entrance to the expanding part of the channel, and then are carried downstream by the flow. The main mass of the particles is concentrated along the mixture feed line (Figures 2b, 3b).

Figures 4, 5 show the calculation results in the case of a decrease in the mass concentration of aluminum particles in the supplied mixture. The coefficient of the angular component of the feed velocity in this calculation is A_z= 50, thus the maximum value of the angle velocity is 1 m/s. Figure 4a shows the gas temperature under the mass concentration of the aluminum particles ρ_{pb} = 0.05 kg/m^3, Figure 5a –ρ_{pb} = 0.075 kg/m^3. Figures 4b, 5b show the distributions of the mass concentration of the particles under ρ_{pb} = 0.05 kg/m^3 and ρ_{pb} = 0.075 kg/m^3. Under the chosen calculation parameters, the shape of the combustion front and the spatial distribution of the particles change.

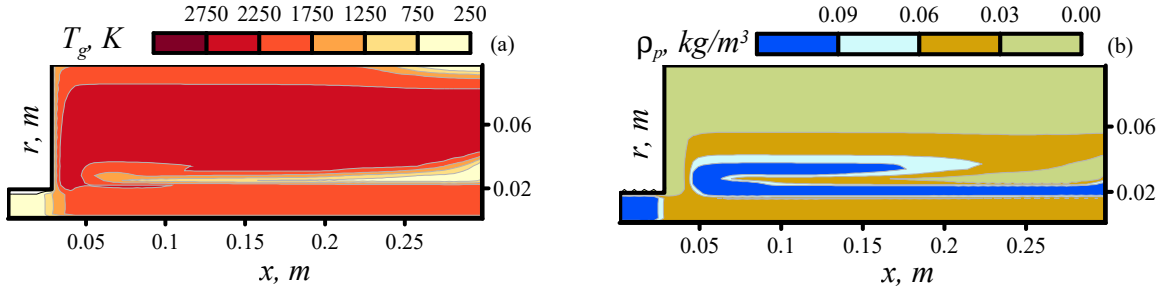

Fig.3. Gas temperature (a), mass concentration of the suspension (b), ρ_{pb}= 0.15 kg/m^3, r_p= 5·10^{-6} m, u_b=1 m/s, A_z=75.

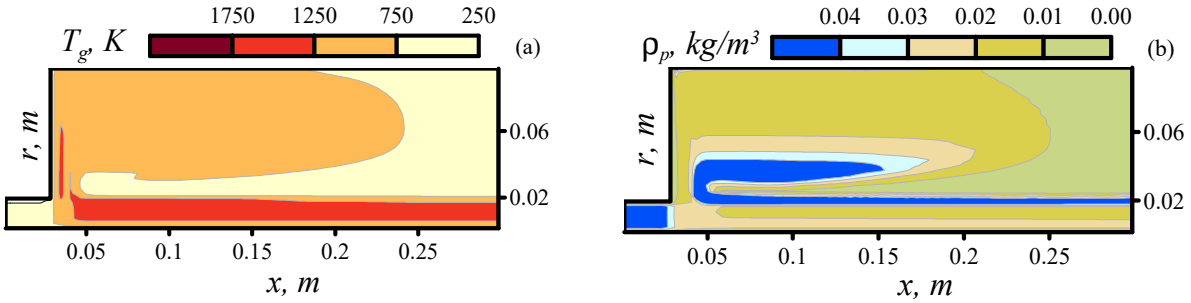

Fig.4. Gas temperature (a), mass concentration of the suspension (b), ρ_{pb}= 0.05 kg/m^3, r_p = 5·10^{-6} m, u_b = 1 m/s, A_z = 50.

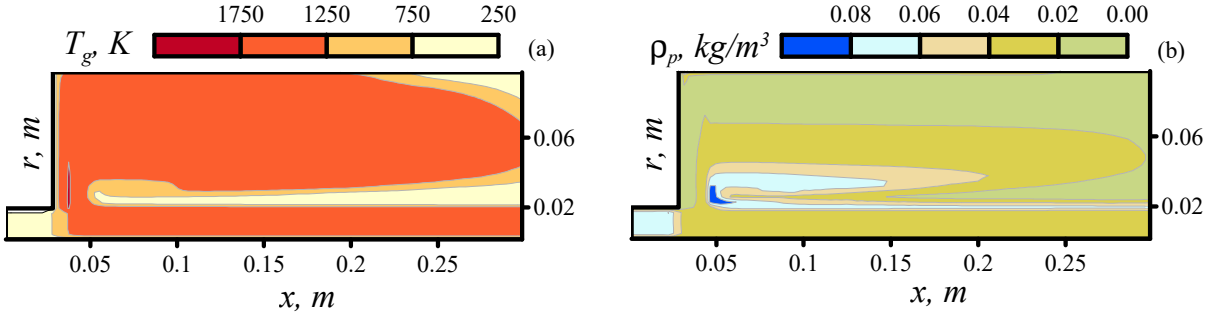

Fig. 5. Gas temperature (a), mass concentration of the suspension (b), ρ_{pb}= 0.075 kg/m^3, r_p=5·10^{-6} m, u_b=1 m/s, A_z = 50.

In the case of the low mass concentrations of the aluminum powder and high angular velocities of the supplied mixture at the inlet, the formation of the combustion front is observed along the axial direction of the mixture supply. The edge of the front corresponds to the width of the input channel (Figure 6). Figure 7 shows the particle velocity vector corresponding to the case plotted in Figure 6. Due to the high feed rate and high angular velocity component, the flame front is formed at a distance from the inlet channel at $x = 0.06$ *m*. Qualitatively similar results had been obtained earlier in [20], where we had investigated the combustion of the coal dust-air suspension in a channel under the swirling flow conditions. In the study, we had conducted the numerical investigation on the influence of the flow swirling velocity on the gas temperature distribution inside the channel without expansion and on the completeness of the coal dust combustion. It had been shown that a particle with the low inertia is carried away by the swirling flow.

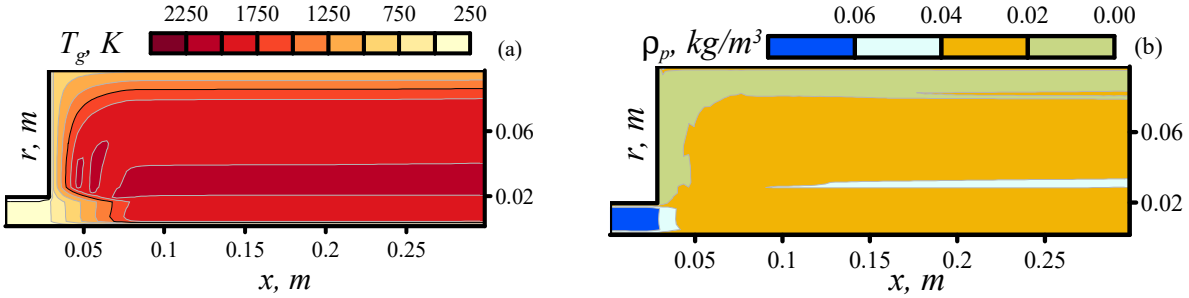

Fig.6. Gas temperature (a), mass concentration of the suspension (b), $\rho_{pb}= 0.075$ *kg/m*^{3}, $r_p = 5\cdot10^{-6}$ *m*, $u=3$ *m/s*, $A_z = 50$.

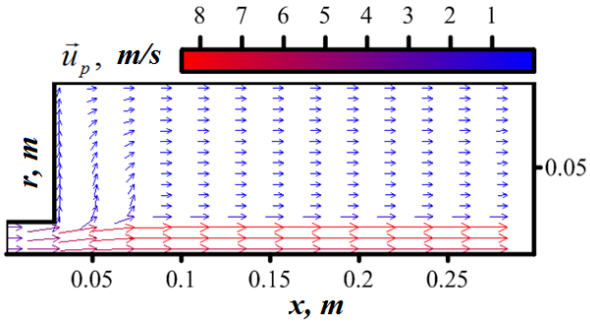

Fig.7. Velocity vector of the particle motion, $\rho_{pb}= 0.075$ *kg/m*^{3}, $r_p = 5\cdot10^{-6}$ *m*, $u_b = 3$ *m/s*, $A_z = 50$.

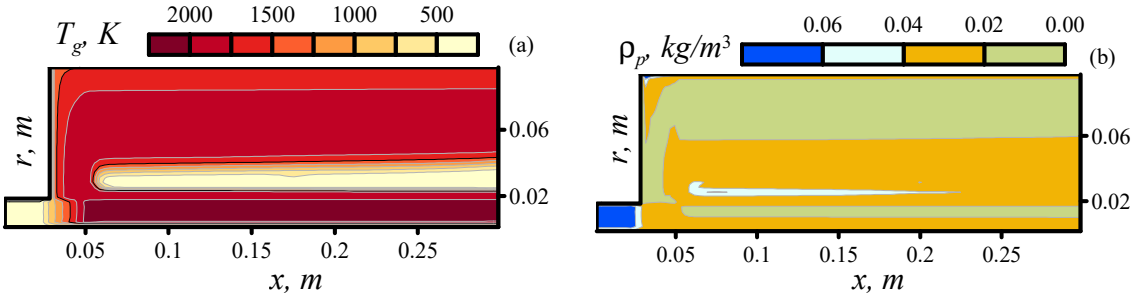

Fig.8. Gas temperature (a) and mass concentration of the suspension (b), $\rho_{pb}= 0.075$ *kg/m*^{3}, $r_p = 10^{-6}$ *m*, $u_b = 10$ *m/s*, $A_z = 75$.

To study the effect of the aluminum particle size on the shape of the flame in the channel, we have conducted several calculation of the ALAS combustion with different particle radii ranged from 10 to 1 μm. The results of two example calculation are shown in Figures 8, 9. Figure 8 shows the gas temperature and mass concentration of the aluminum powder along the channel during the ALAS combustion under the mass concentration $\rho_{pb}= 0.075$ *kg/m*^{3}, particle radius 10^{-6}*m*, the feed velocity $u_b= 10$ *m/s*, and the coefficient of the angular component $A_z = 75$. The intense swirl of the feed flow leads to a lifting of a certain fraction of the

particles closer to the wall of the wide part of the channel. According to the Figure 8, the combustion front is formed along the central part of the channel and in the area near the wall of the wide part of the channel.

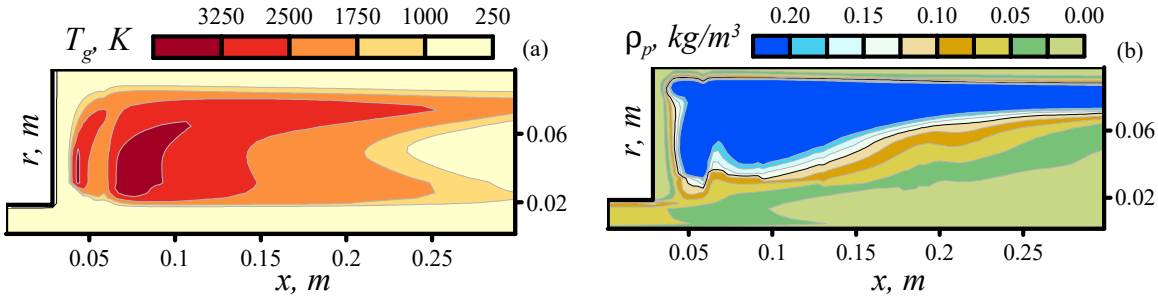

Fig.9. Gas temperature (a) and mass concentration of the suspension (b), ρ_{pb}= 0.075 *kg/m*^{3}, $r_p = 10^{-5}$ *m*, u_b = 5 *m/s*, A_z = 150.

Figure 9 shows the calculation results of the ALAS combustion with the particle radius of 10 μm, under the particle mass concentration of 0.075 *kg/m*^{3}, the feed velocity u_b= 5 *m/s*, and the coefficient of the angular component A_z = 150. The maximum speed along the tangential direction for Figures 8 and 9 was 150 *m/s*. The particles with the radius of 10 *μm* have a sufficiently high inertia, which leads to their lag behind the gas and the formation of the zones of the increased particle concentration close to the channel walls. This effect provokes the formation of a curved flame front with the temperature maximum distant from the channel walls.

Conclusion

Thus, a physical and mathematical model has been developed for the combustion of an air suspension of aluminum powder in a channel with a sudden expansion during swirling of the flow. The model is based on the approaches of the mechanics of two-phase reacting media of R. I. Nigmatulin, and is written in a two-dimensional axisymmetric approximation, taking into account the swirl of the flow along the angular coordinate. The system of equations of the mathematical model is solved numerically by S.K. Godunov and A.N. Kraiko. Verification of the numerical solution of the system of equations showed that the laws of conservation of mass and total energy are satisfied with an accuracy of 99.97%.

The influence of the value of the angular velocity of swirling of the flow at the entrance to the combustion chamber, the mass concentration and size of particles in the air suspension on the shape of the combustion front and the completeness of combustion of aluminum particles is studied numerically. The critical values of the swirling speed, leading to the sowing of aluminum particles onto the walls of the combustion chamber, have been determined. It is shown that, depending on the swirl rate of the air suspension feed at the entrance to the combustion chamber, the combustion front can be formed in the vicinity of the feed zone or be elongated along the channel axis. At high swirling speeds, part of the burning particles is thrown behind the channel turn, which leads to the curvature of the flame front, a two-front combustion mode arises, when the combustion fronts are formed in the center and at the periphery, between the center and the stacks of the burner. The developed physical and mathematical model of combustion of an air suspension of aluminum powder in a channel with a sudden expansion can be used for a preliminary analysis of the design parameters of burners on powder metal fuel.

Acknowledgements

This study was carried out under the financial support of the Ministry of Education and Science of the Russian Federation, No 0721-2020-0036.

REFERENCES

1 Egorov A.G. *Combustion of dispersed aluminum in a stream of air: Monograph*, SSC RAS, Samara, 2008, 305p. [in Russian]

2 Arkhipov V.A., Egorov A.G. , Ivanin S.V., et al. Numerical simulation of aerodynamics and combustion of a gas mixture in a channel with sudden expansion. *Combustion, Explosion and Shock Waves*. 2010, Vol. 46, No. 6, pp. 647 – 655.

3 Egorov A.G. Thermal explosion of aluminum particles suspended in airflow. *IOP Conference Series: Materials Science and Engineering*. 2010, Vol. 734, No. 012189.

4 Egorov A.G., Pavlov D.A. Effect of initial turbulence on ignition, combustion, and flame stabilization in a gas-suspension flow. *Combustion, Explosion and Shock Waves*. 2006, Vol. 42, No. 1, pp. 32-40.

5 Egorov A.G., Tizilov A.S., Niyazov V.Y., et al. Effect of the swirl of cocurrent high-velocity air flow on the geometry of an aluminum-air flame. *Russian Journal of the Physical Chemistry B.* 2014, Vol. 8, No. 5, pp. 712-715.

6 Tizilov A S., Egorov A.G. Limits of flame propagation in an aluminum-air mixture flow. *Russian Journal of Physical Chemistry B*. 2013, Vol. 7, No. 2, pp. 133-136.

7 Piralishvili S.A., Markovich D.M., Lobasov A.S., Vereshchagin I. M. Simulation of the working process of a supersonic combustor with a vortex igniter-stabilizer. *Journal of Engineering Physics and Thermophysics*. 2016, Vol. 89, No. 5, pp. 1325-1332.

8 Mikhailov A.S., Piralishvili S.A., Stepanov E.G., et al. Features of burning of pulverized peat fuel in a vortex burner device. *Journal of Engineering Physics and Thermophysics*. 2018, Vol. 91, No. 4, pp. 925-932.

9 Matvienko O.V., Bubenchikov A.N. Mathematical modeling of the heat transfer and chemical reaction of a swirling flow of a dissociative gas. *Journal of Engineering Physics and Thermophysics*. 2016, Vol. 89, No. 1, pp. 127-134.

10 Kuznetsov V.A., Dekterev A.A., Sentyabov A.V. Numerical study of devolatilization models on the combustion process of pulverized fuel flow swirling. *Journal of Siberian Federal University. Engineering and Technologies*. 2016, Vol. 9, No. 1, pp. 15-23.

11 Gavrilov A.A., Dekterev A.A., Sentyabov A.V. Modeling of swirling flows with coherent structures using the unsteady Reynolds stress transport model. *Fluid Dynamics*. 2015, Vol. 50, No. 4, pp. 471-482.

12 Krainov A., Poryazov V., Krainov D. Numerical simulation of the unsteady combustion of solid rocket propellants at a harmonic pressure change. *Journal of Mechanical Science and Technology*. 2020, Vol. 34, No. 1, pp. 489-497.

13 Krainov A., Poryazov V., Moiseeva K., Krainov D. Metalized solid propellant combustion under high-speed blowing flow. *Journal of Mechanical Science and Technology*. 2020, Vol. 34, No. 5, pp. 2245-2253.

14 Nigmatulin R.I. *Dynamics of Multiphase Media*. Moscow, 1987. [in Russian]

15 Belyaev A.F., Frolov Y.V., Korotkov A.I. Combustion and ignition of particles of finely dispersed aluminum. *Combustion, Explosion, and Shock Waves*. 1968, Vol. 4, No. 3, pp. 182 – 185.

16 Poryazov V.A., Krainov A.Y., Krainov D.A. Simulating the combustion of n powder with added finely divided aluminum. *Journal of Engineering Physics and Thermophysics.* 2015, Vol. 88, No. 1, pp. 94-103.

17 Moiseeva K.M., Krainov A.Y., Dement'ev A.A. Critical conditions of spark ignition of a bidisperse aluminum powder in air. *Combustion, Explosion, and Shock Waves.* 2019, Vol. 55, No. 4, pp. 395-401.

18 Godunov S.K., Zabrodin A.V., Ivanov M.I., et al. *Numerical solution of multidimensional problems of gas dynamics*. Moscow, 1976. [in Russian]

19 Kraiko A.N. On discontinuity surfaces in a medium devoid of "proper" pressure. *Journal of Applied Mathematics and Mechanics.* 1979, Vol. 43, No. 3, pp. 539 – 549.

20 Moiseeva K.M., Krainov A.Y., Tarasenko Y.A. Combustion of a coal dust suspension in a pipe during the swirl. *Journal of Physics: Conference Series*. 2020, Vol. 1404, No. 1, pp. 012063.

Article accepted for publication 23.04.2021

.

DOI 10.31489/2021No2/56-59

UDC 532.5.01

NUMERICAL INVESTIGATION OF THE OCCURRENCE OF A CONCENTRATION-POLARIZATION LAYER

Manatbayev R.K., Kalassov N.B., Amankeldi L.B.

Al-Farabi Kazakh National University, Almaty, Kazakhstan, kalasov.nurdaulet@gmail.com

This work describes the appearance of a concentration polarizing boundary layer on the membrane surface during the separation of the H_2/CO_2 gas mixture. Concentration polarization occurs when the rejection solution accumulates near the surface of the membrane, forming a boundary layer. The inclusion of concentration polarization effects in the processing of porous walls creates additional difficulties. The boundary layer formed by concentration polarization can be considered as a type of a second porous wall with a lower permeability than the membrane. The main difficulty in modeling this situation is to determine the appropriate boundary conditions for the concentration on the wall, since the concentrations on the wall will constantly change, and the wall geometry itself may change over time due to particle deposition. To account for this effect, a numerical approach was developed, which is discussed in this work.

Keywords: membrane, gas separation, concentration polarization, boundary layer

Introduction

Biological processes of hydrogen production offer a method by which renewable energy sources, such as biomass, can be used to generate the cleanest energy source for human use [1-2]. The processes of production of combustible gases are promising for the efficient processing of biomass, wastewater treatment in agriculture, public utilities and food production without the release of carbon dioxide into the atmosphere, provided that aerobic and anaerobic bioreactors are combined in a continuous biotechnological scheme [3].

Extraction of energy from the resulting low-pressure gas mixtures is quite problematic, but can be carried out with the help of gas separation technologies specially selected in such a way as to ensure not only low-energy extraction of components, but also complete recirculation of CO_2 into the process [4-5].

Biogenic mixtures contain macro-components (methane, hydrogen, and carbon dioxide) and other impurities. The release of energy from such mixtures involves their purification. Despite the high level of development of gas separation technologies, the separation of biological synthesis products by standard methods of chemical technology is economically unprofitable due to the low technical parameters of the resulting liquid and gas mixtures [6-7]. Membrane gas separation can be assigned to the most promising processes for the separation of gas mixtures of biogenic origin. Membrane bioreactors are highly precise, selective, and efficient processes. They can contribute to solving the problems associated with the need to use green and intensive technologies [8].

Concentration polarization occurs when the rejected solution accumulates near the surface of the membrane, forming a boundary layer. This accumulation of solute causes a diffusive flow back to the source material, which ultimately reaches a stationary state in which the flow of solute to the membrane surface equals the solute flux through the membrane plus the diffusive flow from the membrane surface back to the source material. The establishment of this boundary layer ensures the subsequent contamination of the membrane layer; thus, the minimization or removal of the concentration polarization layer is the main goal of the membrane study.

In this paper, based on the results of hydrodynamic modeling of membrane separation of gases H_2 / CO_2 [9], an analytical method for the emergence of a concentration polarization boundary layer is described. The basic hydrodynamic model was tested on the basis of experimental and computational data from the literature [10], and the strategy and modeling methods typical for the problem of membrane separation were discussed.

1. Analytical method for determining the mass coefficient

The film theory approach for describing concentration polarization was developed by Michaels et al [11-12]. The film theory simplifies the complex transfer problem to a one-dimensional mass transfer problem by assuming that the axial convection of the solute near the membrane surface is insignificant. Integrating the one-dimensional (transverse) balance of the convective-diffusion mass from the membrane surface to the thickness of the boundary layer (film) of the final mass δ, we obtain the ratio between the concentration polarization and the permeate flow.

$$\frac{C_w - C_p}{C_b - C_p} = \exp\left(\frac{v_w \delta}{D}\right), \tag{1}$$

where C_w – the concentration on the surface of the membrane for the rejected CO_2, C_b and C_p– volume concentration and solute concentration, respectively, $v_w$is the rate of penetration of H_2 on the channel wall, and D – the diffusion coefficient of the solute.

The procedure for estimating the thickness of the convective-diffusion layer in a channel with instant or promptly reacting walls is the basis of most models of the film theory. For a fully developed laminar current in a thin rectangular channel, the thickness of the film layer is described

$$\frac{\delta(x)}{x} = 1.475\left(\frac{h}{x}\right)^{2/3}\left(\frac{D}{u_{max} * h}\right)^{1/3} \tag{2}$$

where x - the longitudinal coordinate, h - half the height of the channel, and u_{max}-the maximum cross-flow velocity at the center of the channel. Assuming a constant diffusion coefficient, the local mass transfer coefficient is described by

$$k(x) = \frac{D}{\delta(x)} = \frac{1}{1.475}\left(\frac{3\bar{u}D^2}{2hx}\right)^{1/3} = 0.538\left(\frac{\dot{\gamma}_w D^2}{x}\right)^{1/3}, \tag{3}$$

where $\bar{u}$- the average volume velocity of the cross-flow and $\dot{\gamma}_w = \frac{3\bar{u}}{h}$-the shear rate of the wall. The main limitation of using film theory to membrane separation is the assumption that the transversal component of convection (permeate flow) does not affect the thickness of the boundary layer, δ.

The channel-averaged mass transfer coefficient k is obtained from the integration of the local flow v_w(x) determined by equations (2) and (3), provided that the permeate and volume concentration, as well as the permeate and cross-flow velocities, remain constant along the length of the membrane channel, L. This assumption is unrealistic for large-scale reverse osmosis systems, but is sensible for short membrane channels where recovery is insignificant. The average channel transfer mass coefficient is expressed as

$$\bar{k} = 0.807\left(\frac{\dot{\gamma}_w D^2}{L}\right)^{1/3}, \tag{4}$$

which is matching to the mass transfer correlation for a laminar flow in a slim channel, usually represented as a Sherwood number,

$$Sh = \frac{\bar{k} d_H}{D} = 1.85(ReScd_H/L)^{1/3} \tag{5}$$

2. Results and discussion

Figure 1 shows the dependence of the tangential voltage on the number Re at the channel input. As can be seen from the resulting graph, the tangential voltage increases with an increase in the speed at the entry to the channel. This confirms that a higher Reynolds number at the input corresponds to a thinner boundary layer of concentration polarization.

By the analytical method, using the hydrodynamic results of equation (4), the average mass transfer coefficient along the length of the channel was calculated. Knowing the average value of the mass transfer coefficient for the corresponding Reynolds number, the Sherwood number was calculated. Figure 2 shows the dependence of the Sherwood number on the Reynolds number. Also, in Figure 3, the change in the mass transfer coefficient along the length of the channel was derived.

.

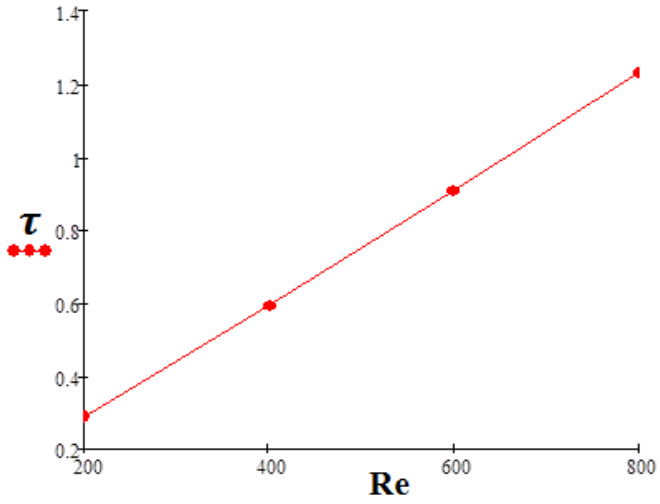

Fig.1. Dependence of the tangential voltage on the number Re at the channel input.

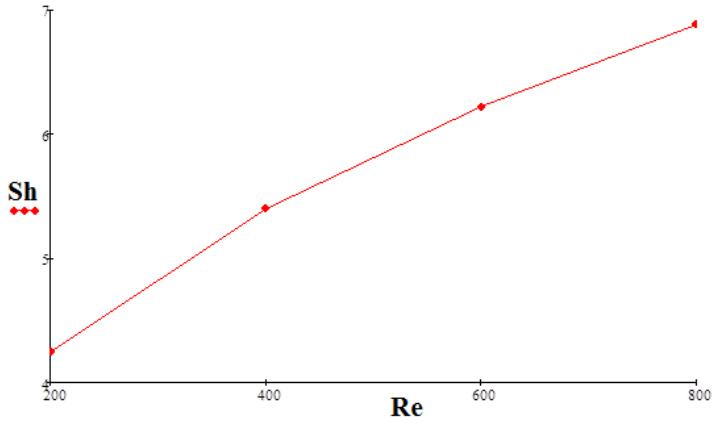

Fig.2. Dependence of the Sherwood number on the Reynolds number.

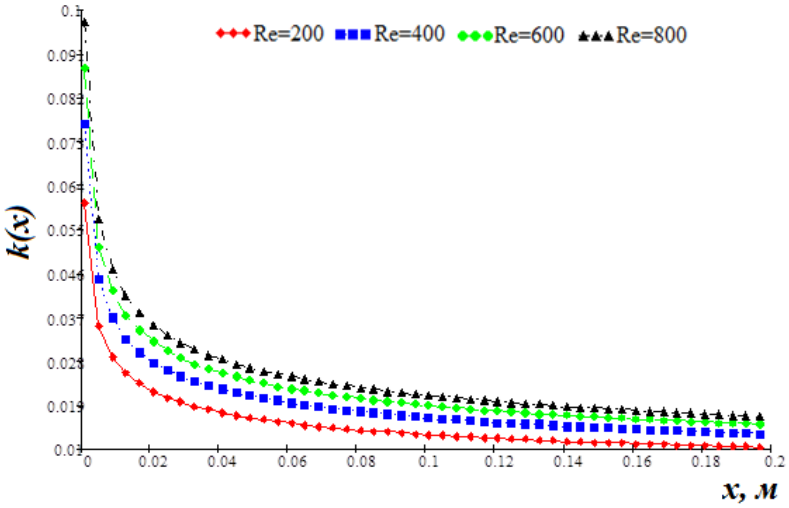

Fig.3. Change in the mass transfer coefficient along the length of the channel.

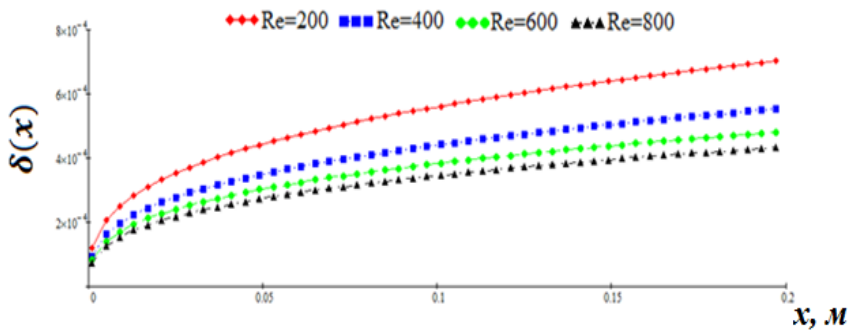

Fig.4. The change in the thickness of the concentration polarization boundary layer along the channel length.

As can be seen in Figure 4, the thickness of the concentration polarization layer increases along the length of the channel. As expected, a higher Reynolds number at the input corresponds to a thinner boundary layer of concentration polarization due to an increased shift that disrupts the boundary layer of concentration polarization.

Conclusion

The inclusion of concentration polarization effects in the treatment of porous membrane walls creates additional difficulties. As expected, a thinner boundary layer of concentration polarization due to an increase in the shift that violates the boundary layer of concentration polarization.Comparison with analytical, experimental and computational data shows that the modern approach to CFD modeling is capable of describing flow conditions for 2D membrane channels. Good agreement is observed from the point of view of the formation of a concentration polarization boundary layer. This gives confidence that the basic hydrodynamic model of the membrane filtration process developed in [9] is satisfactory.

REFERENCES

1 Akinbomi J., Wikandari R., et al. Enhanced fermentative hydrogen and methane production from an inhibitory fruit-flavored medium with membrane capsulated cells. *Membranes*.2015, Vol.5, No. 4, pp. 616–631.

2 Kalassov N.B., Dzhonova D., TsibranskaI., et al. Application of integrated membrane bioreactors in renewable energy industry. *Journal of Chemical Technology and Metallurgy*. 2020, Vol. 55, No. 2, pp. 314-323.

3 Adekunle K.F., Okolie J.A. A review of biochemical process of anaerobic digestion. *Adv. Biosci. Biotechnol.* 2015, Vol. 6, No. 3, pp. 205-207.

4 Bakonyi P., et al. Biohydrogen purification using a commercial polyimide membrane module: studying the effects of some process variables. *Int. J. Hydrogen Energy*. 2013, Vol. 38, No. 35, pp. 15092–15099.

5 Bakonyi P., Nemestóthy N., Bélafi-Bakó K. Biohydrogen purification by membranes: an overview on the operational conditions affecting the performance of nonporous, polymeric and ionic liquid based gas separation membranes. *Int. J. Hydrogen Energy*. 2013, Vol. 38, No, 23, pp. 9673–9687.

6 Ghimire A., Kumar G., Sivagurunathan P., et al. Bio-hythane production from microalgae biomass: key challenges and potential opportunities for algal bio-refineries. *Bioresour. Technol*. 2017, Vol. 241, pp. 525–536.

7 Ghimire A., Frunzo L., Pirozzi F., et al. A review on dark fermentative biohydrogen production from organic biomass: process parameters and use of by-products. *Appl. Energy*. 2015, Vol. 144, 73–95.

8 Rosalinda M., Loredana D.B., Enrico D. *Membrane Bioreactors for Production and Separation. Comprehensive Biotechnology.* 2019,Vol. 2, pp. 374-393.

9 Kalassov N.B., Dzhonova D., Manatbayev R.K. Hydrodynamic modeling of the cross-flow of membrane separation processes. *Bulletin» of the national engineering academy of the republic of Kazakhstan.* 2020, Vol. 75, No.1, pp. 68-76.

10 Geraldes V., Semião V., De Pinho M.N. Flow and mass transfer modelling of nanofiltration. *J. membrane sci.* 2001, Vol. 191, 109-128.

11 Michaels A.S. New separation technique for the CPI. *Chem. Eng. Prog*. 1968, Vol. 64, pp. 31-33.

12 Porter M.C., Concentration polarization with mem-brane ultrafiltration, *Ind. Eng. Chem. Prod. Res. Develop.* 1972, Vol. 11, pp. 234-237.

Article accepted for publication 21.04.2021

DOI 10.31489/2021No2/60-66

UDC 621.43

THERMOACOUSTIC ENGINE AS A LOW-POWER COGENERATION ENERGY SOURCE FOR AUTONOMOUS CONSUMER POWER SUPPLY

Mekhtiyev A.D.[1,2], Sarsikeyev Y.Z.[1], Yugay V.V.[3], Neshina Y.G.[3], Alkina A.D.[3]

[1] S. Seifullin Kazakh Agrotechnical University, Nur-Sultan, Kazakhstan
[2] National Research Tomsk Polytechnic University, Tomsk, Russia
[3] Karaganda Technical University, Karaganda, Kazakhstan, 1_neg@mail.ru

The article deals with the issue of using a thermoacoustic engine as a low-power cogeneration source of energy for autonomous consumer power supply capable of operating on various types of fuel and wastes subject to combustion. The analysis of the world achievements in this field of energy has been carried out. A number of advantages make it very promising for developing energy sources capable of complex production of electrical and thermal energy with a greater efficiency than that of present day thermal power plants. The proposed scheme of a thermal power plant is based on the principle of a Stirling engine, but it uses the most efficient and promising thermoacoustic converter of heat into mechanical vibrations, which are then converted into electric current. The article contains a mathematical apparatus that explains the basic principles of the developed thermoacoustic engine. To determine the main parameters of the thermoacoustic engine, the methods of computer modeling in the DeltaEC environment have been used. A layout diagram of the laboratory sample of a thermal power plant has been proposed and the description of its design has been given. It has been proposed to use dry saturated steam as the working fluid, which makes it possible to increase the generated power of the thermoacoustic engine.

Keywords: cogeneration, energy, thermal power plant, thermoacoustic engine, alternative source, thermoacoustics.

Introduction

An urgent trend in the development of present day decentralized power engineering is the development of alternative energy sources of low power for consumer power supply remote from power centers [1]. The analysis of the literature [2-11] has shown that new designs of heat engines with external heat supply are being developed, which can be a cogeneration source of energy with the capacity of 1 to 100 kW for self-generation of energy at the place of its consumption without transport losses. The literature describes a number of successful projects for developing thermal power plants using engines with external heat supply (EEHS) for autonomous consumers capable of operating on various fuels, as well as waste prone to combustion, their basis is various modifications of EEHS operating according to the Stirling thermal cycle [6, 7, 8]. We can cite as an example the developments of the well-known world manufacturers, such as the Philips, STM Inc., the DaimierBenz, the Solo, the United Stirling, the Ecopower, the WhisperGen, the Microgen, the Lion-Powerblock, the EcoGenViessmann, etc. [1-5]. According to some economic and technical indicators, a Stirling engine (SE) is superior to internal combustion engines (ICE) and gas turbine plants (GTP), which makes it attractive for use in cogeneration energy sources of low power [4-11]. SE is capable of operating in cogeneration mode producing 5-8 kW of thermal energy per 1 kW of electrical energy depending on its design [6, 8]. At the same time, the overall efficiency of cogeneration energy sources based on EEHS can reach up to 90 % with simultaneous production of heat and electricity [4 - 8]. It should be noted the low cost of the produced energy and the long service life of the cogeneration source within 20 years [6 - 8].

The aim of the work is studying a thermoacoustic engine (TAE) operating according to the Stirling thermal cycle with the effect of a standing sound wave, as well as obtaining the dependences of acoustic and electrical power on the working medium pressure and changing pressure of the working medium depending on the heater temperature. Our task is to carry out studies of the thermoacoustic type EEHS [12-23] having a more simplified design in comparison with the classic Stirling engine.

The scientific novelty lies in obtaining new dependences of the TAE parameters with structural differences from their counterparts.

1. Theoretical part of the studies

To calculate the parameters of TAE with a standing sound wave, which is formed when two traveling waves are superimposed [12-23], expressions 1-3 have been used. The condition is accepted that sound waves move towards the opposite axis along the conditional *x* axis, while their frequency and amplitude are the same, $t = 0$ and $\varphi_1 - \varphi_2 = 0$.

$$S = S_1 + S_2 = 2A \cdot \text{coskx} \cdot \cos \omega \text{t} = 2\,\text{Acos}\frac{2\pi x}{\lambda}\cos \omega \text{t}, \quad (1)$$

where $k = \frac{2\pi}{\lambda}$ is the wave number, A is the amplitude, λ is the wave length,

$$S_1 = A \cdot \cos(\omega t - kx),$$

$$S_2 = A \cdot \cos(\omega t + kx). \quad (2)$$

In the experiments there have been used resonators with the length of 500 mm to 1200 mm; for each resonator length, its own vibration frequency corresponds, which can be determined by the well-known expression:

$$\lambda = v / f, \quad (3)$$

where λ is the wave length, v is the sound speed, f is the fluctuations frequency.

The total acoustic power P_{tot} of the TAE can be presented by the expression:

$$P_{tot} = Q_{fil} - Q_{al} - \Delta Q,$$

where ΔQ is the heat loss in heat exchangers.

The acoustic power is directly dependent on temperature gradients, namely the difference in temperature of the working fluid in the "Heater" and "Cooler" systems. An important element of the TAE is a resonator, in which there resonates an acoustic wave caused by the heating of the working medium in a plate heat exchanger. The calculation of the resonator of the TAE studied can be performed by expressing its length as L_{res}, and its diameter as d_{res}. In this case, it is necessary to take into account the pressure fluctuation in the linear generator δ_r, which is the TAE load, and the speed fluctuation v_r. These fluctuations at the entrance to the resonator are related to the pressure fluctuations in the resonator δ_{res} and the speed v_{res} by the following relationship:

$$\delta_{res} = \delta_r \cos(kL_{res}) - \sin(kl_{res})\,4 / \pi d^2 \cdot v_r \rho v_{sou},$$

$$v_{res} = v_r \cos(kL_{res}) - \sin(kl_{res})\,\delta_r \pi d^2 / 4 \cdot \rho v_{sou},$$

where ρ is the working fluid density, v_{sou} is the sound speed, k is the wave number.

The vibration frequency of the magnet attached to the latex rubber membrane can be represented as [12, 15]:

$$\omega = \sqrt{\delta g / m,},$$

where δ is the coefficient depending on the membrane material properties, g is the membrane rigidity, m is the magnet mass.

To estimate the energy parameters of TAE on a standing acoustic wave using theoretical information [12-19], we introduce a parameter associated with generation of acoustic power W_{res} in the regenerator. The volumetric velocity $U_{vol}(x)$ is determined taking into account the second-order acoustic power $\dot{W}(x)$ passing through the conditional point *x*. Let us accept the condition that the linear velocity of the longitudinal movement of the working fluid (gas) in the volume of the regenerator V can be represented as the dependence:

$$U_{vol} = dV / dt, \dot{\text{W}}(\text{x}) = \omega / 2\pi\phi\rho\,\text{Udt} = \omega / 2\phi\rho\,\text{Ud}.$$

.

As a result, we obtain a standard expression associated with averaging over time by the gas flow, at which the work of the acoustic wave is performed [12-18]. The calculation of the thermal efficiency indicator can be performed by the expression:

$$\eta = W_r / Q_{fil},$$

where W_{res} is the power applied to the linear generator.

$$\eta_{ef} = W_{el.out} / Q_{fil},$$

where $W_{el.out}$ is electrical power of the linear generator.

As a result, the efficiency of the TAE thermal Carnot cycle [3, 4] will be shorter and is determined by the expression:

$$\eta_{ef.Karnot} = \eta_{ef} / \eta_{Karnot},$$
$$W_r = 1/2 R_v \left[\delta_r \nu_{res}\right].$$

3. Description of the object of study

The object of study is a TAE operating according to the Stirling thermal cycle with the effect of a standing sound wave. A laboratory specimen of a thermal power plants (TPP) with an output electric power of 30 W based on TAE is shown in Figure 1.

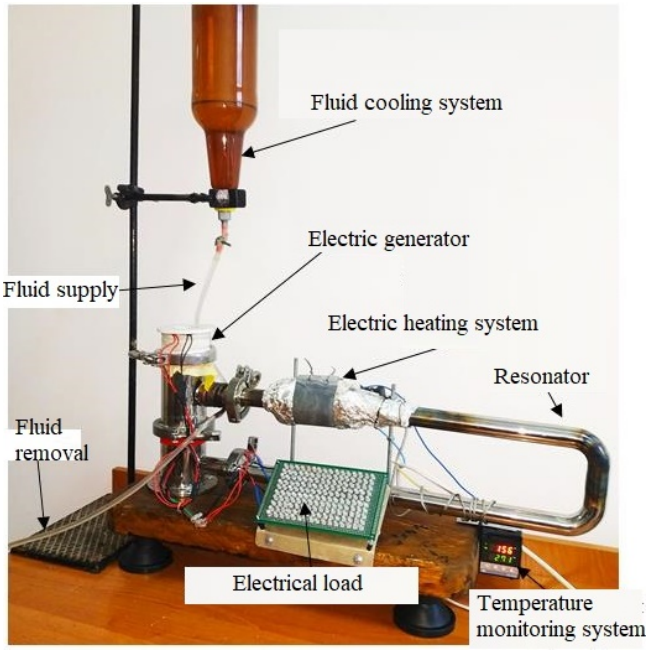

Fig.1. Laboratory TPP specimen base on TAE

Figure 2 shows a diagram of a laboratory specimen a TPP based on TAE. Heating of the working fluid is performed in plate heat exchanger 1. Heating is performed using a 250 W electric spiral heater. In the experiment, air was used as the working medium with adding a small amount of water (vapor-air mixture), which provides the highest power indices of the studied laboratory TAD specimen. The gas pressure inside the resonator housing should be at least 0.15-0.2 MPa [12-15]. The value of the initial pressure of the working fluid in the internal cavity of the TAE affects the value of its power. When heated, the gas volume expands and fills the entire cavity of the resonator, passes through regenerator 3, which is made of a metal mesh with the cell diameter of about 1 mm [12-15]. Passing through, the heated gas gives up partially accumulated heat to the metal mesh of the regenerator; for the resonator tube diameter of 25 to 50 mm, the length of the regenerator should be 50-80 mm. The regenerator increases the thermal efficiency of the engine by 10-15 %, and reduces its heat losses. An important parameter is the developed temperature difference at the extreme regions of the regenerator, the greater it is, the greater its efficiency. Then, a slightly cooled

working fluid enters the cold heat exchanger, where it is cooled and the process of its compression takes place. During cooling and compression, the working fluid (gas) begins to move in the opposite direction (indicated by the dotted line). Passing through the regenerator, the working fluid picks up partially accumulated heat by the regenerator and enters the heater already preheated.

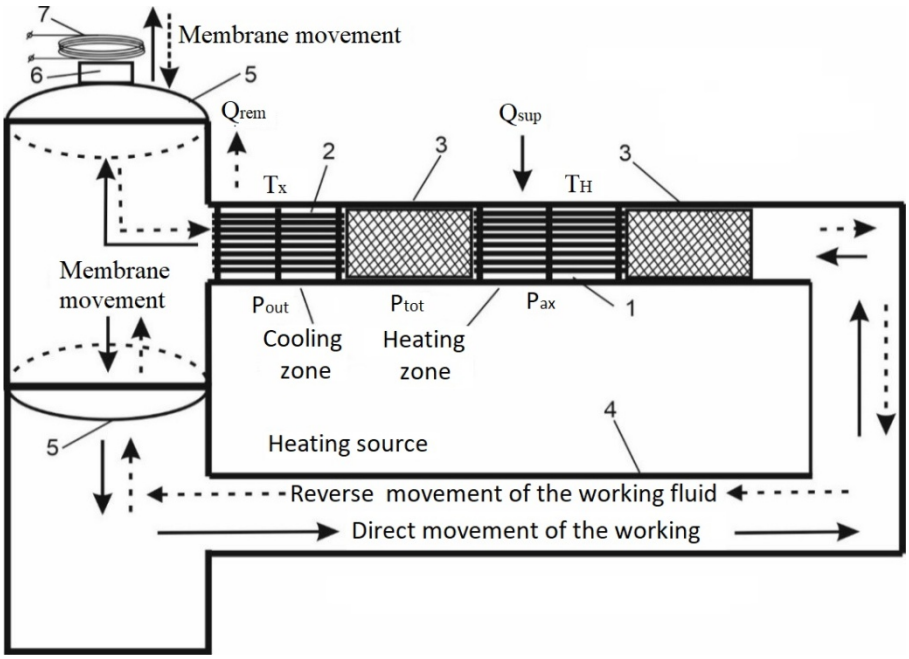

Fig.2. TAE based on the effect of a standing sound wave with an electrical and thermal circuit:
1 - hot heat exchanger, 2 - cold heat exchanger, 3 - regenerator, 4 - resonator, 5 - membrane,
6 - permanent magnet, 7 - coil with copper winding

When the working medium oscillates inside the resonator, its pressure and volume change, which activates membranes 5, one of which is inside resonator 4. When the working medium is heated, an acoustic wave is generated in the range of 150-180 dB, while the generation frequency depends on the length of resonator 4 and parameters of membrane rigidity 5. The movement of gas inside the cavity of resonator 4 is shown in Figure 2, both ends of the resonator are closed by the tube with membranes 5, which are set in motion during the circulation of the working fluid. Permanent magnet 6 is fixed on the upper membrane, under the weight of which the membrane is lowered to the lower position, when the working fluid is compressed and cooled in cold heat exchanger 2, and when it expands, it rises. Magnet 6 reciprocates with the oscillation frequency of the resonator circuit. Magnet 6 moving up and down crosses coil 7 of the copper wire. An electrical load is connected to the output terminals of coil 7. The permanent magnet and the wound coil develop a linear electrical alternator. The use of the water circulation system in cold heat exchanger 2 improves the process of cooling the working fluid and increases the TAE power. Hot heat exchanger 1, cold heat exchanger 2 and regenerator 3 form the TAE working stage, the number of which can be increased to 4, which will reduce the temperature gradient difference between the cold and hot parts of the stage up to 4 times.

2. Experimental results

There has been studied TAE with the resonator length of 1140 mm and the inner diameter of 22 mm, operating with the use of the thermoacoustic effect of a standing acoustic wave in a heated gas. The oscillation frequency of the acoustic wave is within 300 Hz, which is optimal for this type of the TAE design. With decreasing the length of the resonator, increasing the oscillation frequency of the rubber membrane is observed with decreasing the TAE power, and when using a 500 mm resonator, the oscillations of the membrane completely stopped. The air temperature in the room where the TAE tests have been carried out was 22-23 °C. The dependence of changing pressure of the working medium on the temperature of the heater is shown in Figure 3. The efficiency of the TAE operation is largely affected by the temperature of the

.

heater and cooler, as well as by pressure of the working medium in the resonator cavity. The working fluid pressure of the TAE has been measured when the temperature of the working fluid changed from 150 °C to 330 °C. Increasing pressure and temperature allows increasing the power of the TAE, and reduces the time of self-start and the starting its operation. Figure 4 shows the dependence of the acoustic and electric power on the working fluid pressure that is the most important for estimating the TAE total efficiency.

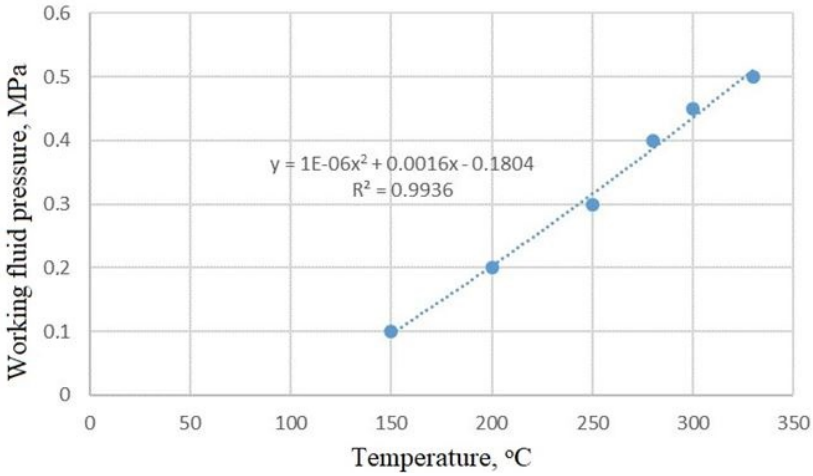

Fig.3. Dependence of the working fluid pressure changing on the heater temperature

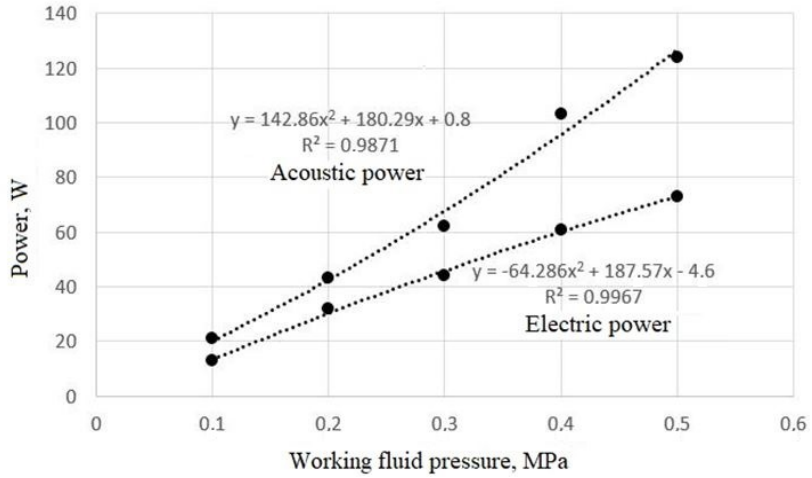

Fig.4. Dependence of the acoustic and electric power on the working fluid pressure

The design is intended for working pressure of 0.5 MPa; for operation at higher pressures in the range of 12-15 MPa, serious changes are required, first of all, the transition from a rubber membrane to a metal one which will also provide increasing the vibration frequency.

The DeltaEC computer program (Design Environment for Low-amplitude Thermo- Acoustic Energy Conversation developed by Los Alamos National Laboratory, USA, free license) has been used to calculate the parameters of the TPP laboratory specimen based on the TAE. This program is used to simulate thermoacoustic engines and to obtain their design parameters. DeltaEC performs numerical integration based on a low-amplitude linear approximation of the Rott equations. When comparing the results obtained experimentally and when modeling TAE with the use of the DeltaEC program, the values of the acoustic power of TAE were on average 30 % higher than the experimental ones, since a lot of assumptions have been formed related to the external factors affecting the operation of TAE. The executed model in the DeltaEC program does not allow accurate reflecting all the design features and parameters of a full-scale specimen and has been used as a tool for preliminary calculation of the expected acoustic power. Subsequently, corrections will be made to this model to gradually approximate its parameters to a full-scale specimen due to the fact that the mechanism for developing heat exchangers and regenerators is insufficiently developed. There is also idealization of heat transfer processes and structural parts of the TAE,

on the basis of which the model has satisfactory accuracy of information of the parameters and geometry (pressure, temperature, dimensions, operating frequency, etc.), but it does not take into account the hydrodynamic features of the flow and transient processes in various components of the pulsation cooler structure. Similar problems with the accuracy of modeling the software product DeltaEC are noted in works [21, 22]. In practical experiments with the laboratory TAE specimen, a microphone and Sound Card Oszilloscope software have been used to measure the amplitude of acoustic pressure in the resonator, which together with a computer performed the functions of a two-channel oscilloscope with the transmission frequency in the range from 20 to 20.000 Hz.

3. Conclusions

The performed theoretical and practical studies allow us to assert that a single-stage TAE can be used as a low-power cogeneration energy source for power supply of autonomous consumers. TAE has a number of advantages, which makes it very promising for the creation of autonomous multi-fuel energy sources capable of more efficiently producing electric and thermal energy in a complex manner than modern thermal power plants (TPPs). The presented design of a single-stage TAE, based on the effect of a standing sound wave, ensures its launch at a temperature of about 150°, which is a rather significant indicator for a single-stage design. The use of an additional regenerator increases the thermal efficiency of the TAE. TAE operates according to the well-known Stirling thermal cycle, but unlike the known energy sources based on the Stirling engine, it does not have pistons and, accordingly, problems with ensuring the reliability of the seals, which makes it possible to increase its resource, as well as the overhaul interval. The use of the free software product DeltaEC made it possible to calculate the TAE parameters and simulate its operation, which reduced the time spent on its creation.

The minimum indicator of the TAE self-start temperature of 186 °C with the load of 30 W was reached with the resonator with the inner diameter of 22 mm and the length of 1140 mm. The proposed air-vapor mixture as a working fluid is capable of effectively operating in the resonator with the length of 1140 mm at the minimum T = 150 °C with pressure P = 0.1 MPa and at the maximum T = 330 °C with pressure P = 0.5 MPa. Increasing the density of the working fluid is a very promising direction for increasing pressure at average temperatures of the working fluid from 150 ° C to 330 ° C, which is not achievable when used in air as a working fluid. This circumstance makes it possible to significantly increase the power of the TAE and create a commercially attractive cogeneration autonomous energy source capable of operating on almost any type of fuel, including waste that is subject to combustion, since only a heat source is needed for its operation.

Acknowledgments

The article was prepared within the framework of the project AP05131751 "Micro thermal power plant of the cogeneration type with heat recovery".

REFERENCES

1 Mekhtiyev A.D., Yugay V.V., Alkina A.D., Kaliaskarov N.B., Esenzholov U.S. Multi-fuel micro-thermal power plant with a capacity of 1-10 kW for remote facilities in rural areas and farms. *Bulletin of the South Ural State University,* 2018, Vol. 18, No. 2, pp. 62-71. [in Russian]

2 Mekhtiyev A.D., Yugay V.V., A.D.Alkina, N.B.Kaliaskarov, U.S. Esenzholov. Multi-fuel power plant with a heat engine External combustion, able to work effectively in the conditions of rural Locations of kazakhstan. *International research journal*, 2018, No.12 (78), pp. 124-131.

3 Mekhtiev A.D., Yugay V.V., Esenzholov U.S., Kaliaskarov N.B. Engine with external heat supply based on thermoacoustic effect for autonomous thermal power plant. *Bulletin of the South Ural State University. Series: Energy*, 2019, No. 2, pp. 22-30. [in Russian]

4 Mekhtiyev A.D., Yugay V.V., Esenzholov U.S., Mekhtiyev R.A. Prospects for the use of ultra-low-power thermal power plants based on an engine with an external heat supply. *Mechanics and technologies, 2019,* No. 2 (64), pp. 166-173. [in Russian]

5 Mekhtiev A.D., Yurchenko A.V., Yugay V.V., Al'kina A.D., Yessenzholov U.S. Multi-fuel power station of ultra-low power with external combustion thermal engine, capable efficiently operate in the conditions of rural areas of Kazakhstan. *News of the national academy of sciences of the republic of Kazakhstan series of geology and technical sciences*, 2019, Vol.3, No.435, pp.136 – 143.

6 Reeder G. *Stirling Engines*. Moscow, Mir,1986, 464 p. [in Russian]

.

7 Walker G. *Stirling Engines*. Moscow, Mechanical engineering, 1985, 408 p. [in Russian]

8 https://ru.wikipedia.org/wiki

9 Makushev Yu.P., Polyakova T.A., Ryndin V.V., Litvinov P.V. Methods for calculating the operating cycle of a petrol engine with construction of the indicator diagram. *Science and technology of Kazakhstan*, 2018, No. 2, pp. 63-81. [in Russian]

10 Volkova A.V., Ryzhenkova A.V., Parygina A.G., Naumova A.V., Druzhinina A.A. Matters Concerned with Development of Autonomous Cogeneration Energy Complexes on the Basis of Microhydropower Plants. *Heat power engineering*, 2018, No. 11, pp. 32–39. [in Russian]

11 Efendiev A.M., Nikolaev Yu.E., Evstafiev D.P. Possibilities of power supply of farms based on small renewable energy sources. *Heat power engineering*, 2016, No. 2, pp. 38-45. [in Russian]

12 Zinoviev E.A., Dovgyallo A.I. To assessment of efficiency indicators of the working process of the thermoacoustic engine. *Bulletin of the Samara State Aerospace University*, 2012, No.3 (34), pp. 145-152. [in Russian]

13 Hamood A., Jaworski A.J., Mao X., Simpson K. Design and construction of a two-stage thermoacoustic electricity generator with push-pull linear alternator. *Energy*, 2018, No.144, pp. 61 – 72.

14 Jin T., Yang R., Wang Y., Feng Y., Tang K. Low temperature difference thermoacoustic prime mover with asymmetric multi-stage loop configuration. *Sci. Rep. UK*, 2017, Vol.7, pp. 1–8.

15 Ceperley P. H. A pistonless Stirling engine – the traveling wave heat engine. *J. Acoust. Soc. Am*, 1979, Vol. 66, No.5, pp. 1508–1513.

16 Piccolo A., Pistone G. Estimation of heat transfer coefficients in oscillating flows: The thermoacoustic case. *Int. J. Heat Mass Tran*, 2006, Vol. 49, pp. 1631–1642.

17 Abduljalil A. S., Yu Z., Jaworski A. J. *Mater. Design*, 2011, Vol. 32, pp. 217–228.

18 Langlois L., Justin R. Dynamic computer model of a Stirling space nuclear power system / Justin L.R. Langlois. *Trident Scholar project report*, 2006, No. 345, pp. 348 – 352.

19 Wang K., Qiu L. Numerical analysis on a four-stage looped thermoacoustic Stirling power generator for low temperature waste heat. *Energ. Convers. Manage, 2017,* Vol. 150, pp. 830–837.

20 Piccolo A., Pistone G. Estimation of heat transfer coefficients in oscillating flows: The thermoacoustic case. *Int. J. Heat Mass Tran*, 2006, Vol. 49, pp. 1631–1642.

21 Nekrasova S.O., Sarmin D.V., Uglanov D.A., Shimanov A.A. Numerical and experimental study of thermoacoustic cooler on a pulse pipe. *Bulletin of the Samara Scientific Center of the Russian Academy of Sciences*, 2015, Vol. 17, No.6 (2), pp.125-135. [in Russian]

22 Gorshkov I.B., Izv V.V. Numerical simulation of a ring four-stage thermoacoustic running wave engine. *Saratov Univ. (N. S.), Ser. Physics*, 2018, Vol. 18, No. 4, pp. 285–296. [in Russian]

Article accepted for publication 21.05.2021

DOI 10.31489/2021No2/67-75

UDC 621.891

INFLUENCE OF BORINATION, BORON CEMENTATION OF STEEL 45 AND VISCOSITY OF A LUBRICANT ON THE PARAMETERS OF ADHESION BOND IN THE STEEL 45 - 40X SYSTEM

Kubich V.I.[1], Cherneta O.G.[2], Yurov V.M.[3]

[1]National University "Zaporizhzhya Polytechnic", Zaporizhia, Ukraine, schmirung@gmail.com
[2]Dniprovsk State Technical University, Kamenskoye, Ukraine, ocherneta@gmail.com
[3] E.A. Buketov Karaganda University, Karaganda, Kazakhstan, exciton@list.ru

In the work, the regularities of changes in the shear strength of the adhesive bond τ and the piezoelectric coefficient β in the metal systems "steel 45 - 40X", "steel 45+B-40X", "steel 45+BC-40X" were obtained during physical modeling of the materials I-20A, Wolf 10W-40, TAD-17i, Litol-24 with distinctive dynamic viscosities using the additional equipment of the SMTs-2 friction machine. It has been established that a twofold increase in the shear rate causes a decrease in the piezoelectric coefficient in the "steel 45+VS - 40X" system by a factor of 1.2-1.6 for Wolf 10W-40, TAD-17i, Litol-24 lubricants and its relative similarity independent of dynamic viscosity. At the same time, a twofold increase in the shear rate in the "steel 45+B-40X" system also causes a decrease in the piezoelectric coefficient by a factor of 1.16-1.38 for all tested lubricants and its alignments, as in the "steel 45+VS" system, does not observed. It was found that the clearly expressed regularity of the effect of the equivalent dynamic viscosity on the strength of the adhesive bond at p = 0 MPa is not revealed, and the nature of the manifestation is predetermined by a possible change in the mechanism of intermolecular interaction, which depends on the structure of the molecules of lubricants. It was determined that the piezoelectric coefficient naturally decreases with an increase in dynamic viscosity in the entire considered range of normal pressures.

Keywords: metal system, tangential strength, shear rate, piezoelectric coefficient, pressure, dynamic viscosity

Introduction

This work is a continuation of work [1], which shows the importance of having numerical values of the parameters of adhesion properties directly for the surfaces of metals of full-scale operational friction units of machines and mechanisms with reversible movement, ie. in which there is a shift with a certain speed of movement, when the manifestation of the molecular (adhesive) component of the friction force has time to manifest itself. Tribophysical assessment of the state of the near-surface layers of metals of parts working under sliding friction with unidirectional movement is also important. This is due to the fact that when some mechanisms are activated, one surface of the part moves relative to the other. In this case, the force parameter of their contact interaction changes from minimum to maximum and back. Such mechanisms include, for example, the gas distribution mechanism of an internal combustion engine (DVZ), in which the cam displacement relative to the end of the valve or pusher at the initial moment of movement occurs with a normal force due to the magnitude of the compression force of the valve spring when it is opened and closed. The shift rate is predetermined by the starting crankshaft rotation speed and depends on the energy consumption of the DVZ electric start system. In addition, each subsequent shift is carried out under conditions of contact through lubricating formations that were previously formed under conditions of amplitude-frequency change in the force and speed parameters of loading the contact pads of the friction surfaces. The efficiency of the DVZ operation depends on the tribophysical state of the camshaft friction surfaces: power, dynamics, efficiency [2, 3]. In most cases, automotive DVZs use one-piece camshaft structures, which are made of structural medium-carbon steel with surface wear-resistant layers. Additional hardness of finished shafts is obtained as a result of hardening: nitriding, laser treatment, bleaching, etc. Surface modification is also possible by saturating the surfaces of the camshaft cams with boron and boron carbide, including with subsequent laser treatment, which leads to the production of new near-surface microstructures with predictably improved parameters of friction and wear [4, 5]. The tribological state of the friction pair "camshaft cam - valve (pusher)" during shear is estimated by the known parameters: shear strength of the adhesive bond τ_0 and piezoelectric coefficient β [5, 9], and the assessment of their manifestation, taking into account the multifactorial influence, seems to be a significant scientific and

.

technical problem in tribology. A particularly significant factor is surface modification, for example with boron, boron carbide, of medium carbon steels and its effect on the surface energy, especially of active centers of adsorption of lubricant molecules. And this, in general, determines the nature of the accumulation of fatigue deformations of the contact interaction areas during multiple shears with different intensities of force, speed loading and viscosity of intermediate lubricant formations, and as a result, wear of the cam surface.

1. Analysis of publications

The interest in boriding process of specialists from various industries is caused by the unique ratio of mechanical, physical, corrosive and tribological properties of the resulting coatings. During the second half of the 20th century, scientific schools in many countries studied this process. A detailed review of the boriding process of many metals is reflected in the dissertations [6, 7]. It is emphasized that over the decades of application of the boriding process, various methods of saturation of products with boron have been proposed, the mechanisms of formation of boride coatings on carbon and alloy steels, their phase composition and properties have been studied. A common disadvantage of all boriding methods is the long duration of diffusion saturation. To solve this problem, methods are being sought to intensify diffusion saturation and reduce costs. The study of adhesive shear in lubricants, which can simulate the gradient viscosity of lubricants with boundary lubrication in friction triads by their viscosity, is a fundamental result, both from a practical and theoretical point of view. There can be three, four or more such lubricants. A lubricant, as an element of a mechanical system, significantly affects the reliability of the entire system, however, during operation, its properties change, therefore, establishing a resource for it is an important problem. The main requirement for lubricants is to ensure the wear resistance of materials of friction pairs in a wide range of loads, speeds and temperatures, therefore, the solution to this problem should be aimed at determining the relationship between the mechanisms of aging of lubricants and wear of materials, the formation of modified protective layers during friction. All these questions are devoted to dissertations [6-8], which contains a list of extensive literature. At the same time, not enough attention has been paid to the issues of assessing the effect of the viscosity of a lubricant on the shear resistance of surfaces when varying the parameters of their modification [5, 9, 10]. This is especially important for materials that have a certain technological heredity of surface properties acquired during the operation of real parts. Such parts include the aforementioned camshaft, made, for example, of 45 medium-carbon structural steel with an HFC-hardened surface layer. Moreover, such information is not only of scientific and applied interest for the development of tribological and materials science aspects of ensuring the reliability of mechanical engineering objects, but also is the initial data for modeling the patterns of changes in their tribological state and control of processes in them. Simulating changes in the viscosity of lubricant formations in the considered friction pair "camshaft cam - valve (pusher)", the basis of which, as a rule, is a mineral, semi-synthetic, synthetic oil is very difficult due to the complexity of reproducing the viscosity of lubricating formations from the same type of environment.

However, it is possible to simulate using lubricants other than the bases, but with known viscosities. Of course, this approach imposes certain restrictions, but it allows, in the first approximation, to establish the direction of the process. Thus, having the surface structures of the camshaft cam fragments modified by boron, boron carbide and definitely selected lubricants, it seems possible to perform a model assessment of the nature of the change in the parameters of its molecular bond with the valve (pusher) material depending on the viscosity of the interaction medium.

2. Objective

The aim of the work is to establish the regularities of changes in the parameters of the adhesive bond in the systems of materials "steel 45-40X", "steel 45+B-40X", "steel 45+BC-40X" in the physical modeling of the shift between small samples in a lubricant environment viscosities using additional equipment of the SMTs-2 friction machine.

3. Research methodology

The parameters of the adhesive bond of materials were determined using additional equipment for the SMTs-2 friction machine in accordance with the methodology proposed in [1]. In this case, the force loading parameter was represented by the normal pressing force of the fixed shoe (a fragment of the camshaft cam -

steel 45) of 140N, 185N, 230N, 280N. The time of t_1 = 0.43 s and t_2 = 1 s for the angular displacement of the shearing disk (material 40X) under the action of the lever mechanism determined the parameter of high-speed loading - the shear rate. The displacement speed of the disk relative to the block was υ_1 = 10.16 ± 0.8 mm/s, υ_2 = 5.08 ± 0.6 mm/s. The average linear displacement of the disk was l = 4.5 mm. The chemical composition of the materials of the system under study is presented in Table 1.

Table 1. Chemical composition of steel, %

Element / Steel	C	Si	Mn	Ni	S	P	Cr	Cu	Fe
45	0.42 - 0.5	0.17 - 0.37	0.5 - 0.8	before 0.25	before 0.04	before 0.035	before 0.25	before 0.25	~97
40X	0.36 - 0.44	0.17 - 0.37	0.5 - 0.8	before 0.3	before 0.035	before 0.035	0.8 - 1.1	before 0.3	~97

Boring and boron cementing of block samples was carried out in accordance with the methodology described in [4], block samples are shown in Fig. 1. Boronated and boron-cemented surfaces with subsequent laser treatment were not used in the presented studies.

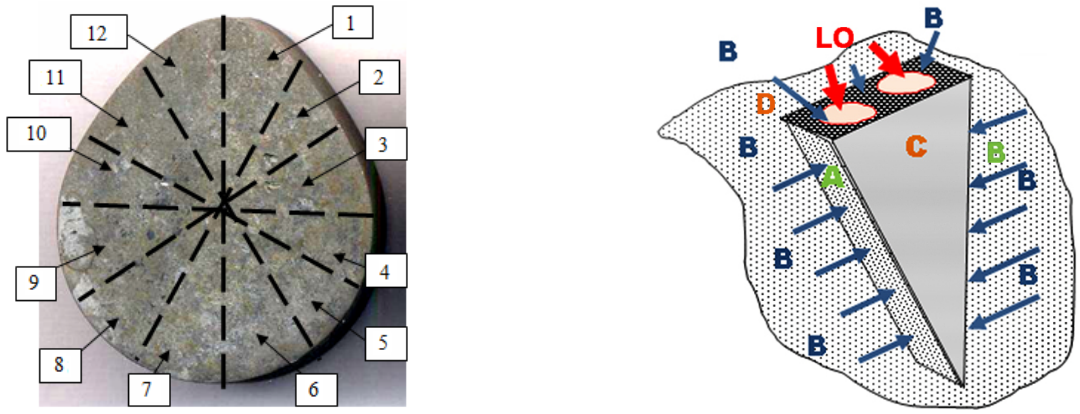

a b

Fig. 1. View of samples for experimental research: a - cross-section of the camshaft cam divided into samples-segments No.1-No.12; b - surface treatment scheme: A, B, C, D - plane of the sample-segment; B - boriding (boron cementation); LO - laser processing

The lubricant was applied in a thin layer to the disk at a temperature of 25 ºC. In the experiment, we used the following lubricants:

- semi-synthetic motor oil Wolf 10W-40 API SL/SF, dynamic viscosity at 40 ºC μ=0.19 Pa•s;
- industrial oil I-20A (GOST 20799-88), dynamic viscosity at 40 ºC μ = 0.027 Pa•s;
- transmission oil TAD-17i (GOST 23652-79), dynamic viscosity at 50 ºC μ = 0.106 Pa•s;
- Litol-24 grease (GOST 21150-2017), dynamic viscosity at 50 ºC μ = 8 Pa•s.

The indicated range of changes in the viscosity of the simulated lubricating medium is quite wide and we think it is significant for experimental studies. At the same time, the lubricants themselves, with the exception of engine oil, cannot be used in the LWD lubrication system. Each of them has its own functional purpose. Motor oil 10W-40 can be used all-season if the temperatures in winter do not drop below -25 °C, unless the car is equipped with a pre-heater, which eliminates the need to crank the crankshaft with the starter on a cold engine. Industrial oil I-20A is used in units of industrial machines and mechanisms: rolling mills, metal-cutting machines, fans, forging and pressing equipment, textile machines, pumps, etc. The grease is well suited for reducing friction between surfaces with low pressure in light and medium loaded gears, sliding and rolling guides. Oil TAD 17i is a universal all-season transmission fluid that is used to lubricate hypoid, spiral-bevel, worm, cylindrical and bevel gears operating at high loads. The material is suitable for automotive and electric vehicles, transport, trucks and special vehicles. The main advantage of Litola-24 is its high mechanical stability, due to which the material is used in units operating under increased loads. However, if we single out the most significant property for specific conditions and operating modes

.

separately, then they can be equally differentiated taken into account in the contact between the cam and the valve end (valve pusher). Those, we can talk about model reproduction of the layer-by-layer viscosity of the forming lubricant formations with a positive gradient to the metal surface. The functionality of the latter is manifested both with boundary and mixed lubrication of friction surfaces. The strength of the adhesive bond at shear (shear resistance of the molecular bond) - tangential strength τ was determined in accordance with the expression:

$$\tau = \frac{M_m}{r \cdot S_b}, \quad (1)$$

where M_m - moment of friction during shear, N•m; r is the radius of the disk, r = 25 mm; Sb - indent area, Sb = 1.5-5.5 mm^2.

4. Research results and their discussion

Graphical approximation of the averaged data in the form of linear dependencies with inverse extrapolation of the shear resistance of displacements is shown in Figure 2.

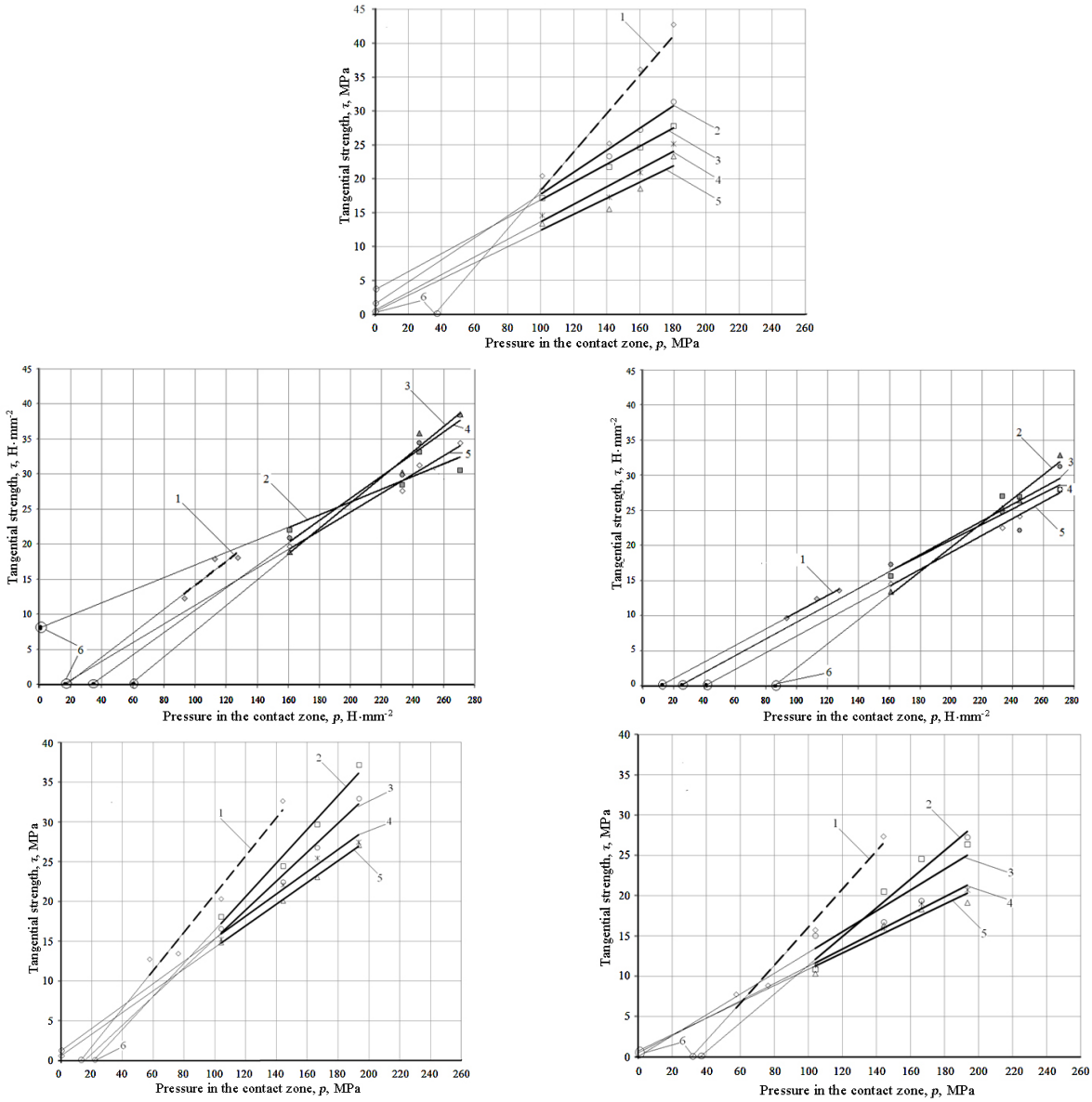

Fig. 2. Tangential strength of the adhesive bond in the contact of materials "40X - steel 45": a - steel 45 without treatment; b, c - steel 45 + BC; d, e - steel 45 + B; 1 - without lubricant; 2 - I-20A; 3 - Wolf 10W-40; 4 - TAD-17i; 5 - Litol-24; 6 - extrapolated values of τ; b, d - shear rate 5 mm/s; a, c, d - shear rate 10 mm/s.

At the same time, their equations and the accuracy of approximation R^2 are determined by the parameters of the trend lines in Excel program, the results are shown in Table 2, 3. Analysis of the data obtained indicates the following. In general, the following picture takes place. The saturation of the surface of steel 45 with boron and boron carbide in almost all cases of shear in lubricating media either leads to a decrease in the values of the piezoelectric coefficient β, or it remains unchanged: the system “steel 45 + VS - TAD-17i - 40X” Fig. 2 c, d; system "steel 45 + VS - Litol-24 - 40X" Fig. 2, the exception is the system "steel 45 + VS - I-20A - 40X" at a shear rate $\upsilon_1 = 10.16 \pm 0.8$ mm/s , for which the value of β increased slightly. A clear decrease in the piezoelectric coefficient β is manifested for the unmodified surface of steel 45 during shear in lubricants. Moreover, a smaller value of β is typical for Litol 24 with the highest dynamic viscosity, Fig. 2 a. An increase in the shear rate in systems with a modified surface of 45 steel causes its ambiguous influence on the manifestation of adhesion parameters. With regard to the parameter τ0, there is a tendency to a decrease in its values for systems of materials with modified steel 45 during shear in lubricating media up to the absence of its manifestation at normal pressure p_0 = MPa.

Table 2. Parameters of approximation of experimental data for the system of materials "40X - steel 45 (+ B, + BC)" without lubricants

Parameter	Steel 45	Steel 45+B	Steel 45+BC
Type of equation	$\tau = 0.28\eth - 10,27$	$\tau = 0.23\eth - 7,5$	$\tau = 0.11\eth - 1,23$
	-	$\tau = 0.24\eth - 3,05$	$\tau = 0.17\eth - 3,53$
Approximation reliability R^2	0.9	0.96	0.97
	-	0.96	0.84
Piezoelectric coefficient β	0.28	0.23	0.11
	-	0.24	0.17
Tangential strength τ_0, MPa	>0 at $p \approx 36$ MPa	>0 at $p \approx 32$ MPa	>0 at $p \approx 11$ MPa
	-	>0 at $p \approx 13$ MPa	>0 at $p \approx 21$ MPa

Note. The upper row of values at a shear rate $\upsilon_1 = 10.16 \pm 0.8$ mm/s, the lower one at $\upsilon_2 = 5.08 \pm 0.6$ mm/s.

The system "steel 45 + VS - 40X" is characterized by the following manifestation of the adhesive bond parameters, Fig. 2 c, d. An increase in the shear rate by a factor of two causes, firstly, a decrease in the values of the β parameter by a factor of 1.2-1.6 for lubricants Wolf 10W-40, TAD-17i, Litol-24, second, its alignments. Those at $\upsilon_1 = 10.16 \pm 0.8$ mm/s, the values of the parameter β do not depend on the dynamic viscosity. The exception is industrial oil I-20A with the lowest viscosity, for which the value of the parameter β, on the contrary, increased by 1.8 times. The graph lines on the coordinate field are located in a narrower corridor than the graph lines without modification of steel 45 with boron carbide. This clearly reflects the features of the manifestation of the variable surface energy of the "steel-45 + VS" system on the formation of adhesive bonds with steel 45 through the compacted layers of the lubricant deformed in the interface zone. Such bonds are clearly reduced, and for reliable adhesion it is necessary to increase the pressure in the contact zone, i.e. the tribological system in the region of low contact pressures, for example, less than 20 MPa, becomes more reliable.

The system “steel 45 + B - 40X” is characterized by the following manifestation of the adhesive bond parameters, Fig. 2 e, f. An increase in the shear rate by a factor of two causes, firstly, a decrease in the β parameter values by 1.16-1.38 times for all tested lubricants, and secondly, its alignments, as in the system "steel 45 + BC "is not observed. Those when the shear rate is doubled, there is a proportional decrease in the parameter β. In this case, the regularity of a decrease in the parameter β with an increase in dynamic viscosity remains. The graph lines on the coordinate field are located in a wider corridor relative to the “steel 5 + BC” system, and approximately equal to the corridor for placing graphs for unmodified steel 45.

This clearly reflects the features of the manifestation of the variable surface energy of the “steel-45 + B” system on the formation of adhesive bonds with steel 45 through the compacted layers of the lubricant deformed in the interface zone. Such bonds decrease somewhat less than in the “steel 45 + BC” system. Such a decrease is less pronounced under the action of the components of the TAD-17i and Litol-24 lubricants, i.e. their properties are manifested to provide increased stickiness in the zones of distributed contact. For this system, the range of normal pressures at which the parameter $\tau_0 > 0$ is approximately two times less than in the “steel 45 + BC” system. This indicates a positive effect of carbon on a decrease in the strength of the adhesive bond in the considered system of materials. According to table 2, graphical dependences are built,

.

Figure 3, which more clearly reflect the nature of the change in the parameters of the adhesive bond in the studied systems of materials.

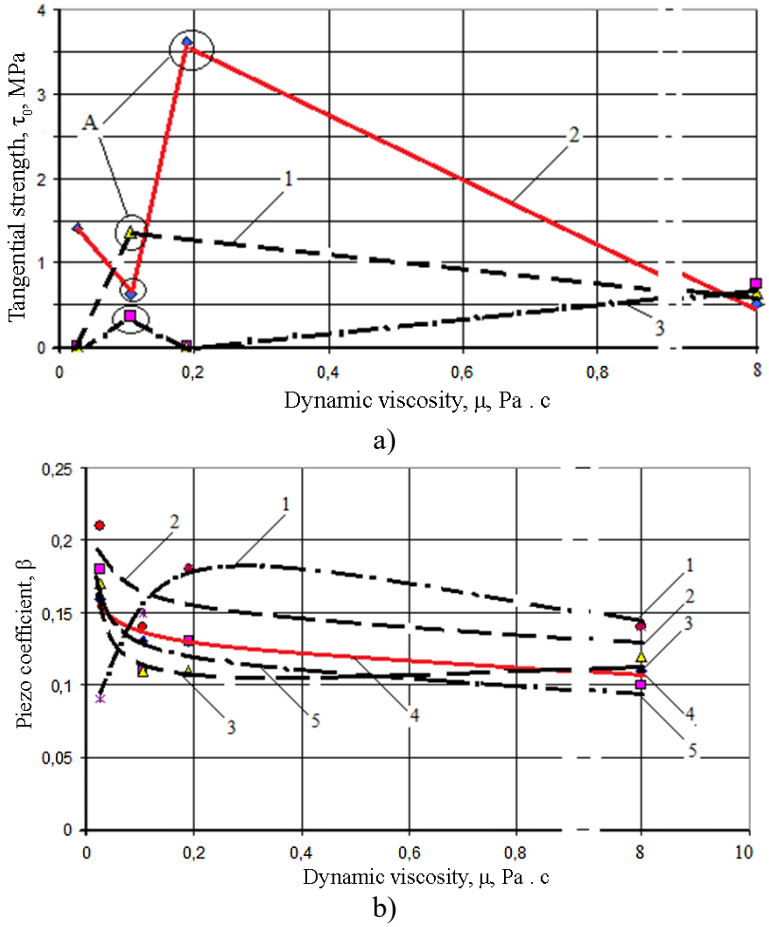

Fig.3. Dependence of the strength of the adhesive bond τ_0 (a) and the piezoelectric coefficient β (b) on the viscosity of the lubricant: 1 - system "steel 45 + BC - 40X" at $\upsilon_2 = 5.08 \pm 0.6$ mm/s; 2 (1 a) - "steel 45 + B - 40X" system at $\upsilon_2 = 5.08 \pm 0.6$ mm/s; 3 - "steel 45 + BC - 40X" system at $\upsilon_1 = 10.16 \pm 0.8$ mm/s; 4 (2 a) - "steel 45 - 40X" system at $\upsilon_1 = 10.16 \pm 0.8$ mm/s; 5 (3 a) - "steel 45 + B - 40X" system at $\upsilon_1 = 10.16 \pm 0.8$ mm/s; A - change in the mechanism of intermolecular interaction

The analysis of the obtained interpretations of the experimental data indicates the following. No clearly pronounced regularity of the influence of different-grade lubricants with increasing dynamic viscosity on the parameter τ_0 was revealed. However, the following trends are visible. First, there is a decrease in the values of the parameter τ_0 for unmodified boron steel 45 in two ranges of values of dynamic viscosity: from 0.027 to 0.106 Pa•s and from 0.19 to 8 Pa•s. At the same time, at points A, changes in the mechanisms of manifestation of intermolecular interaction are possible, depending primarily on the structure of the lubricant molecules.

Secondly, there is a decrease in the values of the parameter τ_0 for steel modified with boron at a shear rate $\upsilon_2 = 5.08 \pm 0.6$ mm/s in the range of dynamic viscosity values from 0.106 to 8 Pa•s, and at $\upsilon_1 = 10.16 \pm 0.8$ mm/s in the range of dynamic viscosity values from 0.106 to 0.19 Pa•s. In this case, in the range of dynamic viscosity values from 0 to 0.106 Pa s, the values of τ_0 increase, which also indicates the manifestation of a change in the mechanism of intermolecular interaction, which depends on the structure of the lubricant molecules. Third, for steel 45 modified with boron carbide, the values of the parameter τ_0 practically do not appear. An exception is frictional contact in the I-20A lubricant, and even then at low shear rates. For the adhesive bond parameter β, clearly expressed regularities of a decrease with an increase in dynamic viscosity are established in the entire considered range. The exception is the system "steel 45 + BC - 40X" at $\upsilon_2 = 5.08 \pm 0.6$ mm/s for which the piezoelectric coefficient increases in the range from 0 to 0.19 Pa•s, and then decreases. This also indicates the manifestation of a change in the mechanism of intermolecular interaction, which depends on the shear rate. In this case, regardless of the nature of the

modification of steel 45 (saturation with boron or boron carbide), at a higher shear rate, a tendency of a regular decrease in β values with respect to its non-modification, and an increase at lower shear rates, appeared.

Table 3. Parameters of approximation of experimental data for the system of materials "40X - steel 45 (+ B, + BC)" in the environment of lubricants

Parameter	Steel 45				Steel 45+B				Steel 45+BC			
Lubricant	I-20	TAD-17i	Wolf 10W40	Lithol-24	I-20	TAD-17i	Wolf 10W40	Lithol-24	I-20	TAD-17i	Wolf 10W40	Lithol-24
Piezo coefficient β	0.16	0.13	0.13	0.11	0.18	0.11	0.13	0.1	0.17	0.11	0.11	0.12
	-	-	-	-	0.21	0.14	0.18	0.14	0.09	0.15	0.18	0.14
Tangential strength τ_0, MPa	1.4	0.63	3.61	0.51	>0 at p≈38 MPa	0.36	0.01	0.75	>0 at p≈86 MPa	>0 at p≈24 MPa	>0 at p≈26 MPa	>0 at p≈42 MPa
	-	-	-	-	>0 at p≈20 MPa	1,36	>0 at p≈13 MPa	0.64	7.88	>0 at p≈35 MPa	>0 at p≈40 MPa	>0 at p≈18 MPa

Note. The upper row of values at a shear rate $\upsilon_1 = 10.16 \pm 0.8$ mm/s, the lower one at $\upsilon_2 = 5.08 \pm 0.6$ mm/s.

The applied application of the obtained experimental data to the "camshaft cam - valve (pusher)" friction pair indicates the following. The saturation of steel 45 with boron carbide is more significant, since this predetermines a decrease in the strength of the adhesive bond during shear at sufficiently high normal pressures $p_i > 26$ MPa, and, accordingly, the intensity of the accumulation of fatigue deformations in the near-surface layers. As a result of this contacting process, the wear of the cam material is reduced.

At the same time, the definable values of normal pressures also predetermine the requirements for the operational state of friction surfaces, on which it is necessary to avoid the formation of micro- and submicro-small contact areas that predetermine the normal pressures of the indicated values, Table 2. This behavior of the tribological system "40X - steel 45" consists in the features of its surface energy. E. Rabinovich [11] proposed the dependence of the relationship between the friction coefficient on the surface energy of solids. According to Rabinovich, the coefficient of friction f:

$$f = \frac{S}{p}\left(1 + \frac{2W_{ab}\tilde{n}tg\theta}{pr} + \cdots\right), \quad (2)$$

where S is the shear resistance of the welding bridges; p is the effective voltage on the contact; W_{ab} is the adhesive bond energy; θ is the angle of inclination of a single irregularity; r is the average radius of the touch spot.

Rabinovich noted that adhesion is especially intense, provided that the bodies have "smooth" surfaces. In this case, the surface energy has a significant effect on the value of the friction coefficient. Taking this into account, Rabinovich points out that the ratio of the adhesion energy and the effective contact stress is an important factor for the selection of friction pairs. If the given expression is large, then the conditions for sliding are bad. In the works of V.D. Kuznetsov, the friction process is considered from the energy side [12]. K. Johnson [13] defined the friction force as a combination of energy and mechanical components

$$F = F_0 + \sqrt{\frac{8}{\pi}} S^{3/2} \sqrt{\sigma E}\ , \quad (3)$$

where F_0 is an external force; σ is the specific surface energy of the material; Δs is the surface area where the force is applied; E - elastic modulus of the material.

In [14], within the framework of the thermodynamic approach for the dry friction coefficient, we obtained the following formula:

$$f = \tilde{N} \cdot \dot{O} \cdot \frac{\sigma \cdot S}{\Delta G^0} \cdot \overline{N}, \quad (4)$$

.

where σ is the specific surface energy of the material, S is the contact area, T is the temperature, ΔG^0 is the Gibbs energy, $\overline{N}$ is the average number of elementary fracture carriers (proportional to the number of defects), C is a constant.

All expressions (2) - (4) differ from each other, but with an increase in the surface energy, the friction coefficient (adhesion energy) increases. In table 4, for steels 45 and 40X, these values are indicated at a temperature close to the melting temperature Tm.

Table 4. Specific surface energy for steels 45 and 40X

Steel	T_m, K	σ, J/m^2
45	1103	0.772
40X	1143	0.800

In [15, 16], it was emphasized that when analyzing the energy picture of the surface layer, one should proceed from the assumption that approximately 25% of the total energy is accumulated in the layer. The remaining 75% of the energy is heat, which comes to the layer and leaves it according to other dependencies. However, the remaining 25% of the energy creates properties that are undoubtedly among the properties that determine the quality of the product. Roughness in combination with sub-roughness significantly affects the surface energy. The magnitude of the surface energy changes the magnitude and nature of the layer of the adsorbed zone, as well as the zone of oxides, etc. Under its influence, the boundary zone can take different positions relative to the main material of the work piece or part. The energy state of the surface layer to the greatest extent depends on the impact on it in the process of technological manufacture of the part. This effect turns out to be very strong in the course of procurement operations, when the action of deforming forces, heat, chemical process, etc. are combined. In [15, 16], as well as from formulas (2) - (4), it follows that the smaller the difference in the surface energies of mating parts made of different materials and under different technological influences, the less will be the coefficient of friction during their mutual movement, and vice versa. This is exactly what Table 4 indicates.

Conclusion

The results obtained in the work revealed the features of the manifestation of the shear strength of the adhesive bond and its piezoelectric coefficient in the studied metal systems. The established graphic patterns and parameters of their mathematical approximation made it possible to determine the direction of the processes of adhesive interaction of the surface of 45 steel modified with boron and boron carbide with 40X steel through compacted lubricating formations with distinctive gradients of dynamic viscosity. It has been established that boriding and boron cementation predetermines the expansion of the range of working normal pressures in lubricating media, excluding the manifestation of the adhesion component of friction, which leads to an increase in the reliability of the operation of friction pairs during shear. The data obtained for Wolf 10W-40 engine oil can be used in analytical calculations for predictive assessment of the effect of the adhesion friction component during the start of the DVZ in the drive of the valve groups of its gas distribution mechanism. It follows from the above formulas that the smaller the difference in the surface energies of the mating parts made of different materials and under different technological influences is, the lower the friction coefficient during their mutual movement, and vice versa.

REFERENCES

1 Kubich V.I., Cherneta O.G., Yurov V.M. Potential difference of metal machine parts methodology for determining the parameters of adhesional properties of materials on the SMC-2 friction machine. *Eurasian Physical Technical Journal*, 2019, Vol.16, No.2(32), pp. 78 – 82.

2 Denisov A.S. *Workshop on the technical operation of vehicles*. Moscow, 2012, 280 p.

3 Rodionov Yu.V., Sevostyanov A.L. *Basics of car repair*. Penza: PGUAS, 2014, 300 p.

4 Cherneta O.G., Kubich V.I., Voloshchuk R.G., Averyanov V.S., Shmatko D.Z. Strengthening of the Restored Surface Layer of Steel Parts 45 by Laser Boring. *International Journal of Engineering & Technology (UAE). Science Publishing Corporation, RAK Free Trade Zone.* Vol 7, No.4.3 (2018), pp. 71 – 75.

5 Cherneta O.G., Kubich V.I., Shcherbina M.A., Averyanov V.S., Shmatko D.Z. Research of steel 45 strugging influence on the parameters of adhesion communication with chrome, chrome-nickel steel. *Mathematical modeling. Kam'yanske. DDTU,* 2019, No. 2 (41), pp. 150-158.

6 Bykova T.M. *The influence of the chemical composition of steel on the structure and properties of diffusion boride coatings*. Dissertation for the degree of candidate of technical sciences, Yekaterinburg, 2016, 164 p.

7 Kovalsky B.I. *Methodology for monitoring and diagnostics of lubricants as elements of drive systems of multicomponent machines*. Dissertation for the degree of Doctor of Technical Sciences, Krasnoyarsk, 2005, 418 p.

8 Davidyan L.V. *Intensification of diffusion saturation with boron of carbon and alloy steels during microarc heating*. Dissertation for the degree of candidate of technical sciences, Rostov-on-Don, 2019, 128 p.

9 Kragelsky I.V., Dobychin M.N., Kombalov V.S. *Fundamentals of Friction and Wear Calculations*. Moscow, Mechanical engineering, 1977, 526 p.

10 Semenov V.I., Shuster L.Sh., Chertovskikh S.V., et al. Influence of the complex parameter of plastic frictional contact and material structure on the strength of adhesive bonds. *Friction and wear*, 2005. Vol. 26, No.1, pp. 74 – 79.

11 Rabinowcz E. Surface Energy Approach to Friction and Wear. *Product Engineering*, 1965, Vol. 36, No 6, pp.95 – 99.

12 Kuznetsov V.D. *Physics of cutting and friction of metals and crystals. Selected Works*. Moscow, 1977, 310 p.

13 Johnson K. *Mechanics of Contact Interaction*. Moscow, Mir, 1989, 510 p.

14 Kubich V.I., Guchenko S.A., Yurov V.M., Zavatskaya O.N. On the coefficient of friction of high-entropy seven-atom alloys. *11th International Scientific. conference. "Chaos and structures in nonlinear systems. Theory and experiment", Karaganda*, 2019, pp. 114 – 118.

15 Musokhranov M.V., Kalmykov V.V., Malyshev E.N., Zenkin N.V. The energy of the surface layer of metals as a tool for influencing the value of the friction coefficient. *Fundamental research*, 2015, No. 2, pp. 251 – 254.

16 Musokhranov M.V., Kalmykov V.V., Logutenkova E.V., Sorokin S.P. Energy state of the surface layer of machine parts. *Modern high technology*, 2016, No. 5, pp. 276 – 279.

Article accepted for publication 23.04.2021

.

DOI 10.31489/2021No2/76-80

UDC 678.072:536.468

COMPARATIVE STUDY OF THE EFFECT OF FLAME RETARDANTS ON THE IGNITION TEMPERATURE OF EPOXY COMPOSITES

Amelkovich Yu.A., Nazarenko O.B., Smirnova I.N., Zadorozhnaya T.A.

National Research Tomsk Polytechnic University, Tomsk, Russia, olganaz@tpu.ru

The disadvantage of polymeric materials, including epoxy resins, is their increased fire hazard. Reducing the flammability of polymeric materials is a serious problem that needs to be addressed. One of the ways to reduce the flammability of polymers is the introduction of special additives into the polymer matrix with flame retarding properties, which leads to a change in the nature of the processes occurring during the combustion of the polymer, or to blocking the combustion process with non-combustible or inhibiting substances. In this work, aluminum trihydroxide, melamine polyphosphate, and melamine poly(magnesium phosphate) were used as flame retardants to enhance the flame-resistant properties of epoxy resin. The filler loading in the epoxy composites was 10 wt. %. The experimental studies have been carried out to determine the ignition temperature of the produced epoxy composites. The data obtained were compared with the ignition temperature of a control sample of epoxy resin without filler. The results indicated that the incorporation of all the flame retardants studied resulted in an increase in the ignition temperature. The ignition temperature of the samples filled with melamine polyphosphate and melamine poly(magnesium phosphate) increased by 28 and 11 °C, respectively. However, the best result was obtained for a sample filled with aluminum trihydroxide: the ignition temperature of this sample was 40 °C higher than that of the unfilled epoxy resin.

Keywords: epoxy resin, composite, flame retardant, ignition temperature.

Introduction

Epoxy resins are multipurpose oligomeric materials used for the production of compounds, composites, as well as for pouring various surfaces and making glue and sealant. Due to the unique combination of useful properties, epoxy resins are widely used in various areas of the national economy. From the whole variety of epoxy resins, an epoxy resin of ED-20 type stands out as an inexpensive, high-quality product. Epoxy resin ED-20 possesses such properties as high density, excellent hardness, good resistance to mechanical damage and moisture, heat resistance, dielectric and anti-corrosion ability, good adhesion to plastic, metal, glass, ceramics, wood, and many other materials, ease of use, low shrinkage. However, the flammability of epoxy resin, as well as most polymeric materials, is a disadvantage that limits the widespread use of polymeric materials in various industries and in everyday life [1]. The increase in the number of fires and material damage can be correlated with the increase in the consumption of polymer materials. Reducing the flammability and fire hazard of polymeric materials is one of the most important tasks, on the solution of which the further development of many sectors of the national economy depends. This task can be facilitated by the introduction of additives with flame retardant properties [2–5]. Such fillers can lead to a change in the nature of the polymer degradation process when heating or blocking the combustion process with non-combustible or inhibiting substances. Besides, the fillers also improve the physical, mechanical, and other functional properties of polymeric materials; their use contributes to reduce the consumption of valuable and often scarce raw materials. Therefore, this direction seems to be attractive from the point of view of the economics of the production of polymer material.

A large group of substances used as flame retardants is substances that upon heating endothermically decompose to form non-flammable products. One of such substances having flame retardant properties is boric acid. At the heating, boric acid releases water in the endothermic process that reduces polymer temperature and degradation. Also, nonflammable boron oxide forms on the polymer surface, which has a barrier effect and protects the polymer from flame action [6, 7]. Aluminum trihydroxide (ATH) also belongs to the group of substances that have flame retardant properties due to endothermic decomposition upon heating [8–10]. It is known that the use of ATH is effective for reducing the flammability of the polymers, as a rule, when introduced in high concentrations of ~ 50 wt. % and more, which contributes to the deterioration

of physical, mechanical, technological, and operational properties, as well as to an increase in the cost of the material [11]. The new generation of flame retardants with excellent flame retardant properties includes melamine polyphosphate (MPP) and melamine poly(magnesium phosphate) (MPMgP) [12–16]. MPP combines the advantages of phosphorus and melamine based flame retardants and is widely used in various polymers to stimulate char formation. An important advantage of MPP is that it is environmentally friendly. It does not contain halogens, which are harmful to the environment.

The aim of this work was a comparative study of the effect of aluminum trihydroxide, melamine polyphosphate, and melamine polyphosphate magnesium on the ignition temperature of the epoxy composites based on epoxy resin ED-20.

1. Experimental part

1.1 Sample preparation

To obtain epoxy composites, we used epoxy resin of grade ED-20 and polyethylene polyamine (PEPA) as a hardener. The concentration of PEPA in the samples was 12 wt. %. Aluminum trihydroxide (ATH), melamine polyphosphate (MPP), and melamine poly(magnesium phosphate) (MPMgP) were used as fillers. The concentration of the fillers in the compositions was 10 wt. %. The resulting mixtures were poured into silicone molds and cured at room temperature for 24 h. For the experiment, five samples having a mass of 3 g of unfilled cured epoxy resin (E0) were prepared, as well as five samples for each type of filler. The samples had a cylindrical shape with the following dimensions: diameter 45 mm, height 2 mm. The images of the filled epoxy composites are shown in Fig. 1.

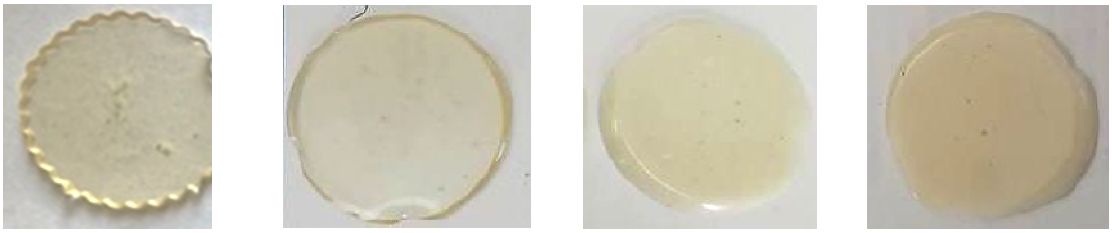

a) b) c) d)

Fig.1. Samples of epoxy composites: a) E0, b) E/ATH, c) E/MPP, d) E/MPP-Mg

1.2 Characterization

The thermogravimetric analysis (TGA) of the unfilled epoxy polymer was made using STA 449C Jupiter thermal analyzer (Netzsch). TGA curves were measured from 25 °C to 900 °C at a rate of heating 10 °C/min under air atmosphere. Test method for determining ignition temperature of the epoxy composites was carried out according to the Russian regulatory document GOST 12.1.044-2018 “Occupational safety standards system. Fire and explosion hazard of substances and materials. Nomenclature of indices and methods of their determination”. The experimental method for determining the ignition temperature consists in heating the substance, at which the evolved gases are ignited, after which the presence of ignition is recorded at a set temperature. The tests were carried out on an installation for determining the ignition temperature and autoignition temperature of solids and materials at a constant temperature of the reaction furnace (Fig. 2).

The principle of operation of the installation is based on setting a constant temperature regime in a reaction furnace (400 °C) and exposure to a burner flame. After introducing the test samples into the reaction furnace, the temperature indicators were monitored. To calculate the ignition temperature of the investigated substance, the arithmetic mean of two temperatures differing by no more than 10 °C was taken.

2. Results and discussion

The results of thermal analysis obtained for the unfilled epoxy sample E0 are shown in Fig. 3. Thermo-oxidative degradation of the epoxy resin was studied using the thermogravimetric method (TG), differential thermogravimetry (DTG), and differential scanning calorimetry (DSC).The initial temperature of degradation of the sample E0 at which the mass loss is 5% was found to be 266 °C. Thermo-oxidative degradation of the epoxy polymer occurs in three stages.

.

Fig.2. Installation for determining the ignition temperature

Three exothermic peaks on the DSC curve are caused by the following processes: homolytic scission of chemical bonds, the depolymerization of polymeric chains followed by a primary carbonaceous char formation, and the oxidation of formed carbonaceous char [17, 18]. The values of the maximum temperature at the first, second, and third peaks for the sample E0 were 285, 428, and 522 °C, respectively. The thermo-oxidative degradation of the unfilled epoxy polymer was finished at ~600 °C.

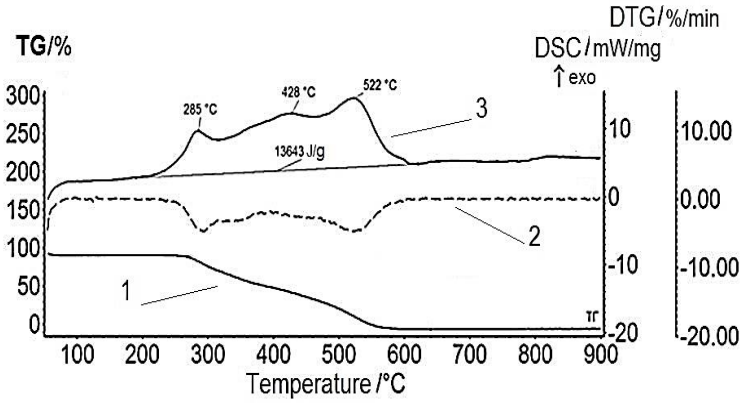

Fig.3. TG (1), DTG (2) and DSC (3) curves of the unfilled epoxy polymer

One of the characteristics of the flammability of materials is ignition temperature. Ignition temperature means the lowest temperature of a substance at which, under the conditions of special tests, a substance emits flammable vapors and gases at such a rate that, when exposed to an ignition source, ignition is observed. The value of the ignition temperature of the test sample must be known to develop measures to ensure fire safety, as well as to determine the degree of flammability of substances. The results of the testing for the ignition temperature of epoxy composites are presented in Table 1. Fig. 4 shows the remains of the materials obtained during testing.

According to the results obtained, the ignition temperature of the control sample E0 was 307 °C. The maximum ignition was obtained for the sample E/ATH and it was 40 °C higher than that of the control sample E0. When heated, ATH decomposes in the endothermic reaction with the release of water and the formation of non-combustible aluminum oxide [8–10]:

$$2Al(OH)_3 \rightarrow Al_2O_3 + 3H_2O,\ \Delta H = 298\ kJ/mol.$$

Thus, the introduction of ATH into the polymer promotes heat removal and dilution of the formed combustible gases during heating and combustion of the polymer. Additionally, the layer of aluminum oxide on the polymer surface provides a physical barrier and prevents the polymer from the action of the flame. The ignition temperature for the samples E/MPP and E/MPMgP was higher by 28 °C and 11 °C,

correspondingly, in comparison with that of the sample E0. The residue after the test was the largest for the samples E/ATH and E/MPP. The sample E/MPMgP burned out almost completely.

Table 1. Ignition temperature of epoxy composites.

Sample	T_{ig}, °C
E0	307
E/ATH	347
E/MPP	335
E/MPP-Mg	318

MPP decomposes endothermically above 350 °C, acting as a heat sink and cooling the combustion zone of the polymer. The released phosphoric acid additionally reacts with the polymer to form carbonaceous char, preventing oxidation of the combustible polymer surface [12, 13]. At the same time, the formation of nitrogen during the decomposition of melamine intensifies the formation of a char layer for additional protection of the polymer.

a) b) c)

Fig.4. Samples of epoxy composites after testing for ignition temperature:
a) E/ATH, b) E/MPP, c) E/MPP-Mg

The results obtained can be explained by the thermal stability of the unfilled epoxy polymer and used in this study flame retardants. It is known that at the heating ATH begins to decompose at the temperature 190 °C with maximum release of water at 350 °C [10], while according to the results of thermal analysis, the initial temperature of degradation of the unfilled epoxy polymer is 266 °C. When the epoxy polymer filled with ATH is heated, ATH decomposes endothermically in aluminum oxide and water, absorbing heat. Additionally, the water formed in this process dilutes the concentration of other gaseous decomposition products and lowers the flame temperature. Upon further heating, solid residues are formed, creating a barrier against oxygen and heat. The MPP starts to degrade at 350 °C, the temperature of 5 wt. % mass loss for MPP is 383 °C and for MPMgP is 368 °C [13, 14]. When the epoxy polymer is heated to such values of temperature, the epoxy polymer loses 52 and 49 % by weight, respectively. The contribution of the flame retardants MPP and MPMgP to the flame suppression process begins at a later stage in comparison with the epoxy polymer filled with ATH.

The obtained results can be compared with the result for determining the ignition temperature of epoxy composites filled with boric acid (10 wt. %) and the composition of boric acid (10 wt. %) and iron nanopowder (5 wt. %) [19]. The ignition temperature was found to be increased to 317 °C for the sample filled with boric acid and 322 °C for the sample filled with boric acid in combination with iron nanopowder.

It should be noted that these conclusions relate to the epoxy resin of the ED-20 type investigated in this work. Thus, among the studied flame retardants, the use of ATH leads to the greatest increase in the ignition temperature and can be recommended for the development of polymer composite materials based on the epoxy resin ED-20.

Conclusions

In this work, the epoxy composites were prepared by incorporation of three kinds of flame retardants in the epoxy matrix: aluminum trihydroxide, melamine polyphosphate, and melamine poly(magnesium phosphate). The concentration of each flame retardant in the epoxy resin was 10 wt. %. The test for

.

determining the ignition temperature of the epoxy composites and unfilled epoxy resin was carried out according to Russian regulatory document GOST 12.1.044-2018. Among the studied flame retardants, when they were introduced into the epoxy resin to reduce flammability, aluminum trihydroxide showed the best results: the ignition temperature was 40 °C higher than that of the unfilled epoxy resin ED-20. The use of melamine polyphosphate and melamine poly(magnesium phosphate) as a flame retardant for other types of epoxy resins requires clarification and more detailed studies, in particular, using thermal analysis. In our future work, we will study the effect of aluminum trihydroxide on the characteristics of the flammability of epoxy polymers in combination with nanodispersed fillers – metal nanoparticles. The results of this study can be applied to study and develop polymer materials with reduced flammability.

Acknowledgments

This research was supported by Tomsk Polytechnic University development program.

REFERENCES

1 Jin F.-L., Li X., Park S.-J. Synthesis and application of epoxy resins: A review. *J. Ind. Eng. Chem*., 2015, Vol. 29, pp. 1–11

2 Laoutid F., Bonnaud L., Alexandre M., Lopez-Cuesta J.M., Dubois P. New prospects in flame retardant polymer materials: from fundamentals to nanocomposites. *Mater. Sci. Eng. R*, 2009, Vol. 63, p. 100–125

3 Camino G., Costa L. Performance and mechanisms of fire retardants in polymers – a review. *Polym. Degradat. Stabil*., 1988. Vol. 20, p. 271–294

4 Morgan A.B., Gilman J.W. An overview of flame retardancy of polymeric materials: Application, technology, and future directions. *Fire Mater*., 2013, Vol. 37, p. 259–279

5 He W., Song P., Yu B., Fang Z., Wang H. Flame retardant polymeric nanocomposites through the combination of nanomaterials and conventional flame retardants. *Prog. Mater. Sci*., 2020, Vol. 114, pp.100687

6 Visakh P.M., Nazarenko O.B., Amelkovich Y.A., Melnikova T.V. Effect of zeolite and boric acid on epoxy-based composites.*Polym. Adv. Technol*. 2016, Vol. 27, pp. 1098 – 1101.

7 Balci S., Sezgi N.A., Eren E. Boron oxide production kinetics using boric acid as raw material. *Ind. Eng. Chem. Res*. 2012, Vol. 51, Iss. 34, pp. 11091–11096.

8 Witkowski A., Stec A.A., Hull T.R. The influence of metal hydroxide fire retardants and nanoclay on the thermal decomposition of EVA. *Polym. Degrad. Stab*., 2012, Vol. 97, pp. 2231 – 2240.

9 Unlu S.M., Dogan S.D., Dogan M. Comparative study of boron compounds and aluminium trihydroxide as flame retardant additives in epoxy resin. *Polym.Advan. Technol*., 2014, Vol. 25, pp. 769–76.

10 Frańczak A., Oleksy M., Oliwa R., Budzik G. Polyethylene composites flame retarded with aluminum hydroxide as coatings for electrical cables. *Polymery*, 2018, Vol. 63(6), p. 458–461.

11 Wypych G. Fillers – *Origin, chemical composition, properties, and morphology.* In: Handbook of Fillers. Ed.: G. Wypych. Toronto: ChemTec Publishing. 2016, pp. 13 – 266.

12 Chen W.Y., Wang Y.Z., Chang F.C. Thermal and flame retardation properties of melamine phosphate-modified epoxy resins. *J Polym Res*., 2004, Vol. 11, pp. 109 –117.

13 Müller P., Schartel B. Melamine poly(metal phosphates) as flame retardant in epoxy resin: Performance, modes of action, and synergy. *J. Appl. Polym. Sci*., 2016, pp. 43549.

14 Lubczak J.M., Lubczak R. Melamine polyphosphate – the reactive and additive flame retardant for polyurethane foams. *Acta Chim Slov*., 2016, Vol. 63, pp. 77 – 87.

15 Liu S.-H., Kuan C.-F., Kuan H.-C., Shen M.-Y., Yang J.-M., Chiang C.-L. Preparation and flame retardance of polyurethane composites containing microencapsulated melamine polyphosphate. *Polymers*, 2017, Vol. 9, pp. 407.

16 Ma X., Meng X., Li Z., Xiao Q., Wang Z., Yan K. Study of the influence of melamine polyphosphate and aluminum hydroxide on the flame propagation and explosion overpressure of aluminum magnesium alloy dust. *J. Loss Prev. Process Ind.*, 2020, Vol. 68, pp.104291

17 Bellenger V., FontaineмE., FleishmannA., SaporitoJ., Verdu J. Thermogravimetric study of amine cross-linked epoxies. *Polym. Degrad. Stab*. 1984, Vol. 9, pp. 195 – 208.

18 Kandola B.K., Biswas B., Price D., Horrocks A.R. Studies on the effect of different levels of toughener and flame retardants on thermal stability of epoxy resin. *Polym. Degrad. Stab*., 2010, Vol. 95, pp. 144–152

19 Nazarenko O., Lipchansky D., Smirnova I. Effect of iron nanopowder on flammability of epoxy composites. *IOP Conf. Ser.: Mater. Sci. Eng*., 2020, Vol. 1019, pp. 012001.

Article accepted for publication 21.05.2021

DOI 10.31489/2021No2/81-89

UDC 521.1

SCALE-INVARIANT AND WAVE NATURE OF THE HUBBLE PARAMETER

Zhanabaev Z.Zh., Ussipov N.M.*, Khokhlov S.A.

Al-Farabi Kazakh National University, Almaty, Kazakhstan, ussipov.nurzhan@kaznu.kz

The value of the global Hubble parameter corresponding to astrophysical observations was determined theoretically without using ΛCDM models. A nonlinear fractal model of the connection between the distance to the observed galaxy and its coordinate is proposed. Distance is defined as a fractal measure, the measurement scale of which, in contrast to the known fractal models, corresponds to the deviation of the desired measure itself from its fixed value (radius of zero gravity), relative to which the scale invariance is assumed. We used the dimension of our proposed specific anisotropic fractal, which simulates the increase in the distance to the observation point. It is shown that this dimension is also the maximum dimension of the strange attractor of the phase portrait of the equation of gravitational waves and sets of galaxies from different catalogs.

Keywords: Hubble parameter, gravitational waves, fractal dimension, expansion of the universe.

Introduction

The works [1-3] present the results of determining the rate of expansion of the universe. At distances of at least 3 million light-years (Mpc), galaxies can separate at a speedof 68 – 73 km/s. The discrepancy between the results and their average is about 4%.

To describe the observed regularity, the expansion of the universe along with ΛCDM model, the cosmological constant Λ is added to the Einstein gravitational field equation, the need to comprehend which led to the unclear concept of dark energy. Recently, modified theories of gravity have been put forward as an alternative to the dark energy hypothesis [4]. These theories are aimed at finding more complex combinations of multidimensional space curvature invariants. It is expected that the modified theory of gravity may be applicable to high energy physics problems. However, the presence of higher derivatives with new additional parameters leads to new problems in the quantitative description of the observation results. Multidimensionality, the need for additional measurements are indicated in contemporary studies on the studied issue. One of the possibilities to take into account additional dimensions is to take into account the fractional dimension of fractal objects, which are scale-invariant and self-similar in structure.

In works [5-7], an alternative possibility to ΛCDM model called the Scale Invariant Vacuum (SIV) theory, where the cosmological constant is multiplicatively related to the theoretically introduced coefficient of scale invariance of space, is developed. Several tests of the SIV results were carried out with cosmological observations of the Hubble parameter, redshift, and its connection with temperature. Good agreement between the results of theory and observations was obtained. It is concluded that observational facts can be described without using hypotheses about dark energy and dark matter.

The scale invariance of geometric objects manifests itself in the form of fractal structures: a small part repeats the shape of the whole. Since the works of B. Mandelbrot, the theory of fractals has been widely used in astrophysics. However, the inconsistency of the theory with some observational facts, for example, with spectral laws, makes it necessary to use “new types of fractals” [8]. We will consider the possibilities of using new models of fractal sets: describing the formation of pre-fractals in only one direction and a nonlinear fractal measure (distance to galaxies), the measurement scale of which depends on the measure itself.

The aim of this work is to determine the value of its fractal dimensions from the attractor obtained from the equation of weak gravitational waves and use them in the equation for the distance to galaxies to determine the global value of the Hubble parameter without using the cosmological constant and to compare the results of theory with observations.

.

1. Scale invariance of the attractor of signals of gravitational waves

Einstein's equations for the gravitational field have the form

$$R_{ij} = 8\pi G\left(T_{ij} - \frac{1}{2}g_{ij}T\right), \tag{1}$$

where $R_{ij}$is the space curvature tensor (Ricci tensor), $T_{ij}$is the energy-momentum tensor,g_{ij} is the metric tensor,G is the gravitational constant, and the speed of light $c = 1$ is taken.

Let us assume that inhomogeneities in the distribution of matter cause inhomogeneities in the geometry of space. Then, in a synchronous frame of reference, the elements of the Galilean metric tensor with small perturbations $\left|h_{\alpha\beta}(R,t)\right| \ll 1$ can be written in the form [8, 9]:

$$g_{00} = 1,\ \ g_{0\alpha} = 0,\ \ \ g_{\alpha\beta} = -a^2(t)\left[\delta_{\alpha\beta} - h_{\alpha\beta}(R,t)\right], \tag{2}$$

where $a(t)$is the scale factor of the expansion of the universe, $h_{\alpha\beta}(R,t)$are linear perturbations of the curvature of space, and $\alpha, \beta$are the components of the spatial variable X.

Taking into account conditions (2) from equation (1) in [8] the equation of gravitational waves is obtained

$$a^{-2}\nabla^2 h_{\alpha\beta} = \ddot{h}_{\alpha\beta} + 3\left(\frac{\dot{a}}{a}\right)\dot{h}_{\alpha\beta}, \tag{3}$$

where ∇ are spatial derivatives, a dot means time derivative.

For the Fourier components with a spatial wavenumber k associated with the length of the transverse gravitational waves $\lambda = 2\pi a(t)/k$, we have the equation for the perturbations of single polarization $h(t)$:

$$\frac{d^2h(R,t)}{dt^2} + 3\left(\frac{\dot{a}}{a}\right)\frac{dh(R,t)}{dt} + \left(\frac{k}{a}\right)^2 h(R,t) = 0. \tag{4}$$

The last term in (4) has the dimension 1 / m^2, and the first two - 1 / s^2, because it was assumed that the speed of light is equal to unity. Let us come in (4) to the spatial derivatives by R: $\frac{\partial}{\partial t} \to v_0\frac{\partial}{\partial R}$, it is assumed that $v_0 = 1$ is the velocity of gravitational waves in a medium with cosmic perturbations of the density of fields and matter:

$$\ddot{h} + 3\left(\frac{\dot{a}}{a}\right)\dot{h} + \left(\frac{k}{a}\right)^2 h = 0, \tag{5}$$

where dots denote derivatives to the coordinate$R$.

The derivation of equation (5) is given in [8]. The choice of this form from the set of equations of gravitational waves [9] can be justified only within the framework of the same used approximations, neglecting the square of small quantities. Equation (5) describes the wave process of change $h(R)$at a fixed time. By definition $\frac{k}{a} = \frac{2\pi}{\lambda}$ is the ratio of the wavenumber to the scale factor. To clarify the meaning of$3\frac{\dot{a}}{a}$,we assume that the mass of matter$M$ with its densityρ, with the scale factor of expansion of the volume$a$, and also with perturbations$d\rho, da$are related as

$$\frac{3}{4\pi}M = \rho a^3,\ \ \frac{3}{4\pi}M = (\rho - d\rho)(a + da)^3. \tag{6}$$

Dividing these equations term by term, neglecting the squares and cubes of small quantities$d\rho,\ da$, through the derivatives$\dot{\rho} = d\rho/dR$,$\dot{\rho} = d\rho/dR$, we obtain

$$-\frac{\dot{\rho}}{\rho} = 3\frac{\dot{a}}{a}. \tag{7}$$

For $\frac{\dot{\rho}}{\rho} > 0$, we have damped oscillations; for$\frac{\dot{\rho}}{\rho} < 0$ Eq. (5) describes undamped oscillations in R.

Let us introduce the Hubble parameter $H = \dot{a}/a$as a dynamic characteristic of the problem and write equation (5) in the form of a system convenient for numerical analysis:

$$\dot{h} = b, \quad \dot{a} = Ha \quad \dot{b} = -3Hb - \left(\frac{a}{R_*}\right)^2 h, \tag{8}$$

In contrast to equation (5), in the system of equations (8) the wavenumber k is represented through a physical characteristic, the radius of zero gravityR_*, since gravitational waves with a characteristic length $\lambda = 2\pi(R_*/a)$ can be realized in clusters of galaxies:

$$\frac{k}{a} = \frac{2\pi a}{\lambda a} = \frac{a}{R_*} \tag{9}$$

Various valueR_* estimatesare accepted. More generally, R_*values can be taken as the Lagrange points of interacting stars. On the scale of galaxies, zero-gravity points lead to fluctuations in the motion of galaxies. Before the establishment of global expansion in distance, both the repulsion and the attraction of galaxies take place, which is observed as fluctuations and instability of their coordinates. The transition to global expansion can be considered as a result of large-scale fluctuations in the form of a phase transition [10]. The stability of the Lagrange points of gravitating systems is analyzed in contemporary studies [11]. Due to the scale invariance of the studied phenomenon, regularities will be established for$R_* = 1$, the values$R_* > 1$ are needed to analyze the role of many galaxies with different R_*.

For short waves ($\frac{\lambda}{R_*} \sim \frac{a}{kR_*} \ll 1$), from (5) a solution for $h(R)$follows in the form of harmonic functions. The shape of long waves is affected by the inhomogeneity of the cosmic background (fluctuations in the density of matter, radiation).As an example the results of a numerical analysis of the system (8) with the initial values $h_0 = 0.01;\ b_0 = 0.01;\ a_0 = 1.01$ and parameters $R_* = 10, H = 10$ are shown in Figure 1.

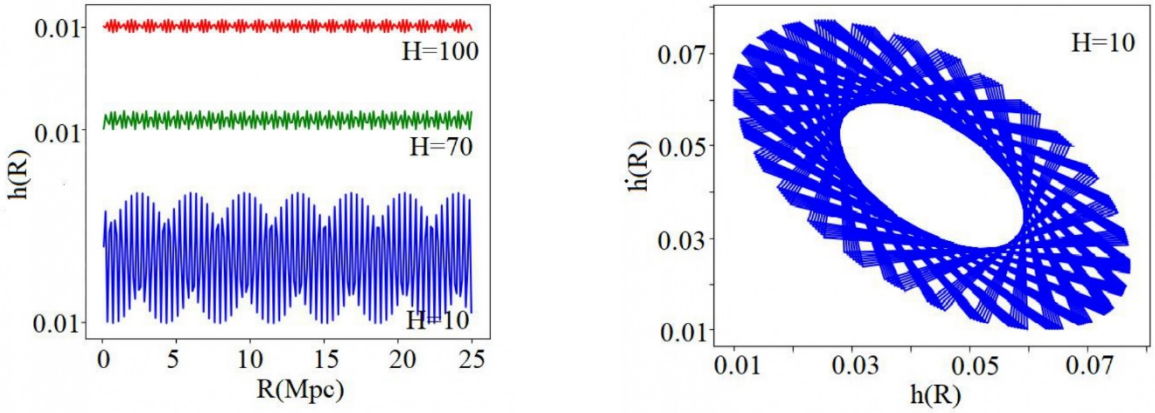

a) b)

Fig.1. Gravitational-wave shapes (a), and its basic portrait (b).

The values $h(R)$ decrease with increasing H and the oscillations become structured chaotic.Dynamical system (8) has phase portraits $\left(h(R), \dot{h}(R)\right)$in the form of fractal sets for different values of the parameter$H$. The correlation dimensions of attractors Dwere determined by the expression

$$D = \lim_{\delta \to 0} \frac{\log C(\delta)}{\log \delta}, \quad C(\delta) = \lim_{N \to \infty} \frac{1}{N^2} \sum_{i=1}^{N} \sum_{j \neq i}^{N} \theta\left(\delta - \left[x_i - x_j\right]\right), \tag{10}$$

where $\delta$is the measurement scale,$C(\delta)$ is the correlation integral,N is the number of points in the set, $\left[x_i - x_j\right]$is the distance between two pairs of points $(i \neq j)$, $\theta(f)$is the Heaviside function.

As the values δincrease, $C(\delta)$ saturate, the corresponding maximum valueD_* is observed in the interval $50 \leq H \leq 75$(Fig. 2).

.

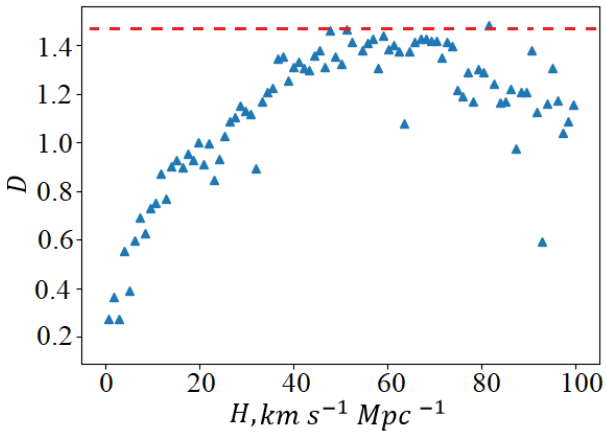

Fig.2. Possibility of maximum fractal dimension of a strange attractor of a dynamical system (8).

According to the theory, we found the value of H divided by the background velocity$v_0 = 1\ kms^{-1}$. The absolute value of the Hubble parameter$H$ is in $kms^{-1}Mpc^{-1}$units. The exact value of the maximum $D = D_* = 1.465$ corresponds to the theoretical model of the original fractal and the analysis of galaxy catalogs, which are given in Section 4.

2. Fractal dimension of the sets of expanding galaxies

There is a geometric model of a fractal with a value$\gamma_* = D - d = 0.465$, where$d$ is the topological dimension, $D$is the fractal dimension. This fractal (Fig. 3), called anisotropic, was proposed by one of the authors of this work to describe turbulence in the boundary layer and to create an information-efficient fractal antenna [12, 13]. Each pre-fractal (hierarchical levels of order n) has 5 links with a relative length of 1/3. The vertical links are not pre-fractals of the next order.

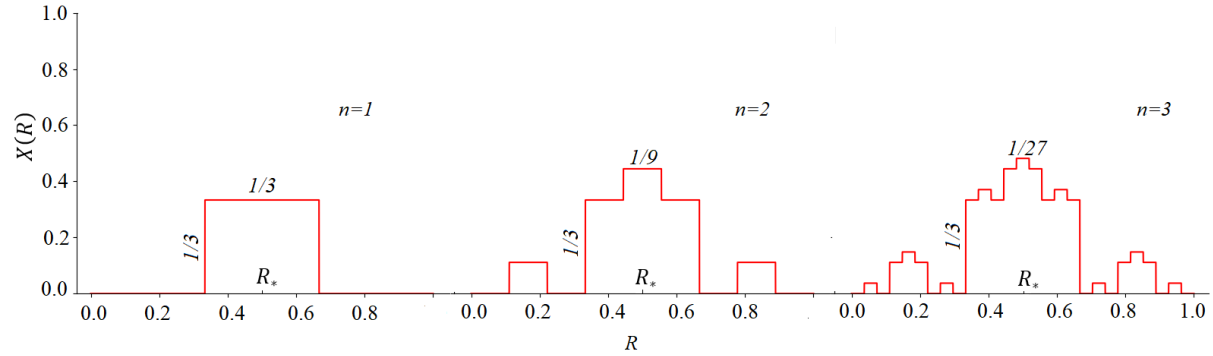

Fig.3. Anisotropic fractal with pre-fractals of order $n = 1, 2, 3$.

The Hausdorff local dimension of all pre-fractals is of order n of an anisotropic fractal$D = D_* = \ln N / \ln(1/\delta) = \ln 5 / \ln 3 = 1.465$, where N is the number of links,δ is the dimensionless measurement scale. Other fractals are known [14] with the same dimension$D$, which does not depend on the direction of formation of pre-fractals, but their topology does not reflect the specifics of the one-sided wave expansion of galaxies. The point is that the dimension D of the set of hierarchies of an anisotropic fractal manifests itself only in one direction (Fig. 3). For astrophysical applications, it can be denoted through a R coordinate, through $X(R)$ – the distance to the galaxy.

3. Nonlinear geometric model of the expansion of the universe

Since the works of B. Mandelbrot, the theory of fractals has been used to describe the structure of the universe on a large scale. However, for a more detailed adequate description of cosmological observations, new concepts of fractal geometry are needed.The well-known theories of fractals imply an independent choice of the scale of measurement of a measure (additive geometric, physical quantity) from the value of

the measure itself. Near critical values, for example, at$R \approx R_*$the measure varies greatly, it is necessary to take into account the indicated dependence. Using the Hausdorff expression, we define the fractal length $X(R,\gamma)$in the form

$$X(R,\gamma) = R\left(\frac{\Delta X(R,\gamma)}{R_*}\right)^d \cdot \left(\frac{\Delta X(R,\gamma)}{R_*}\right)^{-D} = R\left(\left|1 - \frac{X(R,\gamma)}{R_*}\right|\right)^{-\gamma}, \quad (11)$$

where $\Delta X(R,\gamma) = |X(R,\gamma) - R_*|, \gamma = D - d$

The Eq. (11) must be analyzed taking into account the fractality of the desired length$X(R,\gamma)$, which is possible through discrete iteration over pointswith step i as a display:

$$X_{i+1}(R,\gamma) = R\left(\left|1 - \frac{X_i(R,\gamma)}{R_*}\right|\right)^{-\gamma} \quad (12)$$

The value of the index$i+1$ in the notation of a continuous function $X_{i+1}(R,\gamma)$corresponds to the steady-state of the display sequence (12), regardless of the initial conditions. In terms of the cosmological equation[8] $X_{i+1}(R,\gamma)$determines the possible distance to the galaxy with the coordinate$R$, the right side of Eq. (12) is the scale factor $a(t)$multiplied by Rdepending on the coordinateX_i. In what follows, we will use the notation $X(R,\gamma)$omitting the index$i+1$. Changing the measure of space depends on itself. With an increase in the parameterγ, the values $X(R,\gamma)$become chaotic near $R \approx R_*$(Fig. 4).

The results of iterating over the values$X(R,\gamma)$ in points will differ from the results of standard computer methods, where segment iteration is used. For clarity, Fig. 4 shows curves with a large step$\Delta R = 10^{-1}$. When decreasingΔR to 10^{-3}, the smoothed character of curve 3, obtained using the Scipy package, in comparison with curve 2, remains at the same number of samples.

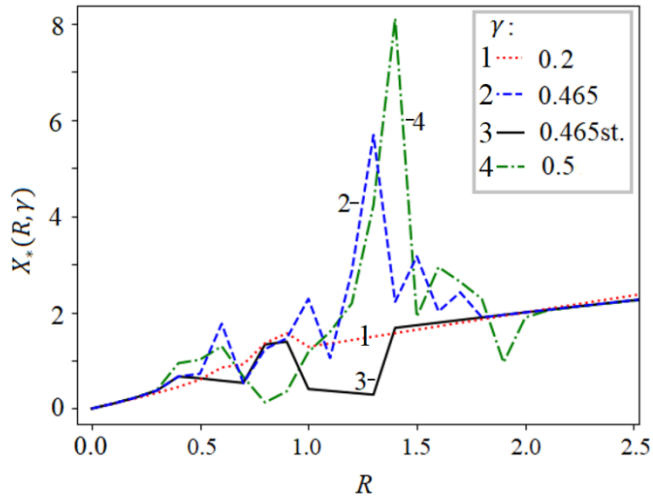

Fig.4. Chaotization of values $X(R,\gamma)$with an increase in the scaling index γat$R_* = 1$.
The number of display iterations (12) equals 10^3.

If relative values of variables$X/R_*R/R_*$ are used in Eq. (12), the form of the equation does not change. Therefore, according to the definition of the Hubble parameter H for$R_* = 1$, we have:

$$H = \frac{1}{X(R,\gamma)}\,(\Delta X(R,\gamma))/\Delta R), \quad (13)$$

where $\Delta X/\ \Delta R$is the rate of removal of galaxies, along the coordinate $R\ \Delta X = X_{i+1} - X_i$, ΔR- coordinate change corresponding toΔX. Let us take the minimum value ΔRequalσ_X - the standard deviation of $X(R,\gamma)$.

A stable value $\sigma_X = \sigma_* = 0.0149$ at$\gamma < \gamma_*$, but γ_* corresponds to the global expansion of the universe. Close values to σ_* are also observed for some forms of singular generalized functions (like δ - the Dirac function) when analyzing their behavior by an iterative method near the point of a burst (“explosion”).

.

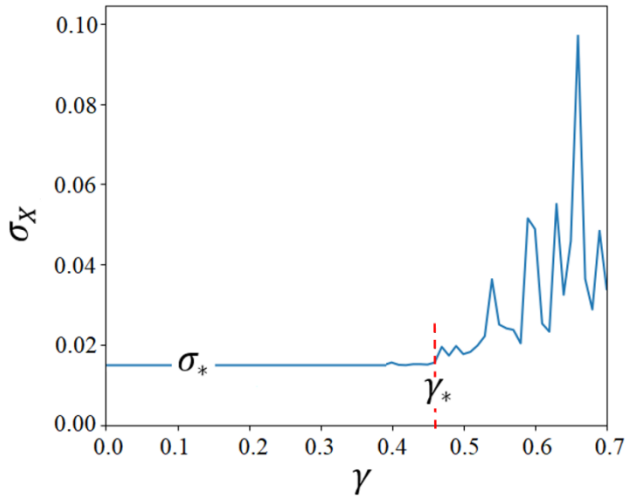

Fig.5. Change in standard deviation $X(R,\gamma)$by γaccording to Eq. (12). $\sigma_* = 0.0149, \gamma_* = 0.465$ (by Figures 2, 3, and subsequent 6, 8).

It should be taken into account that the generalized functions expressed in terms of harmonic functions give a value of $\sigma_x \sim 0.18$ due to the well-known Gibbs phenomenon, which occurs when a jump function is approximated by a Fourier series. Possibilities of decreasing $\sigma_x$in these cases are considered in contemporary studies [15]. Close values to σ_* are observed for examples in the form of a power-law generalized function since the nonlinear fractal measure $X(R,\gamma)$contains a degreeγ. For example, for the function$f(x) = \frac{M}{\sqrt{\pi}} e^{-(nx)^2}$, iterative analysis at $M \to \infty$ in a change range n corresponding to the randomization of the value $x$with a positive Lyapunov exponent gives the result$\sigma_x = 0.018$.

The accuracy of determining the coordinates of galaxies$R$ and the parameter$H$ are interdependent. The root-mean-square deviations σ_R, $\sigma_H$can be estimated from the condition of violation of the coherence of the chaotic characteristics of the gravitational wave near$R \approx R_*$:

$$\Delta\lambda\, \Delta k \geq 2\pi, \tag{14}$$

where $\Delta\lambda, \Delta k$are the moduli of wavelengthλ and wavenumber fluctuations$k$. Wavelength fluctuations are proportional to changes in the geometric characteristics – coordinates$R$: $\Delta\lambda \sim \Delta R$Wavenumber fluctuations are inversely proportional to the change in the fractal distance$\Delta k \sim \Delta\left(\frac{1}{X(R,\gamma)}\right)$. By definition of the Hubble parameter, its change is proportional to $\Delta H \sim \Delta\left(\frac{1}{X(R,\gamma)}\right)$. Consequently,$\Delta k \sim \Delta H$. After that, relation (14) for the relative standard deviations has the form

$$\sigma_R\, \sigma_H \geq 2\pi, \tag{15}$$

where $\sigma_R = ((\Delta R)^2 - (<\Delta R>^2))^{\frac{1}{2}}/R_*, \sigma_H = ((\Delta H)^2 - (<\Delta H>^2))^{1/2}/H_{max}$

A theoretical estimate $H_{max} = H(\gamma_*)$ is possible according to equation (5).

4. Comparison of theoretical results with cosmological observations

The values of the fractal dimension of the sets of galaxies determined from catalogs differ. For example, in [16], the values of fractal dimension D = 1.3 - 1.5 for the SDSS 16th data release catalog were obtained by the correlation method.To increase the accuracy of determining D, we calculated the correlation function in Eq. (10) for$r_{ij_{min}} < \delta < r_{ij_{max}}$, where $r_{ij_{min}}$, $r_{ij_{max}}$are the smallest and largest distance between two points. The choiceof$r_{ij_{max}}$ is determined by the saturation of the number of pairs of points (Figure 6a.).

Indeed, the fractal dimension $D = 1.465$ is installed only on a certain spatial scale (Fig. 7b). Many galaxies form a fractal correlation curve with the topological dimension$d = 1$. The maximum value of the scaling index corresponds to its theoretical value $\gamma_* = D - d = 0.465$.

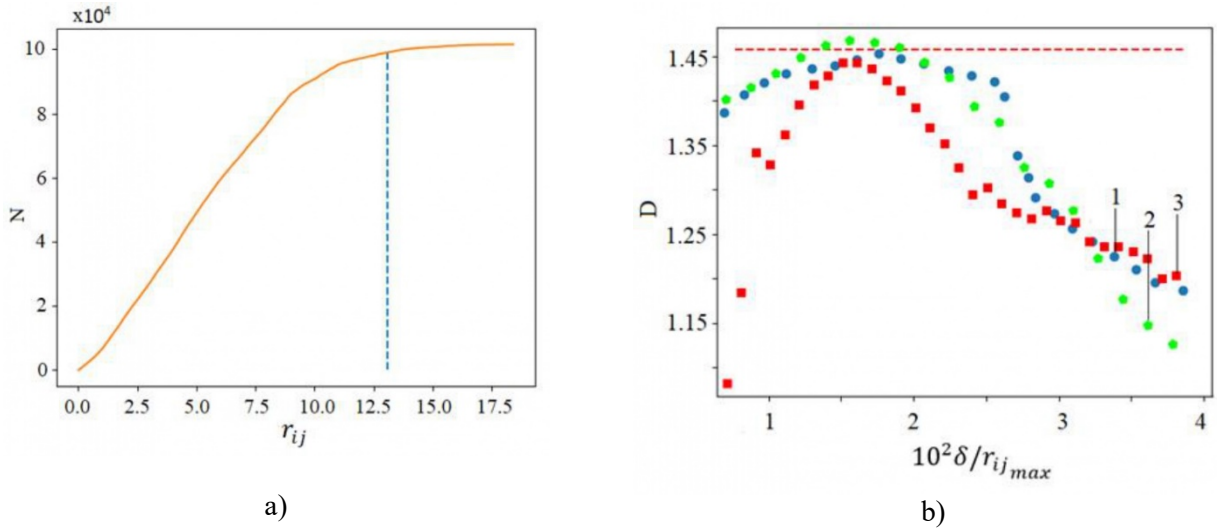

a) b)

Fig. 6. Saturation of the number of pairs of points N by the distance between two points according to the catalog [17] (a). Change in the correlation dimension according to the relative scale of measurement $10^2\delta/r_{ij_{max}}$according to catalogs: 1- [17], 2- [18], 3- [19](b).

Figure 7 shows a Hubble diagram for a set of values$10 \le R_* \le 200, \gamma = \gamma_*$. The theoretical values $H, kms^{-1}Mpc^{-1} = 65, 72, 79$ were obtained for $\frac{\Delta R}{R_*} * 10^2 = 1.36; 1.49; 1.65$ by averaging $N = 10^4$ points. There is no global expansion rate $\gamma < \gamma_*$near the Local Group ($1 \le R \le 3\ Mpc$).

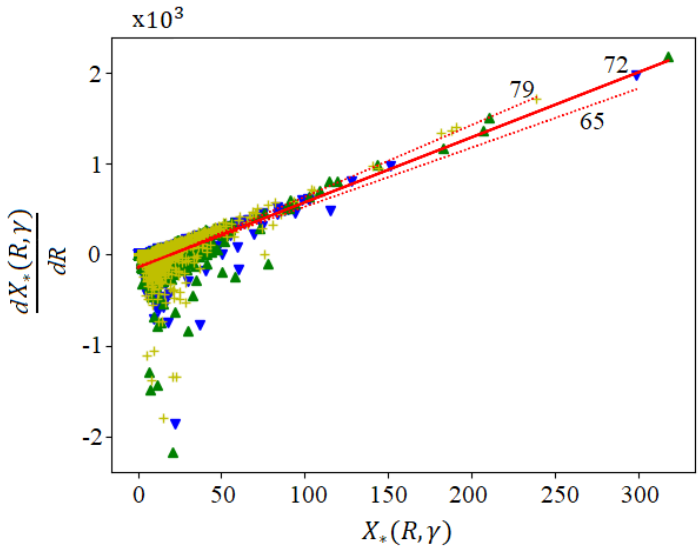

Fig.7. An illustration of the existence of the global value for the Hubble parameter for$\gamma = \gamma_*$. The average value of the interval $H = 65 - 79$ ($inunitskms^{-1}Mpc^{-1}$) according to the results of observations [1-3, 20] is 72 with an error of about 4%. The value H according to the present theory at $\gamma = 0.465, \sigma_R = 0.0149is72, \Delta H = 2\pi/1.49 = 4.21\%$.

The ratio of the speed of galaxies to the speed of the background $\frac{\Delta X(R,\gamma)}{\Delta R}$varies along the coordinate$R$ and can be both positive and negative, as in astrophysical observations [1-3,20]. The global expansion of the universe is described by the value$\gamma_* = 0.465$. Saturation of H value by the increase ofγ toγ_* determined by the analysis of the attractor of gravitational waves (Fig. 2) is also observed from the result of the theory of the distance to galaxies as a nonlinear fractal measure (Fig. 8). Objects of the same luminosity, located at different distances from the observer, will have different apparent values.

Observations [21] show that the luminosity (m-M) increases chaotically with increasing redshift $z$and its behavior towards saturation can be described by the relation:

$$m - M = 5 * (\log_{10} L + 5) \ , \qquad (16)$$

.

where$L$ is the measured redshift distance to the galaxy.

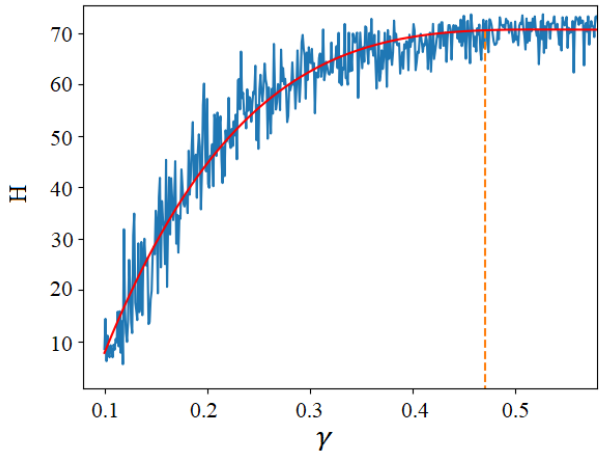

Fig.8. Changes in the Hubble parameter with increasing scaling exponent at$\Delta R = 1.49 * 10^{-2}$.

To compare the result (16) with the present theory, we replace L by$X(R,\gamma)$ fromEq. (12). We define the redshift as the rate of change in the distance along the coordinate$z = \frac{\Delta X(R,\gamma)}{\Delta R}$, select the value$\Delta R = 1.58 * 10^{-2} Mpc$ as corresponding to $H = 68\, kms^{-1}Mpc^{-1}$that adopted in [21], and obtain chaotic values of the luminosity (Fig. 9). The regular curve in this figure, as in [21], corresponds to the values$L = z/H$

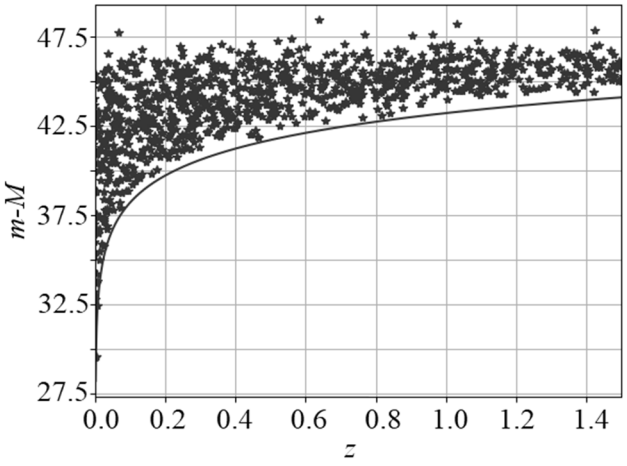

Fig.9. Change of luminosity value by redshift, corresponding to equations (16) and (12).

Conclusion

The equation for weak perturbations of the curvature of space, following from Einstein's equations for the gravitational field, is written in terms of the dependence of the wavenumber on the scale factor of the expansion of the universe and the radius of zero gravity of galaxy clusters R_*. The attractor of this equation has the maximum fractal dimension $D = d + \gamma_* = 1 + 0.465$, which is reached when the Hubble parameter is changed. The value of the scaling exponent γ_*corresponds to the new anisotropic fractal model, various applications of which were previously considered by the authors, and to the correlation fractal dimension of the distribution of galaxies in various catalogs.

The distance to the galaxy is determined through its coordinate as a nonlinear fractal measure, the measurement scale of which, in contrast to the known fractal models, takes into account the deviation of the desired measure itself from its value at the point of zero gravityR_*(at the Lagrange points of gravitating objects). The change in the distance along the coordinate determines the ratio of the galaxy's velocity to the velocity of the system accompanying the gravitational wave and the corresponding Hubble parameter.

Discrete iterative analysis of a singular nonlinear equation with a fractional power for distance gives a scale-invariant value of the root-mean-square deviation of 0.0149 forR_*= 1. Such results are typical for examples of singular generalized functions obtained by discrete iterative analysis, taking into account the structure of the fractal measure. The use of the established minimum measurable interval of the galactic coordinate value is in good agreement with the latest observations of the Hubble parameter, redshift in distance, the dependence of luminosity on redshift. Due to the self-similar wave nature, the value of the Hubble parameter depends on the ratio of the violation of the wavelength coherence and the wavenumber of the gravitational wave. Thus, new models of fractal measures (objects of non-Euclidean geometry) make it possible to describe the basic observational facts of cosmology by Einstein's ideas about homogeneity and Mandelbrot's about the scale invariance of the universe.

Acknowledgements

This research has been funded by the Science Committee of the Ministry of Education and Science of the Republic of Kazakhstan (Grant No. AP08856419).

REFERENCES

1 Riess A. G. et al. A 2.4% determination of the local value of the Hubble constant. *The Astrophysical Journal*. 2016, Vol. 826, No. 1, pp. 56-61.

2 Ade P. A. R. et al. Planck 2013 results. XVI. Cosmological parameters. *Astronomy & Astrophysics*. 2014, Vol. 571, pp. A16.

3 Kuo C. Y. et al. The megamaser cosmology project. V. An angular-diameter distance to NGC 6264 at 140 Mpc. *The Astrophysical Journal*. 2013, Vol. 767, No. 2, pp. 155-159.

4 Nojiri S. I., Odintsov S. D. Introduction to modified gravity and gravitational alternative for dark energy. *International Journal of Geometric Methods in Modern Physics*. 2007, Vol. 4, No. 01, pp. 115-145.

5 Maeder A. An alternative to the ΛCDM model: the case of scale invariance. *The Astrophysical Journal.* 2017, Vol. 834(2), pp. 194-200.

6 Maeder A. Scale-invariant Cosmology and CMB Temperatures as a Function of Redshifts. *The Astrophysical Journal*. 2017, Vol. 847, No.1, pp. 65-69.

7 Maeder A., Gueorguiev V. G. Scale-invariant dynamics of galaxies, MOND, dark matter, and the dwarf spheroidals. *Monthly Notices of the Royal Astronomical Society*. 2020, Vol.492, No.2, pp. 2698 – 2708.

8 Peebles P. J. E. *The large-scale structure of the universe*. Princeton university press. 1980, 440 p.

9 Landau L.D, Lifshitz E.M. *Field theory*. Elsevier Science, 2013, 218 p.

10 Nicolis G., Prigogine I. *Exploring complexity an introduction*. 1989, 107 p.

11 Strong M. D., Crescimanno M. Lagrange point stability for a rotating host mass binary. *Physical Review D*. 2020, Vol.102, No. 2, pp. 024052.

12 Zhanabaev Z.Zh. Fractal model of turbulence in the jet. *Proceedings of the SB Acad. of Sci. USSR. Technical Science series.* 1988, Vol.**4**, pp. 57 – 60. [in Russian].

13 Zhanabaev Z.Zh., et al. Electrodynamic characteristics of wire dipole antennas based on fractal curves. *Journal of Engineering Science and Technology*. 2019, Vol.14, No. 1, pp. 305 – 320.

14 Feder J. *Fractals*. Springer Science & Business Media, 2013, 183 p.

15 Chhoa J. F. An Adaptive Approach to Gibbs' Phenomenon. *Master's Thessis*. 2020, 111 p.

16 García-Farieta J. E., Casas-Miranda R. A. Effect of observational holes in fractal analysis of galaxy survey masks. *Chaos, Solitons & Fractals.* 2018, Vol. 111, pp. 128-137.

17 Karachentsev I.D., *et al.* A catalog of neighboring galaxies. *The Astronomical Journal.* 2004, Vol. 127(4), pp. 2031.

18 Ahumada R., et al. The 16th data release of the Sloan Digital Sky Surveys: first release from the APOGEE-2 Southern Survey and full release of eBOSS Spectra. *The Astrophysical Journal Supplement Series*. 2020, Vol.249, No.1, pp. 3.

19 Boller T., et al. Second ROSAT all-sky survey (2RXS) source catalogue. *Astronomy & Astrophysics*. 2016, Vol. 588, pp. A103.

20 Freedman W. L., et al. Final results from the Hubble Space Telescope key project to measure the Hubble constant *The Astrophysical Journal*. 2001, Vol. 553, No.1, pp. 47.

21 Elvis M., et al. Spectral energy distributions of type 1 active galactic nuclei in the COSMOS survey. I. The XMM-COSMOS sample *The Astrophysical Journal*. 2012, Vol.759, No.1, pp. 6 – 13.

Article accepted for publication 23.04.2021

.

DOI 10.31489/2021No2/90-95

UDC 528.88

SATELLITE DATA PROCESSING ALGORITHM IN THE PROCESS OF FORMATION OF THE TIME SERIES OF VEGETATION INDEXES

Vitkovskaya I.S., Batyrbayeva M.Zh.

Joint-Stock Company "National Center of Space Research and Technology", Almaty, Kazakhstan
madina-iki@mail.ru

The diverse spectral indexes computed from the satellite images are used extensively in the world practice of remote sensing of the Earth from space. This approach proved its validity for the satellite monitoring of the underlying terrain, detection of ongoing changes and trends of their dynamic patters. Accumulated prodigious amount of satellite data, the state-of-the-art methods of thematic interpretation gave rise to creation of services providing free access to both images and to image processing results. Notwithstanding the foregoing, in the furtherance of the local and regional scale it turns out that usage of the end products of thematic processing of space information supplied by the known available services was not efficient on all occasions. Consequently, we may need to generate our own archives of the long-term series of satellite indexes. The volume of files containing the digital index matrices computed based on the MODIS satellite low resolution data subject to the complete coverage of the territory of Kazakhstan surpasses 4 Gb. This often results in the delayed computations, and on frequent occasions in infeasibility of computation of a full matrix when the *medium specs computers are employed. This article is focused on the satellite data processing algorithm in the process of formation of the time series of vegetation indexes. As a consequence, the multi-year archive of vegetation indexes (over a period of 2001-2020), which provided a basis for trend analysis of the underlying terrain, determination of their future trends and forecasting of their changes was created within the territory of the Republic.*

Keywords: remote sensing, satellite images, processing algorithm, long-term data series, vegetation indexes.

Introduction

Application of the Earth remote sensing data (ERS) with the aim of location of objects of the underlying terrain of the Earth, subsequent monitoring of these objects, forecasting of changes in their state in the present state of the art of space technologies became a widespread practice already. Study of the multi-year environmental changes with the aid of tools and methods of the remote sensing data represents one of the most promising modern research areas of examination of the processes observed on the Earth's surface. The multizone space images serve as a basis for the interpretation of the spectral characteristic of soil and vegetation covers, water surfaces for the acquisition of reliable data [1].

The current stage of development of space technologies is characterized by the following special patterns of use of satellite data [2]:

– A growing number of the ERS space vehicles, their spectral and spatial resolution made it possible to perform monitoring of the high-rate processes involving detection of such processes at the early stages of development;

– Steep increase in volume and frequency of supply of satellite data [3], which resulted in the necessity for the development of new approaches and methods of the remote sensing data processing practices [4];

– The present-day ERS satellite system ensure acquisition of not only qualitative information but also of accurate quantative information. In view of this, ERS data is used not only for the qualitative assessment of a situation but also for quantitative assessments and the possibility to make predictions of development of the diverse processes and phenomena;

– As a result of the rising level of information accessibility, implementation of the monitoring system has become more profitable than development of the ground-based and aerial surveillance systems;

– There is a trend towards transition from the use of the local systems of data acquisition and creation of own archives of own space images to services of acquisition of information from the large-scale specialized centers.

Specific traits of the present-day development of services offering the remote sensing data are the reason why it is not advantageous to develop and support the entire data processing cycle. Many remote

sensing systems are targeted at the acquisition of standardized, well-gaged and tailored core products with the previously defined spatial and time formats.

The following differing levels of monitoring – local, regional, national, and global, distinct from each other in their goals – are distinguished. The use of end products of thematic processing of space information in performance of the local and regional tasks does not always prove its efficiency for the spatial and time details of monitoring data. Therefore, a need for the formation of own archives of the long-term series of satellite indexes arises. The volume of files containing the digital index matrices computed based on the MODIS and LANDSAT satellite low resolution data subject to the complete coverage of the territory of Kazakhstan is fairly large. The situation of this sort leads to slowing-down of computations, and in many instances to infeasibility of computation of a full matrix when the low power computers are employed.

This article deals with the technology of generation of the long-term series of vegetation indexes on the basis of satellite data.

1. Materials and Methods

1.1 Satellite Data

The low-resolution Terra MODIS satellite data, MOD09Q1 [5] product, forming digital matrices of the 8-day aggregates 1 and 2 of spectral channels (wavelength 0.620-0.670 μm and 0.841-0.876 μm, respectively), spatial resolution of 250 m, and sinusoidal projection are applied in this article. The data was processed with the consideration of atmospheric correction, reduced cloud effect and shadows of clouds. The entire territory of Kazakhstan is covered with six granules - 21v03, 21v04, 22v03, 22v04, 23v03, and 23v04 (540 Mb each), Figure 1. Further, a mosaic tile is generated using granules for every channel.

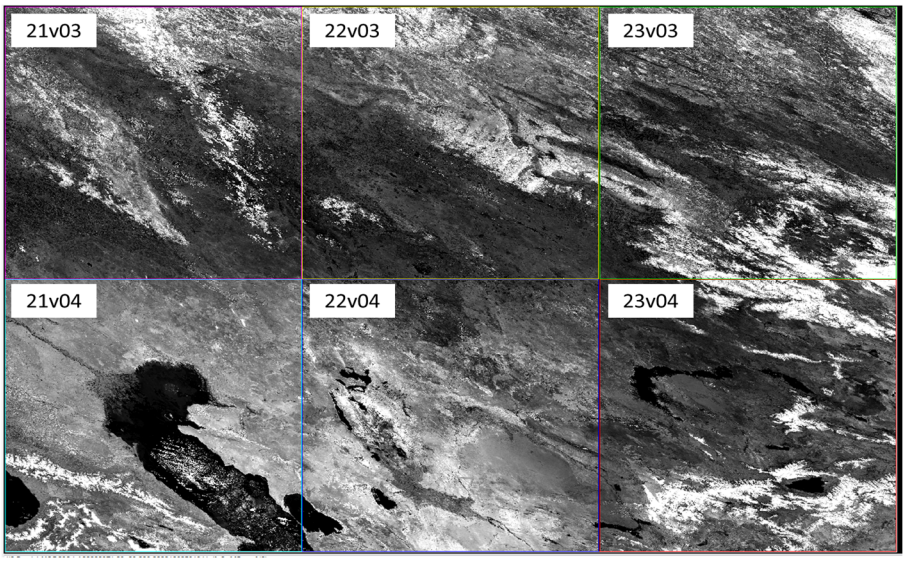

Fig. 1. Layout of granules from the MODIS satellite for the territory of Kazakhstan

1.2 Research Techniques

The vegetation index method intended to use satellite data for solution of a wide variety of specific theoretical and applied problems in the course of monitoring of the underlying terrain has been developed in the world practice of remote sensing of the Earth from space. The indexes are selected in an experimental fashion based on the known peculiarities of spectral reflectance curves of soils and vegetation [6-8].

A state of objects of the underlying terrain according to satellite data shall be estimated based on associations of their state with the spectral reflectance characteristics. This becomes most obvious when passing from the visible band (0.4-0.74 μm) to the near infrared band (0.74-1.3 μm). Application of the method of satellite vegetation indexes for determination of a vegetation response to environment and anthropogenic impact is the common practice of remote sensing of the Earth from space. Existence of the

.

long-time series is essential in the area of problems of impact analysis of the state of the underlying terrain. Table 1 lists vegetation indexes applied during satellite monitoring of the vegetation cover of Kazakhstan.

Table 1. Satellite indexes used during satellite monitoring of the vegetative cover of Kazakhstan

Item name	Formula	Intended use
Normalized Difference Vegetation Index NDVI [9]	$NDVI = \frac{NIR - RED}{NIR + RED}$	Assessment of the seasonal dynamics of state of vegetation cover
Vegetation condition index VCI [10]	$VCI = \frac{NDVI_i - NDVI_{\min}}{NDVI_{\max} - NDVI_{\min}}$	Analysis of weather effects on the state of vegetation cover during the growing season; weather moisture characteristic
Temperature condition index TCI [11]	$TCI = \frac{BT_{\max} - BT}{BT_{\max} - BT_{\min}}$	Temperature environment characteristic
Vegetation health index VHI [7]	VHI = α*VCI + (1- α)*TCI	Assessment of the state of vegetation cover taking into account both temperature exposure and moisture conditions
Integral vegetation index IVI [12]	$IVI = \sum_{t}^{27} NDVIt$ t – number of a ten-day period during the season	Analysis of interseasonal variation of the state of vegetation
Integral vegetation condition index IVCI [12]	$IVCI = \frac{IVI_i - IVI_{\min}}{IVI_{\max} - IVI_{\min}}$	Analysis of interseasonal variations of weather effects on the state of vegetation

The following values: NIR, RED - reflection factors in the near-infrared region (0.75-1.0 μm) and in the read region (0.55-0.75 μm) of the spectrum спектра that are corresponding to values 2 and 1 of the channels, respectively, are applied in the formulae. BT means a brightness temperature defined on the basis of thermal channel data in the range of 3.660 – 14.385 μm. The α coefficient is either determined empirically or is taken equal to 0.5. The maximum and minimum values of every index are selected in each pixel throughout the period of monitoring.

2. Discussion of results

Usage of ready digital matrices of vegetation indexes provided by the services is not convenient in every instance. For instance, on the U.S. Geological Survey website (USGS) [5] one can find freely available products of the thematic processing of satellite data (NDVI, VCI index matrices) obtained from the MODIS space vehicle (SV) with the spatial resolution of 250 m (pixel size), 16-daytime period and 20-year archive depth. Meanwhile, Copernicus Land Monitoring Service [13] site intended for registered users of this e-service offers open access to a number of satellite products, inter alia VCI index matrices. The spatial- time resolution of the product is 1-4 km/pixel, 10-day period. Such spatial-time scale is too small for the tasks of monitoring of the vegetation cover dynamics of local areas.

Generation of own archive of indexes using periodical satellite data at a processing level not below 3A [14] is an alternative solution of this problem. This solution provides an opportunity to obtain satellite products required for achievement of the stated goals and objectives. Authors of this article offer their own ERS data processing algorithm to be used in the process of formation of the time series of vegetation indexes with a computation scheme shown in Figure 2.

In the computation of VCI, IVCI indexes of the digital matrices, a preliminary calculation must be performed in every pixel of the long-term maximum and minimum values of NDVI, IVI, respectively, throughout the period of monitoring. $NDVI_{min}$ and IVI_{min} values are most variable within the territory of Kazakhstan occupying mainly semiarid and arid areas. This fact is attributable to frequently observed dry weather conditions of varying intensity basically in any part of the Republic, which account for such

suppressed state of vegetation. We should consider updating of time series of the used vegetation indexes from two points of view:

– Computation of values of indexes for every new growing season;

– Re-computation of the entire multi-year archive of index values in the *CI format taking into account fresh data. In the computation of *CI (VCI, IVCI, TCI) indexes, matrices of MAX, MIN extremum values are updated in every pixel throughout the period of monitoring. Such procedure is associated with the special aspects of computation of this group of indexes.

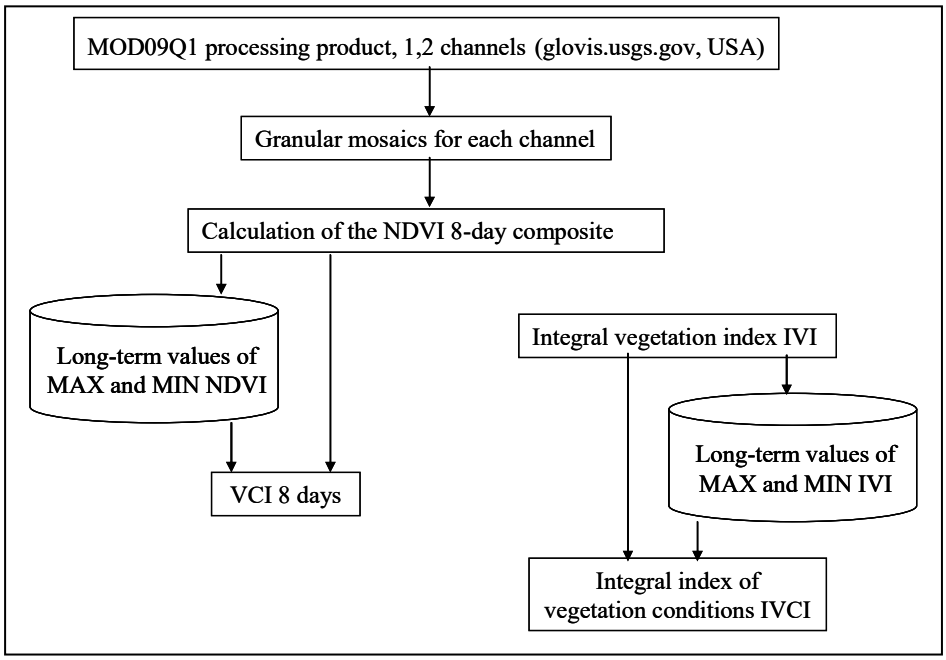

Fig.2. Computation scheme of a set of vegetation indexes based on MODIS data (8-day aggregates)

For this purpose, it is understood that if data of each new growing season is used for computation of the NDVI and IVI values, all long-term series must be recalculated for all other indexes. This is the reason of "weighing" of an index value in the long-term series of values. Notwithstanding the fact that this is an automated procedure, it requires significant computation time and a vast amount of re-computed information. For instance, the number of created files and amount of computed data during update of time series of VI data in 2020 are presented in Table 2.

Table 2. Update of Archive of Vegetation Indexes with the Use of Data for the Year of 2020 (April – October)

Satellite data, vegetation indices	Number of created files
MOD09Q1	162
NDVI	162
NDVImin	162
NDVImax	162
VCI	27
IVI	6
IVImin	6
IVImax	6
IVCI	6

It should be pointed out that the volume of files containing digital matrices of vegetation indexes subject to the complete coverage of the territory of Kazakhstan exceeds 4 Gb, which often results in the delayed

.

computations, and on frequent occasions in infeasibility of computation of a full matrix when the medium specs computers are employed. In the furtherance of this goal, the authors of this article developed the algorithm of generation of times series of vegetation indexes.

3. Algorithm of generation of time series of vegetation indexes

The algorithm of generation of time series of vegetation indexes stipulates for the following steps:

– Building of mosaics of channels 1 and 2 composed of granules blanketing the entire research territory;

– Computation of matrices of NDVI (8-day) index serving as a base index in computation of other indexes;

– An NDVI matrix filtering procedure including rejection of "outlier" values (emission values - noise).

The further processing of the complete matrix becomes complicated due to heavy weight of files. Consequently:

– Division of an available NDVI digital matrix into three parts with the purpose of reduction of processing time (further procedures should be implemented separately for each part);

– Computation in every pixel of $NDVI_{min}$ values over this 8-day period throughout the period of monitoring, including the new season data;

– Computation in every pixel of $NDVI_{max}$ values over this 8-day period throughout the period of monitoring, including the new season data;

– Re-computation of the 8-day VCI values for each growing season throughout the period of monitoring with consideration to updated $NDVI_{min}/NDVI_{max}$ values in every pixel for each of three parts;

– Computation of IVI matrices by summation of NDVI values in every pixel (for each of three distinguished parts),

– Computation in every pixel of IVI_{min} values throughout the period of monitoring, including the new season data,

– Computation in every pixel of IVI_{max} values throughout the period of monitoring, including the new season data,

– Re-computation of IVCI values for every growing season throughout the period of monitoring with consideration to updated IVI_{min}/IVI_{max} values in every pixel.

– "Stitching" (sewing together) of each VCI, IVI, IVCI digital matrix in the unified coverage for the research territory.

Division of the available NDVI digital matrix into parts and subsequent separate processing of every part are dictated by the large file size – over 4 Gb. This approach makes good sense as it allows for the substantial reduction of the data processing time – almost twice in spite of the expanding amount of calculation.

ENVI software developed for visualization and processing of the Earth's remote sensing data was applied for image processing and computation of vegetation indexes.

Conclusion

The article focuses on the algorithm of generation of the long-term series of vegetation indexes based on the low-resolution satellite data acquired from the MODIS space vehicle. A variety of causes triggered the necessity of generation of such algorithm:

– The digital matrices of vegetation indexes provided by the known freely available services in solving of a number of tasks fail to meet certain spatial and time parameters;

– Generation of digital coverage of vegetation indexes within the limits of immense territory (an aggregate of regions, Republic) is a challenge due to the large volume of processed files and processing time.

The developed algorithm was applied across the territory of Kazakhstan. As a result, the long-term archive of vegetation indexes (2001-2020) applicable to the territory of Republic with the spatial resolution of 250 m and 8-day rate of frequency was created for the NDVI, VCI differential indexes. The archive provides a basis for an analysis of changes of the underlying terrain, trend determination and forecast of these changes. The range of use of the set of indexes is quite broad: changes of state of vegetation cover,

water bodies, ecological challenges, agricultural tasks and emergencies. Proposed algorithms are simple and may be applied in any areas.

Acknowledgements

The research was supported by the Ministry of Education and Science of the Republic of Kazakhstan, Grant number AP08957145

REFERENCES

1 Atlas "Deciphering multispectral aerospace imagery: Methodology and results"- Moscow: Science - Berlin, Akademi-ferlag, 1982. - 83 p. [in Russian].

2 Lupyan E., Balashov I., Burtsev M., Efremov V., Kashnitsky A., Kobets D., Krasheninnikova Y., Mazurov A., Nazirov R., Proshin A., Sychugov I., Tolpin V., Uvarov I ., Fleetman E. Creation of technologies for building information systems for remote monitoring. *Modern problems of remote sensing of the Earth from space*, 2015, Vol. 12, No. 5, pp. 53–75 [in Russian].

3 Ramapriyan H. K. Development, Operation and Evolution of EOSDIS – NASA's major capability for managing Earth science data, CENDI/NFAIS *Workshop on Repositories in Science & Technology: Preserving Access to the Record of Science*, 2011, November 30, 31 p.

4 Lupyan E., Savorskiy V., Shokin Yu., Aleksanin A., Nazirov R., Nedoluzhko I., Panova O. Modern approaches and technologies for organizing work with Earth remote sensing data for solving scientific problems. *Modern problems of remote sensing of the Earth from space*, 2012, Vol. 9, No. 5, pp. 21–44, [in Russian].

5 Official websites use.gov. Available at: https://glovis.usgs.gov/

6 GDAL/OGR user docs. Available at: http://gis-lab.info - an independent information resource dedicated to Geographic Information Systems (GIS) and Earth Remote Sensing (ERS).

7 Kogan F. World droughts from AVHRR-based vegetation health indices. *EOS, Trans. American Geophys. Union,* 2002, No. 83, pp. 557-564.

8 Cherepanov A.S. Vegetation indexes, *Geomatics*. Moscow, 2011, No. 2, pp. 98-10, [in Russian].

9 Rouse J. W., Haas R. H., Schell J. A., Deering D. W. Monitoring vegetation systems in the great plains with ERTS. *Third ERTS Symposium NASA* SP-351, 1973, Vol. 1, pp. 309-317.

10 Kogan F.N. Remote sensing of weather impacts on vegetation non-homogenous areas. *Int. J. of Remoute Sensing,* 1990, Vol.11, pp. 1405- 1419.

11 Kogan F.N. Application of vegetation index and brightness temperature for drought detection, *Adv. Space Res*. 1994, Vol. 15, No. 11, pp. 91-100.

12 Spivak L., Vitkovskaya I., Batyrbayeva M. Analysis of inter seasonal variations of productivity of vegetative cover of Kazakhstan using temporal remote sensing rows. *News of Nat. Acad. of Sci. of Kazakhstan. Phys. Math. Ser*. 2008. No. 4, pp. 29 – 32. [in Russian].

13 Belenov A.V. Standard processing levels and formats for presenting remote sensing data from space. World experience, *Geomatics*. Moscow, 2009, No. 4, pp. 18 – 20. [in Russian].

Article accepted for publication 23.04.2021

.

DOI 10.31489/2021No2/96-102

UDC 537.533.34

ABOUT THE POSSIBILITY OF CREATING AN EFFICIENT ENERGY ANALYZER OF CHARGED PARTICLE BEAMS BASED ON AXIALLY-SYMMETRIC OCTUPOLE-CYLINDRICAL FIELD

Kambarova Zh.T.[1]*, Saulebekov A.O.[2], Kopbalina K.B.[3], Tussupbekova A.K.[1], Saulebekova D.A.[4]

[1] E.A. Buketov Karaganda University, Karaganda, Kazakhstan, kambarova@bk.ru

[2] Lomonosov Moscow State University, Kazakhstan branch, Nur-Sultan, Kazakhstan

[3] Karaganda Technical University, Karaganda, Kazakhstan

[4] Institute Curie, Sorbonne University, Paris, France

One of the problems in creating systems for energy analysis of charged particles beams is to determine the deflecting field and calculation the shape of the deflecting electrodes. This article is devoted to the study of the possibility of creating an effective energy analyzer of charged particle beams based on multipole electrode systems. A previously unstudied type of a multipole-cylindrical field - an electrostatic axially-symmetrical octupole-cylindrical field was chosen as the deflecting field. The field is formed by using the superposition of an electrostatic cylindrical field and a circular octupole of various contributions. The family of the equipotentials of cylindrical octupoles with planes of symmetry and antisymmetry is calculated. The calculation and analysis of equipotential portraits of the electrostatic axially-symmetric octupole-cylindrical fields with different weight contributions of the cylindrical field and circular octupole are carried out.

Keywords: energy analyzer, deflecting field, octupole-cylindrical field, equipotential, equipotential portraits, multipole electrode systems.

Introduction

One of the ways to improve the work of the instrumentation of energy analysis of charged particle beams is to modify the deflecting field by changing the shape of the outer electrode of a cylindrical mirror. A cylindrical mirror has a number of advantages, such as high energy resolution, simplicity of construction, etc. Its work is based on the focusing and dispersing action of the field in the space between two coaxial cylindrical electrodes on a charged particlesbeam. The theory and the possibility of practical application of a cylindrical mirror were studied in detail by a group of scientists led by Professor V.V. Zashkvara [1].

The cylindrical mirror type energy analyzers have found wide application in the study of resonance phenomena in gases, in spectroscopy for chemical analysis, for obtaining spectra of secondary electrons, photoelectrons, field electrons, Auger electrons, as well as in space research, in studying the interaction of atomic particles with the solid surface and plasma diagnostics. The cylindrical mirror analyzer has become the basic element of electron spectrometers of various purposes, manufactured in the countries of near and far abroad by leading instrument-making firms [2].

The new class of potential fields called multipole-cylindrical fields is first proposed and classified by V.V. Zashkvara and N.N. Tyndyk in [3-6]. A multipole-cylindrical field is formed by using a superposition of an electrostatic cylindrical field and a circular multipole of various contributions.

The purposes of this work are to study the possibility of creating an effective mirror energy analyzer of charged particle beams based on an axially-symmetric electrostatic octupole-cylindrical field, to calculate and construct equipotential portraits of the corresponding fields for various contributions of the cylindrical field and circular octupole, and to analyze the obtained field equipotentials. Consideration and analysis of superpositions of these fields will make it possible to predict the prospects of choosing one or another scheme of energy analyzer for space experiments.

1. Calculation and analysis

An electrostatic multipole-cylindrical field is formed in the space between two axially symmetric coaxial electrodes, the inner (2) of which has a cylindrical shape (r_0 radius) and is at zero potential; to the outer curvilinear electrode (3) is supplied deflecting potential. The shape of the outer deflecting electrode is interested. The profile of the outer deflecting electrode (3) (Fig. 1) coincides with one of the equipotentials of the cylindrical multipole. A charged particles beam can be introduced into the area of the mirror field and removed from it through the corresponding aperture windows in the cylindrical electrode.

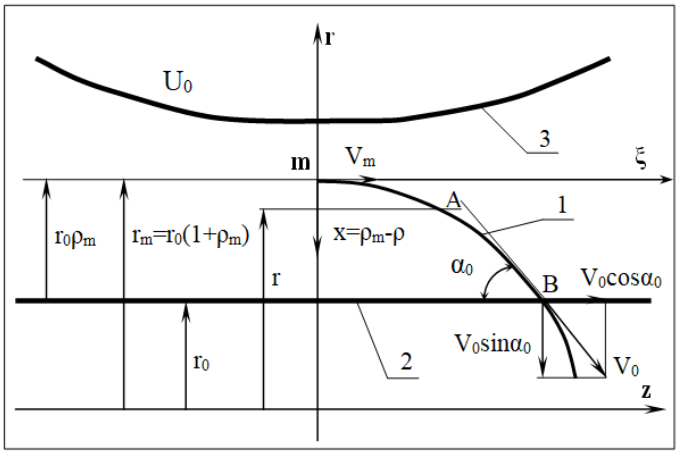

Fig.1. The electron-optical scheme of an energy analyzer based on a multipole-cylindrical field^
1- Trajectory of charged particles, 2 - cylindrical electrode, 3 - outer deflection electrode

Earlier, the corpuscular-optical schemes of mirror energy analyzers of charged particle beams based on electrostatic multipole-cylindrical fields were studied in sufficient detail; a large number of works, for example, [7-11], were aimed at studying their corpuscular-optical characteristics, at finding optimal schemes with high quality focusing and energy resolution. Using the electrode system of an axially-symmetric electrostatic decapole-cylindrical field to build energy analyzer of charged particles for space research was proposed in [12]. It was determined from the calculations that the value of the specific dispersion in energy, which characterizes the energy resolution of the decapole-cylindrical field, calculated for particles with an initial angular divergence of 12°, is twice the value of the specific dispersion of the classical cylindrical mirror analyzer. The device makes it possible to register elementary particle beams from outer space, to obtain various spectra with high resolution.

According to [4], the $g(R,\xi)$ field of energy analyzer can be designed as a superposition of the base field and a set of circular multipoles which coaxial with the base field. In the case of an electrostatic deflection field, this design looks like this:

$$g(R,\xi) = \ln R + qU_q(R,\xi) + sU_S(R,\xi) + \omega U_{oct}(R,\xi) + dU_{dec}(R,\xi) + ..., \qquad (1)$$

where $\ln R$ is the basic cylindrical field, $U_q, U_S, U_{oct}, U_{dec}$ are circular multipoles (quadrupole, hexapole, octupole, decapole, etc., $q, s, \omega, d, ...$ are the weight coefficients of the multipoles, $R = r/r_0$ and $\xi = z/z_0$ are the relative radial and axial coordinates, r_0 is the radius of the axially circular trajectory of the analyzed beam of charged particles (Fig. 1).

The uniqueness of the multipole-cylindrical field (1) is that circular multipoles have different effects on the electron-optical parameters of the energy analyzer of various orders:

- the quadrupole component in (1) determines the first-order angular focusing conditions - linear energy dispersion, magnification;

- the connection of the hexapole component affects (along with the quadrupole) the second-order angular aberrations;

.

- the connection of the octupole affects the characteristics, starting from the third-order, etc.

The potential of an octupole-cylindrical field is described in the *r, z* coordinate system by the following expression:

$$U(r,z) = \mu \ln r + \omega U_{oct}(r,z) \tag{2}$$

where ln *r* is the potential of the cylindrical field, μ is the coefficient specifying the weight contribution of the cylindrical field ln*r*, U_{oct} is the potential of a first type circular octupole, $\omega$is the weight contribution of the circular octupole.

The $U_{oct}(\rho,\xi)$ functions constructed according to the summation symmetry rule are below:

$$\begin{aligned} U_{oct}(\rho,\xi) &= \frac{1}{4!}\xi^4 + \frac{1}{2}\xi^2\left\{\frac{1}{4}\left[1-(1+\rho)^2\right]+\frac{1}{2}\ln(1+\rho)\right\}+ \\ &+\frac{1}{64}(1+\rho)^4+\frac{1}{16}(1+\rho)^2-\frac{1}{8}\ln(1+\rho)\left[\frac{1}{2}+(1+\rho)^2\right]-\frac{5}{64} \end{aligned} \tag{3}$$

$$\begin{aligned} U'_{oct}(\rho,\xi) &= \frac{1}{5!}\xi^5 + \frac{1}{3!}\xi^3\left\{\frac{1}{4}\left[1-(1+\rho)^2\right]+\frac{1}{2}\ln(1+\rho)\right\}+ \\ &+\frac{1}{64}\xi\left\{(1+\rho)^4+4(1+\rho)^2-8\ln(1+\rho)\left[\frac{1}{2}+(1+\rho)^2\right]-5\right\} \end{aligned} \tag{4}$$

Field (3) is called a component of a cylindrical circular octupole with a symmetry plane. For this field $U_{oct}(\rho,-\xi)=U_{oct}(\rho,\xi)$. Field (4) is called a component of a cylindrical circular octupole with an antisymmetry plane. This field satisfies the requirement for antisymmetry relative to the plane $\xi=0$: $U'_{oct}(\rho,-\xi)=-U'_{oct}(\rho,\xi)$.

After expanding (3) and (4) into series in ρ and ξ around the axial circle $\rho=0$, $\xi=0$, and selecting the group of terms with the least powers, we get:

$$U_{oct}(\rho,\xi) \sim \xi^4 - 6\xi^2\rho^2 + \rho^4 \quad , \tag{5}$$

$$U'_{oct}(\rho,\xi) \sim \xi\left(\frac{1}{5}\xi^4 - 2\xi^2\rho^2 + \rho^4\right) \tag{6}$$

Function (5) is an analogue of a planar multipole with a rectilinear axis in a symmetric representation - an octupole, and function (6) is a component of a planar multipole with a rectilinear axis, but in an antisymmetric representation.

A family of equipotentials of an electrostatic axially-symmetric octupole-cylindrical field is calculated. Fig.2 shows field equipotentials U_{oct} and U'_{oct} at intervals of 0.1 of the relative value of the potential. In the ρ,ξ plane section, each of the fields is divided into alternating regions in which the potentials are opposite to the sign. These areas are separated by lines of zero potential, close to straight lines and converging at the nodal point O_1 ($\rho=\xi=0$). From Fig. 2 it follows that for each type of symmetry relative to the plane $\xi=0$, the presented fields are formed by octupole sets of electrodes carrying an alternating potential.

Let's get an presentation of the structure of the superposition of the electrostatic octupole and the cylindrical field. When the fields are added, the central circle of the octupole isaligned with the zero equipotential of the logarithmic field. Series of Fig. 3 show the families of equipotentials of the superposition of a cylindrical field and a cylindrical octupole:

$$U(\rho,\xi) = \omega U_{oct}(\rho,\xi) + \mu \ln(1+\rho) \tag{7}$$

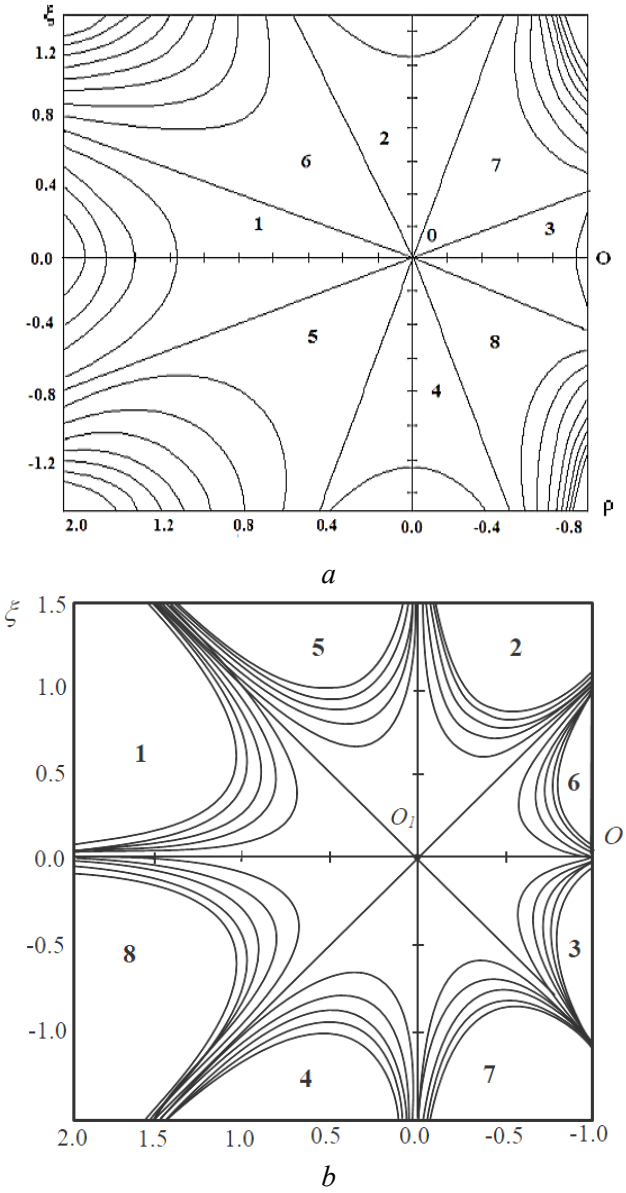

Fig. 2. Family of equipotentials of a cylindrical octupole having a symmetry plane (*a*) and an antisymmetry plane (*b*)

For a series of Fig.3 (*a-f*) ω = - 1.5, - 1, 0.001, 0.005, 1, 1.5at a constant value of the contribution of the cylindrical field μ= 1. From the figures we can trace how gradually with increasing ω the weight contribution of the circular octupole the structure of the field changes. At small values of ω (Fig. 3 *c* and *d*), the structure of the field is transformed from an octupole to a field close to cylindrical, and the nodal point O_1 is also eliminated. For $\omega<0$ (Fig.3*a* and *b*), the removal of vertices occurs along the ρ axis, which then leads to the displacement of regions 1 and 3 (Fig. 2a).

Series of Fig. 4 (*a-d*) show the families of equipotentials of the superposition of a cylindrical field and a cylindrical octupole. For this series of Fig. 4 (*a-f*) the values of the weight contribution of the cylindrical field μ=2,5; 1at a constant value of the weight contribution of the circular octupole ω = 1. As can be seen from the figures, the addition of a cylindrical field $\ln(1+\rho)$ to the circular octupole $U_{oct}(\rho,\xi)$ leads to a change in the field, namely, the approach of regions 2 and 4 to the nodal point. It was determined from the analysis of equipotential portraits of $U(\rho,\xi)=\omega U_{oct}(\rho,\xi)+\mu\ln(1+\rho)$ field, that with a small change in the value of the weight contribution $\mu$of the cylindrical field does not lead to large transformations of the field.

.

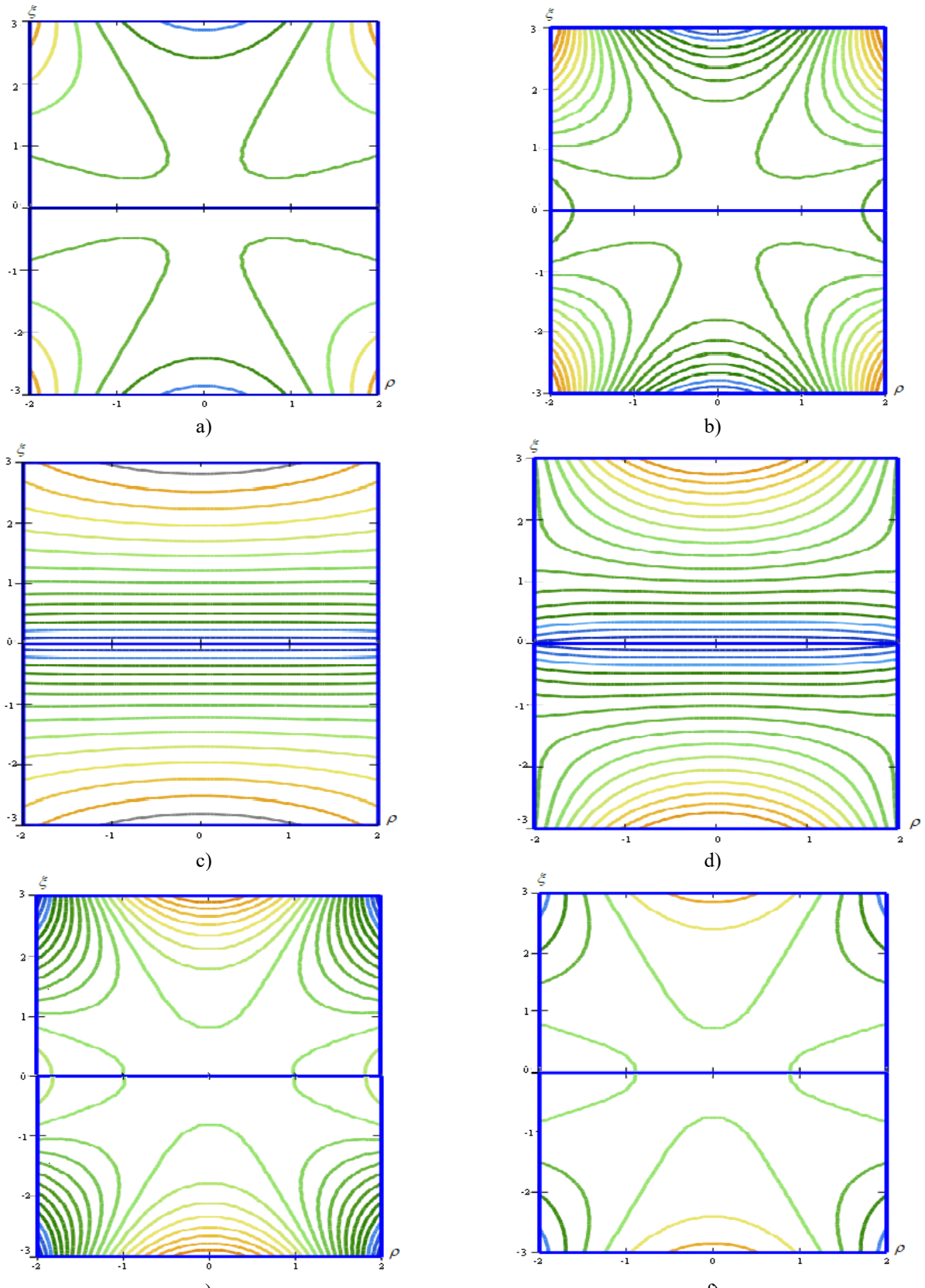

Fig. 3. Equipotential fields $U(\rho,\xi)=\omega U_{oct}(\rho,\xi)+\mu\ln(1+\rho)$ at $\rho(-2,2)$:

a) ω = - 1.5, μ=1; b) ω= - 1, μ=1; c) ω = 0.001, μ= 1
d) ω = 0.005, μ= 1; e) ω = 1, μ=1; f) ω = 1.5, μ=1.

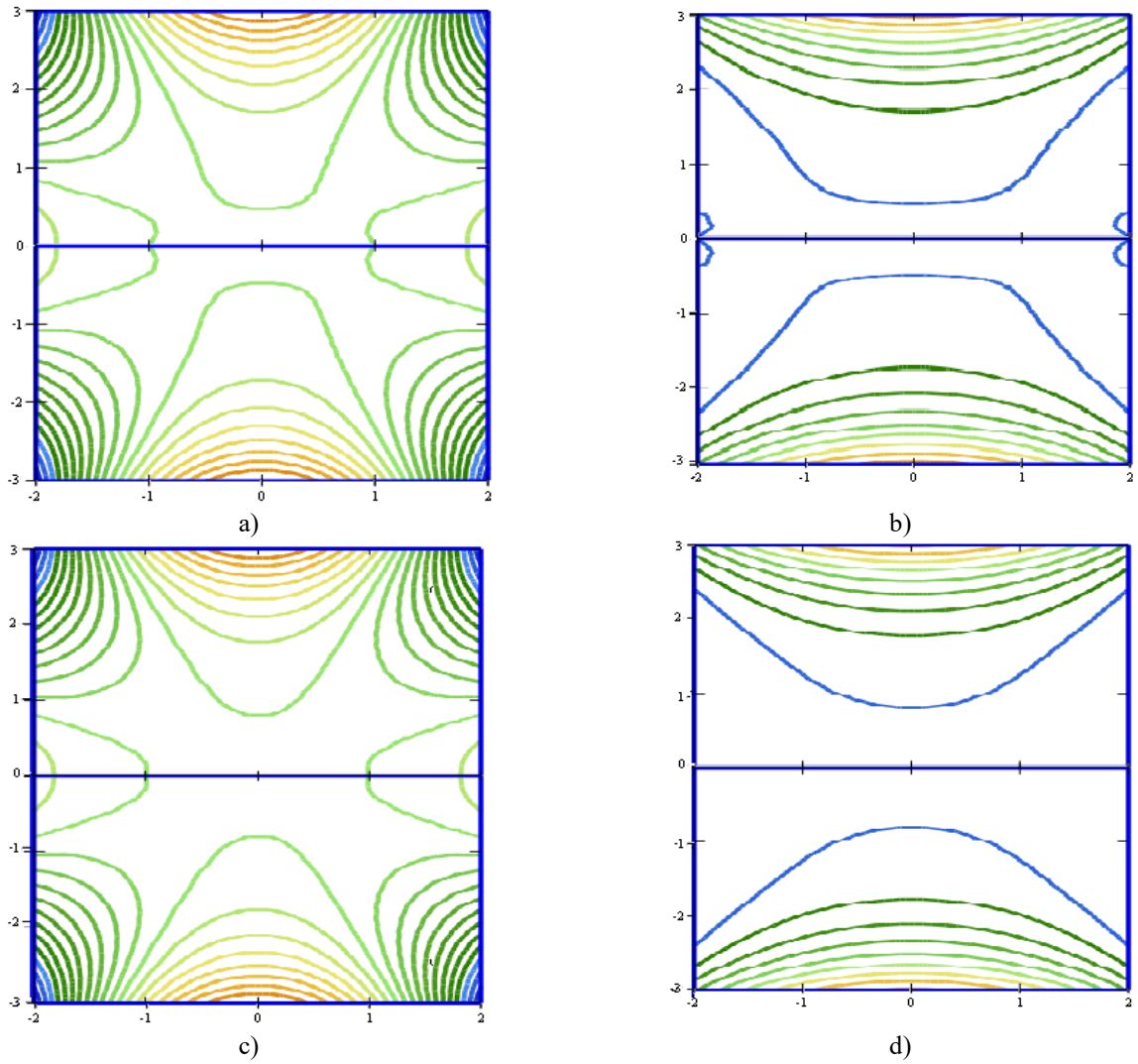

Fig.4. Equipotential fields $U(\rho,\xi)=\omega U_{oct}(\rho,\xi)+\mu\ln(1+\rho)$:
a) μ=2.5, ω= 1; $\rho(-2,2)$: b)μ=2.5, ω= 1; $\rho(-1,1)$
c) μ=1, ω= 1; $\rho(-2,2)$ d); μ=1, ω= 1; $\rho(-1,1)$

Figure 5 shows an example of the image of the equipotential field $U(\rho,\xi)=\omega U_{oct}(\rho,\xi)+\mu\ln(1+\rho)$ in the three-dimensional coordinate system Surface Plot with the values ω= - 1.5, μ=1.

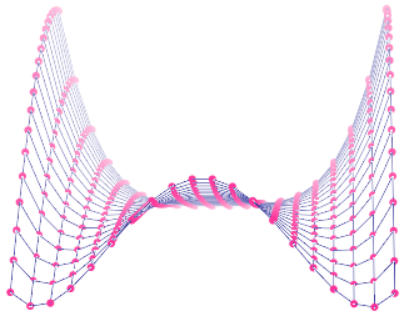

Fig.5. Equipotential field $U(\rho,\xi)=\omega U_{oct}(\rho,\xi)+\mu\ln(1+\rho)$
in the three-dimensional coordinate system Surface Plot at ω= - 1.5, μ=1

.

Conclusions

The superposition of a cylindrical field and a cylindrical octupole is interesting for the implementation of an axially-symmetric electrostatic mirror consisting of a cylindrical electrode at zero potential and an axially-symmetric deflecting electrode, the generatrix of which coincides with one of the equipotentialsof $U(\rho,\xi)=\omega U_{oct}(\rho,\xi)+\mu\ln(1+\rho)$ field. A charged particles beam can be introduced into the area of the mirror field and removed from it through the corresponding aperture windows in the cylindrical electrode. Thus, the profile of the outer deflecting electrode is determined from the calculation of the equipotential lines of the octupole-cylindrical field.

Acknowledgements

The research was supported by the Ministry of Education and Science of the Republic of Kazakhstan, Grant number AP09058188

REFERENCES

1 Zashkvara V.V., Korsunsky M.I., Kosmachev O.S. Focusing properties of an electrostatic mirror with a cylindrical field. *Zhurnal tekhnicheskoy fiziki*, 1966, Vol. 36, pp. 132 – 138. [in Russian].

2 Zashkvara V.V., Ashimbaeva B.U., Bylinkin A.F. Spectrograph regime in an energy analyzer of two cylindrical mirrors. *Zhurnal tekhnicheskoy fiziki,* 1988, Vol.58, No. 10. - pp.2021-2025.[in Russian]

3 Zashkvara V.V., Tyndyk N.N. Axial symmetric electrostatic multipoles and their applications.*Zhurnal tekhnicheskoy fiziki*,1991, Vol.61, No. 4. - pp.148-157.[in Russian]

4 ZashkvaraV.V., Tyndyk N.N. Electrostatic axially symmetric multiple in deflector-type analyzers. *Nuclear Instruments & Methods in Physics Research*, 1992, Vol. A313.- pp. 315-327.

5 Zashkvara V.V., Ashimbaeva B.U., Chokin K.Sh. Calculation of trajectories in a multipole cylindrical field. *Journal of Electron Spectroscopy and Related Phenomena*, 2002, Vol. 122, - pp.195-202.

6 Zashkvara V.V., Tyndyk N.N. The method for the calculation of multipole-cylindrical fields. *Nuclear Instruments & Methods in Physics Research. Section A,* 1999, A370, - pp. 223-231.

7 Saulebekov A.O., Vénos D., Kambarova Zh.T., Saulebekova D.A., Vassilyeva K.I., Seidualy K.B. Development of energy analyzer of charged particles based on the basis non-uniform electrostatic field. *Eurasian Physical Technical Journal*, 2019, Vol.16, No.1(31). pp. 24 - 29.

8 Kambarova Zh.T., Saulebekov A.O. Development of mirror energy analyzer based on electrostatic quadrupole-cylindrical field. *Eurasian Physical Technical Journal,* 2017, V.14, No. 2 (28). pp. 42 – 47.

9 Assylbekova S.N., Saulebekov A.O., Kambarova Zh.T. Numerical modeling of the electrostatic energy analyzer based on hexapole-cylindrical field with a concave outer electrode. *Eurasian Physical Technical Journal*, 2015, V.12, No. 1 (23). – pp.25-29.

10 Kambarova Zh.T., Trubitsyn A.A., Saulebekov A.O. Axially symmetric energy analyzer based on the electrostatic decapole-cylindrical field. *Technical Physics,* 2018, Vol. 63, No. 11, pp. 1667–1671.

11 Kambarova Z.T., Saulebekov A.O., Saulebekova D.A. Modeling of electrostatic decapole-cylindrical mirror analyzer. *IOP Conference Series: Materials Science and Engineering*, 2017, No. 12, pp. 012078. DOI:10.1088/1757-899X/168/1/012078

12 Saulebekov A.O., Venos D., Kambarova Zh.T. The high resolution electrostatic energy analyzer for space research. *Eurasian Physical Technical Journal*, 2020, V.17(33). pp.163-168.

Article accepted for publication 21.05.2021

SUMMARIES	ТҮСІНІКТЕМЕЛЕР	АННОТАЦИИ

Шишулин А. В., Потапов А. А., Шишулина А. В.
ФРАКТАЛДЫ МОРФОЛОГИЯҒА ИЕ МЕЗОКЕУЕКТІ МАТЕРИАЛДАРДАҒЫ ФЕРРОМАГНИТТІК ЖӘНЕ ПАРАМАГНИТТІК КҮЙЛЕР АРАСЫНДАҒЫ АУЫСУ ТУРАЛЫ
Берілген жұмыста мезокеуекті ферромагниттік материалдардағы кеуектердің болуы және олардың морфологиясының магниттік өзгерістердің температурасына әсері көрсетілген. Модельдік есептеулердің нәтижелерінен Кюри температурасының айтарлықтай төмен мәндері кезінде макроскопиялық мезокеуекті құрылымдарды алу мүмкіндігі анықталды, оның мөлшері кеуек пішінінің «күрделенуімен» қосымша кемиді. Нәтижелер материалдың Кюри температурасы мен оның когезия энергиясы арасындағы эксперименттік тексерілген корреляциясы негізінде алынған және таза мезокеуекті темір, никель және кобальт мысалында суреттелген. Фракталдық геометрия әдістерін пайдалана отырып, кеуектердің морфологиясының сипаттамасы жүргізілген. Соңғы бөлімде Кюри температурасының басқарылатын мәнімен кеуекті материалдарды практикалық қолданудың әр түрлі нұсқалары талқыланады.

Шишулин А.В., Потапов А.А., Шишулина А.В.
О ПЕРЕХОДЕ МЕЖДУ ФЕРРОМАГНИТНЫМИ И ПАРАМАГНИТНЫМИ СОСТОЯНИЯМИ В МЕЗОПОРИСТЫХ МАТЕРИАЛАХ С ФРАКТАЛЬНОЙ МОРФОЛОГИЕЙ
В настоящей работе продемонстрировано влияние присутствия пор и их морфологии на температуры магнитных превращений в мезопористых ферромагнитных материалах. Из результатов модельных расчетов следует возможность получения макроскопических мезопористых структур с заметно сниженными значениями температуры Кюри, величина которой дополнительно уменьшается при «усложении» формы пор. Результаты получены на основе экспериментально верифицированной корреляции между температурой Кюри материала и его энергией когезии и проиллюстрированы на примере чистых мезопористых железа, никеля и кобальта. Описание морфологии пор произведено с использованием методов фрактальной геометрии. В заключительной части обсуждаются различные варианты практического применения пористых материалов с управляемым значением температуры Кюри.

Ибраев Н.Х., Джанабекова Р.Х., Аманжолова Г.С.
N-ЖӘНЕ S-ТОПТАРЫ БАР КӨМІРТЕКТІ КВАНТТЫҚ НҮКТЕЛЕРДІҢ СПЕКТРЛІК ЖӘНЕ ЛЮМИНЕСЦЕНТТІК ҚАСИЕТТЕРІ
Ұсынылған жұмыста лимон қышқылы мен L-цистеин негізінде микротолқынды синтез әдісімен көміртекті кванттық нүктелер алынды. Алынған бөлшектер электронды және зондты микроскопия, жарықтың динамикалық шашырауы және Фурье түрлендіруі бар инфрақызыл спектроскопия әдістерімен сипатталды. Спектрлік-люминесценттік қасиеттер бастапқы ерітінді үшін, сондай-ақ синтезделген өнімнің диализі нәтижесінде алынған ерітінділер үшін зерттелді. Барлық ерітінділер бірдей оптикалық қасиеттерді көрсетеді. Сонымен қатар, кванттық шығымдарды өлшеу кезінде диализдік мембрана арқылы өтетін көміртекті нүктелері жақсы флуоресцентті қабілетке ие екенін көрсетті.

Ибраев Н.Х., Джанабекова Р.Х., Аманжолова Г.С.
СПЕКТРАЛЬНЫЕ И ЛЮМИНЕСЦЕНТНЫЕ СВОЙСТВА УГЛЕРОДНЫХ КВАНТОВЫХ ТОЧЕК, ФУНКЦИОНАЛИЗИРОВАННЫХ N- И S-СОДЕРЖАЩИМИ ГРУППАМИ
В представленной работе получены углеродные квантовые точки методом микроволнового синтеза на основе лимонной кислоты и L-цистеина. Полученные частицы были охарактеризованы методами электронной и зондовой микроскопии, методом динамического рассеяния света и инфракрасной спектроскопии с Фурье преобразованием. Спектрально-люминесцентные свойства были исследованы для исходного раствора, а также растворов, полученных в результате диализа синтезированного продукта. Показано, что все образцы демонстрируют одинаковые оптические свойства. В то же время измерение квантовых выходов показало, что лучшей флуоресцентной способностью обладают углеродные точки, прошедшие через диализную мембрану.

Суржиков А.П., Малышев А.В., Лысенко Е.Н., Шевелева Е.А.Стары О., Гынгазов А.С.
РАДИАЦИЯЛЫ-ТЕРМИЯЛЫҚ ЖАҒДАЙЛАРДА ҚАҚТАЛҒАН КЕРАМИКАЛЫҚ ЛИТИЙ-ТИТАН ФЕРРИТТЕРІНДЕГІ ЭЛЕКТР ТАСЫМАЛДАУ
Радиациялық–термиялық жағдайларда қақталған ферриттердің Li–Ti керамикалық үлгілерінде электртасымалдаудың зерттеулері жүргізілген. Радиациялық әсерлерді анықтау үшін термиялық жағдайларда қақталған үлгілерінде ұқсас өлшеулер жүргізілген. Дән аралық шекаралардың күйі және жеңіл қорытылатын

қоспаның бар болуының қақталатын ферриттердің электрлік қасиеттеріне әсері зерттелді. Радиациялық-термиялық синтездеу кезінде ферриттің электрлік қасиеттері үшін ең маңызды құрылымның қайта құрылуы қақталудың алғашқы кезеңдерінде, оның ішінде қыздыру кезеңінде жүретіні және сұйық фазаның ұнтақтар массиві бойынша таралудың радиациялық интенсификациясымен және дәнаралық шығып кетуімен байланысты екендігі анықталды.

Суржиков А.П., Малышев А.В., Лысенко Е.Н., Шевелева Е.А.Стары О., Гынгазов А.С.
ЭЛЕКТРОПЕРЕНОС В КЕРАМИЧЕСКИХ ЛИТИЙ-ТИТАНОВЫХ ФЕРРИТАХ, СПЕЧЕННЫХ В РАДИАЦИОННО-ТЕРМИЧЕСКИХ УСЛОВИЯХ
Выполнены исследования электропереноса в керамических образцах Li–Ti ферритов, спеченных в радиационно-термических условиях. Для выявления радиационных эффектов аналогичные измерения проводились на образцах, спеченных в термических условиях. Изучено влияние состояния межзеренных границ и наличия легкоплавкой добавки на электрические свойства спекаемых ферритов. Установлено, что наиболее существенная для электрических свойств феррита перестройка структуры при радиационно-термическом спекании происходит на ранних стадиях спекания, включая период разогрева, и связывается с радиационной интенсификацией растекания жидкой фазы по массиву порошинок и стимуляцией межзеренного проскальзывания.

Козловский А.Л.
ГЕЛИЙ ЖӘНЕ СУТЕГІ ИОНДАРЫМЕН СӘУЛЕЛЕНГЕН КЕЗДЕ AIN КЕРАМИКАЛАРДЫҢ РАДИАЦИЯЛЫҚ ЗАҚЫМДАНУЛАРЫНЫҢ ШЕКТІ ДОЗАЛАРЫН АНЫҚТАУ
Жұмыс гелий және сутегі иондарымен сәулелендіру кезінде алюминий нитридіне негізделген поликристалды керамикалардағы жылу өткізгіштік, оқшаулау және механикалық қасиеттердің радиациялық зақымдану кинетикасын зерттеуге, сондай-ақ максималды қайтымсыз салдарларды тудыратын сыни дозаларды анықтауға арналған. Сәулелендіру үшін иондарды таңдау кейіннен газ толтырылған көпіршіктердің пайда болуымен беттік қабатының құрылымында гелий мен сутегі иондарының жинақталуы кезіндегі радиациялық зақымдану процестерін модельдеу мүмкіндігімен байланысты. Жүргізілген зерттеулер барысында $1x10^{17}$ ион/см^2 жоғары гелий иондарымен сәулелену дозалары кезінде жылу өткізгіштіктің күрт төмендеуі және керамикаға төзімділіктің кемуі байқалады, бұл гелий көпіршіктерінің пайда болуының басталуымен және беттік қабаттың ішінара сыңғақтануымен байланысты. Алайда сәулелену дозасының $5x10^{17}$ ион/см^2-ден жоғары мәндері жылу өткізгіштіктің және оқшаулау сипаттамаларының елеулі өзгерістеріне әкелмейді, бұл радиациялық зақымданулардың жинақталу әсерін және керамиканың тозу жылдамдығының төмендеуін көрсетеді. Гелий иондарымен сәулеленуден айырмашылығы, сутегі иондарымен $1\text{-}3x10^{17}$ ион/см^2-ден жоғары дозаларға дейін сәулелену жылу оқшаулау сипаттамаларының айтарлықтай өзгерістеріне әкелмейді, бұл керамиканың гидрлеу процестеріне тұрақтылығын көрсетеді.

Козловский А.Л.
ОПРЕДЕЛЕНИЕ КРИТИЧЕСКИХ ДОЗ РАДИАЦИОННЫХ ПОВРЕЖДЕНИЙ ALN КЕРАМИК ПРИ ОБЛУЧЕНИИ ИОНАМИ ГЕЛИЯ И ВОДОРОДА
Работа посвящена исследованию кинетики радиационных повреждений теплопроводящих, изоляционных и механических свойств в поликристаллических керамиках на основе нитрида алюминия при облучении ионами гелия и водорода, а также определению критических доз, вызывающих максимальные необратимые последствия. Выбор ионов для облучения обусловлен возможностью моделирования процессов радиационных повреждений при накоплении ионов гелия и водорода в структуре приповерхностного слоя с последующим образованием газонаполненных пузырьков. В ходе проведенных исследований установлено, что при дозах облучения ионами гелия выше $1x10^{17}$ ион/см^2 наблюдается резкое ухудшение теплопроводности и снижение сопротивления керамик, что связано с началом формирования гелиевых пузырьков и частичному охрупчиванию приповерхностного слоя. Однако увеличение дозы облучения выше $5x10^{17}$ ион/см^2 не приводит к существенным изменениям теплопроводности и изоляционных характеристик, что свидетельствует об эффекте накопления радиационных повреждений и снижению скорости деградации керамик. В отличие от облучения ионами гелия, облучение ионами водорода до доз выше $1\text{-}3x10^{17}$ ион/см^2 не приводит к существенным изменениям теплоизоляционных характеристик, что свидетельствует об устойчивости керамик к процессам наводораживания.

Ибраев Н.Х., Афанасьев Д.А., Омарова Г.С.
АНОДТАЛҒАН АЛЮМИНИЙ КЕУЕКТЕРІНДЕГІ МЕРАЦИАНИНДІ БОЯҒЫШТЫҢ МӘЖБҮРЛЕНГЕН СӘУЛЕЛЕНУІНІҢ ЕРЕКШЕЛІКТЕРІ
Кеуекті алюминий оксидінің қабыршағындағы мерацианинді бояғыш молекулаларының спектрлік-люминесценттік қасиеттерін және мәжбүрленген сәулеленуін зерттеу нәтижелері келтірілген. Кеуекті

алюминий оксидінің қабыршақтарына күміс нанобөлшектерді қосу жұтылу қимасының өсуіне және кеуекті алюминий оксидінің қабыршақтарындағы боyғыштың флуоресценттік кванттық шығуының жоғарылауына әкеледі. Алайда, күміс нанобөлшектері бар кеуекті алюминий оксидінің қабыршақтарында бояғыш молекулалардың мәжбүрленген сәулеленуінің генерациясы табылған жоқ. Сонымен қатар, бояғышы бар кеуекті алюминий оксидінің қабыршақтарының бетіне жағылған полиметилметакрилат полимерінің спектрлік-люминесценттік қасиеттеріне және осы бояғыштың мәжбүрленген сәулеленуінің пайда болуына әсері зерттелді. Бояғыштың жұтылу жолағында оптикалық тығыздықтың өсуі және полиметилметакрилат қабыршағы бар үлгілерде флуоресценция қарқындылығының жоғарылауы байқалады. Полиметинді бояғыштың генерация шегі полиметилметакрилаты бар кеуекті алюминий оксидінің үлгісінде 40 есе азаяды.

Ибраев Н.Х., Афанасьев Д.А., Омарова Г.С.
ОСОБЕННОСТИ ВЫНУЖДЕННОГО ИЗЛУЧЕНИЯ МЕРАЦИАНИНОВОГО КРАСИТЕЛЯ В ПОРАХ АНОДИРОВАННОГО АЛЮМИНИЯ
Приведены результаты исследования спектрально-люминесцентных свойств и генерации вынужденного излучения молекул мерацианинового красителя в пленках пористого оксида алюминия. Добавление наночастиц серебра в пленки пористого оксида алюминия приводит к росту сечения поглощения и увеличению квантового выхода флуоресценции красителя в пленках пористого оксида алюминия. Однако, в пленках пористого оксида алюминия с наночастицами серебра генерация вынужденного излучения молекул красителя не обнаружена. Так же изучено влияние полимера полиметилметакрилата, нанесенного на поверхность пленок пористого оксида алюминия с красителем, на спектрально-люминесцентные свойства и генерацию вынужденного излучения данного красителя. Наблюдается рост оптической плотности в полосе поглощения красителя и рост интенсивности флуоресценции в образцах с нанесенной пленкой полиметилметакрилата. Порог генерации полиметинового красителя снижается в 40 раз в образце пористого оксида алюминия с полиметил-метакрилатом.

Рахадилов Б.К., Акатан К., Маулет М., Кабдрахманова С.К., Мағазов Н.М.
ЭЛЕКТРОН ШОҒЫРЫНЫҢ ПОЛИАМИД 6 –НЫҢ ФИЗИКА-ХИМИЯЛЫҚ ҚАСИЕТТЕРІНЕ ӘСЕРІН ЗЕРТТЕУ
Берілген зерттеу жұмысында РА6 полиамидінің қасиеттері мен құрылымына электрон шоғырының әсері зерттелінген. Өңдеу ауада 100-400 кГр диапазонындағы сәулелену дозасымен өнеркәсіптік импульсті үдеткіште жүргізілді. Өңделген полимер Фурье түрлендіруі бар инфрақызыл спектроскопия, сканерлеуші электрондық микроскопия, рентген фазалық талдау және дифференциалды сканерлеуші калориметрия әдістерімен зерттелінген. Зерттеу нәтижелері бойынша электронды-сәулелік өңдеу РА6-полиамидінің кристалды құрылымына әсер етіп, оның өлшемін төмендететіні анықталды. Сондай-ақ, 200 кГр сәулелену дозасы 100, 300 және 400 кГр-мен салыстырғанда кристалл құрылымының сақталуы үшін оңтайлы екендігі анықталды.

Рахадилов Б.К., Акатан К., Маулет М., Кабдрахманова С.К., Мағазов Н.М.
ИССЛЕДОВАНИЕ ВЛИЯНИЯ ЭЛЕКТРОННОГО ПУЧКА НА ФИЗИКО-ХИМИЧЕСКИЕ СВОЙСТВА ПОЛИАМИДА 6
В данной исследовательской работе было изучено влияние электронного облучения на свойства и структуру полиамида РА6. Обработка проводилась на промышленном импульсном ускорителе на воздухе с дозой облучения в диапазоне 100-400 кГр. Обработанный полимер также исследовали с помощью инфракрасной спектроскопии с преобразованием Фурье, сканирующей электронной микроскопии, рентгенофазового анализа и дифференциальной сканирующей калориметрии. По результатам исследования выявлено, что электронно-лучевая обработка влияет на кристаллическую структуру полиамида-РА6, уменьшая его размер. Также было обнаружено, что доза облучения 200 кГр является оптимальной для сохранения кристаллической структуры по сравнению с 100, 300 и 400 кГр.

Зейниденов А.К., Абишева А.К., Ильясов Б.Р., Аймуханов А.К., Абильмажинов С.Е.
ZNO ҚАБЫРШАҚТАРЫНЫҢ ҚҰРЫЛЫМДЫҚ ЕРЕКШЕЛІКТЕРІНІҢ КЕРІ ПОЛИМЕРЛІ КҮН ЭЛЕМЕНТТЕРІНІҢ ОПТИКАЛЫҚ ЖӘНЕ ФОТОЭЛЕКТРЛІК СИПАТТАМАЛАРЫНА ӘСЕРІ
Берілген жұмыста мырыш ацетаты ерітіндісін алдын-ала қыздыру арқылы қалыптасқан ZnO қабыршақтарының құрылымдық, морфологиялық, оптикалық және фотовольтаикалық сипаттамалары полимерлі күн элементтерінің қасиеттеріне әсері зерттелді. Алдын-ала қыздыру температурасы ZnO қабыршақтарының морфологиясы мен құрылымына айтарлықтай әсер ететіндігі анықталды. Қыздыру температурасы 200^{o}C төмен болған жағдайда, қабыршақтар жоғары рельефті морфологияға ие болады, керісінше 200^{o}C-тан жоғары болса, қабыршақ морфологиясы тегістеледі. ZnO қабыршақтарының рельефтілігі күн элементтерінің фототок тығыздығына әсер етеді: морфологиясы кедір-бұдыр қабыршақтар тегіс қабыршақтарға қарағанда фототоктың

үлкен мәндерін көрсетті. Себебі мұнда жарықтың қатты шашырауы байқалады және осыған байланысты күн элементтерінің фотоактивті қабатында жарықтың оптикалық жолы арта түседі. Ал оптикалық жолдың артуы ZnO кедір-бұдырлы морфологиялық қабыршағындағы жарықтың бірнеше рет шағылуына байланысты болып табылады. Сондай-ақ, қабыршақтарды қыздыру температурасын арттырған сайын күн элементтерінің заряд тасымалдаушылардың рекомбинация жылдамдығы, кернеуі артатыны, сәйкесінше заряд тасымалдаушылардың диффузия коэффициентінің кемуі нәтижесінде ZnO кристалдық тор дефектісінің тығыздығы артатыны байқалады. Жалпылама айтқанда, бұл мақалада мырыш ацетаты ерітіндісінен кедір-бұдырлы және тегіс морфологиялы ZnO жұқа қабықшаларын алуға болатыны көрсетілген.

Зейниденов А.К., Абишева А.К., Ильясов Б.Р., Аймуханов А.К., Абильмажинов С.Е.

ВЛИЯНИЕ СТРУКТУРНОЙ ОСОБЕННОСТИ ПЛЕНОК ZNO НА ОПТИЧЕСКИЕ И ФОТОЭЛЕКТРИЧЕСКИЕ ХАРАКТЕРИСТИКИ ИНВЕРТИРОВАННЫХ ПОЛИМЕРНЫХ СОЛНЕЧНЫХ ЭЛЕМЕНТОВ.

В данной работе исследовалось влияние предварительного отжига пленок раствора ацетат цинка на морфологию, структуру, оптические свойства формируемых пленок ZnO и также на фотовольтаические свойства полимерных солнечных ячеек на основе полученных пленок ZnO. Установлена, что температура предварительного отжига значительно влияет на морфологию и структуру полученных пленок ZnO. При температурах предотжига ниже 200 ^{o}C пленки имеют сильно рельефную морфологию (морщинистую морфологию), тогда как при температурах предотжига выше 200 ^{o}C, морфология поверхности пленок получается гладкой. Рельефность пленок ZnO влияет на плотность фототока солнечных ячеек, ячейки на основе пленок ZnO с морщинистой морфологией показали большее значение фототока по сравнению с гладкой морфологией, что обусловлена сильным рассеянием света и за счет этого увеличивается оптически путь света в фотоактивном слое за счет многократного отражения света в морщинистой структуре ZnO. Кроме того, с увеличением температуры предотжига пленок увеличивается фотонапряжения солнечных ячеек, увеличивается скорость рекомбинации носителей заряда и уменьшается коэффициент диффузии носителей заряда, что указывает об увеличении плотности дефектов кристаллической решетки ZnO. Таким образом, показано, что из раствора ацетата цинка можно получать гладкие или сильно рельефные тонкие пленки ZnO с контролируемыми свойствами.

Моисеева К.М., Крайнов А.Ю., Крайнов Д.А.

ЖОҒАРЫ ЖЫЛДАМДЫҚТЫ БҰРАЛҒАН АҒЫНДАҒЫ АЛЮМИНИЙ ҰНТАҒЫНЫҢ АЭРОЖҮЗІНДІСІНІҢ ЖАНУ ЕРЕКШЕЛІКТЕРІ

Мақала бұралған ағыны бар жану камерасындағы ұнтақталған металл отынының жану мәселесін сандық шешуге арналған. Алюминий ұнтағының ауа суспензиясының ағынының физика-математикалық моделі кенеттен кеңейетін бұралған ағынына ие цилиндрлік жану камерасында ұсынылған. Мәселенің физика-математикалық тұжырымы екі фазалы әрекеттесетін ортаның механикасының әдіс-тәсілдеріне негізделген. Шешім еркін үзілісті ыдырау әдісімен жүзеге асырылды. Алюминий ұнтағының ауа суспензиясының жану ерекшеліктерінің оның құрамына, жану камерасына кіретін қоспаның осьтік шығынына және бұралу жылдамдығының мәніне байланысты сандық параметрлік зерттеу нәтижелері келтірілген.

Моисеева К.М., Крайнов А.Ю., Крайнов Д.А.

ОСОБЕННОСТИ ГОРЕНИЯ АЭРОВЗВЕСИ ПОРОШКА АЛЮМИНИЯ В ВЫСОКОСКОРОСТНОМ ЗАКРУЧЕННОМ ПОТОКЕ

Статья посвящена численному решению задачи о горении порошкового металлического топлива в камере сгорания с закрученным потоком. Представлена физико-математическая модель течения воздушной взвеси алюминиевого порошка закрученным потоком в цилиндрической камере сгорания с внезапным расширением. Физико-математическая постановка задачи основана на подходах механики двухфазных реагирующих сред. Решение проводилось методом распада произвольного разрыва. Приведены результаты численного параметрического исследования особенностей горения воздушной взвеси алюминиевого порошка в зависимости от ее состава, осевого расхода смеси на входе в камеру сгорания и значения скорости закрутки.

Манатбаев Р.К., Каласов Н.Б., Аманкелді Л.Б.

КОНЦЕНТРАЦИЯЛЫҚ-ПОЛЯРИЗАЦИЯ ҚАБАТЫНЫҢ ПАЙДА БОЛУЫН САНДЫҚ ЗЕРТТЕУ

Жұмыста H_2/CO_2 газ қоспасын бөлу процесінде мембрана бетіндегі концентрациялық поляризациялық шекара қабатының пайда болуы сипатталған. Концентрациялық поляризация қабылданбаған ерітінді мембрана бетіне жақын жиналып, шекара қабатын құрған кезде пайда болады. Кеуекті қабырғаларды өңдеуге концентрациялық поляризация әсерін қосу қосымша қиындықтар туғызады. Концентрациялық поляризация нәтижесінде пайда болған шекаралық қабатты мембранаға қарағанда өткізгіштігі төмен екінші кеуекті қабырғаның бір түрі ретінде

қарастыруға болады. Бұл жағдайды модельдеудегі негізгі қиындық қабырғадағы шоғырланудың тиісті шекаралық жағдайларын анықтау болып табылады, өйткені концентрациялар қабырғада үнемі өзгеріп отырады, ал бөлшектердің тұнып кетуіне байланысты қабырға геометриясының өзі уақыт өте келе өзгеруі мүмкін. Бұл әсерді ескеру үшін бұл жұмыста талқыланатын сандық тәсілдер әзірленді.

Манатбаев Р.К., Каласов Н.Б., Аманкелды Л.Б.
ЧИСЛЕННОЕ ИССЛЕДОВАНИЕ ВОЗНИКНОВЕНИЯ КОНЦЕНТРАЦИОННО-ПОЛЯРИЗАЦИОННОГО СЛОЯ

В работе описывается возникновение концентрационного поляризационного пограничного слоя на поверхности мембраны в процессе сепарации газовой смеси H_2/CO_2. Концентрационная поляризация возникает, когда отбракованный раствор накапливается рядом с поверхностью мембраны, образуя пограничный слой. Включение концентрационных поляризационных эффектов в обработку пористых стенок создает дополнительные трудности. Граничный слой, образованный концентрационной поляризацией, можно рассматривать как разновидность второй пористой стенки с меньшей проницаемостью, чем мембрана. Основная трудность при моделировании этой ситуации заключается в определении соответствующих граничных условий концентрации на стенке, поскольку концентрации будут постоянно изменяться на стенке, а сама геометрия стенки может меняться со временем из-за осаждения частиц. Для учета этого эффекта был разработан численный подход, который обсуждается в данной работе.

Мехтиев А.Д., Сарсикеев Е.Ж., Югай В.В., Нешина Е.Г., Алькина А.Д.
АВТОНОМДЫ ТҰТЫНУШЫЛАРДЫ ЭНЕРГИЯМЕН ҚАМТАМАСЫЗ ЕТУ ҮШІН ТӨМЕН ҚУАТТЫ ЭНЕРГИЯНЫҢ КОГЕНЕРАЦИЯЛЫҚ КӨЗІ РЕТІНДЕ ТЕРМОАКУСТИКАЛЫҚ ҚОЗҒАЛТҚЫШ

Мақалада әр түрлі отын түрлері мен жағылатын қалдықтарда жұмыс істей алатын тұтынушыларды автономды энергиямен қамтамасыз ету үшін төмен қуаттың когенерациялық көзі ретінде термоакустикалық қозғалтқышты пайдалану мәселесі қарастырылады. Энергетика саласындағы әлемдік жетістіктерге талдау жасалды. Оның бірқатар артықшылықтары қазіргі заманғы жылу электрстанцияларына қарағанда тиімділігі жоғары электр және жылуэнергиясын өндіруге қабілетті энергия көздерін дамыту үшін өте перспективті етеді. ЖЭО-тың ұсынылған сұлбасы Стирлинг қозғалтқышының принципіне негізделген, бірақ онда тиімді және перспективті термоакустикалық жылу түрлендіргішін механикалық тербелістерге пайдаланады, содан кейін олар электр тогына айналады. Мақалада әзірленген термо-акустикалық қозғалтқыштың негізгі жұмыс принциптерін түсіндіретін математикалық аппарат ұсынылған. Термоакустикалық қозғалтқыштың негізгі параметрлерін анықтау үшін DeltaEC ортасында компьютерлік модельдеу әдістері қолданылды. Жылуэлектрстанциясының зертханалық үлгісінің орналасу сұлбасы ұсынылған және оның дизайнына сипаттама берілген. Жұмыс денесі ретінде құрғақ қаныққан буды пайдалану ұсынылады, бұл жылуакустикалық қозғалтқыштың генерацияланған қуатын арттыруға мүмкіндік береді.

Мехтиев А.Д., Сарсикеев Е.Ж., Югай В.В., Нешина Е.Г., Алькина А.Д.
ТЕРМОАКУСТИЧЕСКИЙ ДВИГАТЕЛЬ КАК КОГЕНЕРАЦИОННЫЙ ИСТОЧНИК ЭНЕРГИИ МАЛОЙ МОЩНОСТИ ДЛЯ ЭНЕРГООБЕСПЕЧЕНИЯ АВТОНОМНЫХ ПОТРЕБИТЕЛЕЙ

В статье рассматривается вопрос использования термоакустического двигателя в качестве когенерационного источника малой мощности для автономного энергоснабжения потребителей, способных работать на различных видах топлива и сжигаемых отходах. Проведен анализ мировых достижений в этой области энергетики. Ряд преимуществ делает его очень перспективным для разработки источников энергии, способных комплексно производить электрическую и тепловую энергию с большей эффективностью, чем у современных тепловых электростанций. Предлагаемая схема ТЭЦ основана на принципе двигателя Стирлинга, но в ней используется наиболее эффективный и перспективный термоакустический преобразователь тепла в механические колебания, которые затем преобразуются в электрический ток. В статье представлен математический аппарат, поясняющий основные принципы работы разработанного термоакустического двигателя. Для определения основных параметров термоакустического двигателя использовались методы компьютерного моделирования в среде DeltaEC. Предложена компоновочная схема лабораторного образца тепловой электростанции и дано описание ее конструкции. В качестве рабочего тела предложено использовать сухой насыщенный пар, что позволяет увеличить генерируемую мощность термоакустического двигателя.

Кубич В.И., Чернета О.Г., Юров В.М.
«БОЛАТ 45 - 40Х» ЖҮЙЕСІНДЕГІ АДГЕЗИЯЛЫҚ БАЙЛАНЫС ПАРАМЕТРЛЕРІНЕ 45 БОЛАТТЫҢ БОРЛАУДЫҢ, БОРОЦЕМЕНТАЦИЯСЫНЫҢ ЖӘНЕ МАЙЛАУ МАТЕРИАЛЫНЫҢ ТҰТҚЫРЛЫҒЫНЫҢ ӘСЕРІ

Жұмыста СМЦ - 2 үйкеліс машинасының қосымша жабдығын пайдалана отырып, ерекше динамикалық

тұтқырлығына ие И-20А, Wolf 10W-40, ТАД-17и, Литол-24 майлау материалдары ортасында шағын габаритті үлгілер арасындағы ығысуды физикалық модельдеу кезінде «болат 45-40Х», «болат 45+В-40Х», «болат 45+ВС-40Х» металдар жүйелеріндегі τ адгезиялық байланысының ығысу беріктігінің және β пьезокоэффициенттің өзгеру заңдылықтары алынды. Ығысу жылдамдығының екі есе артуы Wolf 10W - 40, ТАД-17и, Литол-24 майлау материалдары үшін «болат 45+ВС-40Х» жүйесінде пьезокоэффициенттің 1,2-1,6 есе азаюына және оның динамикалық тұтқырлыққа тәуелді болмайтын салыстырмалы бірдейлігіне байланысты екені анықталды. Бұл кезде «болат 45+в - 40Х» жүйесінде ығысу жылдамдығының екі есе артуы барлық сынақ майлау материалдары үшін пьезокоэффициенттің 1,16-1,38 есе азаюына себепші болады, ал «болат 45 +ВС» жүйесіндегідей оның тегістелуі байқалмайды. p=0 МПа кезінде эквивалентті динамикалық тұтқырлықтың адгезиялық байланыс беріктігіне әсер етудің айқын заңдылығы анықталмайды және оның көріну сипаты майлау материалдары молекулаларының құрылымына байланысты молекулааралық өзара әрекеттесу механизмінің мүмкін болатын өзгеруімен анықталады. Пьезокоэффициент барлық қарастырылған қалыпты қысым диапазонында динамикалық тұтқырлықтың жоғарылауымен табиғи түрде төмендейтіні анықталды.

Кубич В.И., Чернета О.Г., Юров В.М.

ВЛИЯНИЕ БОРИРОВАНИЯ, БОРОЦЕМЕНТАЦИИ СТАЛИ 45 И ВЯЗКОСТИ СМАЗОЧНОГО МАТЕРИАЛА НА ПАРАМЕТРЫ АДГЕЗИОННОЙ СВЯЗИ В СИСТЕМЕ «СТАЛЬ 45 - 40Х»

В работе получены закономерности изменения сдвиговой прочности адгезионной связи τ и пьезокоэффициента β в системах металлов «сталь 45 - 40Х», «сталь 45+В - 40Х», «сталь 45+ВС - 40Х» при физическом моделировании сдвига между малогабаритными образцами в среде смазочных материалов И-20А, Wolf 10W-40, ТАД-17и, Литол-24 с отличительными динамическими вязкостями с использованием дополнительного оборудования машины трения СМЦ-2. Установлено, что увеличение скорости сдвига в два раза обуславливает уменьшение пьезокоэффициента в системе «сталь 45+ВС - 40Х» в 1,2-1,6 раза для смазочных материалов Wolf 10W-40, ТАД-17и, Литол-24 и его относительную одинаковость не зависящую от динамической вязкости. При этом увеличение скорости сдвига в два раза в системе «сталь 45+В - 40Х» обуславливает также уменьшение пьезокоэффициента в 1,16-1,38 раза для всех испытываемых смазочных материалов а его выравниваний, как в системе «сталь 45 +ВС» не наблюдается. Установлено, что явно выраженная закономерность влияния эквивалентной динамической вязкости на прочность адгезионной связи при p=0 МПа не выявляется, и характер проявления предопределяется возможной сменой механизма межмолекулярного взаимодействия зависящего от строения молекул смазочных материалов. При этом определено, что пьезокоэффициент закономерно уменьшается с увеличением динамической вязкости во всем рассматриваемом диапазоне нормальных давлений.

Амелькович Ю.А., Назаренко О.Б., Смирнова И.Н., Задорожная Т.А.

АНТИПИРЕНДЕРДІҢ ЭПОКСИДТІ КОМПОЗИТТЕРДІҢ ТҰТАНУ ТЕМПЕРАТУРАСЫНА ӘСЕРІН САЛЫСТЫРМАЛЫ ЗЕРТТЕУ.

Полимерлі материалдардың, соның ішінде эпоксидті шайырлардың кемшілігі олардың жоғары өрт қаупі болып табылады. Полимерлі материалдардың жанғыштығының төмендеуі шешімді қажет ететін күрделі мәселе болып табылады. Полимерлердің жанғыштығын төмендетудің бір әдісі - полимер матрицасына жалын басатын қасиеттері бар арнайы қоспаларды енгізу болып табылады, бұл полимер жанған кезде пайда болатын процестердің сипатын өзгертуге немесе жану процесін жанбайтын немесе ингибиторлық заттармен бұғаттауға әкеледі. Берілген жұмыста эпоксидті шайырдың отқа төзімді қасиеттерін жақсарту үшін алюминий гидроксиді, меламин полифосфаты және меламин полифосфаты-магний деген жалынға қарсы заттар ретінде қолданылды. Эпоксидті композиттердегі толтырғыштардың концентрациясы 10 % масса болды. Алынған эпоксидті композиттердің тұтану температурасын анықтау үшін эксперименттік зерттеулер жүргізілді. Алынған мәліметтер толтырғышсыз эпоксидті шайырдың бақылау үлгісінің тұтану температурасымен салыстырылды. Нәтижелер барлық зерттелген антипирендерді қолдану тұтану температурасының жоғарылауына әкелгенін көрсетті. Меламин полифосфаты мен меламин магний полифосфатымен толтырылған үлгілердің тұтану температурасы сәйкесінше 28 және 11 °С-қа жоғарылады. Алайда, алюминий гидроксидімен толтырылған үлгі үшін жақсы нәтиже алынды: бұл үлгінің тұтану температурасы толтырылмаған эпоксид шайырымен салыстырғанда 40 °С жоғары болды.

Амелькович Ю.А., Назаренко О.Б., Смирнова И.Н., Задорожная Т.А.

СРАВНИТЕЛЬНОЕ ИССЛЕДОВАНИЕ ВЛИЯНИЯ АНТИПИРЕНОВ НА ТЕМПЕРАТУРУ ЗАЖИГАНИЯ ЭПОКСИДНЫХ КОМПОЗИТОВ.

Недостатком полимерных материалов, в том числе и эпоксидных смол, является их повышенная пожарная опасность. Снижение горючести полимерных материалов является серьезной проблемой, требующей решения. Одним из способов снижения горючести полимеров является введение в полимерную матрицу специальных добавок, обладающих пламягасящими свойствами, что приводит к изменению характера процессов,

происходящих при горении полимера, или блокированию процесса горения негорючими или ингибирующими веществами. В данной работе для улучшения огнестойких свойств эпоксидной смолы в качестве антипиренов были использованы гидроксид алюминия, полифосфат меламина и полифосфат-магний меламина. Концентрация наполнителей в эпоксидных композитах составляла 10 масс. %. Проведены экспериментальные исследования по определению температуры воспламенения полученных эпоксидных композитов. Полученные данные были сопоставлены с температурой воспламенения контрольного образца эпоксидной смолы без наполнителя. Результаты показали, что использование всех изученных антипиренов привело к повышению температуры воспламенения. Температура воспламенения образцов, наполненных полифосфатом меламина и полифосфатом-магний меламина увеличилась на 28 и 11 °С, соответственно. Однако лучший результат был получен для образца, наполненного гидроксидом алюминия: температура воспламенения этого образца была на 40 °С выше, чем у ненаполненной эпоксидной смолы.

Жанабаев З.Ж., Үсіпов Н.М, Хохлов С.А.

ХАББЛ ПАРАМЕТРІНІҢ МАСШТАБТЫ-ИНВАРИАНТТЫ ЖӘНЕ ТОЛҚЫНДЫҚ ТАБИҒАТЫ.

Астрофизикалық бақылауларға сәйкескелетін Хаббл параметрінің мәні теориялық тұрғыдан ΛCDM моделін қолданбай анықталған. Бақыланған галактика мен оның координатасына дейінгі ара-қашықтықтың бейсызық фракталдық моделі ұсынылған. Қашықтық фракталдық өлшем ретінде анықталады, оның өлшеу масштабы белгілі фракталдық модельдерден айырмашылығы, қажетті өлшемнің өзінің бекітілген мәнінен (нөлдік ауырлық радиусы) ауытқуына сәйкес, оған қатысты масштабты инвариант қабылданды. Біз ұсынған нақты анизотропты фракталдың өлшемі пайдаланылды, ол байқауға дейінгі қашықтықтың өсуін модельдейді. Бұл өлшем сонымен қатар әр түрлі каталогтардан алынған гравитациялық толқындар мен галактикалар жиынтығы теңдеуінің фазалық портретінің таңғажайып тартқышының максималды өлшемі екендігі көрсетілген.

Жанабаев З.Ж., Усипов Н.М, Хохлов С.А.

МАСШТАБНО-ИНВАРИАНТНАЯ И ВОЛНОВАЯ ПРИРОДА ПАРАМЕТРА ХАББЛА

Значение глобального параметра Хаббла, соответствующее астрофизическим наблюдениям, определено теоретически, без использования ΛCDMмодели. Предложена нелинейная фрактальная модель связи расстояния до наблюдаемой галактики с ее координатой. Расстояние определяется как фрактальная мера, масштаб измерения которой, в отличие от известных моделей фракталов, соответствует отклонению самой искомой меры от ее фиксированного значения (радиуса нулевой гравитации), относительно которого принимается масштабная инвариантность. Использована размерность предложенного нами специфического анизотропного фрактала, который моделирует рост расстояния до наблюдения. Показано, что эта размерность является также максимальной размерностью странного аттрактора фазового портрета уравнения гравитационных волн и множеств галактик по различным каталогам.

Витковская И.С., Батырбаева М.Ж.

ВЕГЕТАЦИЯЛЫҚ ИНДЕКСТЕРДІҢ УАҚЫТ ҚАТАРЛАРЫН ҚАЛЫПТАСТЫРУ КЕЗІНДЕ СЕРІК МӘЛІМЕТТЕРІН ӨҢДЕУ АЛГОРИТМІ

Әлемді ғарыштан қашықтықтан зондтаудың әлемдік тәжірибесінде серік суреттерінен есептелген әр түрлі спектрлік көрсеткіштер кең қолданылады. Бұл тәсіл төсеніш бетті ғарыштық бақылауда, олардың динамикасындағы болып жатқан өзгерістер мен тенденцияларды анықтауда өзін ақтады. Жерсеріктік мәліметтерінің жинақталған үлкен көлемі, тақырыптық дешифрлеу әдістерінің заманауи дамуы суреттерге де, оларды өңдеу нәтижелеріне де еркін қол жеткізуді ұсынатын қызметтердің құрылуына әкелді. Алайда, жергілікті және аймақтық масштабтағы мәселелерді шешу кезінде белгілі қызметтердің ұсынатын ғарыштық ақпараттарды тақырыптық өңдеу үшін дайын өнімді пайдалану әрдайым тиімді бола бермейді. Осыған байланысты серік индекстердің ұзақ мерзімді қатарлары туралы өзіміздің мұрағатымызды қалыптастыру қажеттілігі туды. Индекстердің сандық матрицаларына ие файлдардың көлемі MODIS серігінен төмен ажыратуға ие мәліметтер бойынша есептелген, ондағы Қазақстан аумағын толық қамтитын файлдардың көлемі 4 ГБ-тан асады. Бұл есептеулердің баяулауына және көбінесе орташа қуатты компьютерлерде толық матрицаны есептеу мүмкін еместігіне әкеледі. Мақалада вегетациялық индексінің уақыттық қатарын құруда серік мәліметтерін өңдеу алгоритмі келтірілген. Нәтижесінде, республика аумағына арналған вегетациялық индекстерінің ұзақ мерзімді мұрағаты құрылды (2001-2020 жж.), бұл төсеніш бетіндегі өзгерістерді талдауға, олардың тенденцияларын анықтауға және осы өзгерістерді болжауға негіз болады.

Витковская И.С., Батырбаева М.Ж.

АЛГОРИТМ ОБРАБОТКИ СПУТНИКОВЫХ ДАННЫХ ПРИ ФОРМИРОВАНИИ ВРЕМЕННЫХ РЯДОВ ВЕГЕТАЦИОННЫХ ИНДЕКСОВ

В мировой практике дистанционного зондирования Земли из космоса широко используются различные спектральные индексы, рассчитываемые по спутниковым снимкам. Этот подход оправдал себя при

космическом мониторинге подстилающей поверхности, детектировании происходящих изменении и тенденций их динамики. Накопленный колоссальный объем спутниковых данных, современное развитие методов тематического дешифрирования привели к созданию сервисов, предлагающих в свободном доступе, как сами снимки, так и результаты их обработки. Однако, при решении задач локального и регионального масштаба использование готовых продуктов тематической обработки космической информации, представляемых известными сервисами, не всегда является эффективным. В связи с этим, возникает необходимость формирования собственных архивов многолетних рядов спутниковых индексов. Объем файлов, содержащих цифровые матрицы индексов, рассчитанных по данным низкого разрешения спутника MODIS, при полном покрытии территории Казахстана, превышает 4 Гб. Это приводит к замедлению расчетов, а зачастую к невозможности расчета полной матрицы на компьютерах средней мощности. В статье представлен алгоритм обработки спутниковых данных при формировании временных рядов вегетационных индексов. В результате создан многолетний архив индексов вегетации (2001-2020 гг.) на территорию Республики, являющийся основой для анализа изменений подстилающей поверхности, определения их тенденций и прогноза этих изменений.

Қамбарова Ж.Т., Сәулебеков А.О., Көпбалина Қ.Б., Тусупбекова А.К., Сәулебекова Д.А.

ОСЬТІК СИММЕТРИЯЛЫҚ ОКТУПОЛЬДІ-ЦИЛИНДРЛІК ӨРІС НЕГІЗІНДЕ ЗАРЯДТАЛҒАН БӨЛШЕКТЕР АҒЫНДАРЫНЫҢ ТИІМДІ ЭНЕРГИЯ ТАЛДАҒЫШЫН ҚҰРУ МҮМКІНДІГІ ТУРАЛЫ

Зарядталған бөлшектердің шоқтарын энергия бойынша талдау жүйесін құрудағы мәселелерінің бірі – ауытқытушы өрісті анықтау және ауытқытушы электродтардың пішінін есептеу болып табылады. Берілген мақала мультипольдік электродты жүйелер негізінде зарядталған бөлшектер ағындарының тиімді энергия талдағышын құру мүмкіндігін зерттеуге арналған. Ауытқытушы өріс ретінде бұрын зерттелмеген мультипольді-цилиндрлік өрістің түрі - электрстатикалық осьтік-симметриялық октупольді-цилиндрлік өріс таңдалды. Өріс әр түрлі үлестердегі электрстатикалық цилиндрлік өрістің және дөңгелектік октупольдің суперпозициясы көмегімен құрылған. Симметрия және антисимметрия жазықтықтарына ие цилиндрлік октупольдердің эквипотенциалдар жиыны есептелген. Цилиндрлік өріс пен дөңгелектік октупольдің әр түрлі салмақтық үлестері кезінде электрстатикалық аксиальді-симметриялық октуполь-цилиндрлік өрістердің эквипотенциалдық суреттерінің есептеуі және талдауы жүргізілген.

Камбарова Ж.Т., Саулебеков А.О., Копбалина К.Б., Тусупбекова А.К., Саулебекова Д.А.

О ВОЗМОЖНОСТИ СОЗДАНИЯ ЭФФЕКТИВНОГО ЭНЕРГОАНАЛИЗАТОРА ПОТОКОВ ЗАРЯЖЕННЫХ ЧАСТИЦ НА ОСНОВЕ ОСЕСИММЕТРИЧНОГО ОКТУПОЛЬНО-ЦИЛИНДРИЧЕСКОГО ПОЛЯ

Одной из проблем в создании систем энергоанализа пучков заряженных частиц является определение отклоняющего поля и расчет формы отклоняющих электродов. Данная статья посвящена изучению возможности создания эффективного анализатора энергий пучков заряженных частиц на основе мультипольных электродных систем. В качестве отклоняющего поля выбрано ранее не изученный вид мультипольно-цилиндрического поля - электростатическое аксиально-симметричное октупольно-цилиндрическое поле. Поле формируются с помощью суперпозиции цилиндрического электростатического поля и кругового октуполя различных вкладов. Рассчитано семейство эквипотенциалей цилиндрических октуполей, имеющих плоскость симметрии и антисимметрии. Проведен расчет и анализ эквипотенциальных портретов электростатических аксиально-симметричных октупольно-цилиндрических полей при различных весовых вкладов цилиндрического поля и кругового октуполя.

INFORMATION ABOUT AUTHORS | **АВТОРЛАР ТУРАЛЫ МӘЛІМЕТТЕР** | **СВЕДЕНИЯ ОБ АВТОРАХ**

Abilmazhinov, S.E. - Master's student, Sh.Ualikhanov Kokshetau University, Kokshetau, Kazakhstan

Abisheva, A.K. - PhD, student, E.A Buketov Karaganda University, Karaganda, Kazakhstan

Afanasyev, D.A. – PhD, Associate Professor, Acting Director of the Institute of Applied Mathematics, E.A. Buketov Karaganda University, Karaganda, Kazakhstan

Aimukhanov, A.K. – Candidate of phys.-math.science**s,** Professor, E.A Buketov Karaganda University, Karaganda, Kazakhstan

Akatan, K. – Senior Researcher of the Testing Laboratory Physical and Chemical Research, S.Amanzholov East Kazakhstan University, Ust-Kamenogorsk, Kazakhstan

Alkina, A.D. - Master, Senior Lecturer, Karaganda Technical University, Karaganda, Kazakhstan

Amankeldi, L.B. - Master student, Department of Thermophysics and Technical Physics, Al-Farabi Kazakh National University, Almaty, Kazakhstan

Amanzholova, G.S. - PhD student, Master (Sci.), E.A. Buketov Karaganda University, Karaganda, Kazakhstan

Amelkovich, Yu.A. – Candidate of techn.sciences, Assistant professor, Tomsk Polytechnic University, Tomsk, Russia

Batyrbayeva, M.Zh. - Candidate of tech. sciences, Leading researcher, JSC "National Center of Space Research and Technology", Almaty, Kazakhstan

Cherneta, O.G. - Candidate of techn.sciences, Associate Professor, Department of Cars and Automotive Economy, Dniprovsk State technical university, Kamenskoye, Ukraine

Dzhanabekova, R.Kh. – Master (Sci.), Junior Researcher, Scientific Center of Nanotechnologies and Functional Nanomaterials, E.A. Buketov Karaganda University, Karaganda, Kazakhstan

Ghyngazov, A.S. - Head of the laboratory, NIKI Joint Stock Company, Tomsk, Russia

Ibraev, N.Kh. - Doctor of phys.-math. sciences, Professor, Director of the Institute of Molecular Nanophotonics, E.A. Buketov Karaganda University, Karaganda, Kazakhstan

Ilyassov, B.R. - PhD, E.A Buketov Karaganda University, Karaganda, Kazakhstan, Sh.Ualikhanov Kokshetau University, Kokshetau, Kazakhstan

Kabdrakhmanova, S.K. – Candidate of techn.sciences, Acting Director of the Department of Innovative Development and Commercialization, S.Amanzholov East Kazakhstan University, Ust-Kamenogorsk, Kazakhstan

Kalassov, N.B. – PhD student, Senior Lecturer, Department of Thermophysics and Technical Physics, Al-Farabi Kazakh National University, Almaty, Kazakhstan

Kambarova, Zh.T. - PhD, Associate Professor, Physical and Technical Faculty, E.A Buketov Karaganda University, Karaganda, Kazakhstan

Khokhlov, S.A. – PhD, Senior Lecturer, al-Farabi Kazakh National University, Almaty, Kazakhstan

Kopbalina, K.B. – Master, Senior Lecturer, Karaganda Technical University, Karaganda, Kazakhstan

Kozlovskiy, A.L. - PhD, Leading Researcher, Solid State Physics Laboratory, Institute of Nuclear Physics, National Nuclear Center of the Republic of Kazakhstan, Almaty; Postdoctoral student of Kh. Dosmukhamedov Atyray university, Atyrau, Kazakhstan

Krainov, A.Yu. – Doctor of phys.-math.sciences, Professor, Head of department, National Research Tomsk Polytechnic University, Tomsk, Russia

Krainov, D.A. – Candidate of phys.-math.sciences, Associative Professor, National Research Tomsk Polytechnic University, Tomsk, Russia

Kubich, V.I. - Candidate of techn.sciences, Associate Professor, Department of Cars, National University "Zaporizhzhya polytechnic", Zaporizhia, Ukraine

Lysenko, E.N. - Doctor of techn. sciences, Professor, Head of the Research Laboratory, National Research Tomsk Polytechnic University, Tomsk, Russia

Magazov, N.M. – Engineer of the Research center "Surface Engineering and Tribology", S.Amanzholov East Kazakhstan University, Ust-Kamenogorsk, Kazakhstan

Malyshev, A.V. – Candidate of phys.-math. sciences, Senior Researcher, National Research Tomsk Polytechnic University, Tomsk, Russia

Manatbayev, R.K. - Candidate of tech. sciences, Associate Professor, Department of Thermophysics and Technical Physics, Al-Farabi Kazakh National University, Almaty, Kazakhstan

Maulet, M. – Junior Researcher of the Research center "Surface Engineering and Tribology", S.Amanzholov East Kazakhstan University, Ust-Kamenogorsk, Kazakhstan

Mekhtiyev, A.D. - Candidate of techn.sciences, Professor, S. Seifullin Kazakh Agrotechnical University, Nur-Sultan, Kazakhstan

Moiseeva, K.M. – Candidate of phys.-math.sciences, Associative Professor, National Research Tomsk Polytechnic University, Tomsk, Russia

Nazarenko, O.B. – Doctor of techn.sciences, Professor, Tomsk Polytechnic University, Tomsk, Russia

Neshina, Y.G. - Master, Head of Department, Karaganda Technical University, Karaganda, Kazakhstan

Omarova, G.S. – PhD student**,** E.A. Buketov Karaganda University, Karaganda, Kazakhstan

Potapov, A.A. – Doctor of phys.-math.sciences, Professor, V.A. Kotel'nikov Institute of radio engineering and electronics, Russian Academy of sciences, Moscow, Russia; Chief researcher, IREE joint laboratory of fractal method & signal processing, Jinan University, Guangzhou, China

Rakhadilov, B.K. – PhD, Associate Professor, Senior Researcher of the Research center "Surface Engineering and Tribology", S.Amanzholov East Kazakhstan University, Ust-Kamenogorsk, Kazakhstan

Sarsikeyev, Y.Z. - Candidate of techn.sciences, PhD, Head of Department, S. Seifullin Kazakh Agrotechnical University, Nur-Sultan, Kazakhstan

Saulebekov, A.O. – Doctor of phys.-math. sciences, Professor, Professor, Kazakhstan branch of Lomonosov Moscow state University, Nur-Sultan, Kazakhstan

Saulebekova, D.A. - PhD student, Institute Curie, Sorbonne University, Paris, France

Sheveleva, E.A. - Candidate of techn.sciences, Associate Professor, Department of Control and Diagnostics, National Research Tomsk Polytechnic University, Tomsk, Russia

Shishulin, A.V. – Junior researcher, G.A. Razuvaev Institute of Organometallic Chemistry, Russian Academy of sciences, Nizhny Novgorod, Russia

Shishulina, A.V. – PhD, Associate professor, R.E. Alekseev Nizhny Novgorod State technical University, N.I. Lobachevsky Nizhny Novgorod State University, Nizhny Novgorod, Russia

Smirnova, I.N. – Student, Tomsk Polytechnic University, Tomsk, Russia

Stary, Oldrich - Doctor of techn. sciences, Professor, Vice-rector, Czech Technical University in Prague, Prague, Czech Republic

Surzhikov, A.P. - Doctor of phys.-math. sciences, Professor, Head of Department of Control and Diagnostics, National Research Tomsk Polytechnic University, Tomsk, Russia

Tussupbekova, A.K. – PhD, Associate Professor, Physical and Technical Faculty, E.A Buketov Karaganda University, Karaganda, Kazakhstan

Ussipov, N.M. – PhD student, Senior Lecturer, al-Farabi Kazakh National University, Almaty, Kazakhstan

Vitkovskaya, I.S. - Candidate of phys.-math.sciences, Leading researcher, JSC "National Center of Space Research and Technology", Almaty, Kazakhstan

Yugay, V.V. - PhD, Head of Department, Karaganda Technical University, Karaganda, Kazakhstan

Yurov, V.M. - Candidate of phys.-math.sciences, Associate Professor, Director of the Scientific Research Center, E.A. Buketov Karaganda University, Karaganda, Kazakhstan

Zadorozhnaya, T.A. – Candidate of techn.sciences, Assistant professor, Tomsk Polytechnic University, Tomsk, Russia

Zeinidenov, A.K. – PhD, Associate Professor, Dean of the Physical and Technical Faculty, E.A Buketov Karaganda University, Karaganda, Kazakhstan

Zhanabaev, Z.Zh. – Doctor of phys.-math. sciences, Professor, Chief Researcher, al-Farabi Kazakh National University, Almaty, Kazakhstan

About «Eurasian Physical Technical Journal»

ISSN 1811-1165 (Print); ISSN 2413-2179 (Online)
Abbreviated key title: Eurasian phys. tech. j.

Eurasian Physical Technical Journal (Eurasian phys. tech. j.) is a peer-reviewed open access international scientific journal publishing original research results on actual problems of Technical Physics and other related fields. Since 2004 «Eurasian phys. tech. j.» is published in English. E.A. Buketov Karaganda University is the main organizer and financial sponsor of Eurasian phys. tech. j. The international editorial board consists of leading physicists from 8 countries.

Since 2008, "Eurasian Physics and Technology Journal" has been included in the list of publications recommended by the Ministry of Education and Science of the Republic of Kazakhstan for publishing the main results of candidate and doctoral dissertations in physical and mathematical sciences. This status is confirmed in accordance with Science Committee Order No. 52 dated January 28, 2021.

Since May 2019 «Eurasian phys. tech.j.» has been indexed in the Scopus database on four scientific areas: Energy, Engineering, Materials Science, Physics and Astronomy. As of June 4, 2021 (data is updated monthly) Eurasian Physics and Technology Journal's CiteScoreTracker 2020 is 0.5 with a maximum percentile of 23% in Energy, https://www2.scopus.com/sourceid /21100920795#tabs=0

Re-registration Certificate No.KZ50VPY00027647 of the «Eurasian phys. tech. j.» issued October 6, 2020 by Information Committee of the Ministry of Information and Public Development of the Republic of Kazakhstan. According this since 2021 Eurasian phys. tech. j. will be published quarterly.

Publication Ethics and Malpractice Statement

Submission of an article to the Eurasian phys. tech. j. implies that the paper described has not been published previously, that it is not under consideration for publication elsewhere, that its publication is approved by all authors and tacitly or explicitly by the responsible authorities where the paper was carried out, and that, if accepted, it will not be published elsewhere in the same form, in English or in any other language, including electronically without the written consent of the copyright holder. In particular, translations into English of papers already published in another language are not accepted.

For information on Ethics in publishing and Ethical guidelines for journal publication see http://www.elsevier.com/publishingethics and http://www.elsevier.com/journal-authors/ethics.

The Eurasian phys. tech. j. follows the Code of Conduct of the Committee on Publication Ethics (COPE), and follows the COPE Flowcharts for Resolving Cases of Suspected Misconduct (http://publicationethics.org/files/u2/New_Code.pdf).

To verify originality, your article may be checked by the originality detection service Cross Check http://www.elsevier.com/editors/plagdetect.

Authors are responsible for the content of their publications. No other forms of scientific misconduct are allowed, such as plagiarism, falsification, fraudu-lent data, incorrect interpretation of other works, incorrect citations, etc. Authors are obliged to participate in peer review process and be ready to provide corrections, clarifications, retractions and apologies when needed. All authors of a paper should have significantly contributed to the research.

Reviewers should provide objective judgments and should point out relevant published works which are not yet cited. Reviewed articles should be treated confidentially. The reviewers will be chosen in such a way that there is no conflict of interests with respect to the research, the authors and/or the research funders.

Editors have complete responsibility and authority to reject or accept a paper, and they will only accept a paper when reasonably certain. They will preserve anonymity of reviewers and promote publication of corrections, clarifications, retractions and apologies when needed.

The acceptance of a paper automatically implies the copyright transfer to the Eurasian phys. tech. j.

All submitted papers will the sent for reviewing to leading experts in the given area.

The Editorial Board of the Eurasian phys. tech. j. will monitor and safeguard publishing ethics.
The editors reserve the right to accept or reject manuscripts.

GUIDELINES FOR AUTHORS

Research articles are accepted for exclusive publication in the «**Eurasian phys. tech. j.»** in English. The manuscripts must contain original results of investigation in the following scientific areas:

ENERGY;

ENGINEERING;

MATERIALS SCIENCE;

PHYSICS AND ASTRONOMY.

The publications of manuscripts should be recommended by official a Cover letter of the organization (University) in which the work was performed.

The author who submitted an article for publication will be considered as a corresponding author.

A scientific article should contain the results of original scientific research previously unpublished and not intended for publication in other publications. Scientific articles submitted for publication in scientific journals should comprise at least 70% of the original text.

The structure of the article includes the following sections:

Title: includes a separate line on the left the **UDC** index, information about the authors (surname and initials, name of institution, city, country, e-mail of a corresponding author, title of the article.

Abstract should consist of at least 5-6 sentences, not exceeding 200 words without formula, references, abbreviations. An abstract is a short and powerful summary that describes the focus of a research paper. It could contain the information about why the research study was done, background, what the methodology was and something about the findings of the author(s).

Keywords: at least 3-10 basic terms or short phrases used in the article.

The text should be divided on structural parts: **Introduction, Theoretical part, Methods and materials or Experimental technique, Results and Discussion, Conclusions**.

Conclusions: formulating main results; a comparison of the results with the existing data on this topic; assessment of scientific novelty and practical value of the results**.**

Acknowledgments may be shown at the end of the article text, before References**.**

References: a bibliographic list is compiled according to the requirements:

- Books, abstracts, patents: Surname and initials of the authors (it is enough to indicate the first three or one surnames, et al), *Title of the book* in italics, publish house or city, year and total number of pages.

- Journals, collections of papers, conference proceedings - Surname and initials of the authors (the first three are enough), the title of the article, the *Title of the journal* in italics (you can use the abbreviated title), city and / or country, year, volume, issue number, pages of the "begining and end" (pp. … - … .).

- Internet links also must to indicated the authors, the title and URL

Title, Abstract and Keywords are given in English, Qazaq, and Russian.

The volume of the article, including bibliography, should not exceed 6-10 pages including tables, figures (no more than 6-8) and references (no more than 30-35) of text typed on a computer (Microsoft Word editor. A review paper must not be more than 15-20 pages (including no more than 10 figures).

Fields of the manuscript should be: left, upper, lower - 30 mm, right - 15 mm; font - Times New Roman, size - 11 pt; line spacing - single; alignment - in width; indent - 0.8 cm.

All abbreviations and acronyms, with the exception of obviously well-known, should be deciphered at first use in the text.

All references must be numbered in the text (for example, [1], [2-4]) and listed in numerical order.

Equations in your paper have to be written using the Microsoft Equation Editor or the MathType.

Tables must be inserted into the text.

Figures should be prepared in a digital form suitable for direct reproduction. Figures shall be submitted on the separate sheets or can be included into the text.

The following files must be submitted via e-mail:

- Article text (*.doc);
- Figures (fig1.jpg, fig2.pcx, …);
- Figure captions (*.doc).

The file should be contained data about all authors, organizations, postal code, postal address, telephone, fax, E-mail, scientific topic of the paper, and Cover letter.

It is possible to use **rar** or **zip** compressors and to transmit the files as an attachment.

Title page (specimen)

UDC

TITLE

Smith J.H., Zeinidenov A.K. Cooper H.J.*

E.A. Buketov Karaganda University, Karaganda, Kazakhstan, email@for_correspondence.kz

Abstract: 5-6 sentences

Keywords: no less 3, but no more 10.

Introduction

Article text. Article text. Article text. Article text. Article text. Article text. Article text. Article text. Article text. Article text Article text. Article text. Article text. Article text. Article text Article text. Article text. Article text. Article text. Article text Article text. Article text. Article text. Article text. Article text Article text. Article text. Article text. Article text. Article text……

References Format (specimen)

1 Conrad H., Muhlbauer A., Thomas R. *Elektrothermische Verfahrenstechnik*. Vulkan-Verlag, Essen Publ. House, 2008, 240 p.

2 Nahar J., Wahedra M. Elastic scattering of positrons and electrons by argon. *Physical Rewiew A,* 2016, Vol. 35, No. 5, pp. 2051 – 2064.

3 Rivoalen H., et al. Electrotubular heat exchanger in chemical industry. *Proceeding of the 12th Intern. Congress on Electricity Applications.* Birmingham, 2017, pp. 29 – 39.

4 Muravleva O. Resource saving prospects based on accuracy theory. *Proceeding of the Intern. Conf. on Computer as a Tool.* 2007*,* pp. 1845-1850, doi: 10.1109/EURCON.2007.4400413.

5 Bochkarev V.P. *Development of physical and chemical principles for assessing the effect of surface energy on the properties of materials and processes for microelectronic technology*. Doctor Diss. of the Techn. Science degree, Moscow, 2020. - 299 p. [in Russian]

6 Zhanabaev Z.Zh., Ibraimov M.K., Sagidolda E. Electrical properties of fractal nanofilms of porous silicon. *Eurasian phys. tech. j.* 2013, Vol. 10, No. 1(25), pp. 3 – 6.

7 X-ray Oxford-Instruments Microfocus Tubes. Available at: www.oxford-instruments.com/products/x-ray-tubes-and-integrated-sources/microfocus-x-ray-systems (Jan13, 2020).

The authors should represent References according to the requirements of international journals on physics, but should to consult preliminarily for standard abbrevi-ations of journal's names.

For more information on references guidelines for journal publication you see Harvard reference system: http://www.emeraldgrouppublishing.com/authors/guides/write/harvard.htm?part=2